BODLEIAN LIBRARY OXFORD
DEPOSITED
THESIS
22-8-84

Some Aspects of High Voltage Electron Radiation Damage Studies in Copper Aluminium Alloys

Volume 2

Figures and Plates

DAVID WILSON

Corpus Christi College

Oxford

A dissertation submitted for the degree of

Doctor of Philosophy in the University of Oxford

January, 1978.

Fig. 1/1. Displacement cross sections for copper as calculated by Oen (1965).

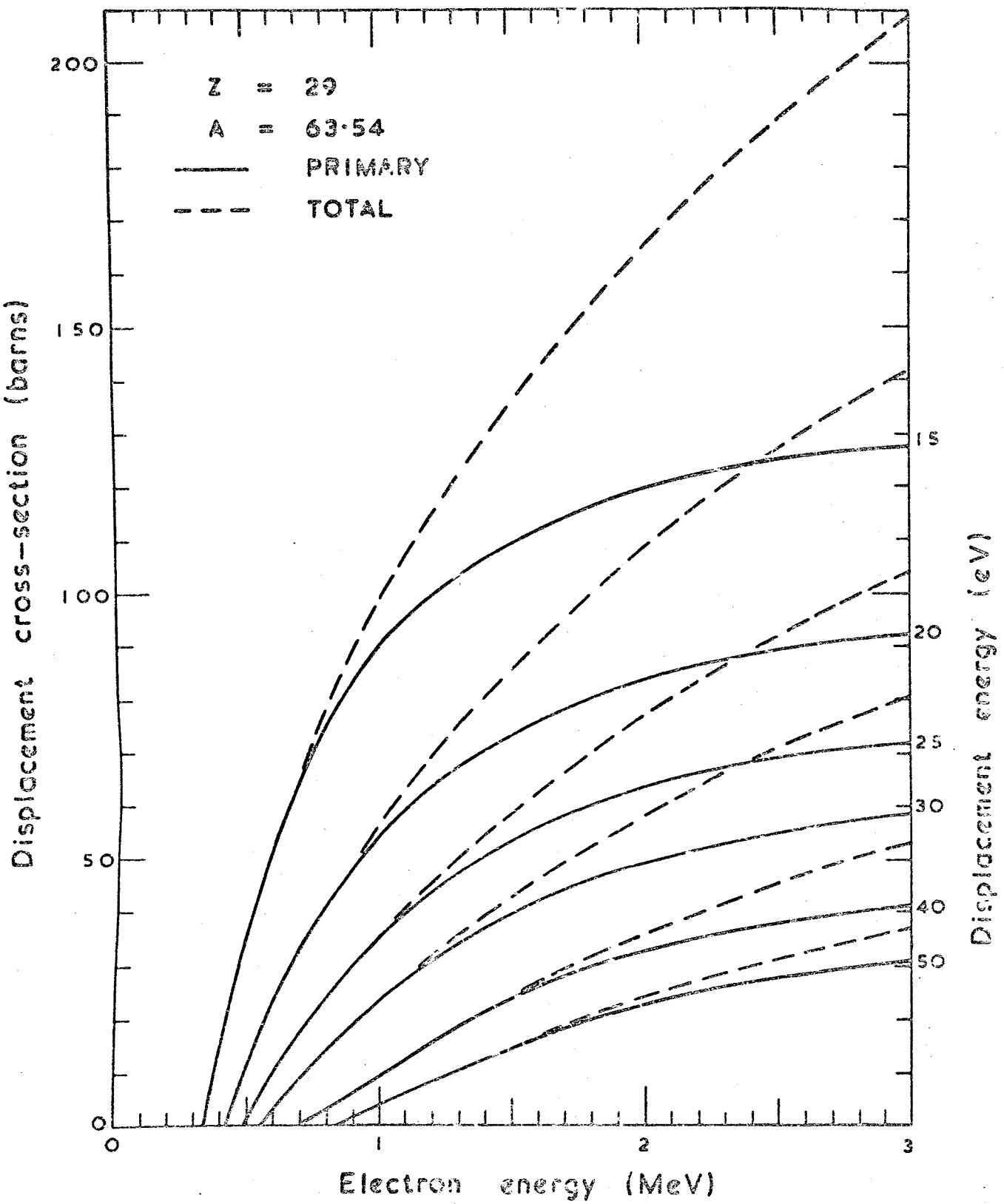
Z = 29
A = 63·54
PRIMARY
TOTAL
Displacement cross-section (barns)
Displacement energy (eV)
Electron energy (MeV)
200
150
100
50
0
0
1
2
3
15
20
25
30
40
50

Fig. 2/1 illustrates the effects that changes in the jetting current have on the disc profile.

Specimens were polished using different currents, and examined in a stereomicroscope. Profile (D) was found to give the best specimens and all subsequent foils were polished using the same conditions.

When the final electropolishing takes place, it is normal practice to hold the specimen in the tweezers as shown in (F). However, if the foil is held as shown in (E), improved specimens were obtained since the viscous layer on the foil surface was not disturbed by the bubbles or sediment falling from the specimen-tweezer contact area.

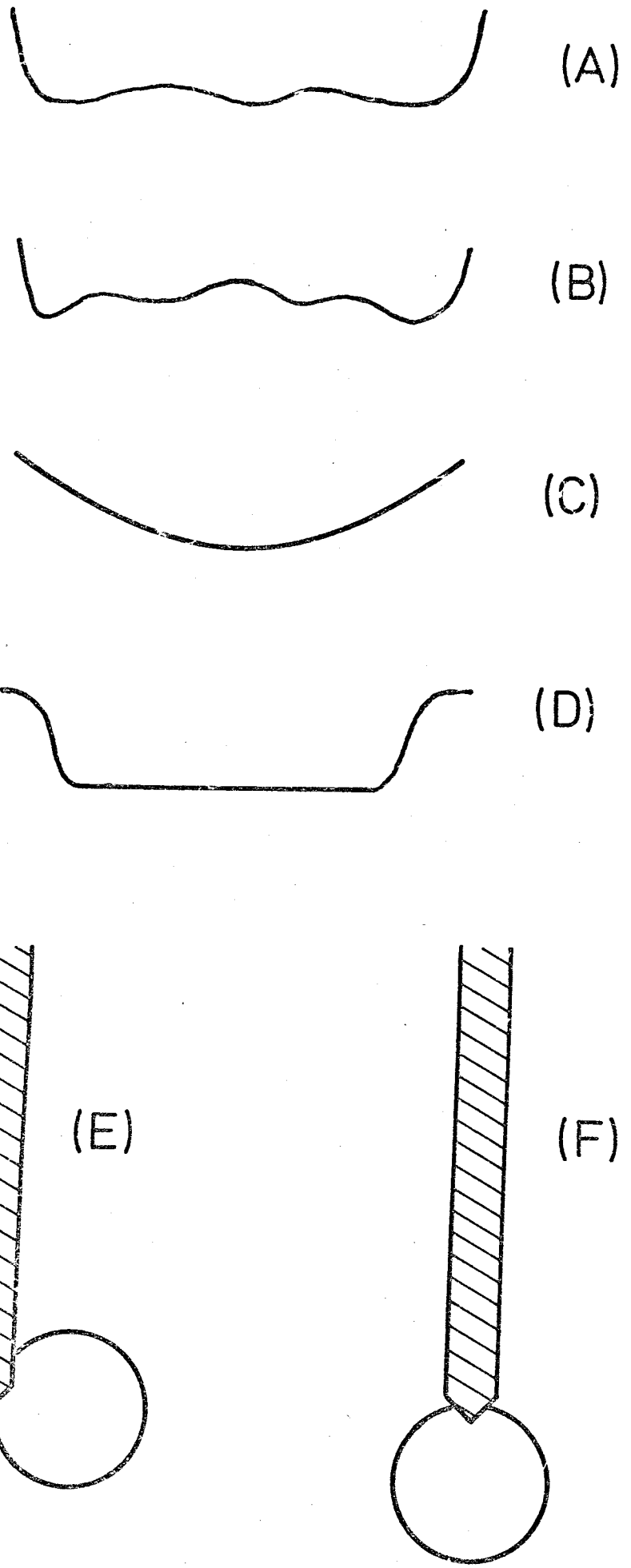
(A)
(B)
(C)
(D)
(E)
(F)

Fig. 2.2 shows the change in jet polish removal rate for copper foils, as the temperature of the electrolyte varied.

The temperature of the electrolyte varied between 15° and $27^{o}C$, depending on the number of specimens polished and the temperature of the laboratory. Since low temperature final electropolish removal rates were found to be $\triangleq$ 600 times slower than the jetting rate, accurate polish rates were required, to reduce the time of final polish. Since each specimen jetted caused an increase in electrolyte temperature graphs of removal rate as a function of temperature were plotted. In this way the removal rate for any of the alloys at any given temperature could accurately be forecast, and final electropolish times of 90 minutes reduced to $\triangleq$ 25 minutes.

It was also necessary to replace the electrolyte frequently since contamination affected the removal rate.

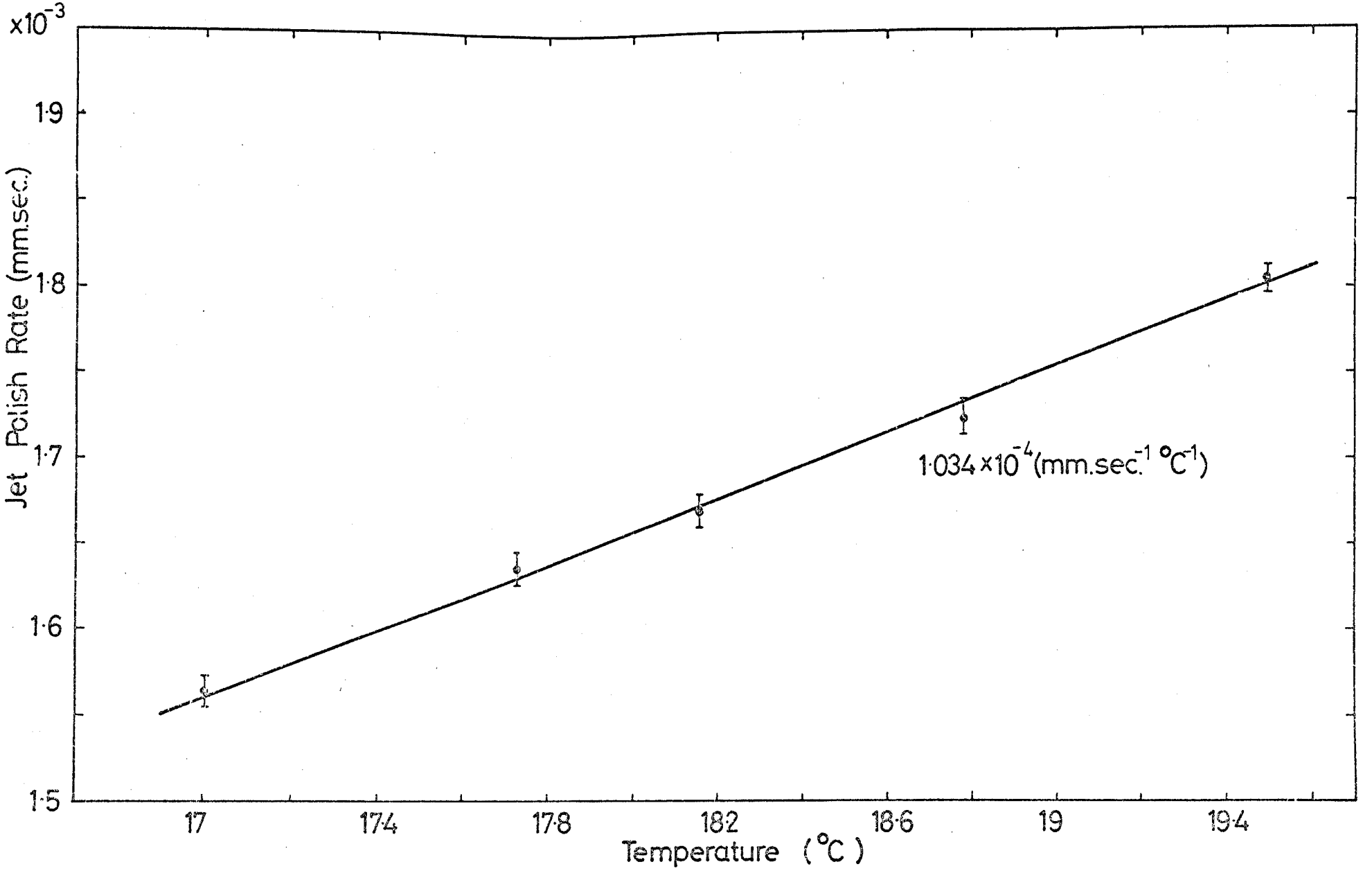
x10⁻³
1·9
1·8
1·7
1·6
1·5
Jet Polish Rate (mm.sec.)
1·034 x 10⁻⁴ (mm.sec.⁻¹ °C⁻¹)
17
17·4
17·8
18·2
18·6
19
19·4
Temperature (°C)

Fig. 2/3 Specimen Electropolish equipment.

(A) Thermometer to ensure a constant electropolish temperature.

(B) Double walled glass beaker (500 c.c.)

(C) Optical window

(D) Variable speed magnetic stirrer

(E) Asbestos covering

(F) Viewing telescope

(G) Stainless steel cathode

(H) Magnet to hold tweezers

(I) Lacquered tweezers

(J) Outlet to liquid nitrogen dewar and pump

(K) Light source

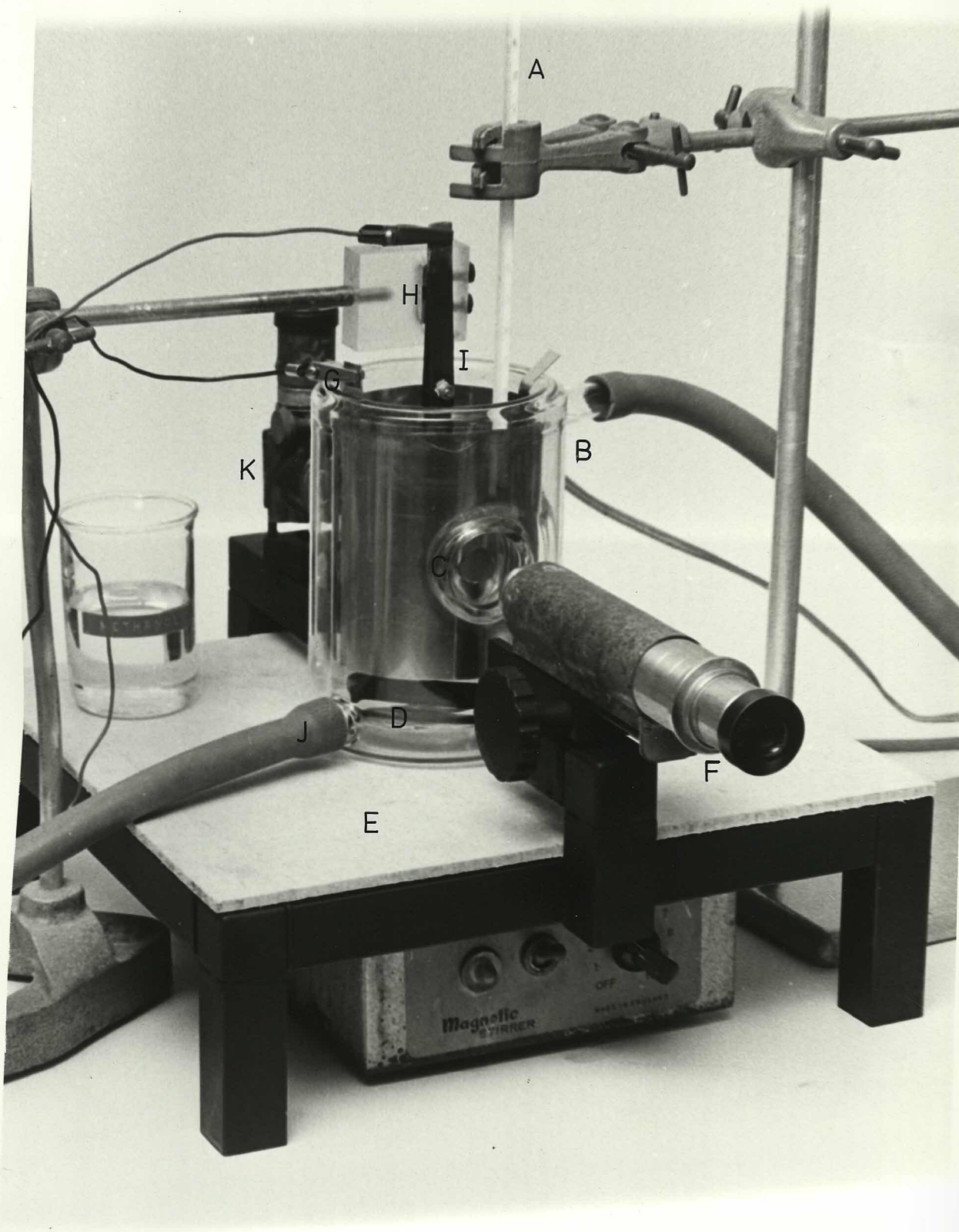
A
H
I
G
K
B
C
D
J
F
E
Magnetic
STIRRER
OFF

Fig. 3/1 (A) The Thomson Tetrahedron. Atom D is at 0,0,0 and those at A, B and C are $(\frac{1}{2},0,\frac{1}{2})$, $(0,\frac{1}{2},\frac{1}{2})$ and $(\frac{1}{2},\frac{1}{2},0)$.

$\overline{AB}$ are lattice vectors

$\overline{A\delta}$ are the Burger's vectors of Shockley partials

(B) Tetrahedron opened at D.

α, β, γ and δ represent the planes $(\bar{1}1\bar{1})$, $(1\bar{1}\bar{1})$, $(\bar{1}\bar{1}1)$ and (111). The direction of the plane normals are out of the tetrahedron.

$\overline{AB}$ direction and magnitude of Burger's vector $\frac{a}{2}[\bar{1}10]$

$\overline{A\delta}$ direction and magnitude of Burger's vector $\frac{a}{6}[\bar{1}2\bar{1}]$

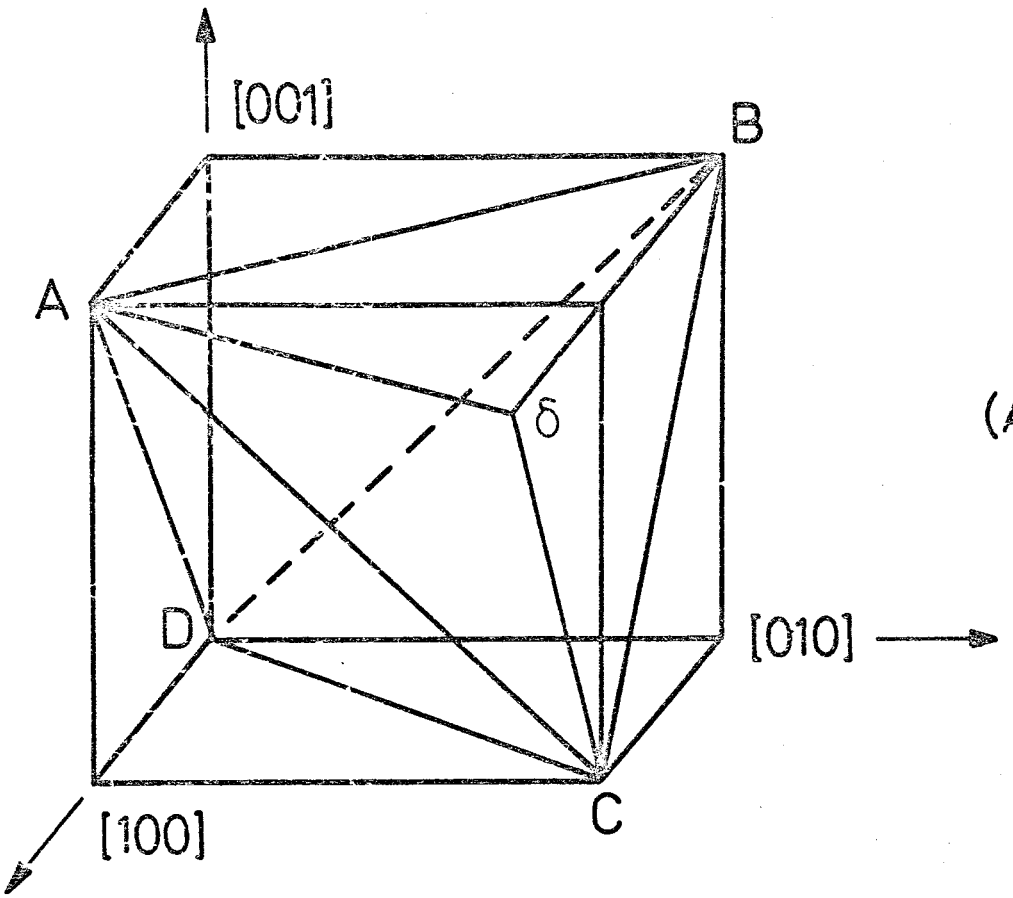
[001]
B
A
δ
D
[010]
C
[100]

(A)

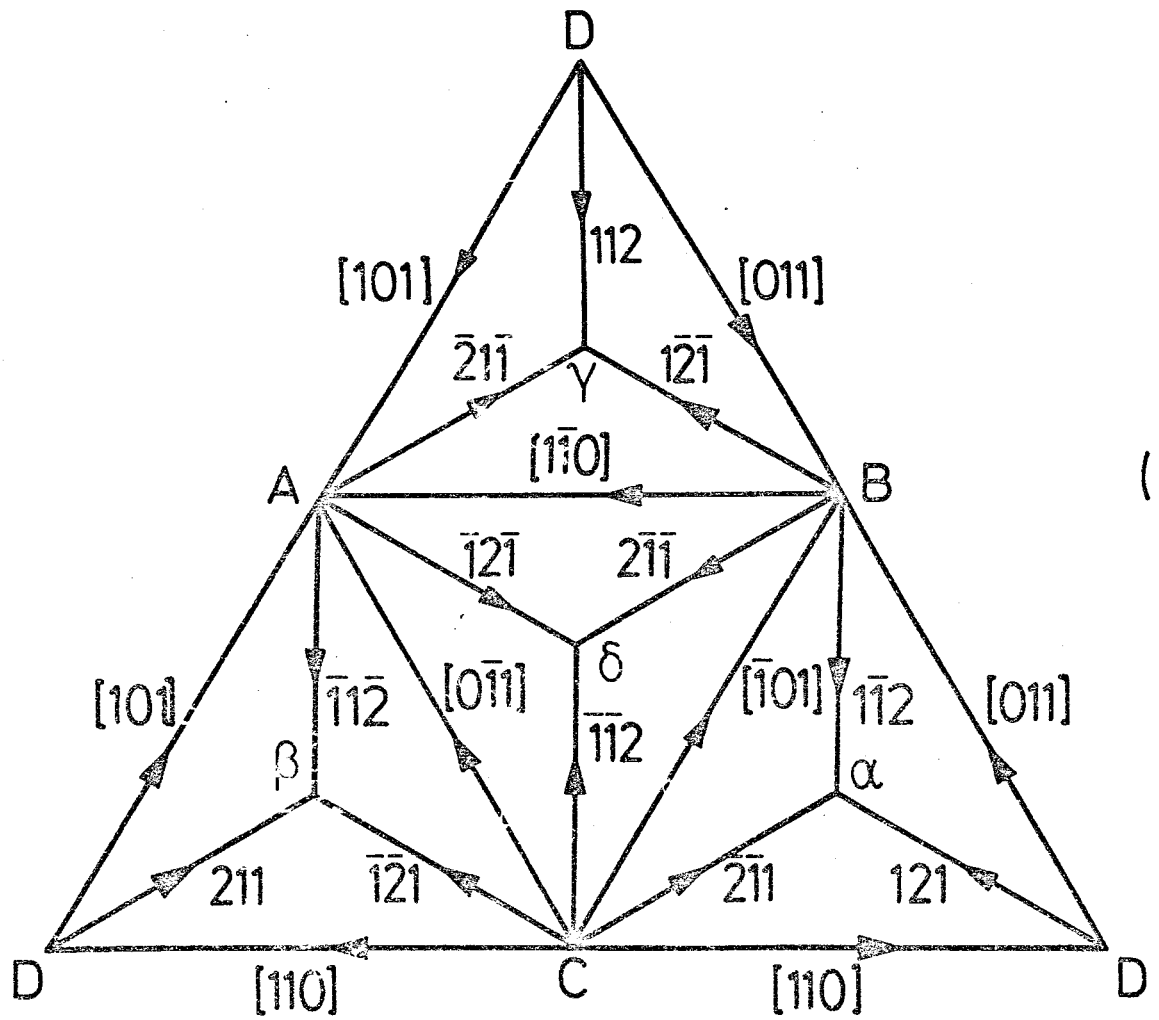
D
112
[101]
[011]
2̄11̄
γ
12̄1̄
[11̄0]
A
B
1̄2̄1̄
2̄11̄
[10̄1]
1̄11̄2
[01̄1]
δ
[1̄01]
11̄2
[011]
β
1̄12̄
α
211
1̄21
2̄11
121
D
[110]
C
[110]
D

(B)

Fig. 3/2 illustrates the possible ways of orientating the Thompson tetrahedron, for the analysis of the inside/outside contrast of dislocation loops.

Orientations (A) and (B) are identical in that g $[\bar{2}20]$ points to the left. Orientations (C) and (D) are also identical in that g $[2\bar{2}0]$ points to the right.

(A) and (C) are the orientations where the apex D points into the plane of the paper.

In this thesis, the tetrahedron was used, with the apex D pointing downwards and the direction [111] upwards. Using this convention, the labelling of the diffraction vector is given by figure (E), when looking from above.

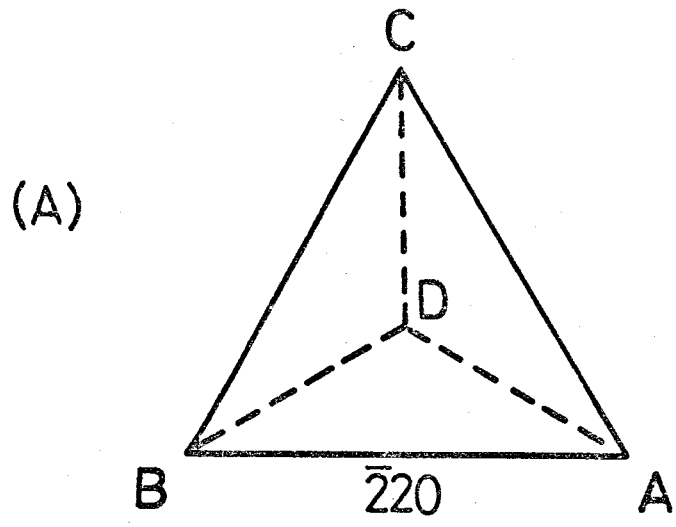
(A)
C
D
B
$\bar{2}20$
A

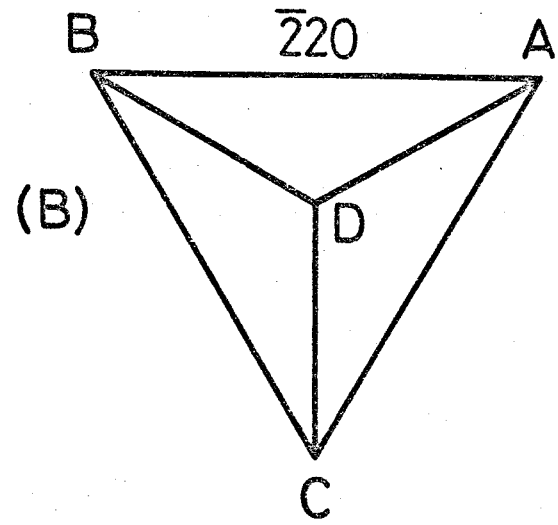
(B)
B
$\bar{2}20$
A
D
C

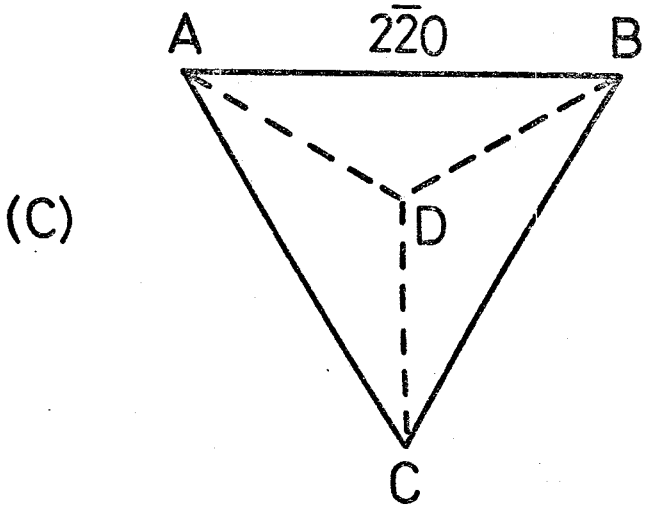
(C)
A
$2\bar{2}0$
B
D
C

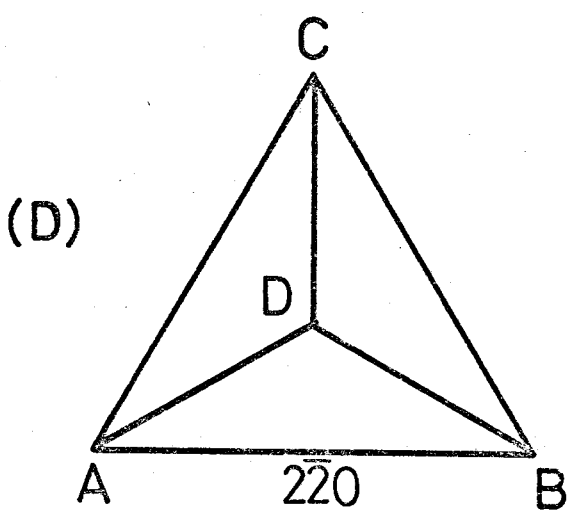
(D)
C
D
A
$2\bar{2}0$
B

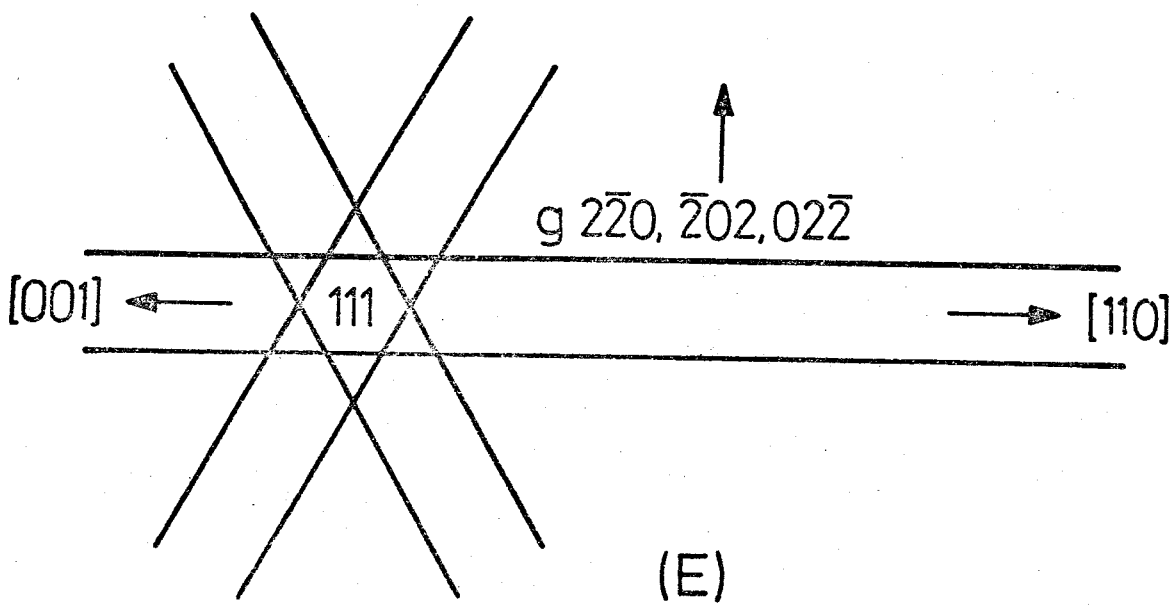
g $2\bar{2}0$, $\bar{2}02$, $02\bar{2}$
[001]
111
[110]
(E)

Fig. 3/3 Convention used in this thesis for characterizing the sense of irradiation produced loops.

All micrographs were printed emulsion up. In the analysis, the FS.RH convention was used.

These conventions define the conditions for interstitial loops

$$(g.b)s > 0 \text{ and } \bar{n}.\bar{b} \quad 0$$

where $\bar{n}$ = loop normal

$\bar{b}$ = loop Burger's vector

g = diffraction vector

s = deviation from Bragg angle

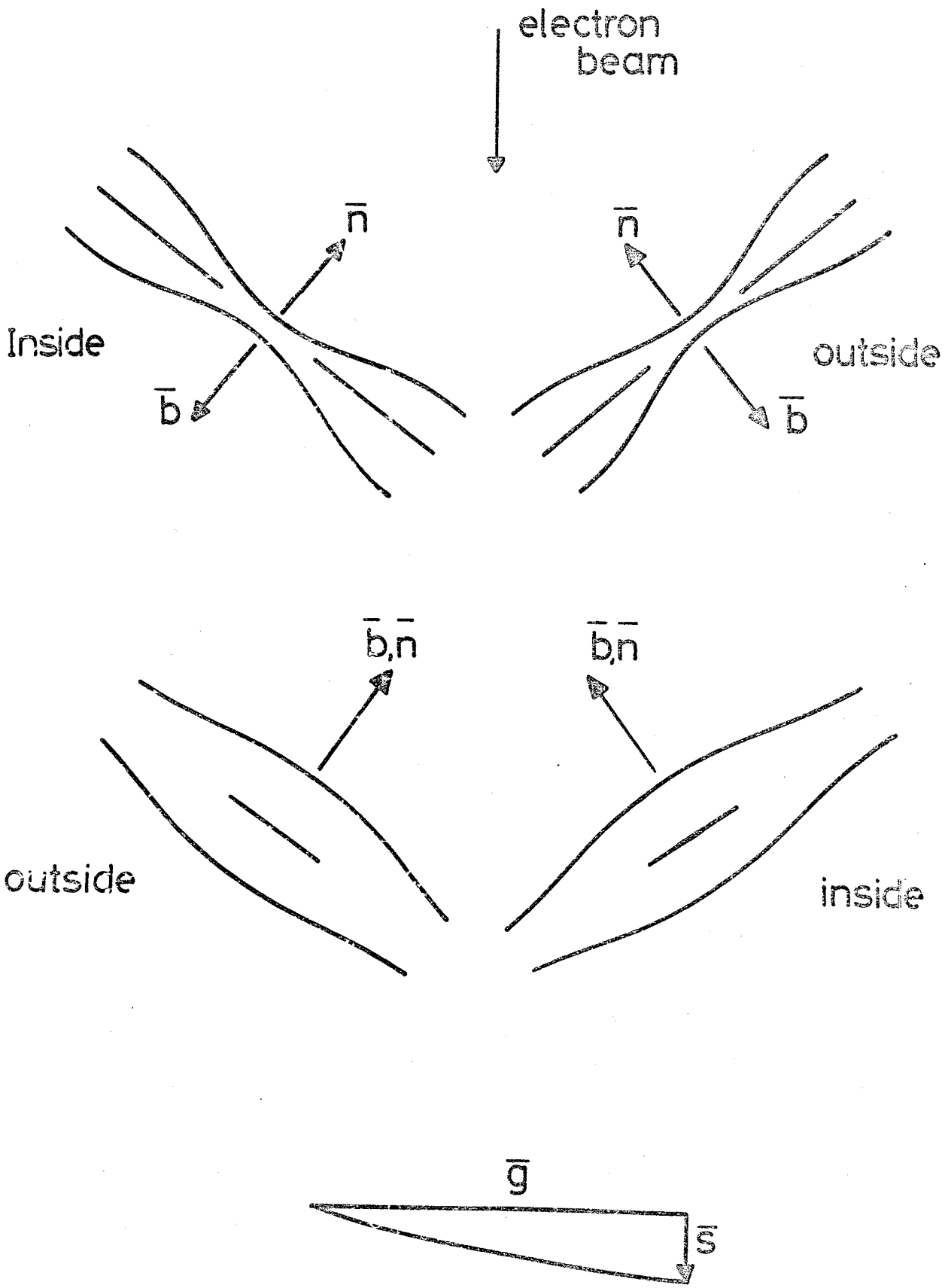
electron
beam
$\bar{n}$
$\bar{n}$
Inside
outside
$\bar{b}$
$\bar{b}$
$\bar{b},\bar{n}$
$\bar{b},\bar{n}$
outside
inside
$\bar{g}$
$\bar{s}$

Fig. 3/4 Burger's vector analysis of Frank loops in a Cu .007% Al specimen.

loop A $\bar{b} = \frac{a}{3}[111]$

loop B $\bar{b} = \frac{a}{3}[11\bar{1}]$

loop C $\bar{b} = \frac{a}{3}[\bar{1}11]$

loop D $\bar{b} = \frac{a}{3}[1\bar{1}1]$

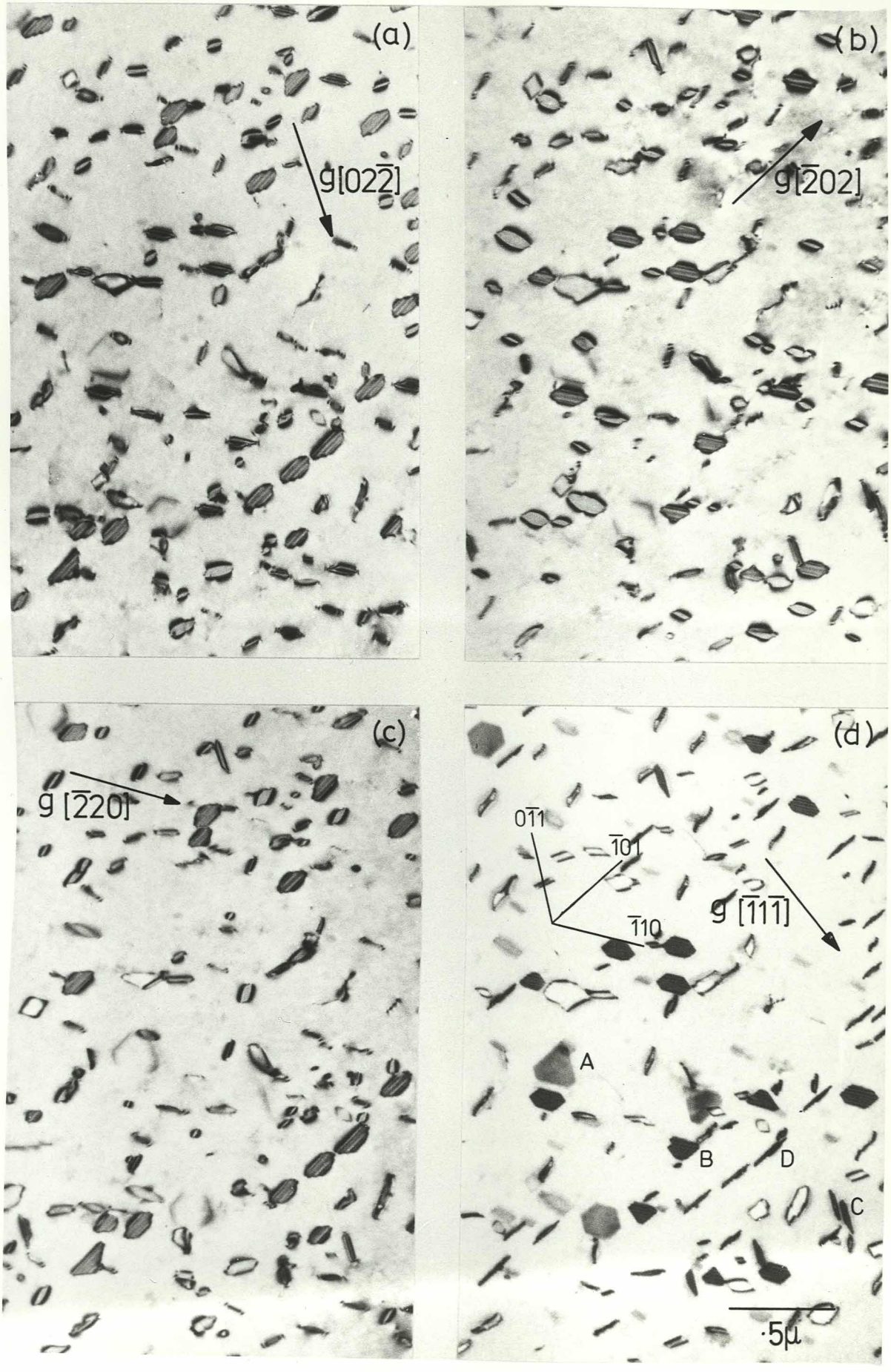
(a)
g[02$\bar{2}$]
(b)
g[$\bar{2}$02]
(c)
g [$\bar{2}$20]
(d)
0$\bar{1}$1
$\bar{1}$01
$\bar{1}$10
g [$\bar{1}\bar{1}\bar{1}$]
A
B
D
C
·5μ

Fig. 3/5 Inside-outside contrast analysis of electron produced Frank loops in copper

$g = \pm [\bar{1}13]$

$\bar{z} = [110]$

loop 1 $\vec{b} = \frac{a}{3}[111]$

loop 2 $\vec{b} = \frac{a}{3}[11\bar{1}]$

$(g.b)s > 0$ for interstitial loops FS/RH convention.

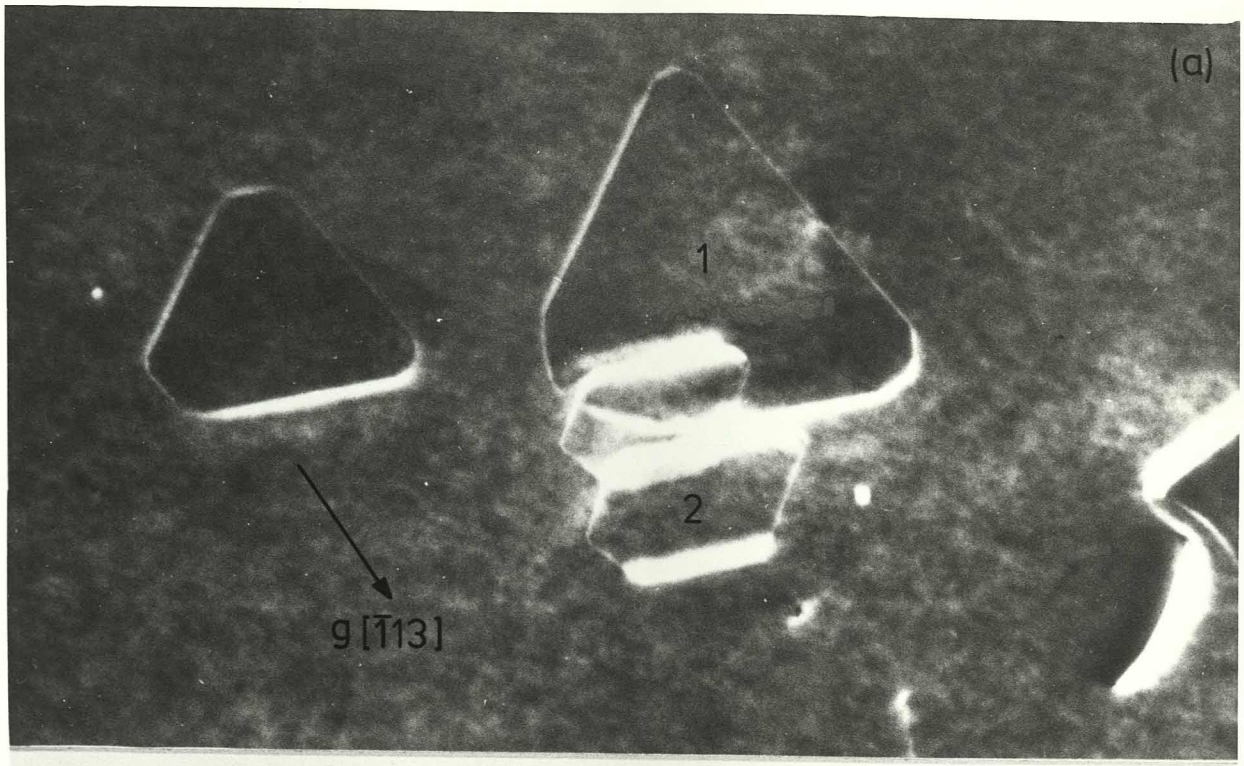
(a)
1
2
g [$\bar{1}$13]

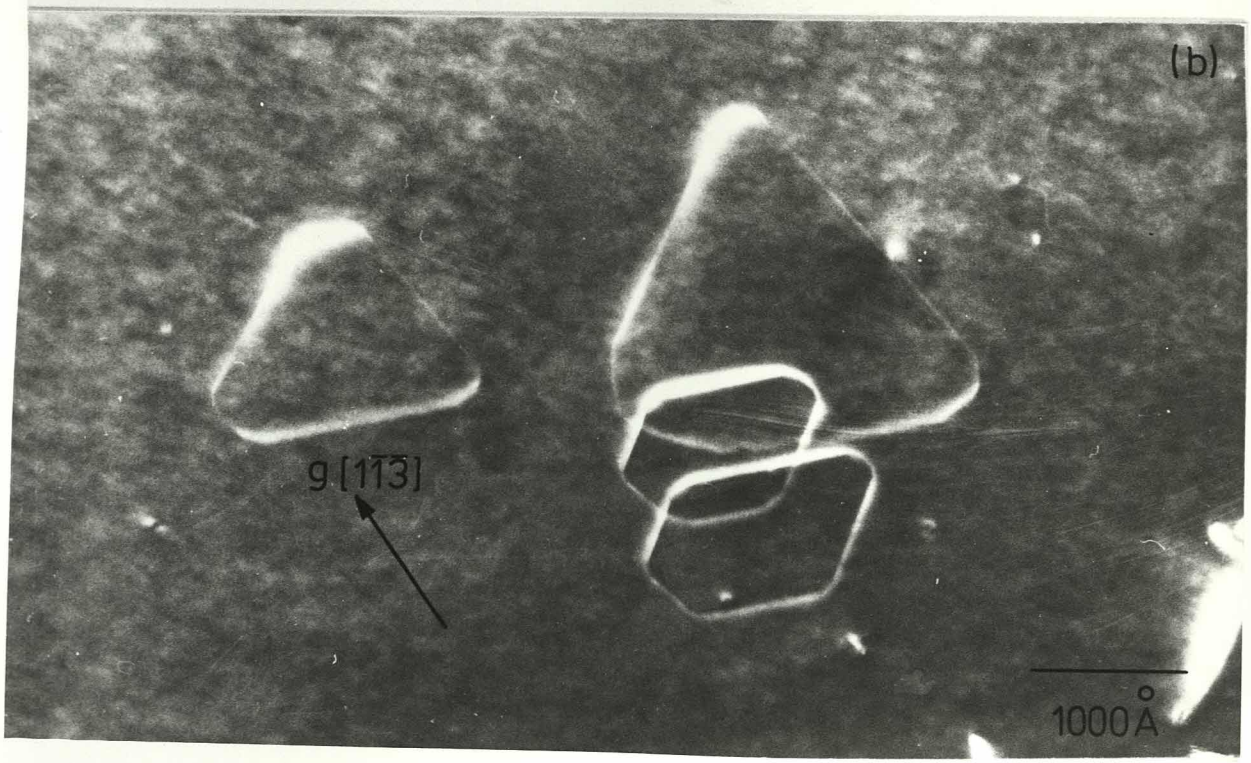
(b)
g [1$\bar{1}$3]
1000 Å

Fig. 3/6 Analysis of the nature of Frank loops in a foil of Cu 16% Al using $g.b = \pm \frac{2}{3}$ criteria.

(A) and (B) imaged at $\bar{z} = [101]$

(C) and (D) imaged at $\bar{z} = [\bar{1}10]$

Foil annealed for 5 minutes at 550°C in the H.V.E.M. prior to irradiation.

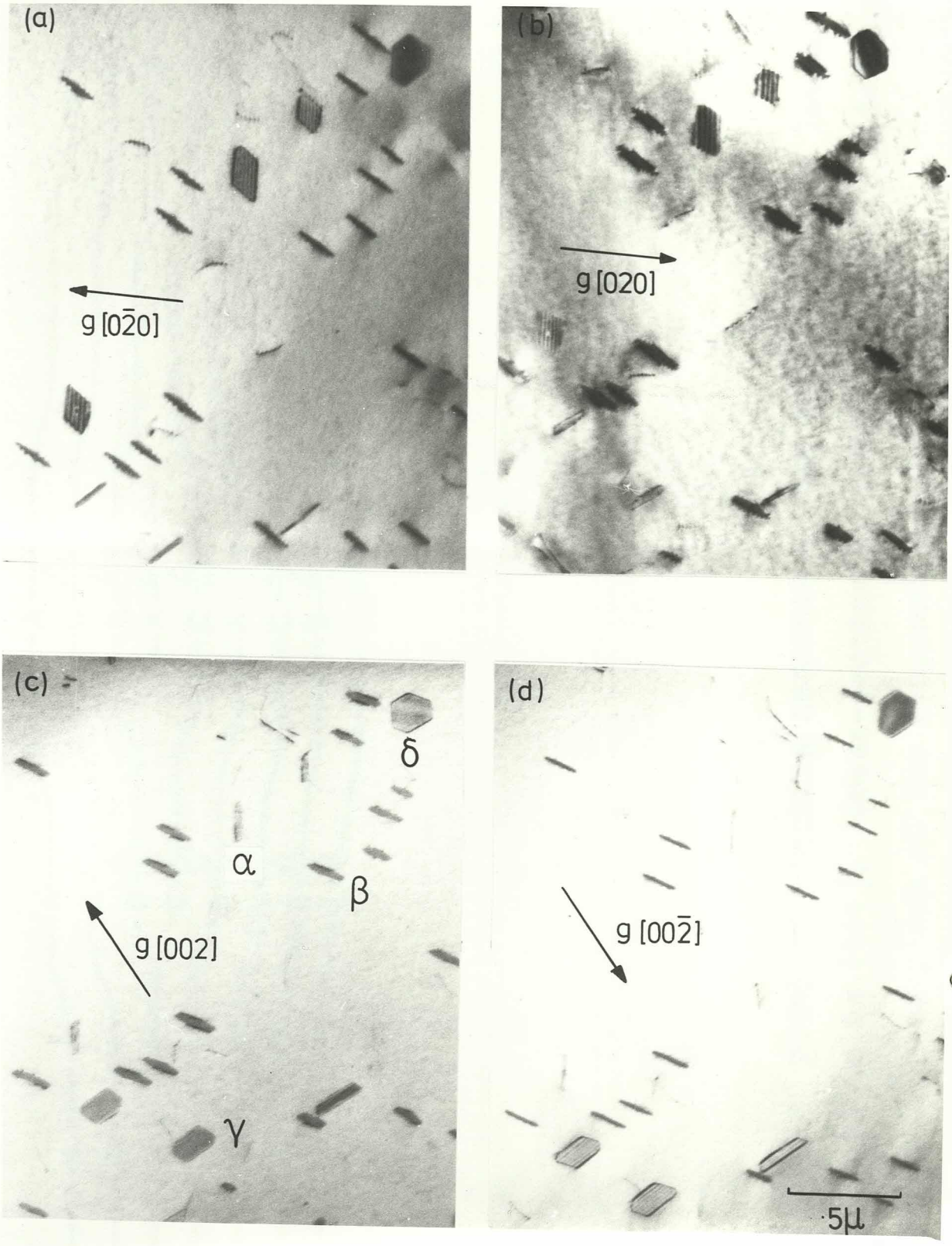
(a)
g [0$\bar{2}$0]
(b)
g [020]
(c)
δ
α
β
g [002]
γ
(d)
g [00$\bar{2}$]
5μ

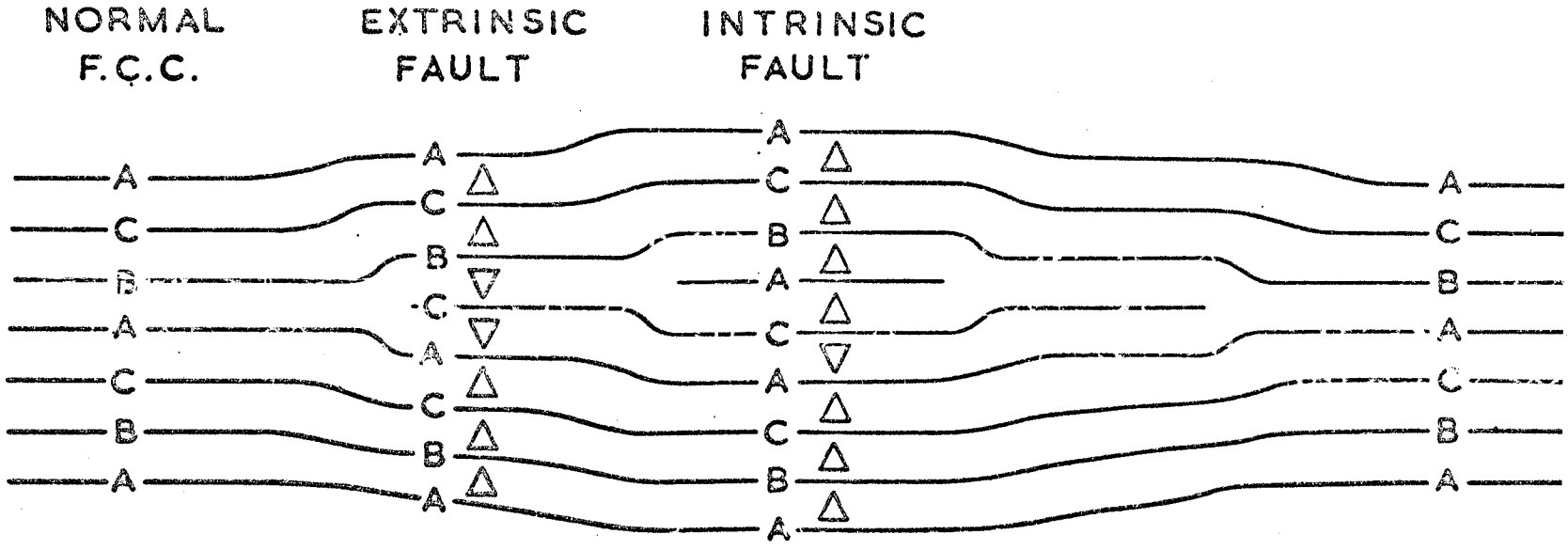

Model of possible stacking sequence of the double-faulted loops. Loop plane is (111). Cross-section is viewed from $(10\bar{1})$ which is normal to the plane of the compound loop.

Fig. 3/8 Irregular Frank loops grown in Cu 16% Al foils at $\triangleq 260^{\circ}C$.

The loops on the (111) planes, parallel to the foil surface develop edges along directions other than <110>, as a result of the interaction of neighbouring loops or dislocations.

The large Frank partial dissociation allows the loops to grow to very large sizes, before becoming unstable.

(Fast grown crystal.)

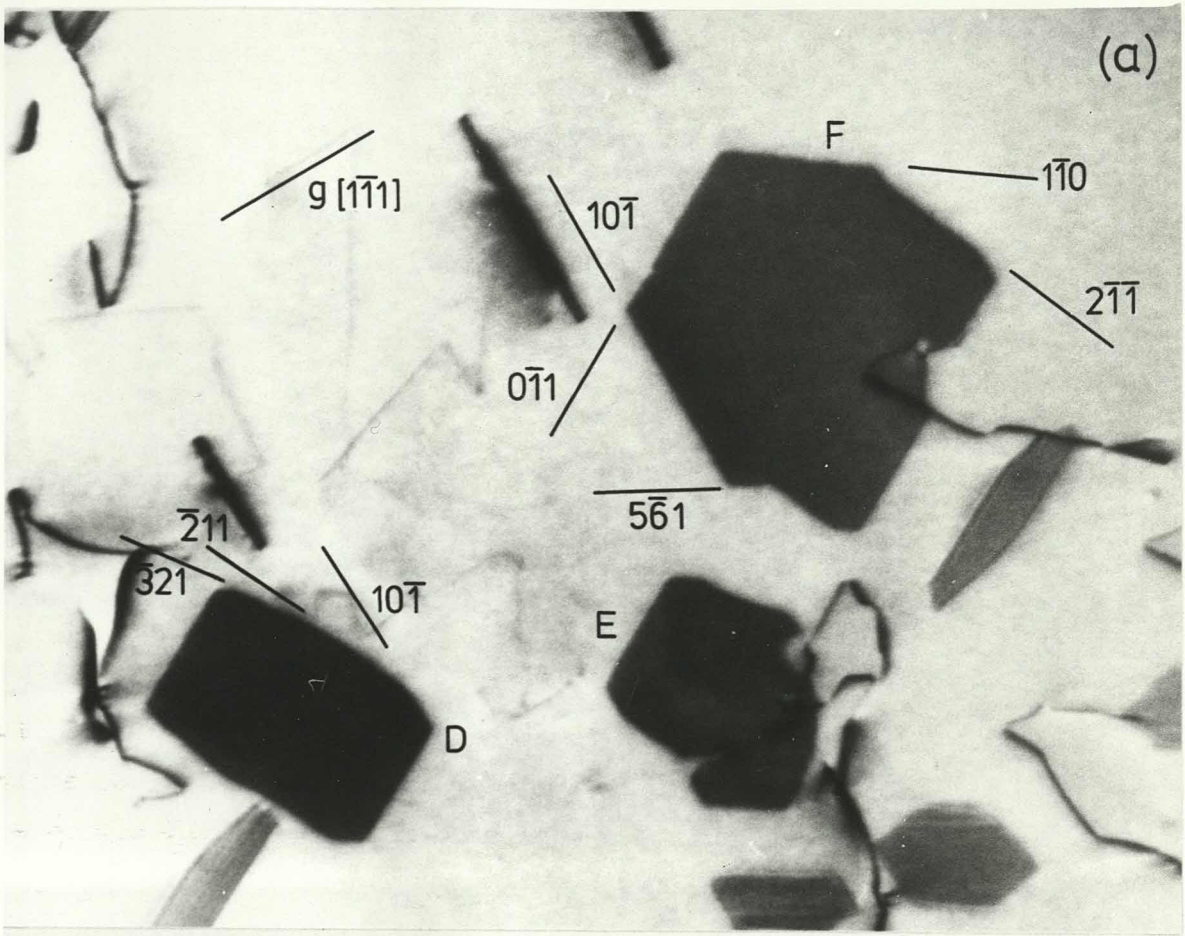
(a)
g [1$\bar{1}$1]
10$\bar{1}$
F
1$\bar{1}$0
2$\bar{1}$1
0$\bar{1}$1
5$\bar{6}$1
$\bar{2}$11
$\bar{3}$21
10$\bar{1}$
E
D

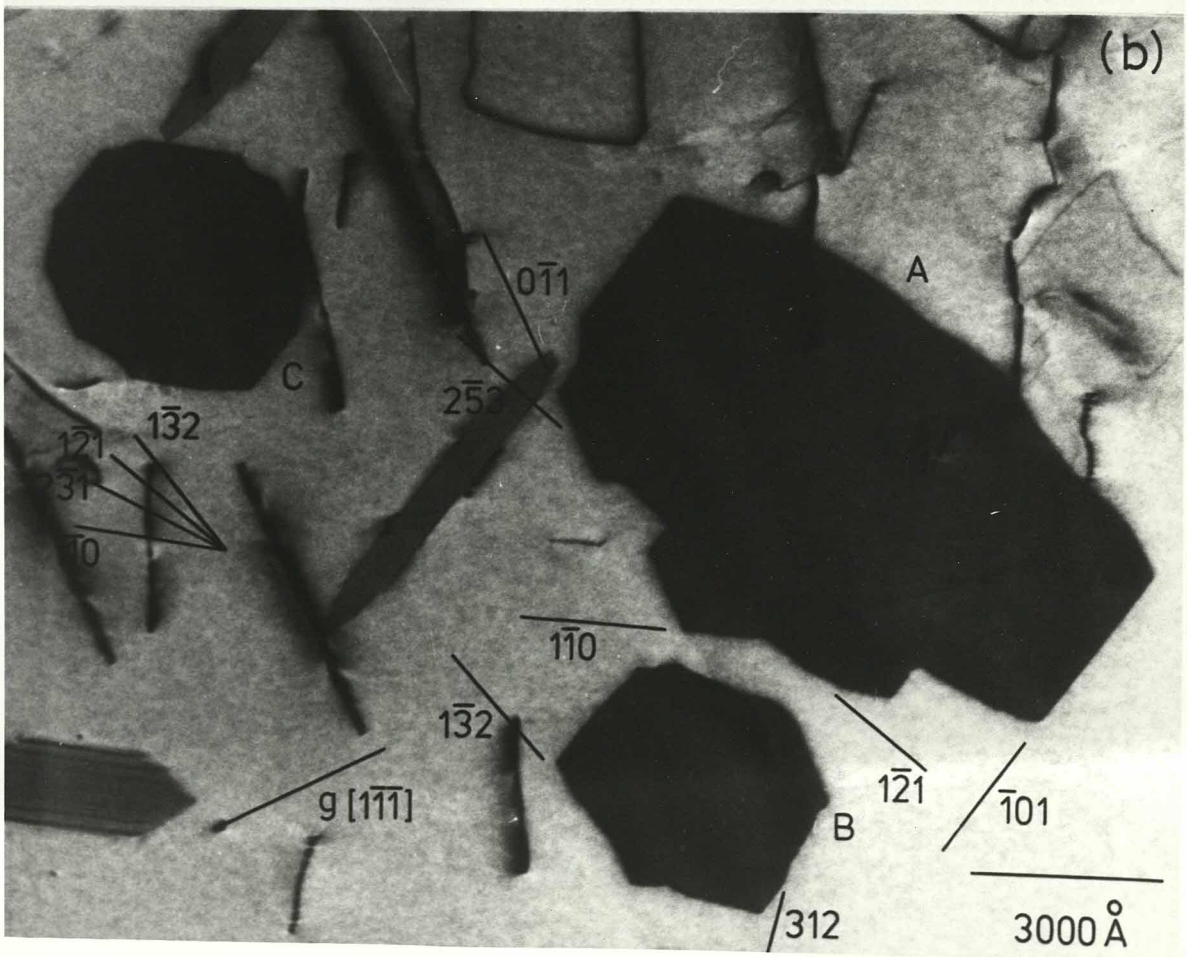
(b)
0$\bar{1}$1
A
C
2$\bar{5}$3
1$\bar{3}$2
1$\bar{2}$1
$\bar{3}$1
$\bar{1}$0
1$\bar{1}$0
1$\bar{3}$2
g [1$\bar{1}$1]
B
1$\bar{2}$1
$\bar{1}$01
312
3000 Å

Fig. 3.9 Large irregular Frank loops growing parallel to the foil surface.

(A) Cu 5% Al. This loop originated as a trapezium shape. T_i = 308°C.

(B) Isolated triangular loop in Cu 16% Al foil that has developed additional edges along <112>, <123> and <532> directions. T_i = 260°C.

(Fast grown crystals.)

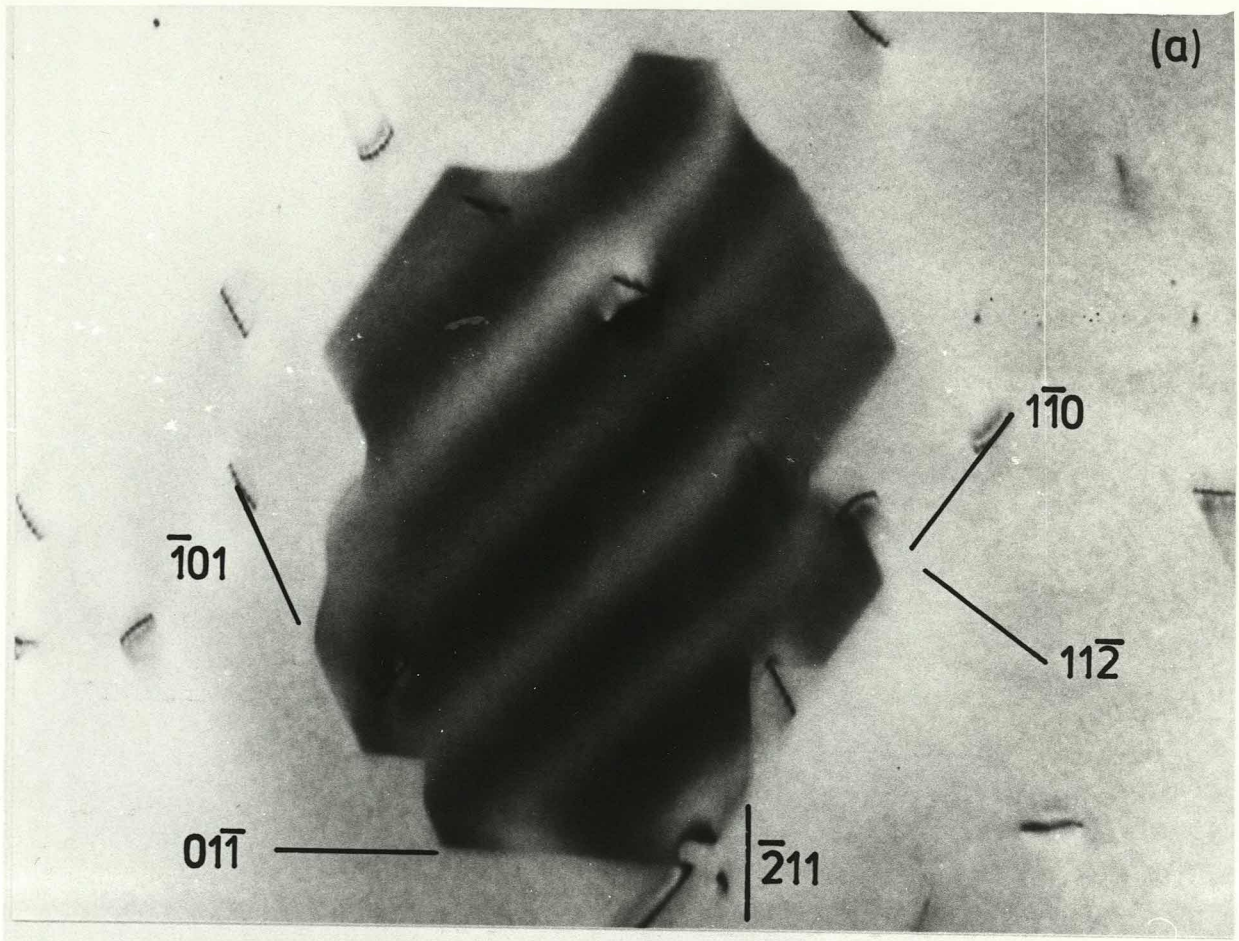
(a)
$1\bar{1}0$
$\bar{1}01$
$11\bar{2}$
$01\bar{1}$
$\bar{2}11$

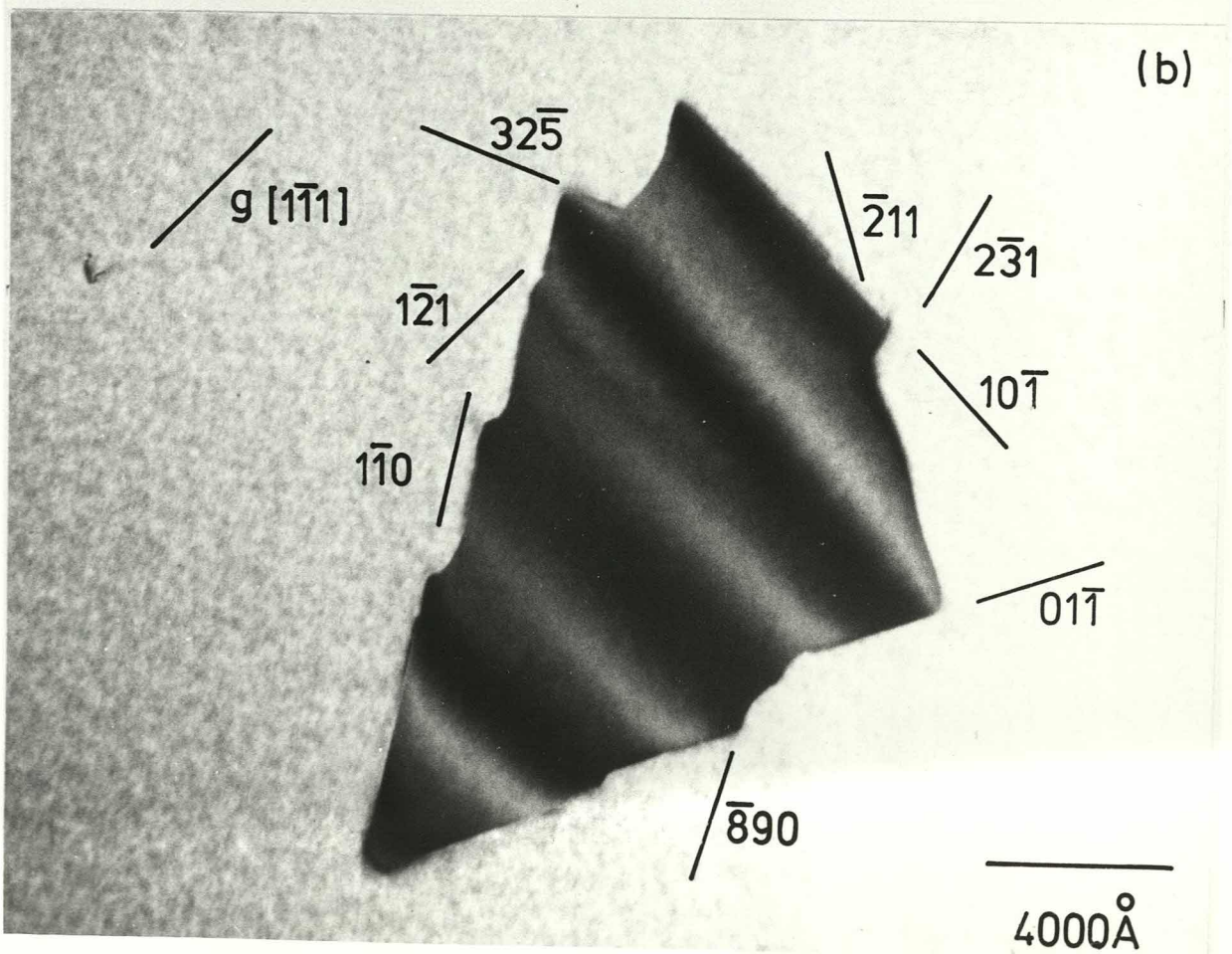
(b)
$32\bar{5}$
g [$1\bar{1}1$]
$\bar{2}11$
$2\bar{3}1$
$12\bar{1}$
$10\bar{1}$
$1\bar{1}0$
$01\bar{1}$
$\bar{8}90$
4000Å

Fig. 3/10 Growth of petal shaped loops in a foil of copper after 20 minutes irradiation at $\simeq 220^{\circ}C$.

The Frank loops develop curved edges, indicative of the presence of vacancies. These loop shapes contrast with the straight edged irregular Frank loops observed growing in Cu 16% Al under the same conditions.

A further contrast, is that there is no nucleation of small loops after the initial nucleation stage has passed. Loops α and β, which have sheared from Frank loops have sides of greater curvature, indicative of greater rotation than the corresponding loops in Cu/Al alloys.

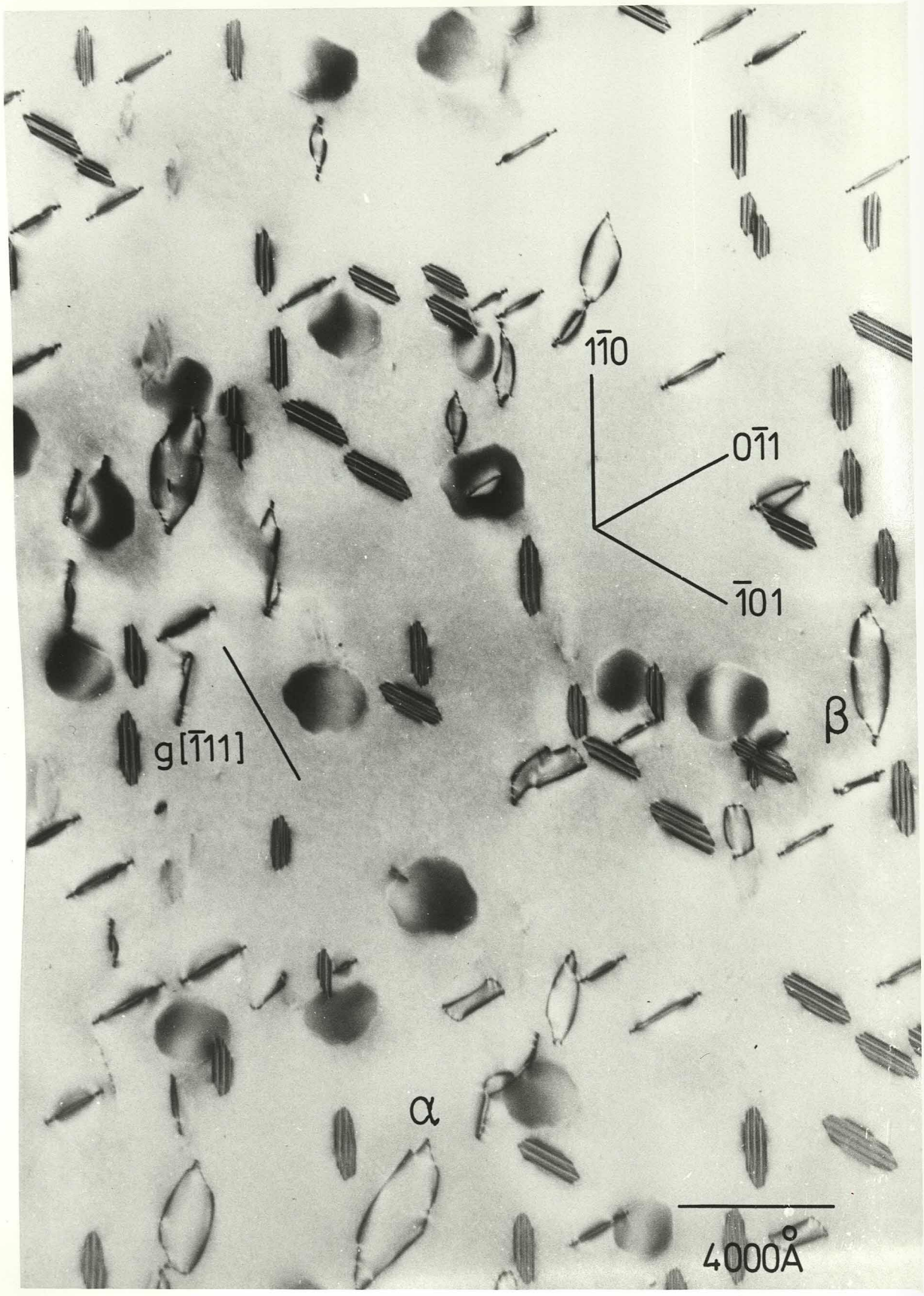
1$\bar{1}$0
0$\bar{1}$1
$\bar{1}$01
g[$\bar{1}$11]
β
α
4000Å

Fig. 3/11 shows the Frank dislocation dissociation reaction

$$\delta D = \delta\gamma + \delta D$$

$$\frac{1}{3}[\bar{1}\bar{1}\bar{1}] = \frac{1}{6}[\bar{1}\bar{1}0] + \frac{1}{6}[\bar{1}\bar{1}\bar{2}]$$

using a Thompson tetrahedron. The stair-rod $\frac{a}{6}[\bar{1}\bar{1}0]$ lies at the intersection of the γ and δ planes while the Shockley partial is glissile on the inclined γ plane.

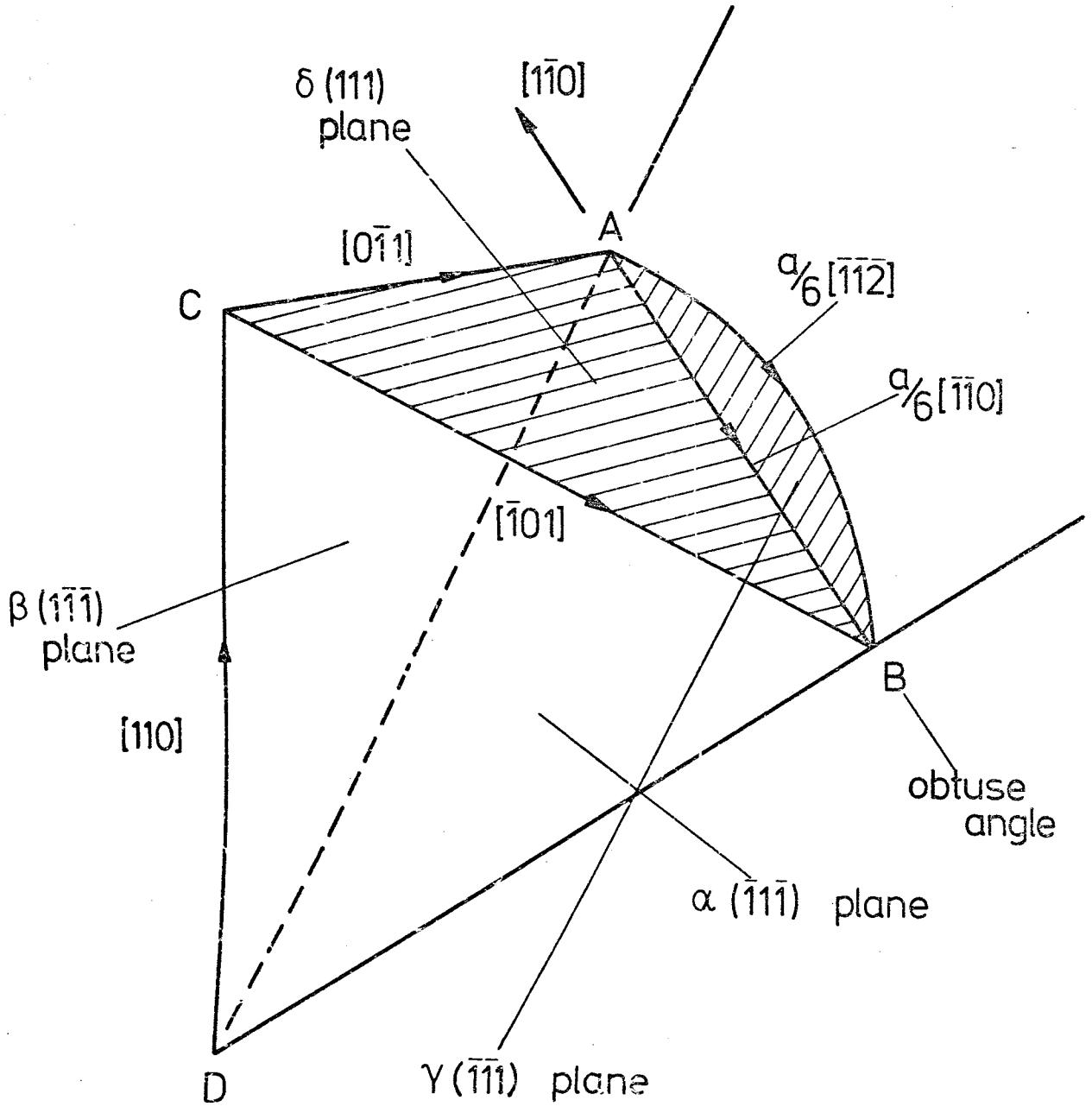
δ (111) plane
[1$\bar{1}$0]
A
[0$\bar{1}$1]
C
a/6[$\bar{1}\bar{1}$2]
a/6[$\bar{1}\bar{1}$0]
[$\bar{1}$01]
β (1$\bar{1}\bar{1}$) plane
[110]
B
obtuse angle
α ($\bar{1}$1$\bar{1}$) plane
D
γ ($\bar{1}\bar{1}$1) plane

Fig. 3/12 shows the possible dissociations of intrinsic and extrinsic Frank loops.

Frank loops formed after irradiation in the H.V.E.M. have been identified as extrinsic in nature, with the stacking fault on the inclined plane as intrinsic. The resulting configuration is a truncated tetrahedron as shown in fig. (B). This suggests that $\gamma_I \lesssim \gamma_E$.

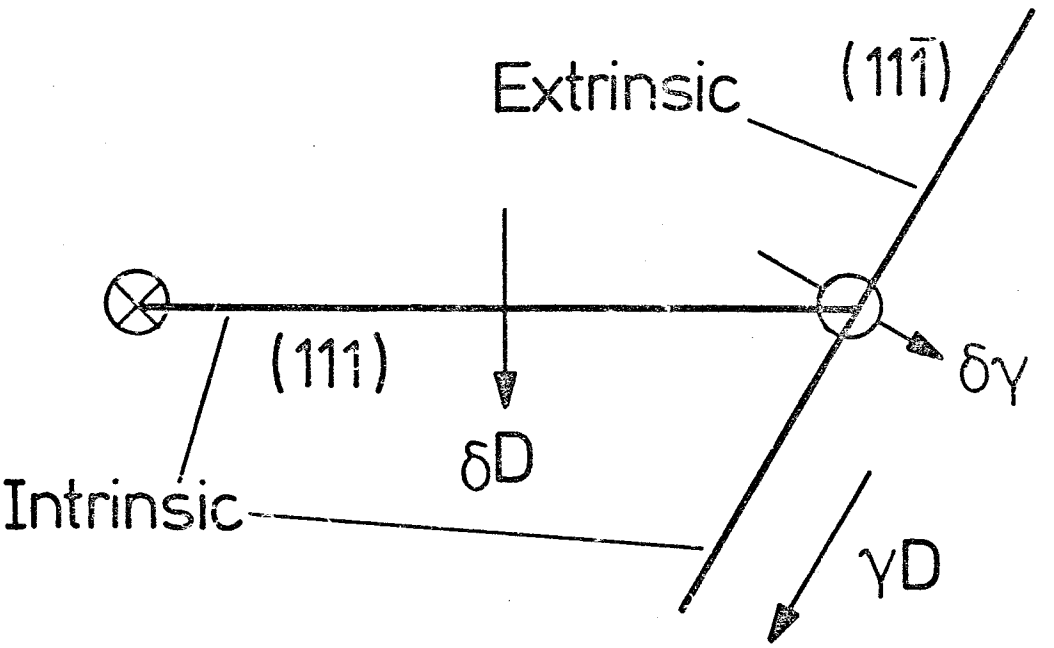
Extrinsic
(11$\bar{1}$)
(111)
δγ
δD
Intrinsic
γD

(A)

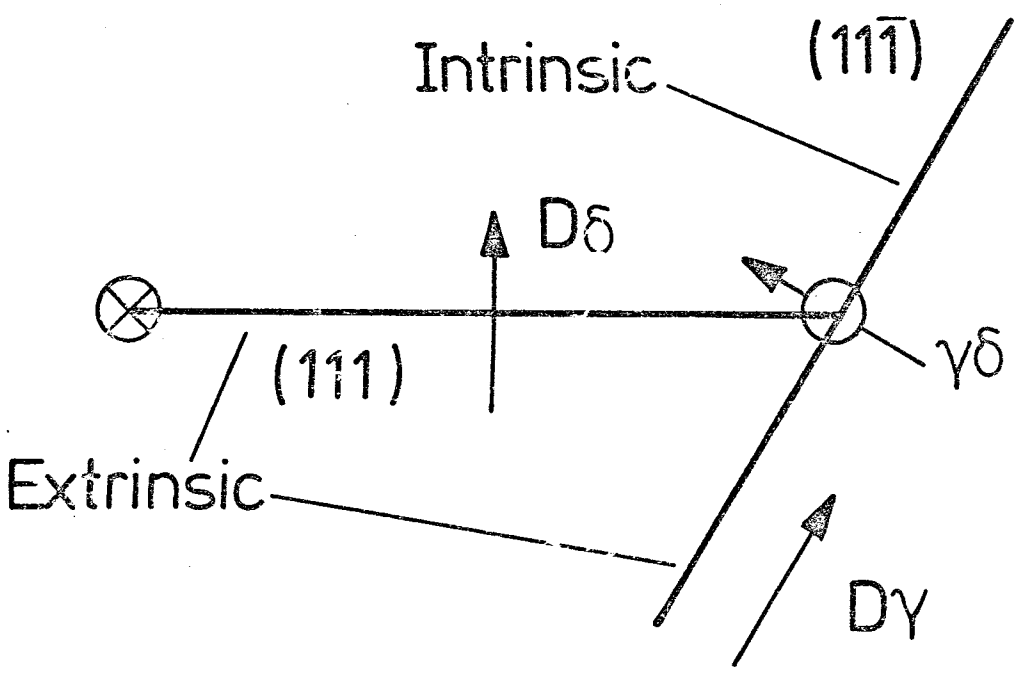
Intrinsic
(11$\bar{1}$)
Dδ
(111)
γδ
Extrinsic
Dγ

(B)

Fig. 3/13 illustrates some of the loop orientations used in the contrast experiments to image the Shockley and stair-rod dislocations bounding the faulted Frank loop.

Since the foil normal is parallel to [111], the loop in configuration (B) on the (111) plane is parallel to the surface. If the beam direction is <110>, and the loop is imaged in a <113> reflection only the stair-rod and Shockley dislocations are in contrast. When other diffraction vectors are imaged at this normal the stacking faults on the δ or γ planes are visible, making identification of the stair-rod difficult. In this orientation, the angle of projection between the dissociation plane and the beam direction is 35°.

The widest dissociation width is observed when the beam direction and foil normal are both <111>. This can be seen in fig. (C). However, the stacking fault on the inclined plane $(1\bar{1}\bar{1})$ is always in contrast using a <220> reflection.

To image the dissociation stacking fault the 'edge on' loop can be imaged, using a <111> reflection at the <112> beam direction, as shown in fig. (D).

Configuration (B) was most commonly used in this thesis, since the dislocations could be clearly identified.

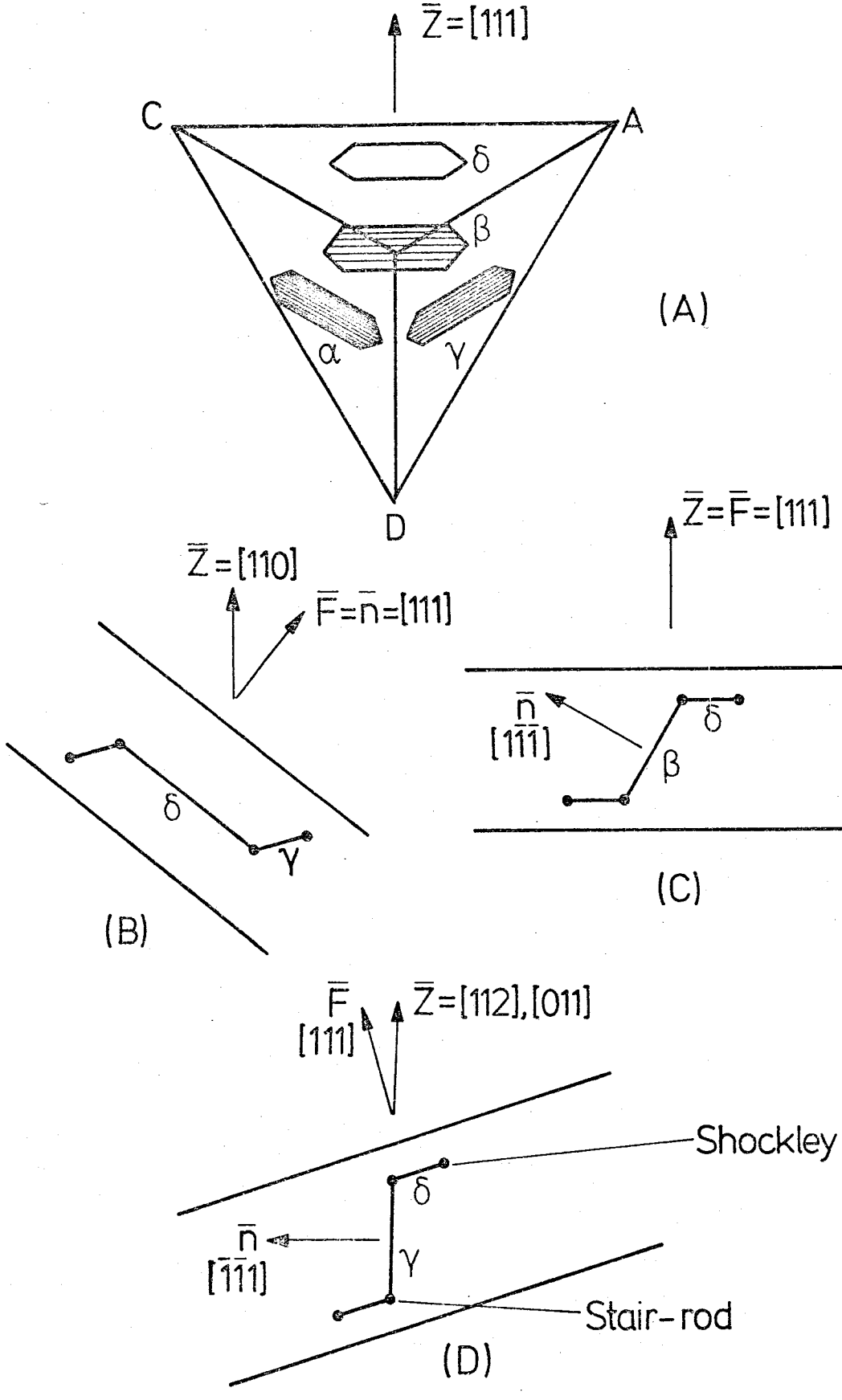
$\bar{Z}=[111]$
C
A
D
δ
β
α
γ
(A)
$\bar{Z}=[110]$
$\bar{F}=\bar{n}=[111]$
δ
γ
(B)
$\bar{Z}=\bar{F}=[111]$
$\bar{n}$
$[1\bar{1}\bar{1}]$
δ
β
(C)
$\bar{F}$
$[111]$
$\bar{Z}=[112],[011]$
Shockley
δ
$\bar{n}$
$[\bar{1}\bar{1}1]$
γ
Stair-rod
(D)

Fig. 3/14 Weak beam micrographs of a triangular Frank interstitial
3/15 loop in Cu 10% Al after electron irradiation in the H.V.E.M. at $\triangleq 200^{\circ}C$. (Micrographs imaged using the JEM100B).

The electron beam directions used were:-

(a) g $[1\bar{1}\bar{3}]$ z = [110]
(b) g $[1\bar{3}1]$ z = [101]
(c) g $[\bar{1}1\bar{1}]$ z = [110]
(d) g $[1\bar{1}\bar{3}]$ z = [110]
(e) g $[\bar{1}\bar{1}1]$ z = [011]
(f) g $[\bar{1}1\bar{1}]$ z = [110]
(g) g $[\bar{3}1\bar{1}]$ z = [011]
(h) g $[\bar{1}\bar{1}1]$ z = [101]

Foil thickness $\triangleq 2400$ Å.

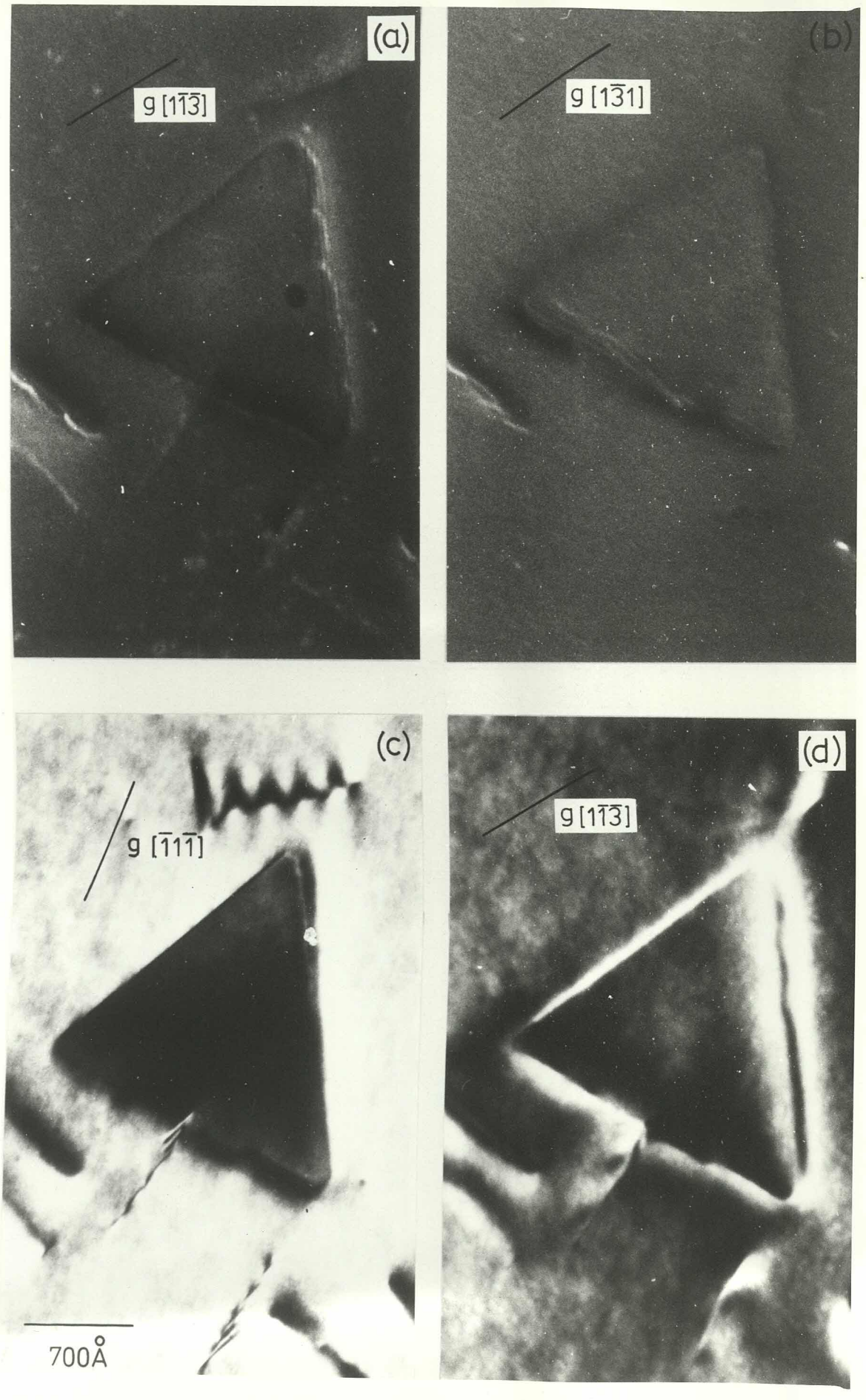

Fig.3/14

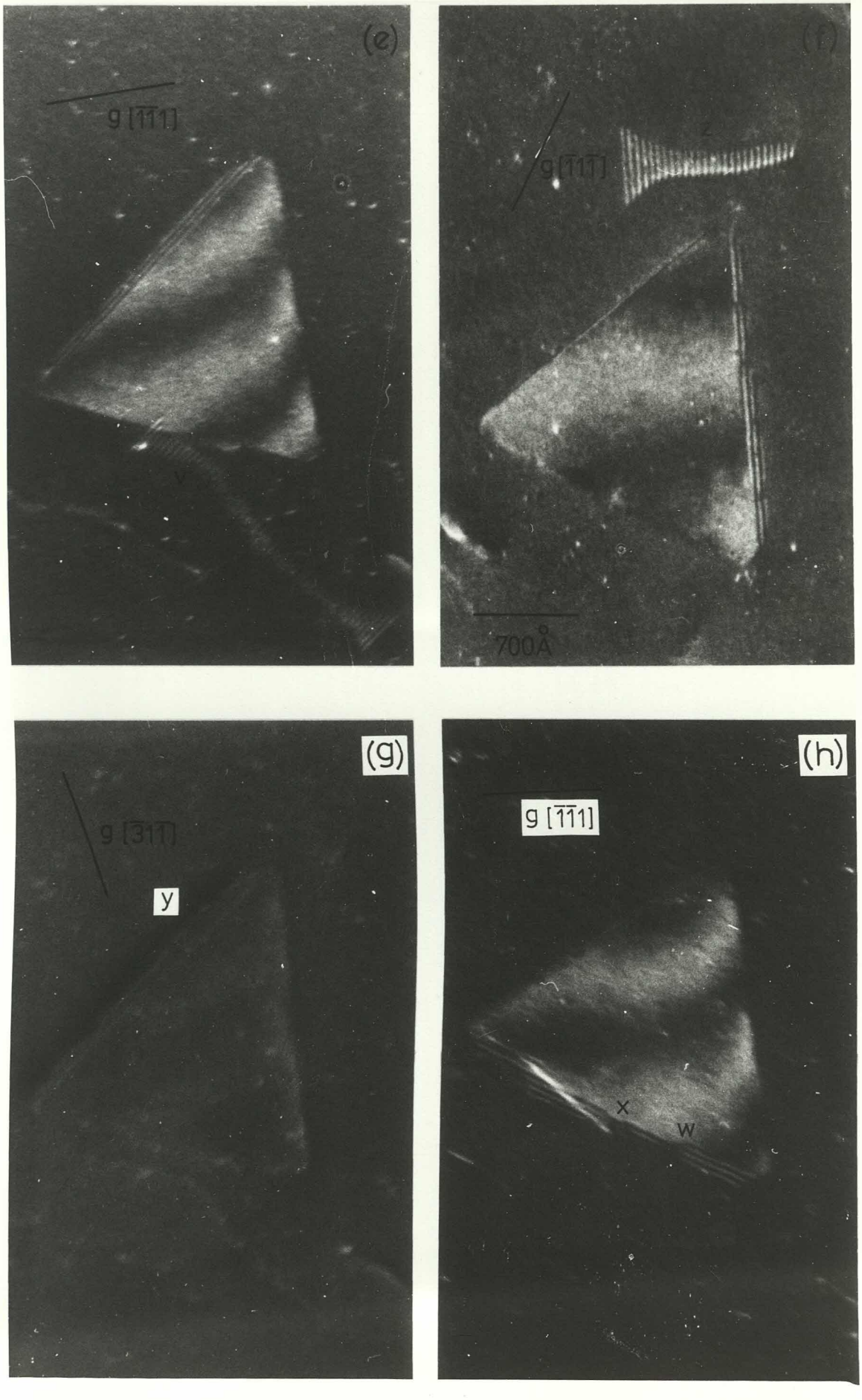

Fig.3/15

Fig. 3/16 Micrographs showing the widths of dissociation of the Frank partial into Shockley and stair-rod dislocations as a function of alloy concentration.

(A) Copper

(B) Cu 5% Al

(C) Cu 10% Al

(D) Cu 16% Al

Thin foils irradiated in the H.V.E.M. at temperatures $\triangleq 200^{\circ}C$ were subsequently imaged in g <113> at $\bar{z}$ <110>.

Foil thicknesses $\triangleq$ 2200 Å.

Crystals were fast grown.

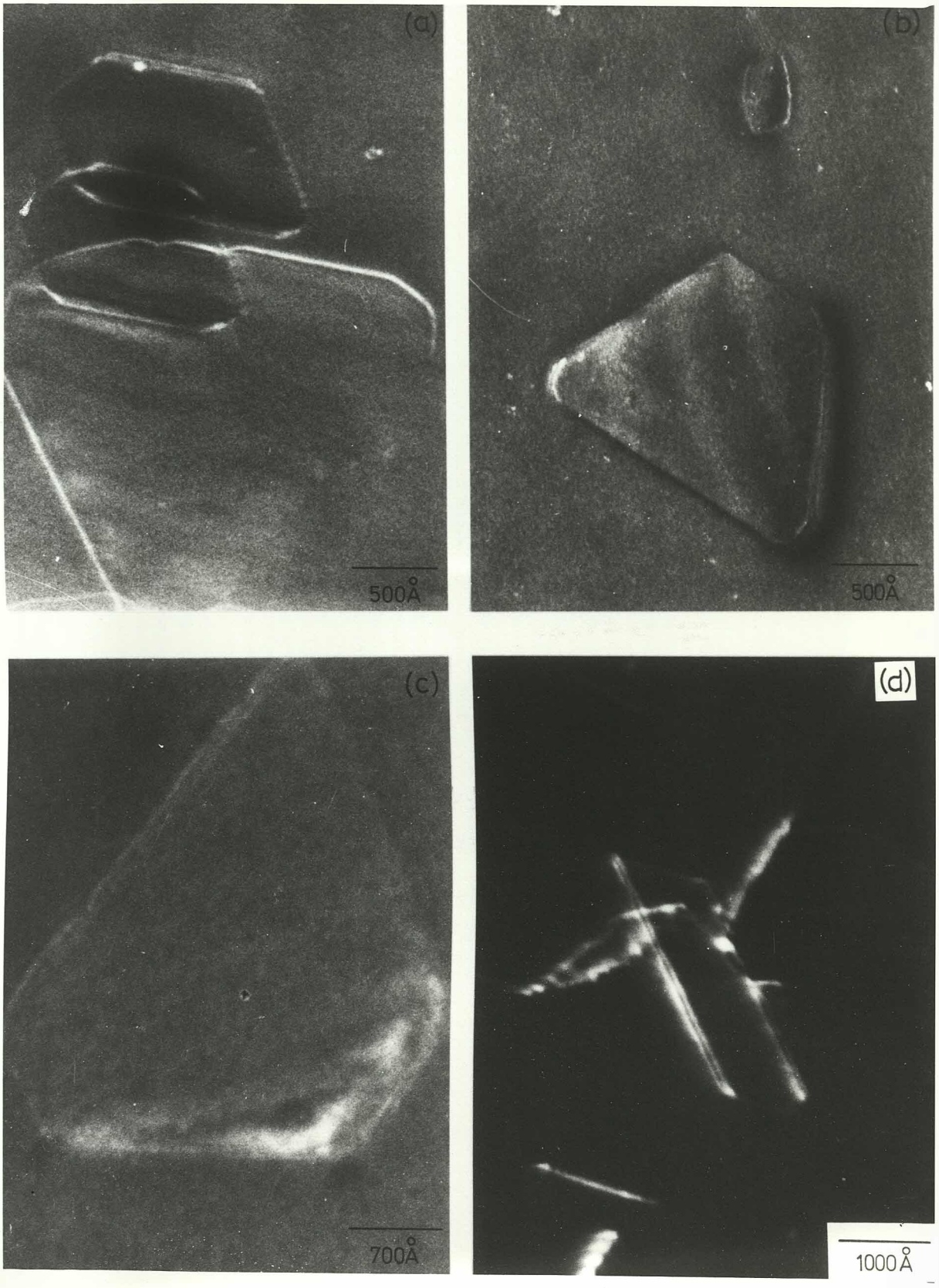
(a)
500Å
(b)
500Å
(c)
700Å
(d)
1000Å

Fig. 3/17 shows the experimental and theoretical results of the reaction

$$D\delta = D\gamma + \gamma\delta$$

for a series of Cu/Al alloys, as a function of stacking fault energy γ.

- ● Δ_{obs} Experimental averages of separations measured using a densitometer along long straight segments of the Frank loop side under dissociation.
- × Calculated separation.
- □ Corrected values of experimental separation taking into consideration inside or outside contrast effects.

$$\Delta = \Delta_{obs} - 7.5 \pm 7.5 \text{ Å} \quad \text{outside}$$
$$\Delta = \Delta_{obs} + 7.0 \pm 7.5 \text{ Å} \quad \text{inside.}$$

- ▲ Average of all the measured separations for the Cu 10% Al alloy.

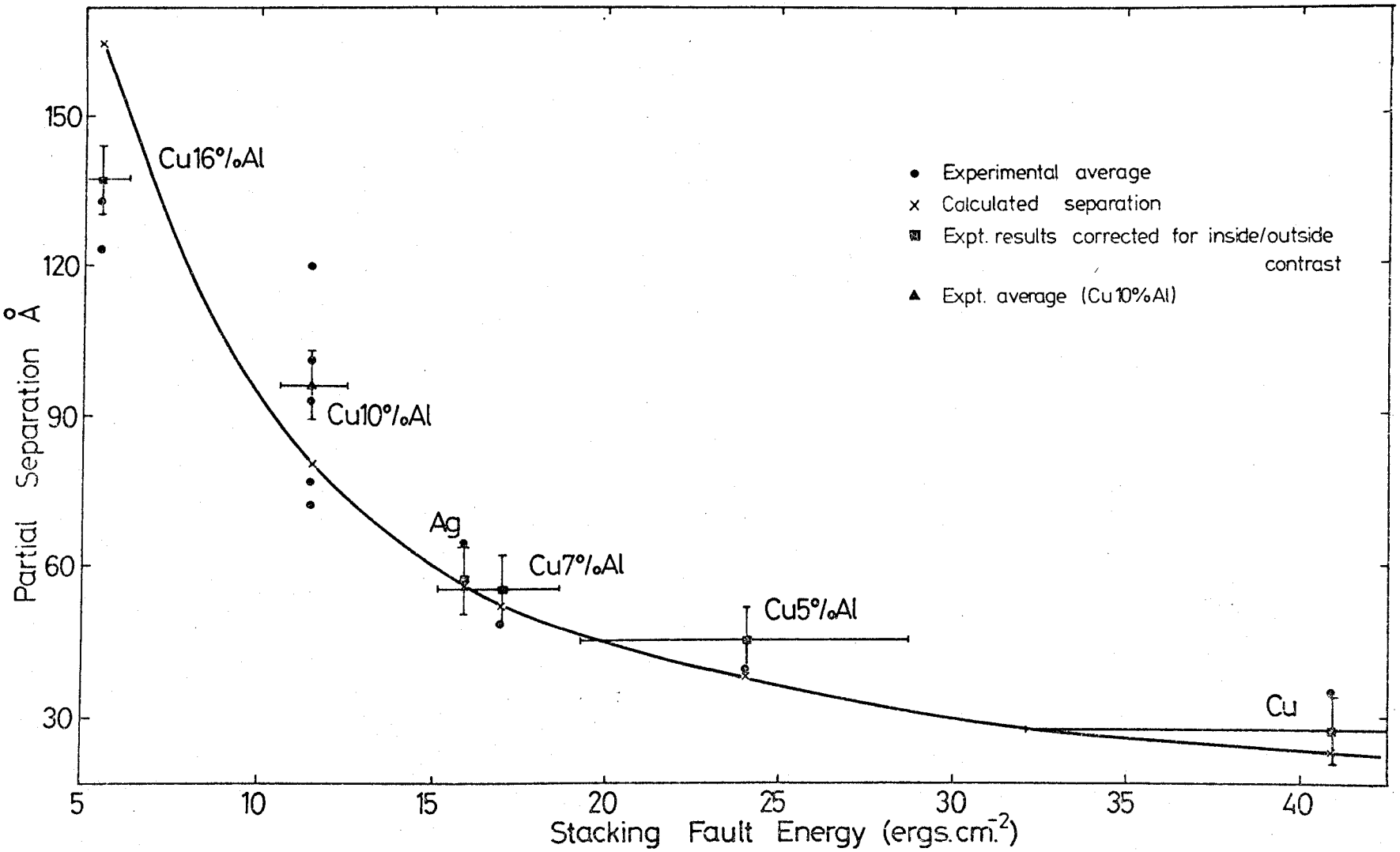
Partial Separation Å
150
120
90
60
30
5
10
15
20
25
30
35
40
Stacking Fault Energy (ergs.cm.$^{-2}$)
Cu16%Al
Cu10%Al
Ag
Cu7%Al
Cu5%Al
Cu
Experimental average
Calculated separation
Expt. results corrected for inside/outside contrast
Expt. average (Cu10%Al)

Fig. 3/18 Frank partial dissociation into Shockley partial and stair-rod dislocations in a foil of Cu 10% Al.

$g = [1\bar{1}\bar{3}]$

$\bar{z} = [110]$

Foil thickness $\simeq 2500$ Å $\quad T_i = 220^{\circ}C$

Fast grown crystal.


(a)
g [1$\bar{1}$3]
β
α
700Å

Fig. 3/19 Fig. (A) shows the measured SFE as a function of temperature for a Cu 7.3% Al alloy. At high temperatures, the effect of the solute impedance contribution causes the true S.F.E. to be higher than the S.F.E. measured at low temperatures.

Fig. (B) is a plot of S.F.E. against the aluminium concentration in a Cu/Al alloy.

γ_{cc} = S.F.E. Corrected for solute impedance
γ_{c} = uncorrected S.F.E.

The effect of solute impedance is significant at the high aluminium concentrations.

(A)

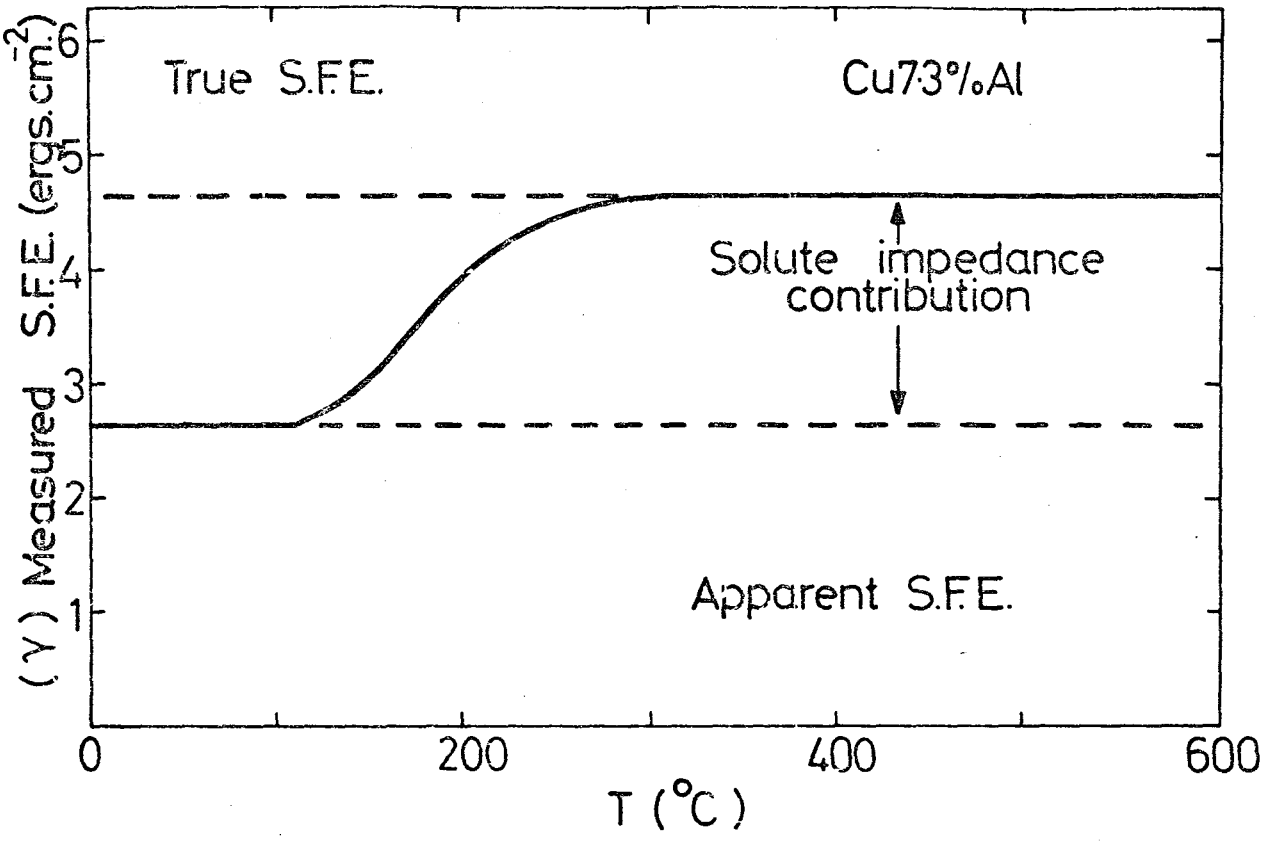
True S.F.E.
Cu7·3%Al
Solute impedance contribution
Apparent S.F.E.
(γ) Measured S.F.E. (ergs.cm.$^{-2}$)
1
2
3
4
5
6
0
200
400
600
T (°C)

(B)

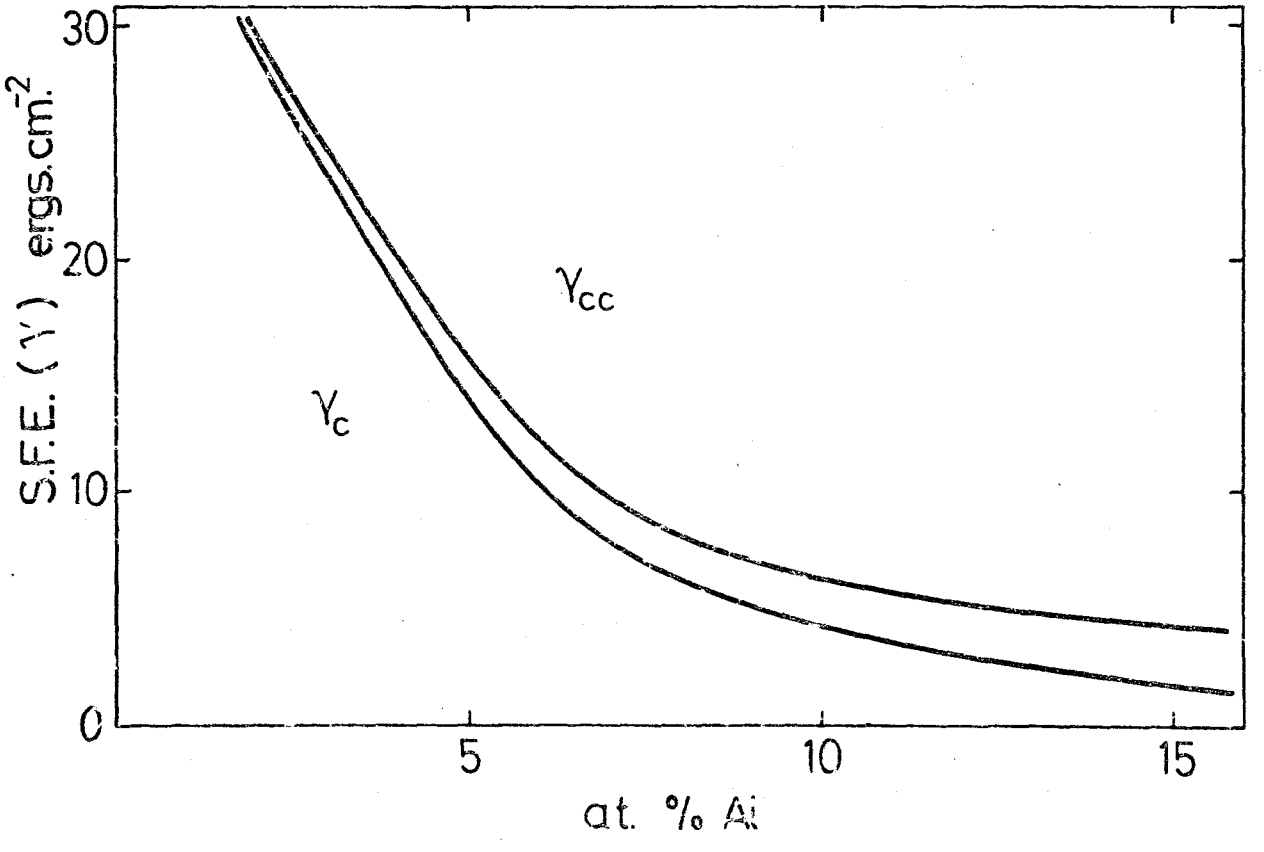
S.F.E. (γ) ergs.cm.$^{-2}$
0
10
20
30
γ_{cc}
γ_c
5
10
15
at. % Al

Fig. 3/20 Fig. (A) shows the energy of a dissociated hexagonal Frank loop $E_H = f(\alpha,h)$ in μb^3 units as a function of h/b, with the variables SF $\gamma = .7 \times 10^{-3}$ μb

$L = 1000$ Å

and $\alpha = \pi/4$

where h = separation of Shockley and stair-rod dislocation

α = angle between the tangent to the Shockley partial and the stair-rod.

The energy of an undissociated circular loop of similar area is also shown. At equilibrium, the energy of the dissociated loop becomes lower than that of the circular Frank loop.

Fig. (B) Each value of α gives a new curve analogous to fig. (A), Fig. (B) shows a plot of the energy minima versus α and equilibrium is obtained for $\alpha = 37^o$ and $h/b = 32$, which gives configuration (C) for a Cu 9.4 at.% Al.

(From Gaboriaud and J. Grihle 1972).

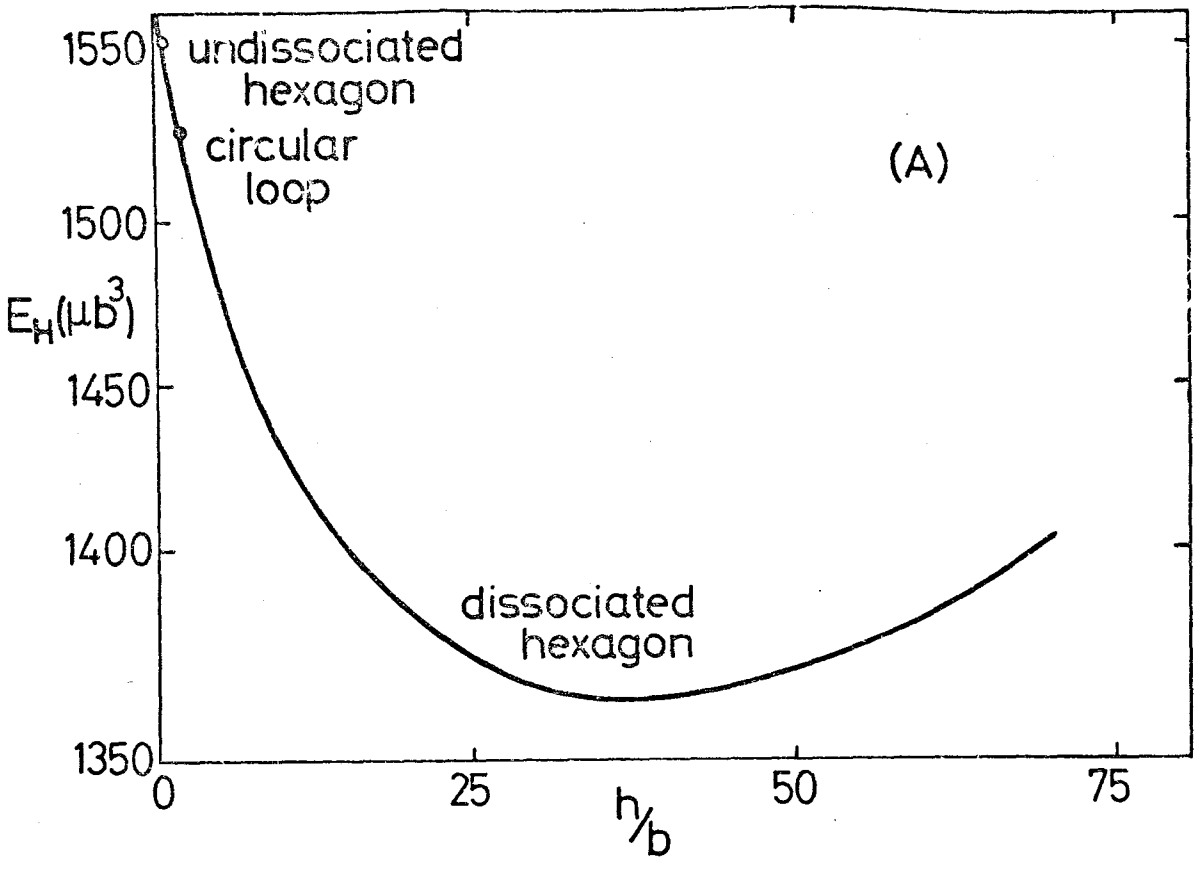
1550
1500
1450
1400
1350
$E_H(\mu b^3)$
undissociated hexagon
circular loop
(A)
dissociated hexagon
0
25
50
75
h/b

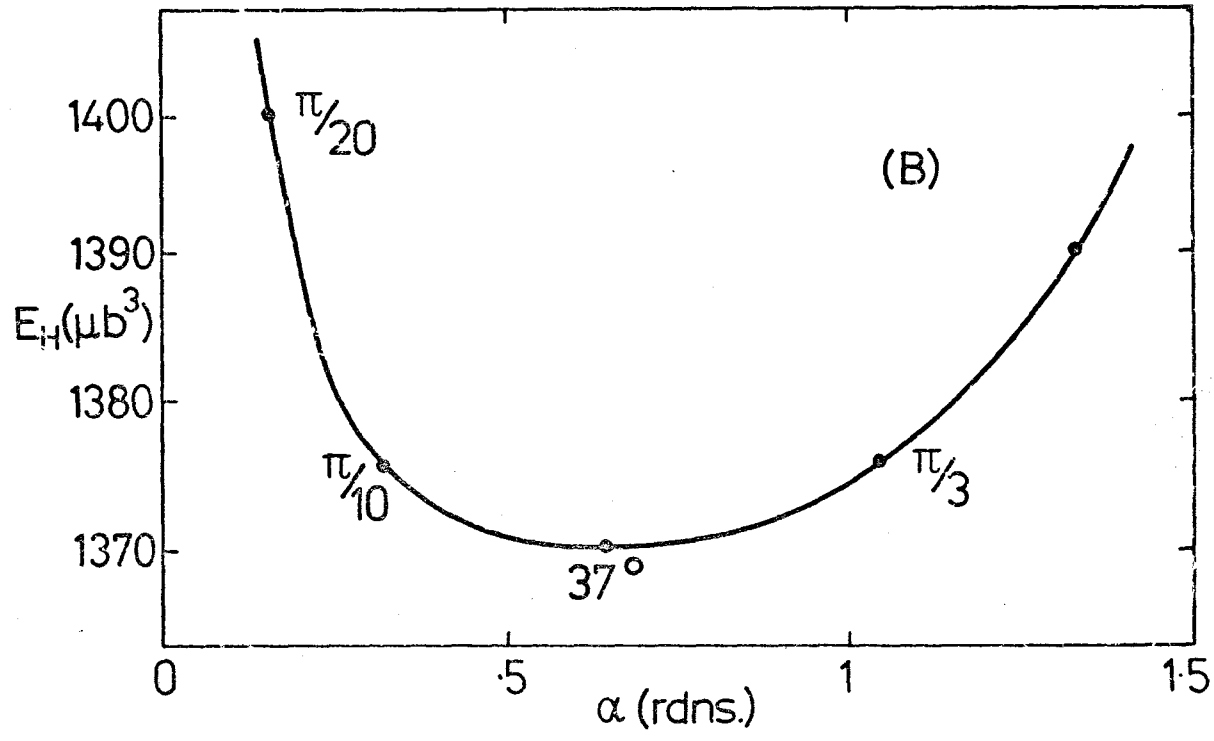
1400
1390
1380
1370
$E_H(\mu b^3)$
π/20
(B)
π/10
π/3
37°
0
·5
1
1·5
α (rdns.)

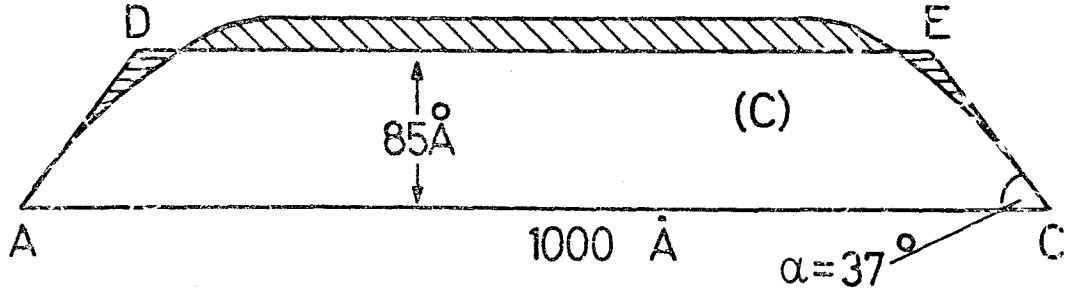
D
E
85Å
(C)
A
1000 Å
α=37°
C

Figs. 3/21 Micrographs illustrating the structure of rhombus perfect
3/22 loops in a foil of Cu 16% Al after irradiation at
3/23 220°C.

(a)	$\bar{g}$ [11$\bar{1}$] $\bar{z}$ [112]	
(b)	$\bar{g}$ [$\bar{1}$1$\bar{1}$] $\bar{z}$ [121]	
(c)	$\bar{g}$ [$\bar{1}$11] $\bar{z}$ [211]	
(d)	$\bar{g}$ [0$\bar{2}$2] $\bar{z}$ [111]	Weak beam g/3g satisfied.
(e)	$\bar{g}$ [$\bar{2}$20] $\bar{z}$ [113]	g/3g
(f)	$\bar{g}$ [$\bar{2}$02] $\bar{z}$ [101]	g/3g
(g)	$\bar{g}$ [$\bar{2}$02] $\bar{z}$ [111]	g/3g
(h)	$\bar{g}$ [$\bar{2}$20] $\bar{z}$ [111]	g/3g
(i)	$\bar{g}$ [$\bar{1}$11] $\bar{z}$ [211]	g/5g
(j)	$\bar{g}$ [$\bar{1}$1$\bar{1}$] $\bar{z}$ [121]	g/5g
(h)	$\bar{g}$ [11$\bar{1}$] $\bar{z}$ [112]	g/5g

(slow grown crystal)

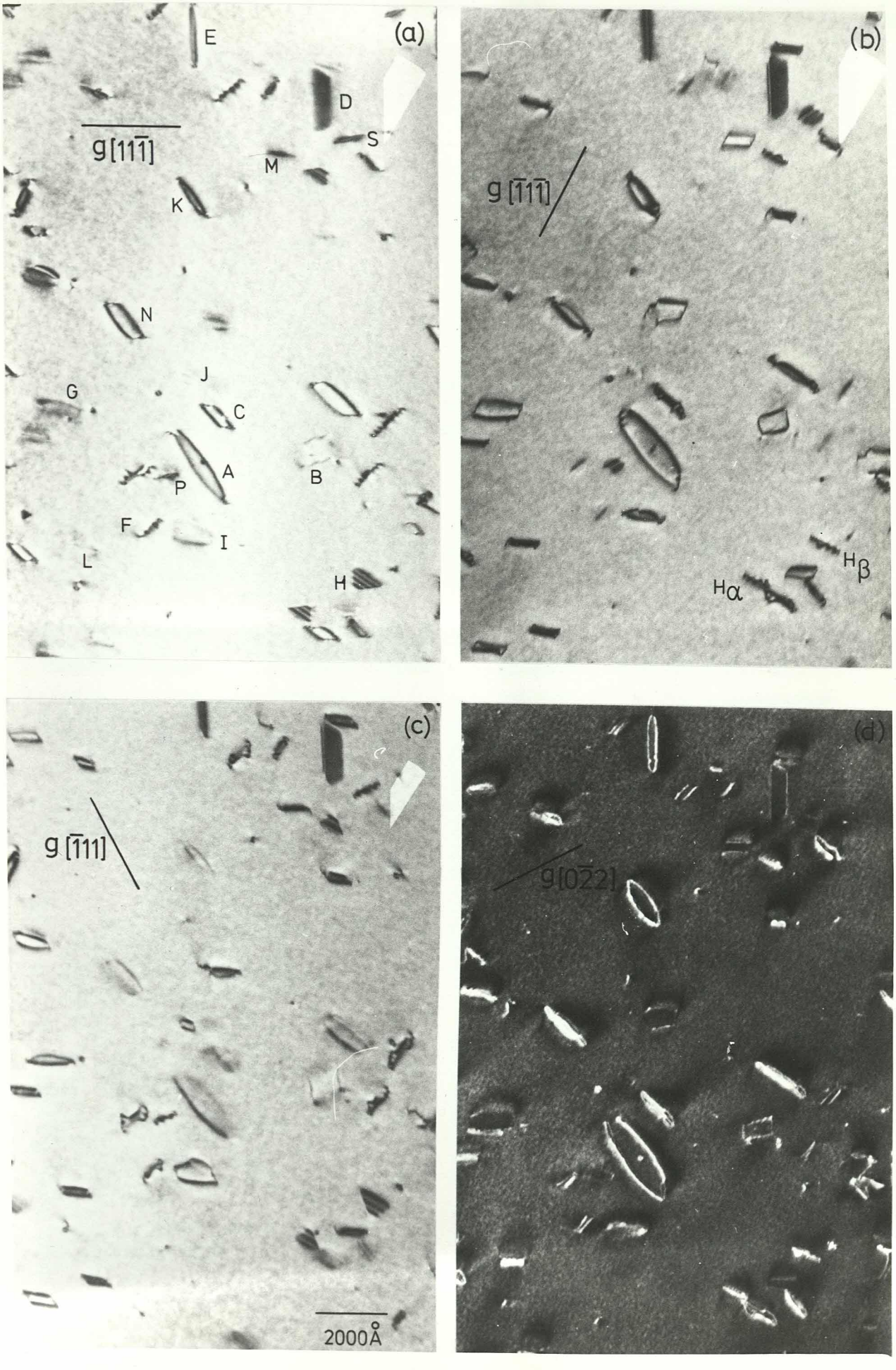
(a)
E
D
S
M
K
g[11$\bar{1}$]
N
J
G
C
A
P
B
F
I
L
H
(b)
g[$\bar{1}\bar{1}\bar{1}$]
Hβ
Hα
(c)
g[$\bar{1}$11]
2000Å
(d)
g[0$\bar{2}$2]

Fig.3/21

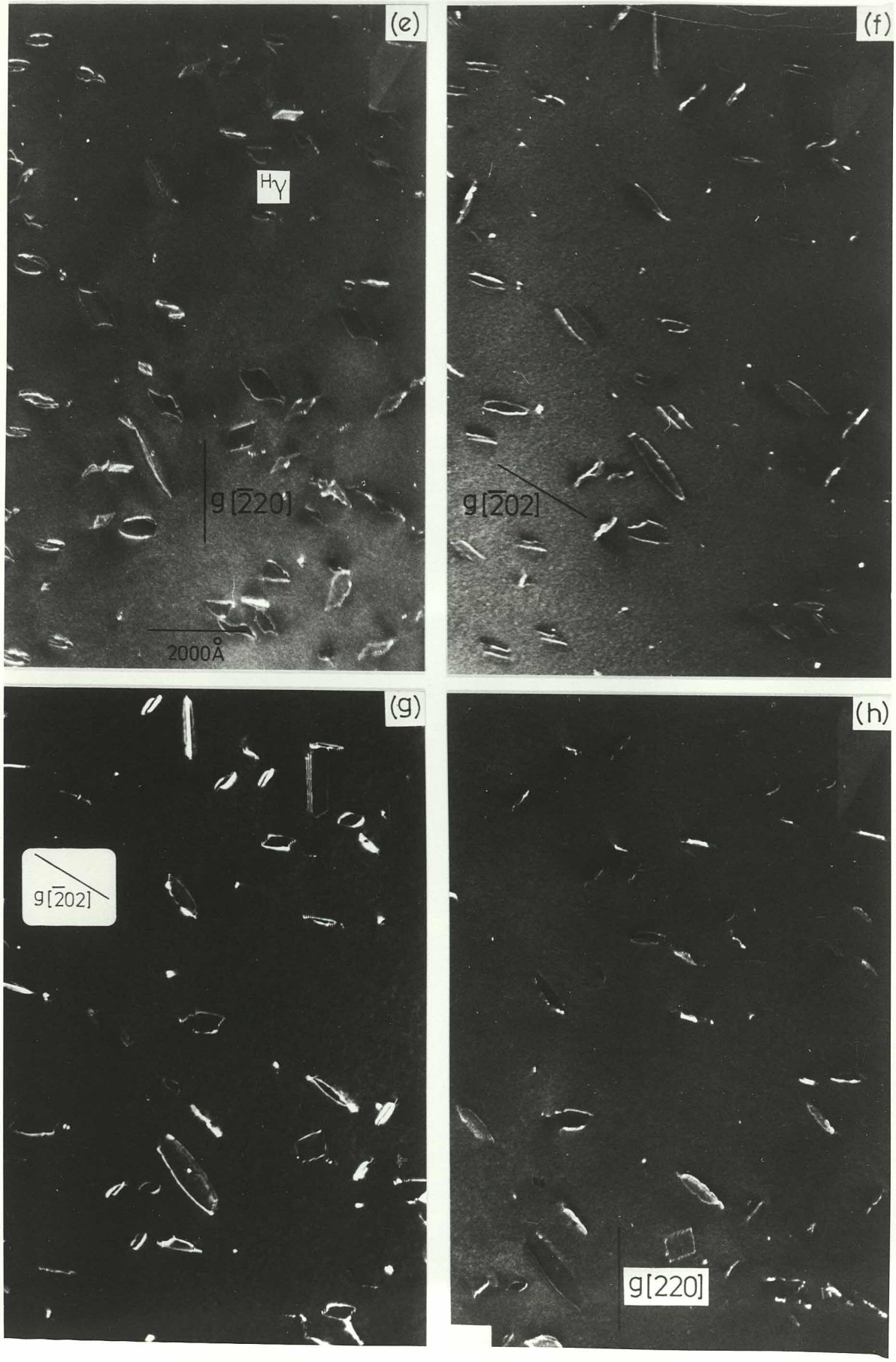

Fig.3/22

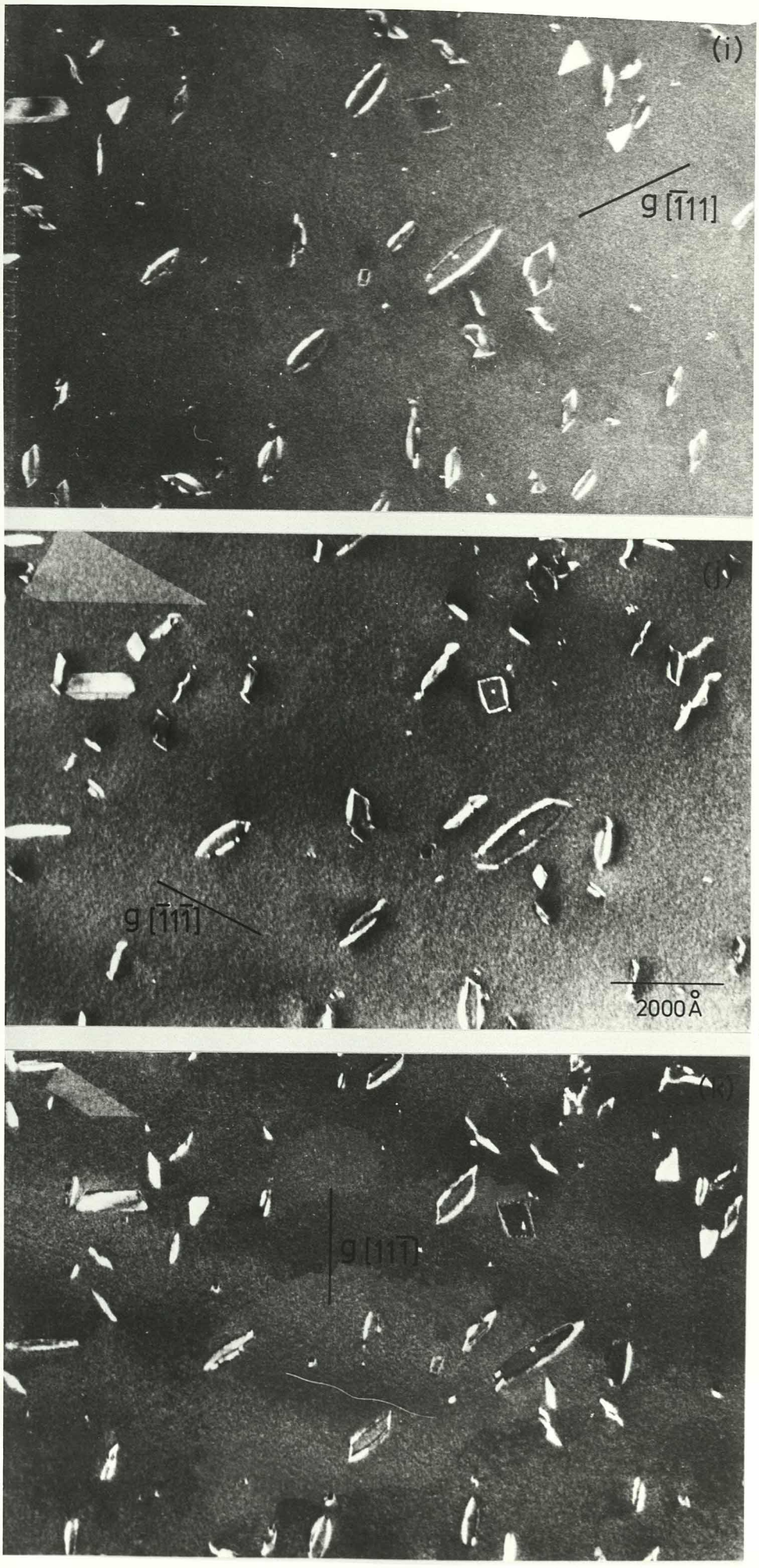

Fig.3/23

Fig. 3/24 Dissociation of rhombus loops in a Cu 16% Al foil of thickness 2200 Å after irradiation in the H.V.E.M.

$g = [\bar{2}20]$ $\bar{z} = [113]$

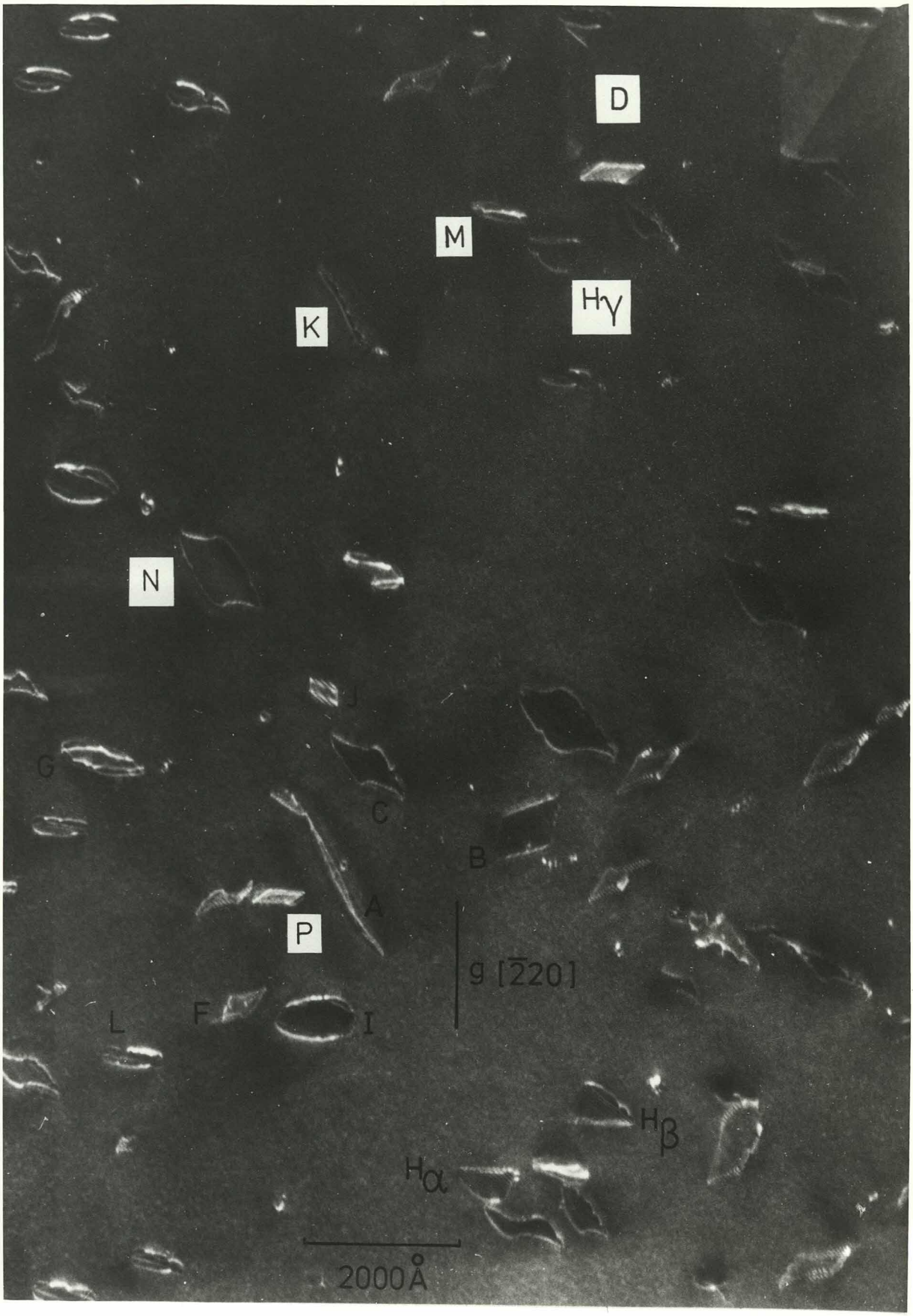
D
M
Hγ
K
N
J
G
C
B
A
P
g [$\bar{2}$20]
L
F
I
Hβ
Hα
2000 Å

Fig. 3/25 shows the dissociation of a Frank loop at a 300° corner. Since the dissociation of the Shockleys is in the upward direction, they can form a stair-rod at the intersection of the $(\bar{1}1\bar{1})$ and $(\bar{1}\bar{1}1)$ planes. (Fig. B). Fig. C shows the same reaction from a [110] beam direction

Fig. (D) shows that constriction of the Shockleys also occurs at a 240° corner.

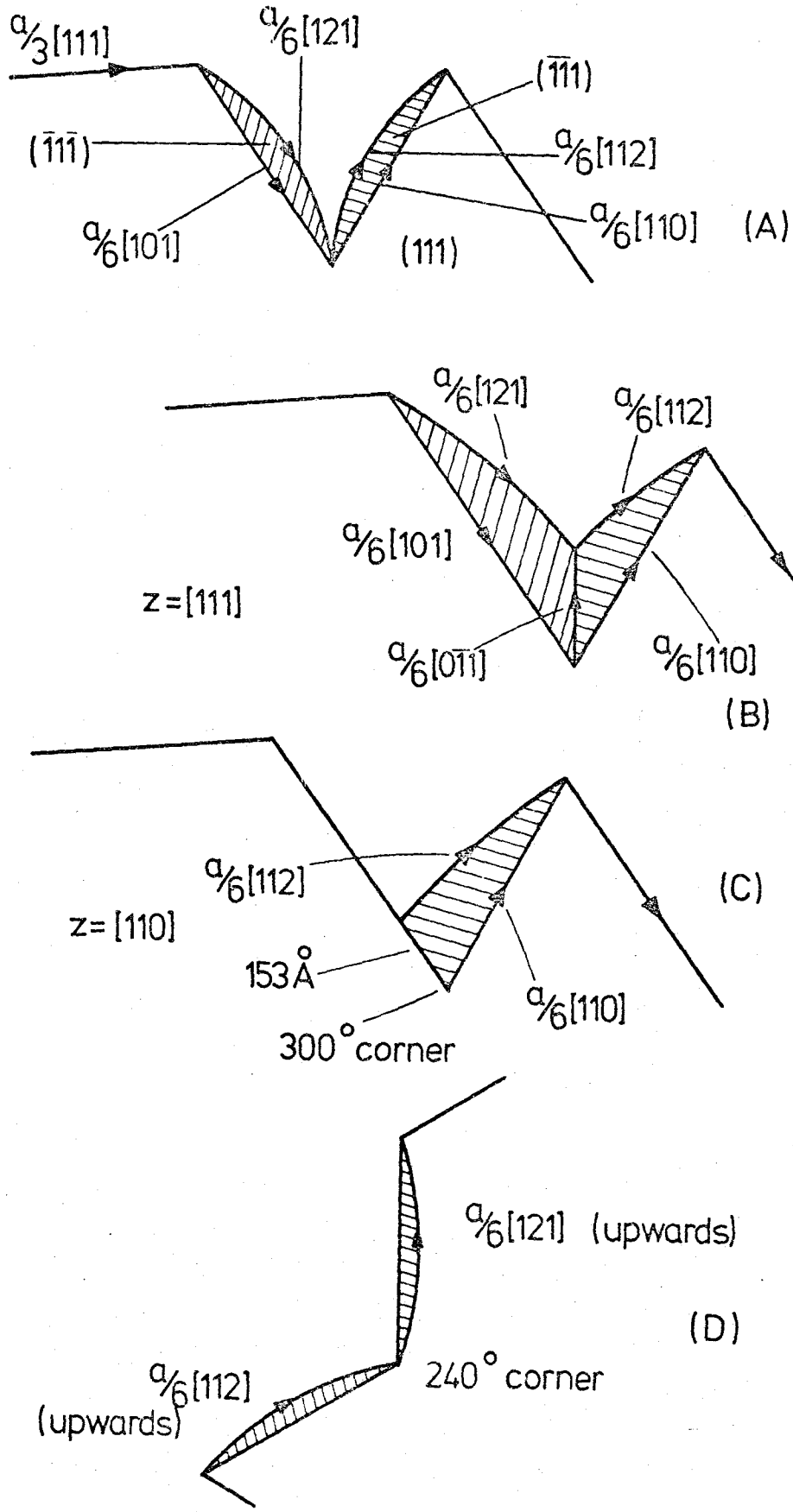
a/3[111]
a/6[121]
(1̄11)
(1̄11̄)
a/6[112]
a/6[101]
a/6[110]
(111)
(A)
a/6[121]
a/6[112]
a/6[101]
a/3[111]
z=[111]
a/6[01̄1]
a/6[110]
(B)
a/6[112]
(C)
z=[110]
153 Å
a/6[110]
300° corner
a/6[121] (upwards)
(D)
a/6[112]
(upwards)
240° corner

Fig. 3/26 Dissociation of a Frank partial into Shockley and stair-rod dislocations at a 300° corner. At this corner, a stair-rod joins the Shockley partials on the inclined {111} planes.

(a) g $[\bar{3}1\bar{1}]$ z [011]

(b) g $[1\bar{1}\bar{3}]$ z [110]

(c) g $[\bar{1}1\bar{1}]$ z [110]

(d) g $[20\bar{2}]$ z [111]

Cu 10% Al foil. $T_i \triangleq 200^{\circ}C$ foil thickness $\triangleq$ 2400 Å

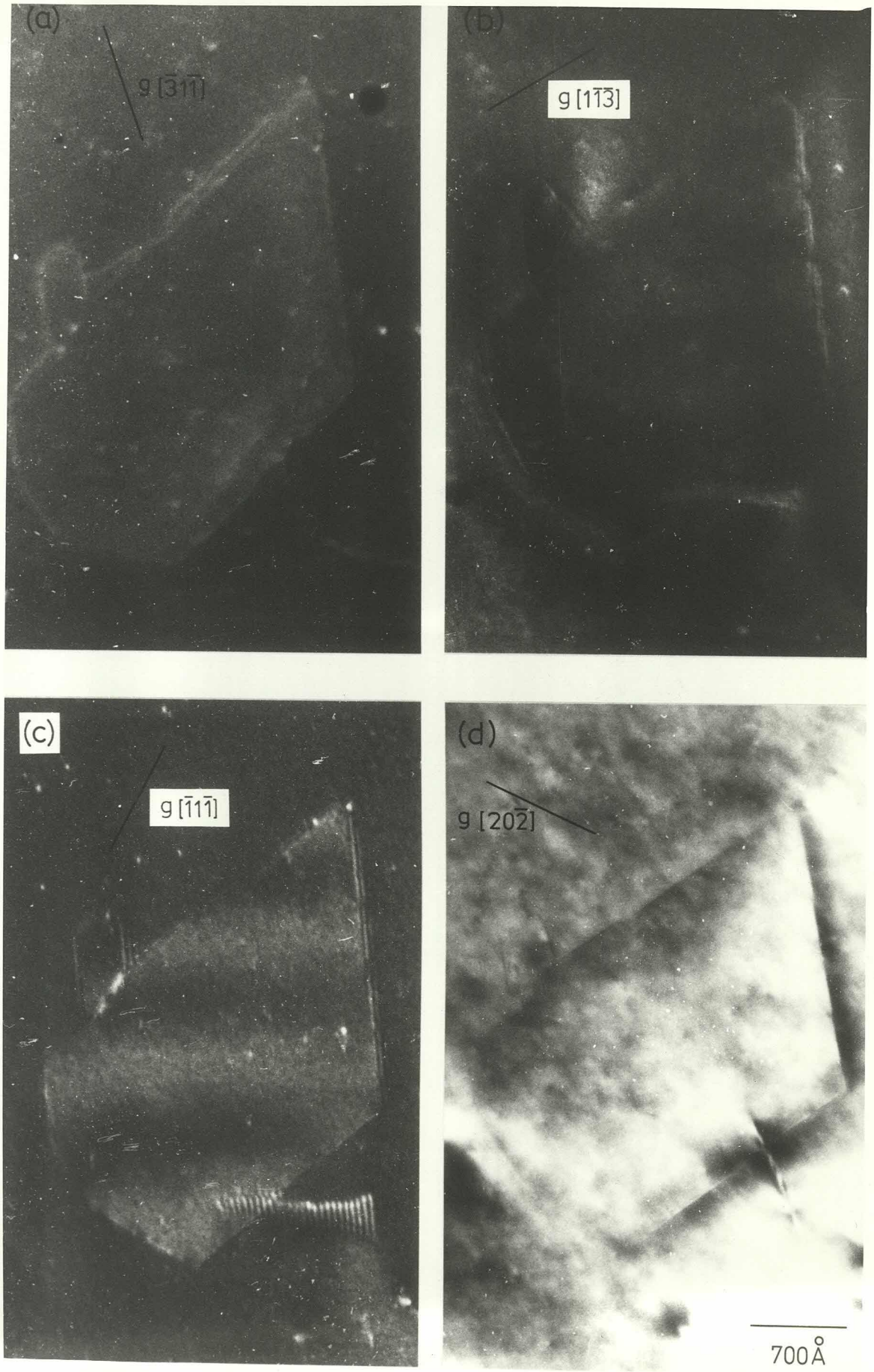
(a)
g [3̄11̄]
(b)
g [11̄3̄]
(c)
g [1̄11̄]
(d)
g [202̄]
700 Å

Fig. 3/27 illustrates how, during an in-situ annealing experiment vacancies can attach themselves to the corners of a loop with <110> edges, producing lengths of <112> edge.

The constriction of Shockley partials at 60° and 120° corners in a dissociated interstitial Frank loop is also illustrated.

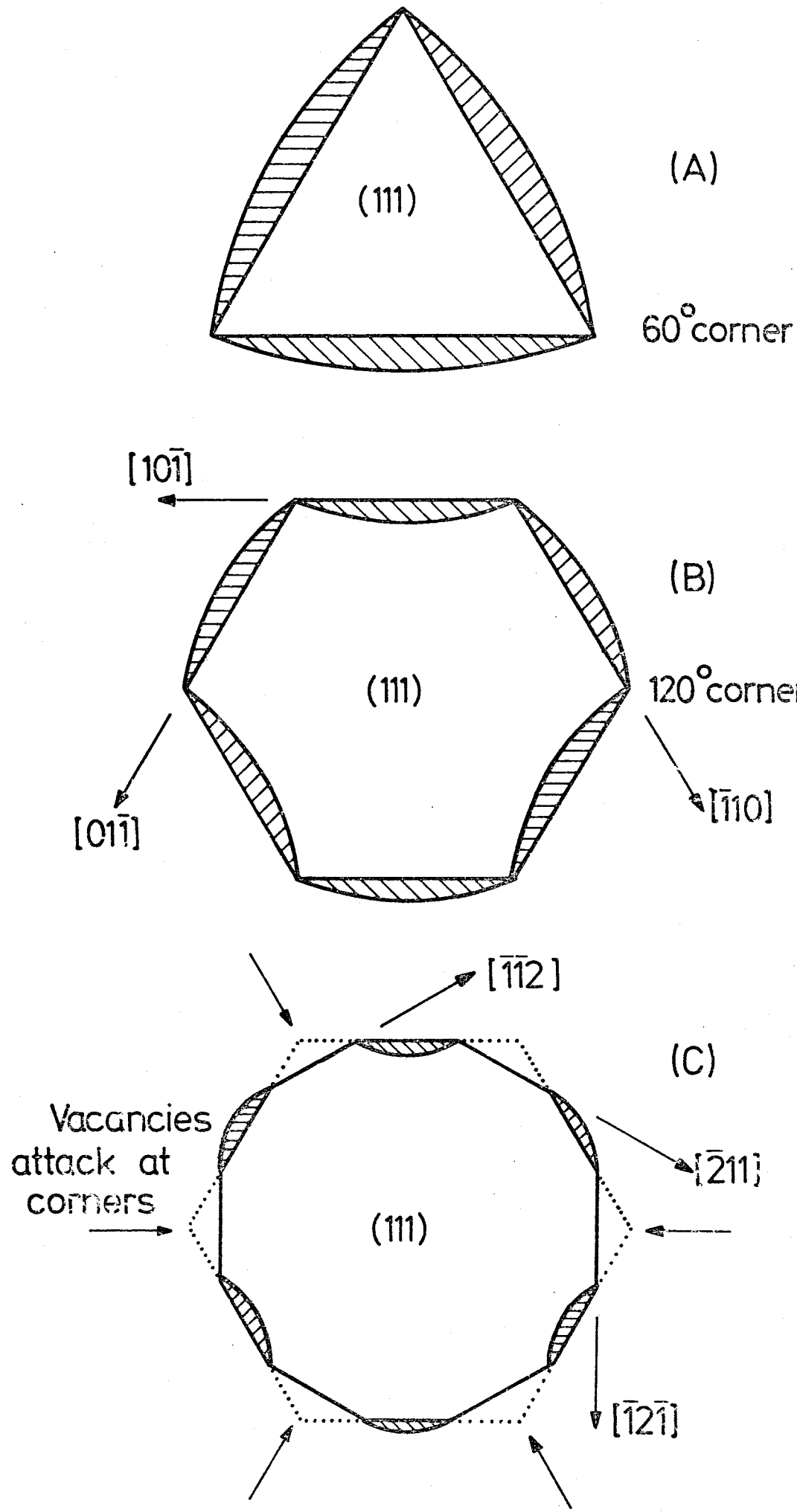
(A)
(111)
60° corner
[10$\bar{1}$]
(B)
(111)
120° corner
[01$\bar{1}$]
[$\bar{1}$10]
[$\bar{1}\bar{1}$2]
(C)
Vacancies attack at corners
[$\bar{2}$11]
(111)
[$\bar{1}$2$\bar{1}$]

Fig. 3/28 Cu 7% Al foil irradiated at 220°C for 10 minutes to form Frank loops, then annealed at this temperature for 5 minutes. The vacancies left in the foil have migrated to the corners of the loop producing the $[1\bar{2}1]$ edge, which is not dissociated. (z). Points x and y show constrictions in the dissociation.

Loop α on the (111) plane dissociated onto the $(\bar{1}\bar{1}1)$ plane, the Shockley partial being $\frac{a}{6}[112]$.

Loop β on the $(\bar{1}\bar{1}1)$ plane dissociated onto the (111) plane, the Shockley partial being $\frac{a}{6}[\bar{2}11]$

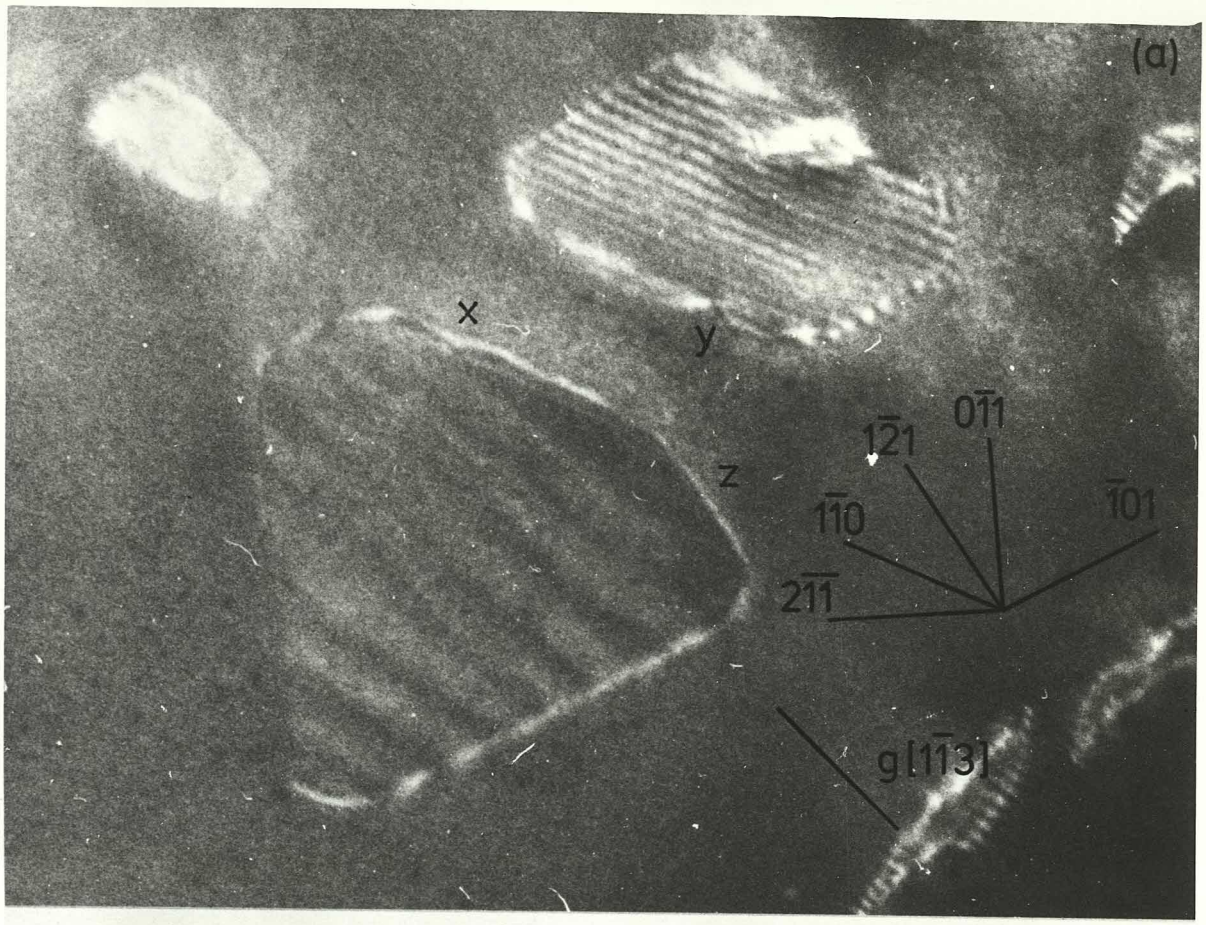
(a)
x
y
z
$0\bar{1}1$
$1\bar{2}1$
$\bar{1}10$
$\bar{1}01$
$2\bar{1}\bar{1}$
$g[1\bar{1}3]$

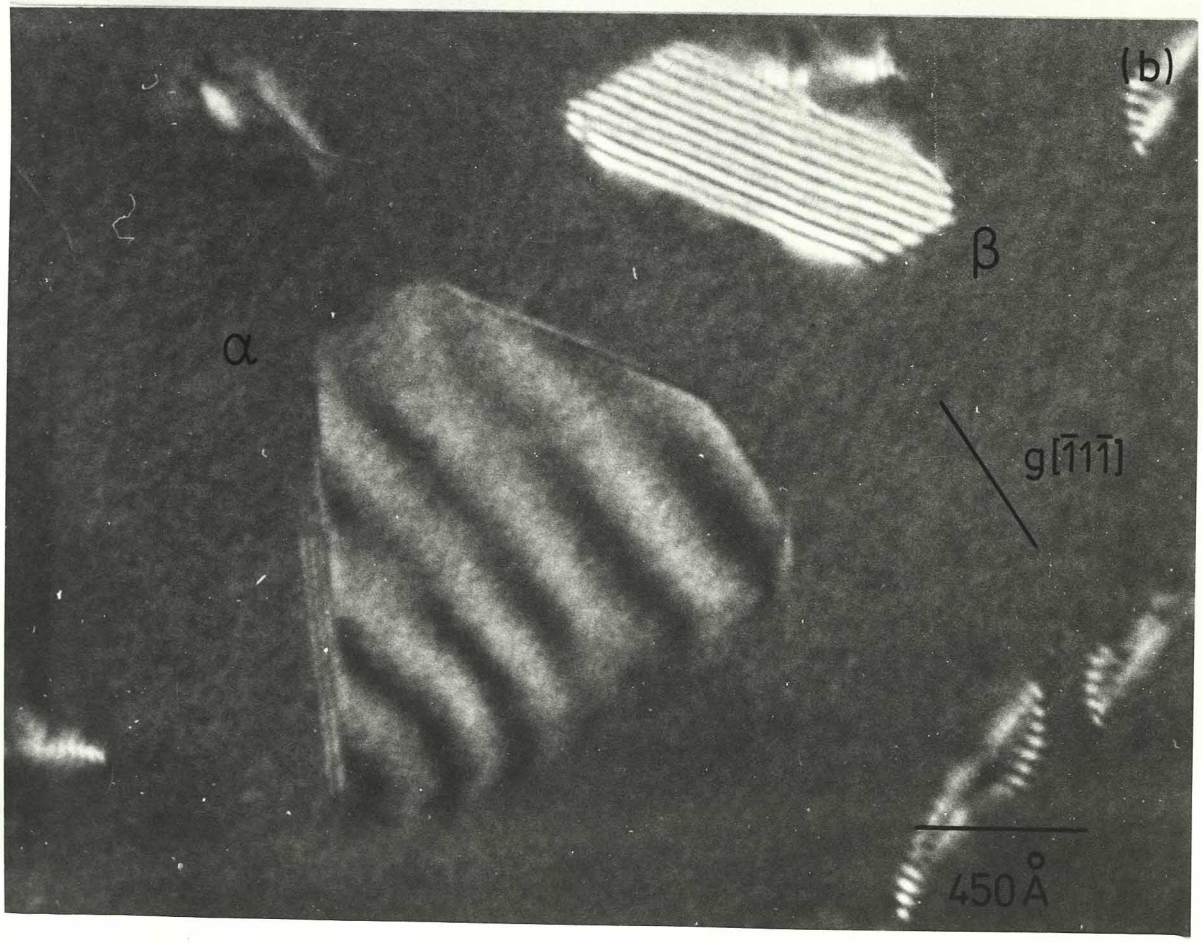
(b)
α
β
$g[\bar{1}1\bar{1}]$
450 Å

Fig. 3/29 This diagram shows the geometry of the Frank loop in relation to the foil normal $\bar{F}$ and beam direction $\bar{z}$, when imaging the Frank dissociation.

The loop normal $\bar{n}$ and foil normal are parallel to [111] and the beam direction is [110]. The stair-rod (in the direction of the plane of the paper) has a line direction $\bar{u} = [1\bar{1}0]$ and $\bar{b} = \frac{a}{6}[\bar{1}\bar{1}0]$.

A and B are the possible positions of the Shockley partial $b = \frac{a}{6}[\bar{1}\bar{1}2]$ on the inclined $(\bar{1}\bar{1}1)$ plane.

Also shown are the possible diffraction vectors which can be used to image the dissociated dislocations.

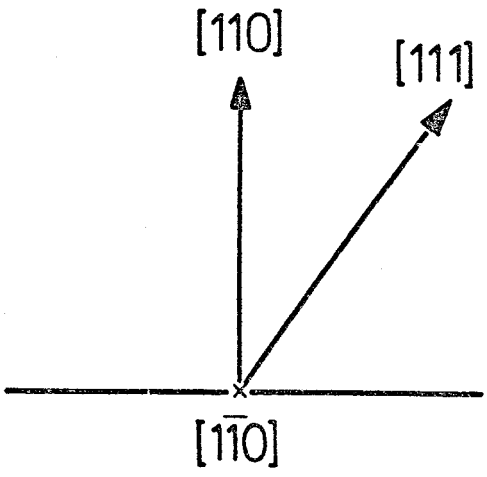
[110]
[111]
[1$\bar{1}$0]

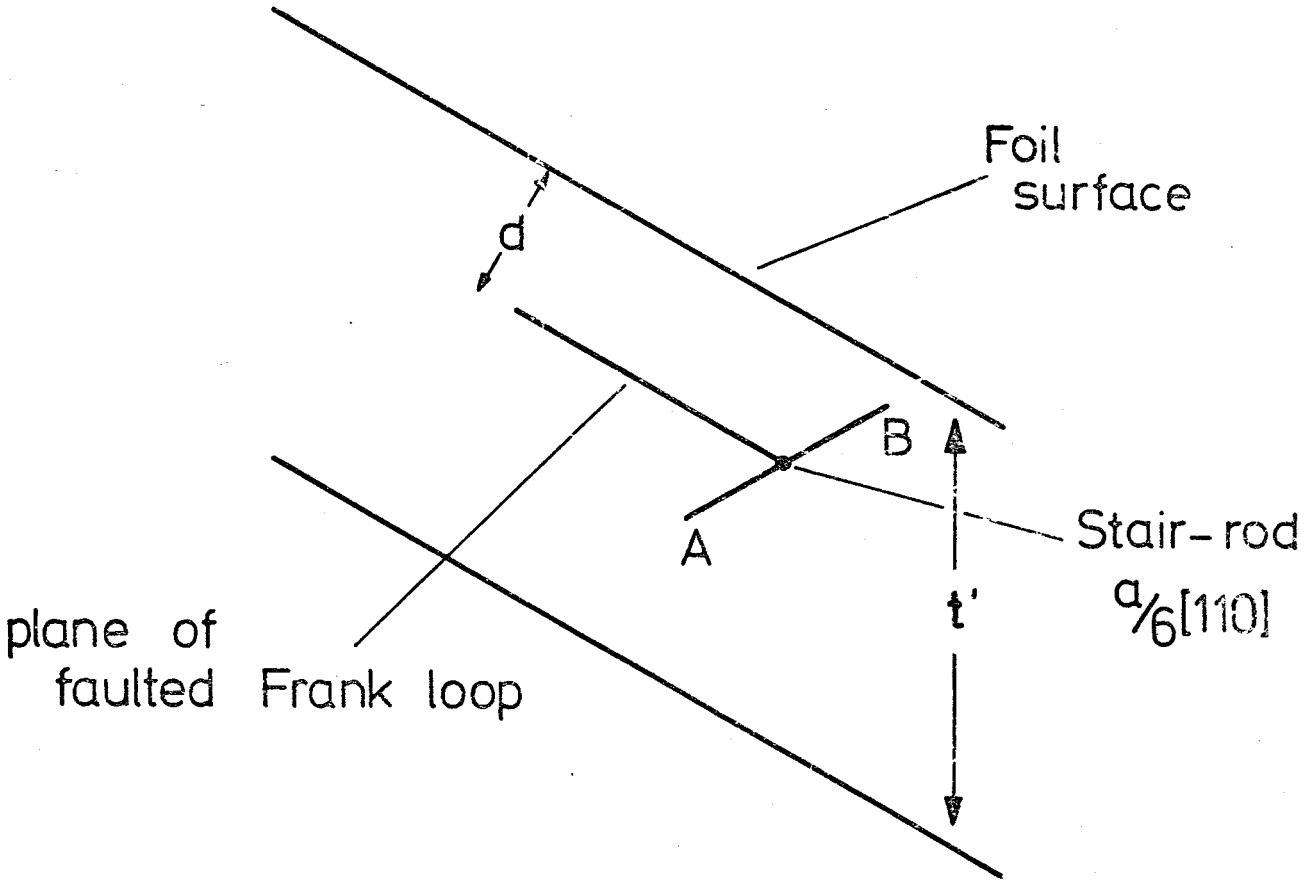
Foil surface
d
B
A
Stair-rod
a/6[110]
t'
plane of faulted Frank loop

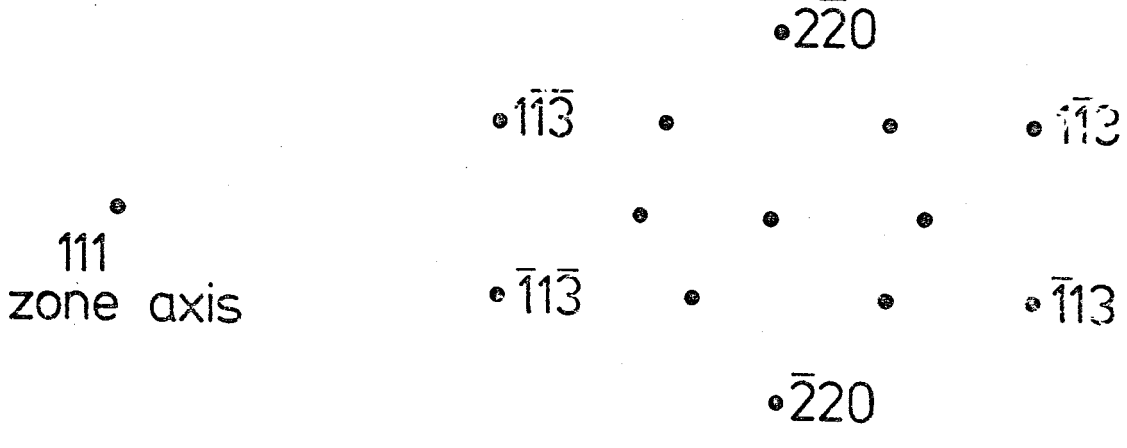
•2$\bar{2}$0
•1$\bar{1}$3
•1$\bar{1}$3
111
zone axis
•$\bar{1}$13
•$\bar{1}$13
•$\bar{2}$20

Fig. 3/30 This diagram shows a plot of column length and foil thickness versus the dissociation of Shockley and stair-rod (in units of ξ_g = 536 Å, the extinction distance).

The variation in peak position for a dissociated Frank partial has been computed assuming a parallel beam approximation, with a dissociation width of 79 Å. The stair-rod has been adjusted to be at a depth of d = 1.0 ξ_g.

The parallel beam approximation predicts two peaks for each partial, while the shaded regions represent the position of the two peaks assuming a fully divergent beam.

(Calculations by Dr. S.M. Holmes).

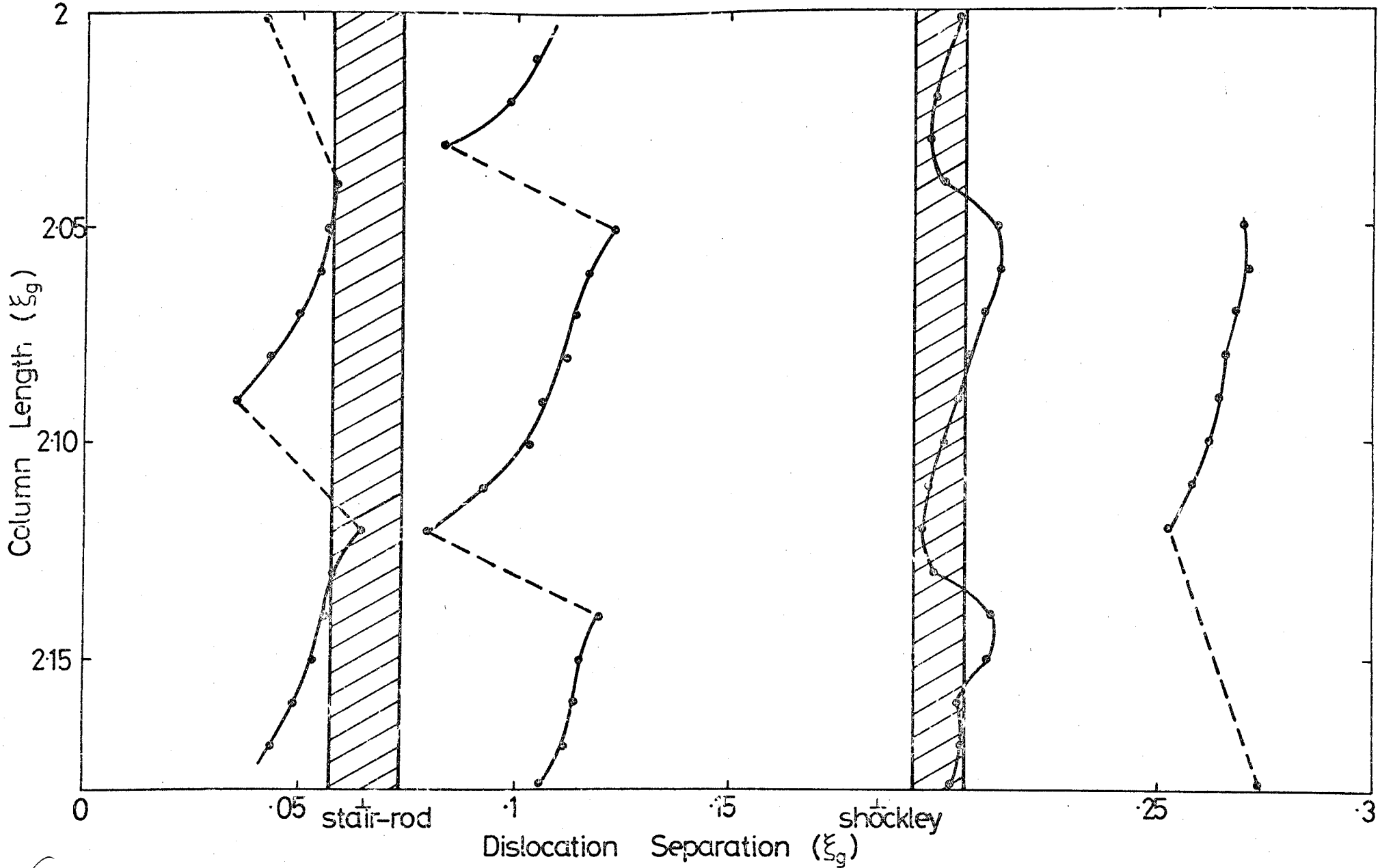
2
2·05
2·10
2·15
Column Length (ξ_g)
0
·05
stair-rod
·1
·15
shockley
·25
·3
Dislocation Separation (ξ_g)

Fig. 3/31 Diagram (A) shows parallel beam image profiles of a dissociated Frank partial. The intensity of the images has been plotted against the partial separation. The width of splitting equals 79 Å.

$$g = [1\bar{1}3]$$

t' (foil thickness) = $2.08\ \xi_g$

Curve (1) represents the profile expected when the stair-rod is at depth $1.00\ \xi_g$, while curve (2) shows the profile with the stair-rod at depth $1.04\ \xi_g$.

Diagram (B) shows the fully divergent beam image profiles of dissociated Frank partials, at different depths. The small peak is that of the stair-rod.

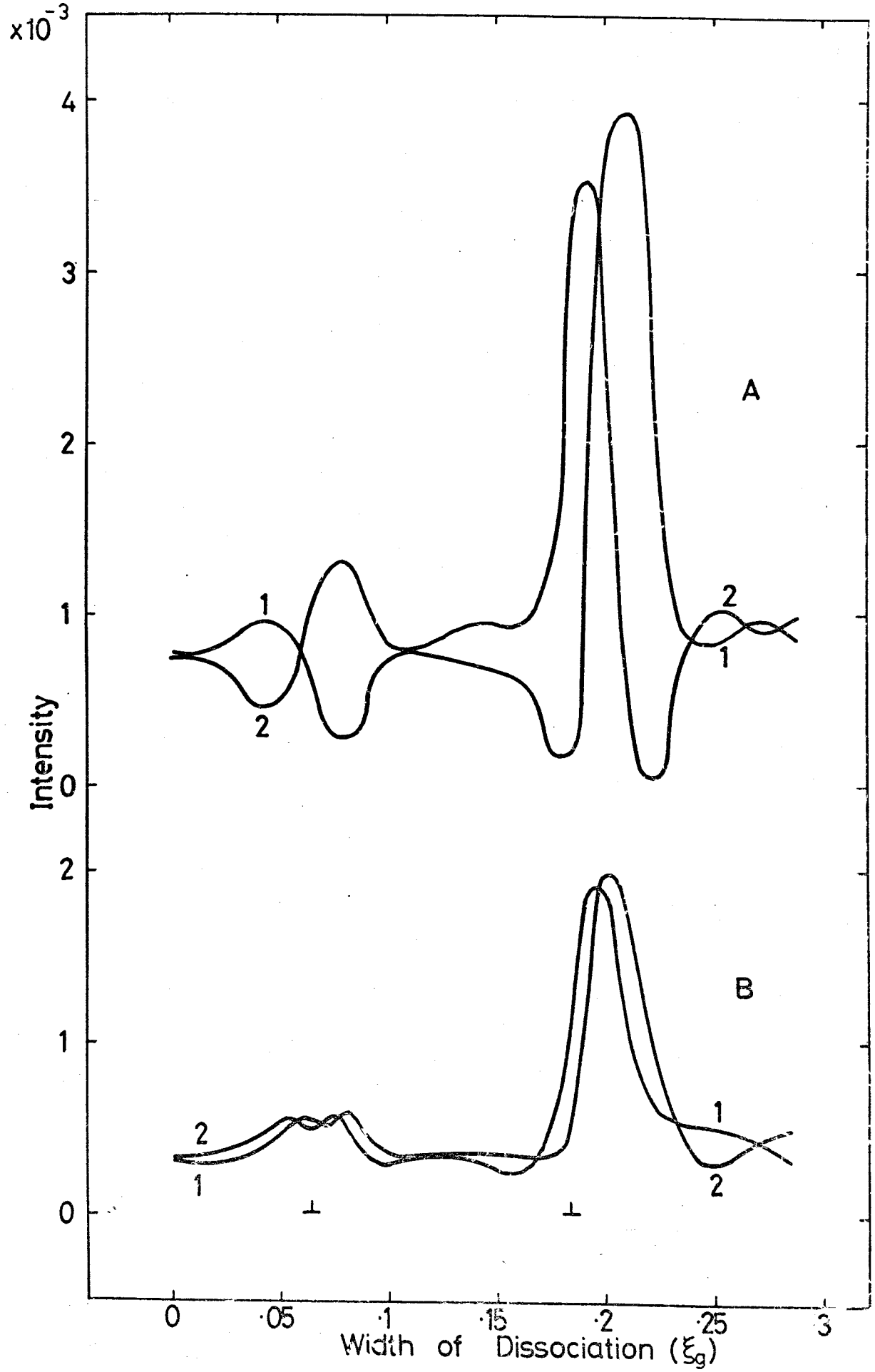
x10⁻³
4
3
2
1
0
Intensity
A
1
2
2
1
B
2
1
1
2
⊥
⊥
0
·05
·1
·15
·2
·25
3
Width of Dissociation (ξg)

Fig. 3/32 Transformation of Frank loops to perfect loops in a Cu .077% Al foil during irradiation at 210°C.

Loop α:- Frank loop on the $(\bar{1}1\bar{1})$ plane has sheared by the passage of Shockley partials to a perfect loop with $\bar{b} = \frac{a}{2}[1\bar{1}0]$ and $\bar{n}$ $(\bar{1}1\bar{1})$

Loop β:- Due to the curvature of the loop sides, it was not possible to obtain an exact determination of the loop normal. However, partial rotation towards $\bar{n} = (0\bar{1}1)$ has occurred.

x and z illustrates the amalgamation of perfect loops together.

y shows the only amalgamation of Frank loops observed during the experimental work carried out for this thesis.

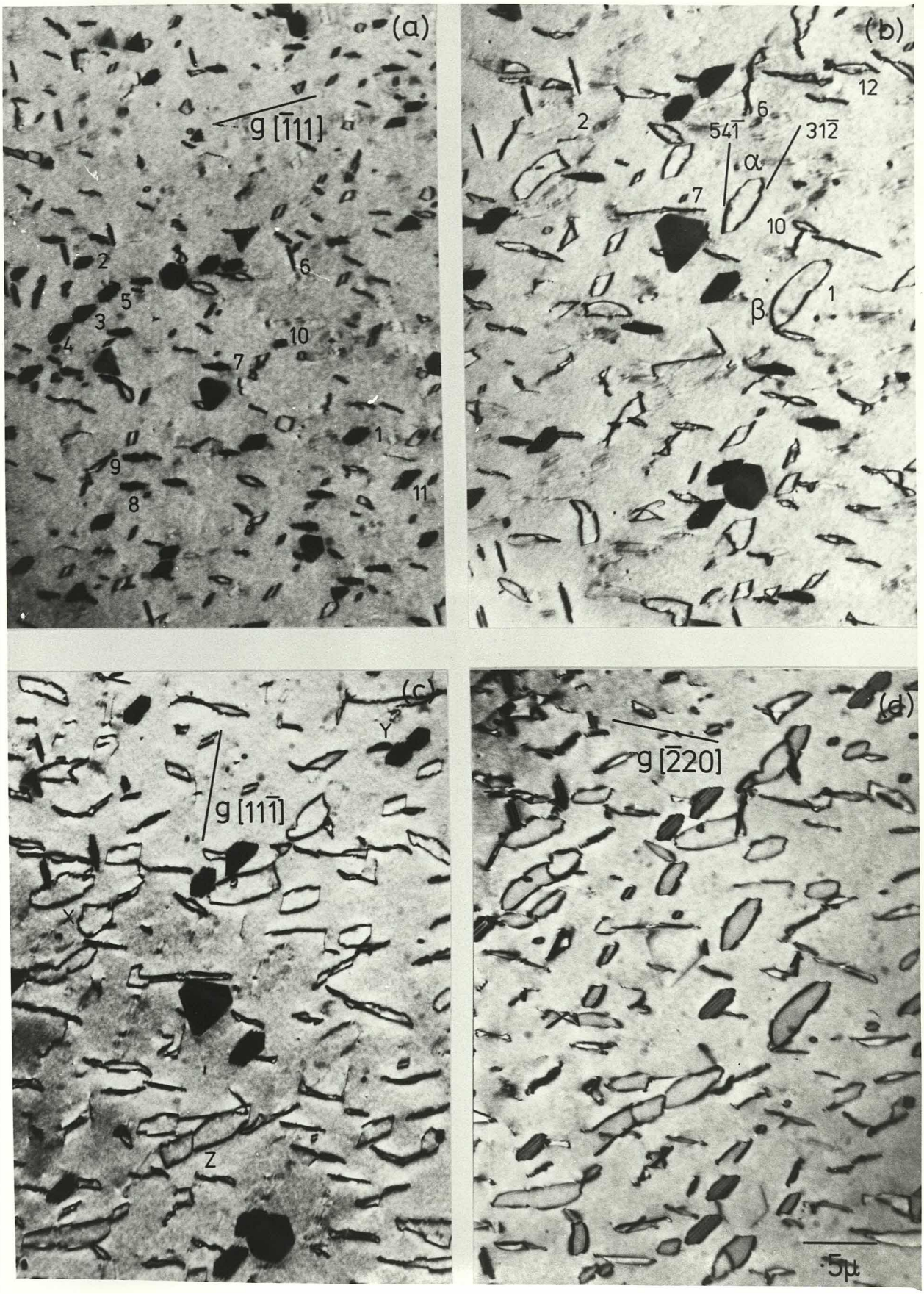
(a)
g [$\bar{1}11$]
2
5
3
4
6
10
7
1
9
8
11
(b)
12
2
6
54$\bar{1}$
31$\bar{2}$
α
7
10
β
1
(c)
Y
g [11$\bar{1}$]
X
Z
(d)
g [$\bar{2}20$]
5μ

Fig. 3/33 Micrographs illustrating the shear of Frank loops into perfect loops in a foil of Cu .077% Al.

Loop α: shear of Frank loop $\bar{b} = \frac{a}{3}[\bar{1}\bar{1}1]$ into a perfect loop $\bar{b} = \frac{a}{2}[10\bar{1}]$

The final orientations of loops β and γ appear to be on two different planes.

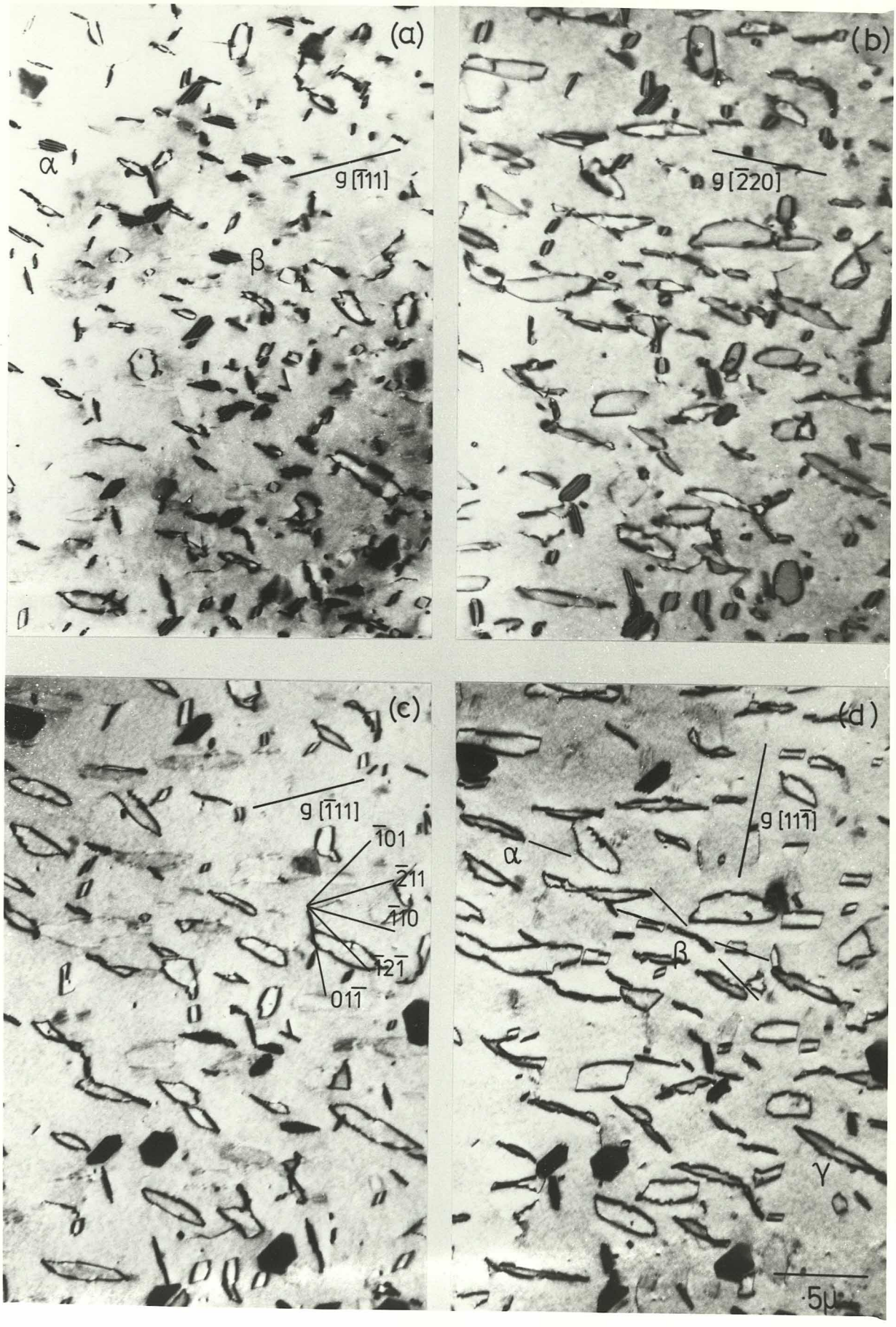
(a)
α
g [$\bar{1}$11]
β
(b)
g [$\bar{2}$20]
(c)
g [$\bar{1}$11]
$\bar{1}$01
$\bar{2}$11
$\bar{1}$10
$\bar{1}$2$\bar{1}$
01$\bar{1}$
(d)
g [11$\bar{1}$]
α
β
γ
5μ

Fig. 3/34 Transition of Frank loops in a Cu 16% Al foil into perfect loops after shearing, by the passage of two Shockley partial dislocations across the stacking fault.

Very little rotation of the loops takes place after the transition. Loops 1, 2, 3 and 10 have retained their original shapes on the {111} planes.

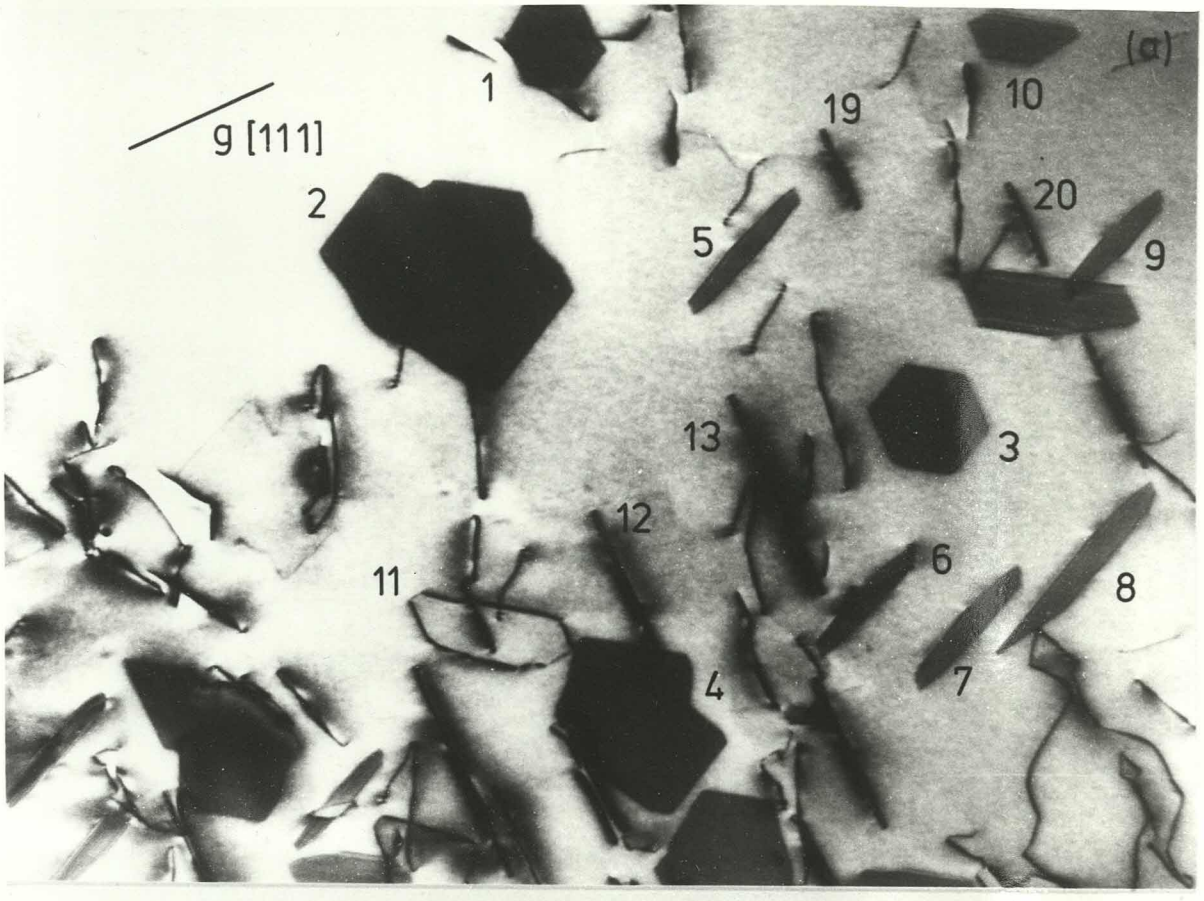
(a)
g [111]
1
19
10
2
20
5
9
13
3
12
6
11
8
4
7

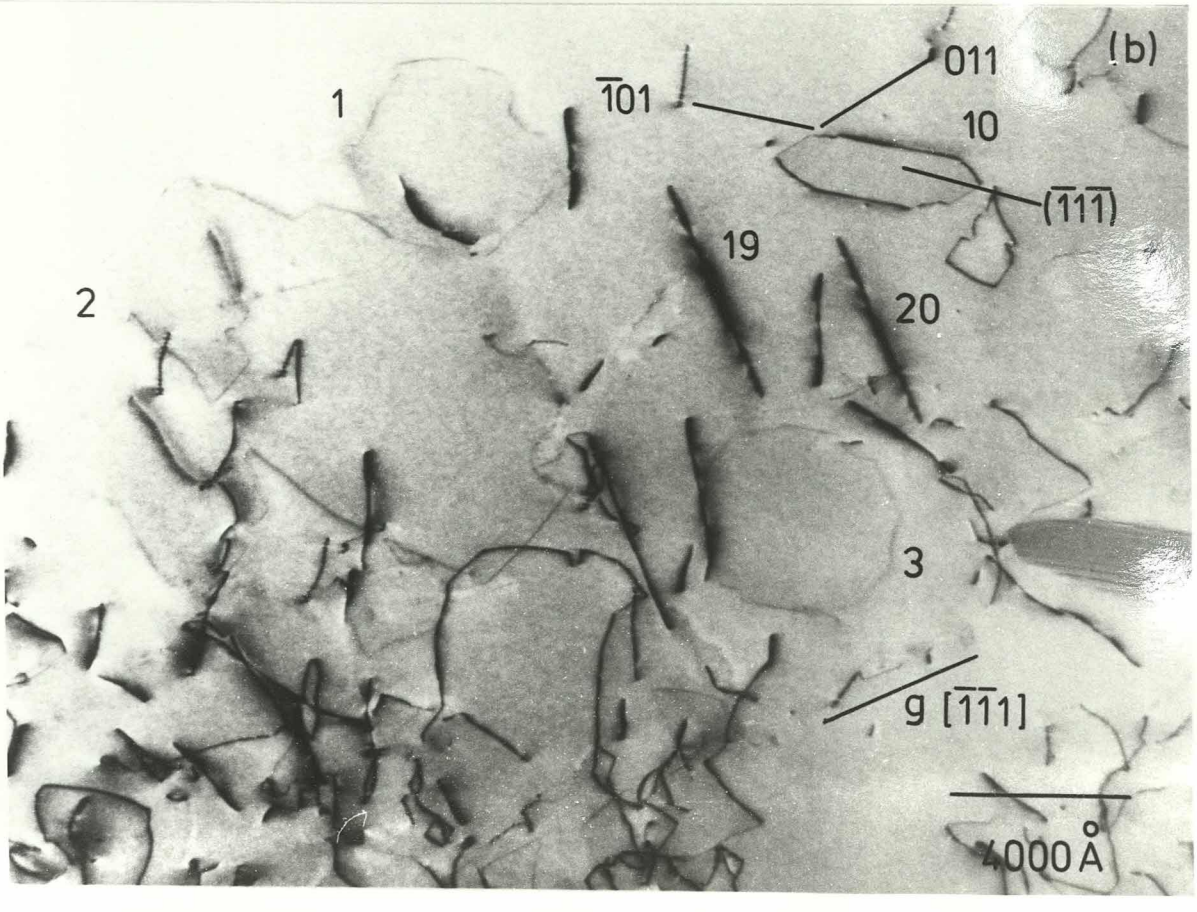
(b)
011
1
$\bar{1}01$
10
$(\bar{1}1\bar{1})$
19
2
20
3
g [$\bar{1}\bar{1}$1]
4000 Å

Fig. 3/35 Diagram illustrates schematically the dislocations of the Frank loop in fig. 3/36 and 3/37.

Fig. 3/36
3/37 Weak beam micrographs of a Frank loop on the (111) plane in the process of shearing by the passage of Shockley partials into a perfect loop.

This shearing process was nucleated by the interaction of an inclined loop with a corner of the (111) Frank loop.

(a) $g = [\bar{2}02]$ z $[121]$ weak beam g/3g
(b) $g = [\bar{1}1\bar{1}]$ z $[121]$ weak beam g/5g
(c) $g = [\bar{1}1\bar{3}]$ z $[110]$ B.F.
(d) $g = [\bar{1}1\bar{3}]$ z $[110]$ g/2.4g
(e) $g = [1\bar{3}\bar{1}]$ z $[101]$ B.F.
(f) $g = [1\bar{1}\bar{3}]$ z $[110]$ g/2.4g
(g) $g = [3\bar{1}1]$ z $[011]$ g/2.4g
(h) $g = [\bar{3}\bar{1}1]$ z $[011]$ g/2.4g

Fig.3/35

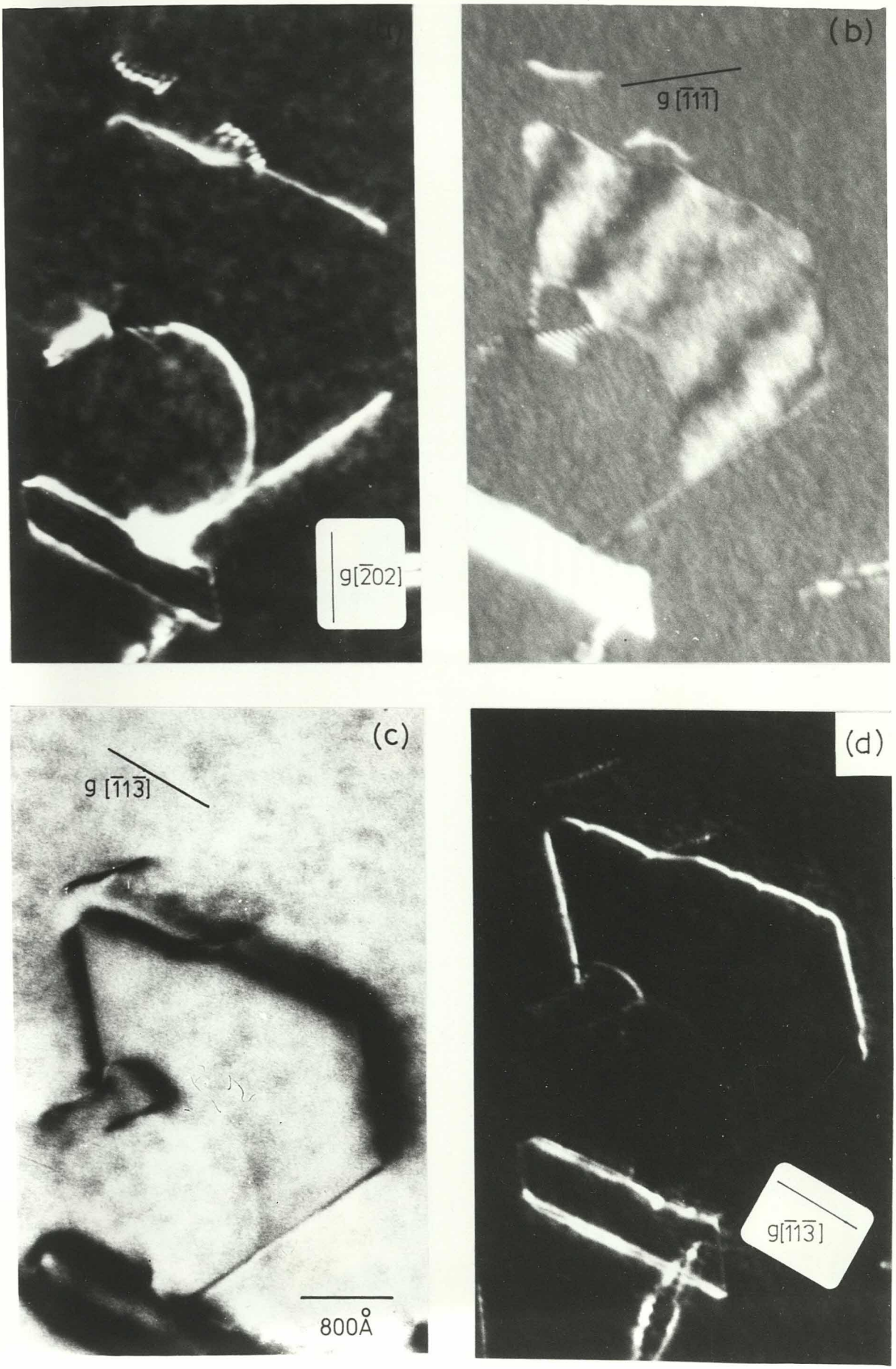

Fig. 3/36

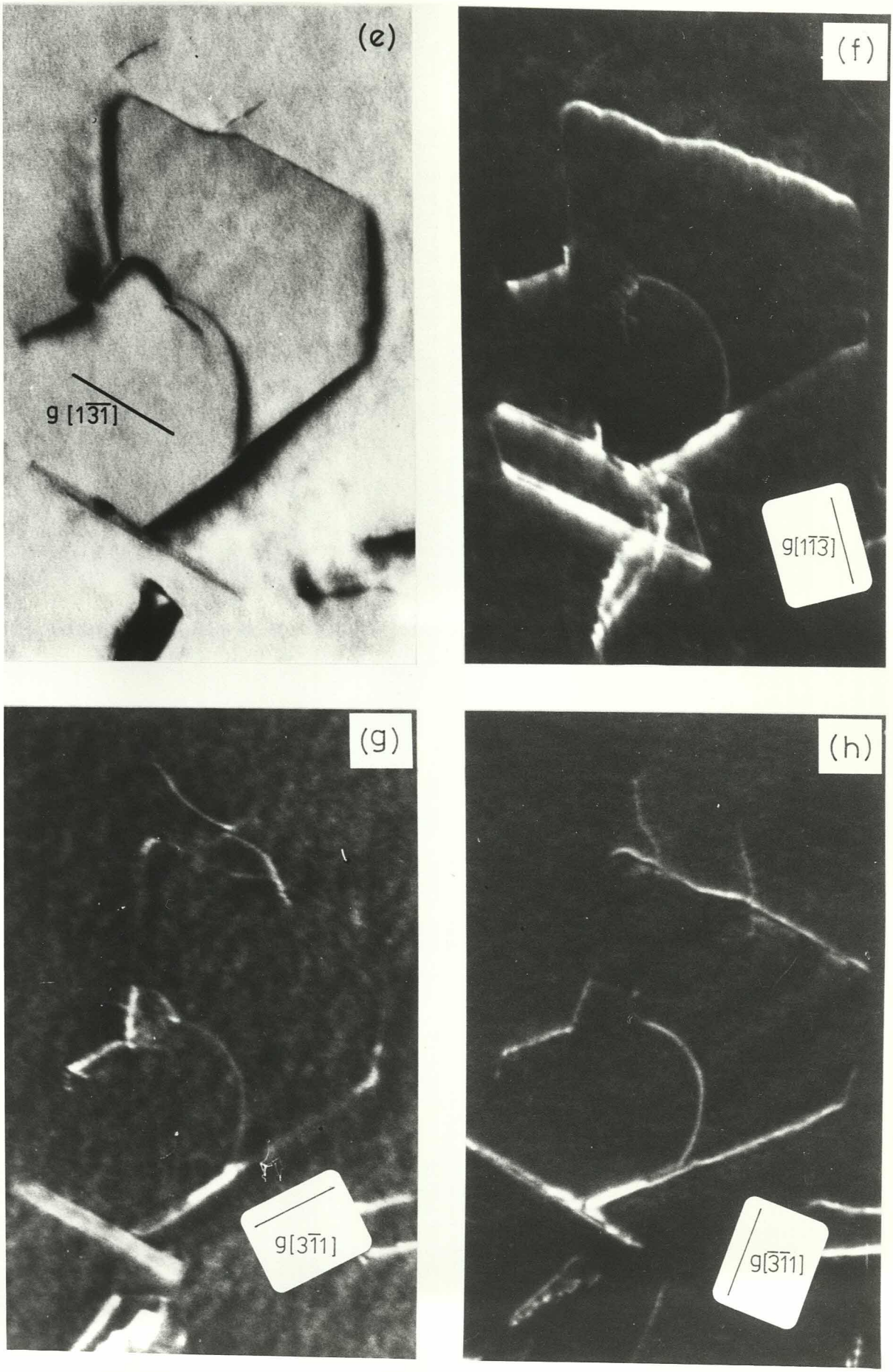

Fig. 3/37

Fig. 3/38 shows schematically the nature of the Shockley partials involved in removing the stacking fault from the Frank loop on the (111) plane, fig. 3/36 and 3/37. The perfect dislocations $b = \frac{a}{2}[1\bar{1}0]$ and $\frac{a}{2}[101]$ run from the loop to the foil surface.

Since the loop is interstitial, two Shockley partials are needed for the shearing process:

$$\frac{a}{6}[2\bar{1}\bar{1}] = \frac{a}{6}[1\bar{2}1] + \frac{a}{6}[11\bar{2}]$$

and $$\frac{a}{6}[1\bar{2}1] = \frac{a}{6}[2\bar{1}\bar{1}] + \frac{a}{6}[\bar{1}\bar{1}2]$$

The separation of these dislocations is small and they exhibit contrast, as if from a single dislocation:-

thus $\frac{a}{6}[2\bar{1}\bar{1}]$ and $\frac{a}{6}[1\bar{2}1]$

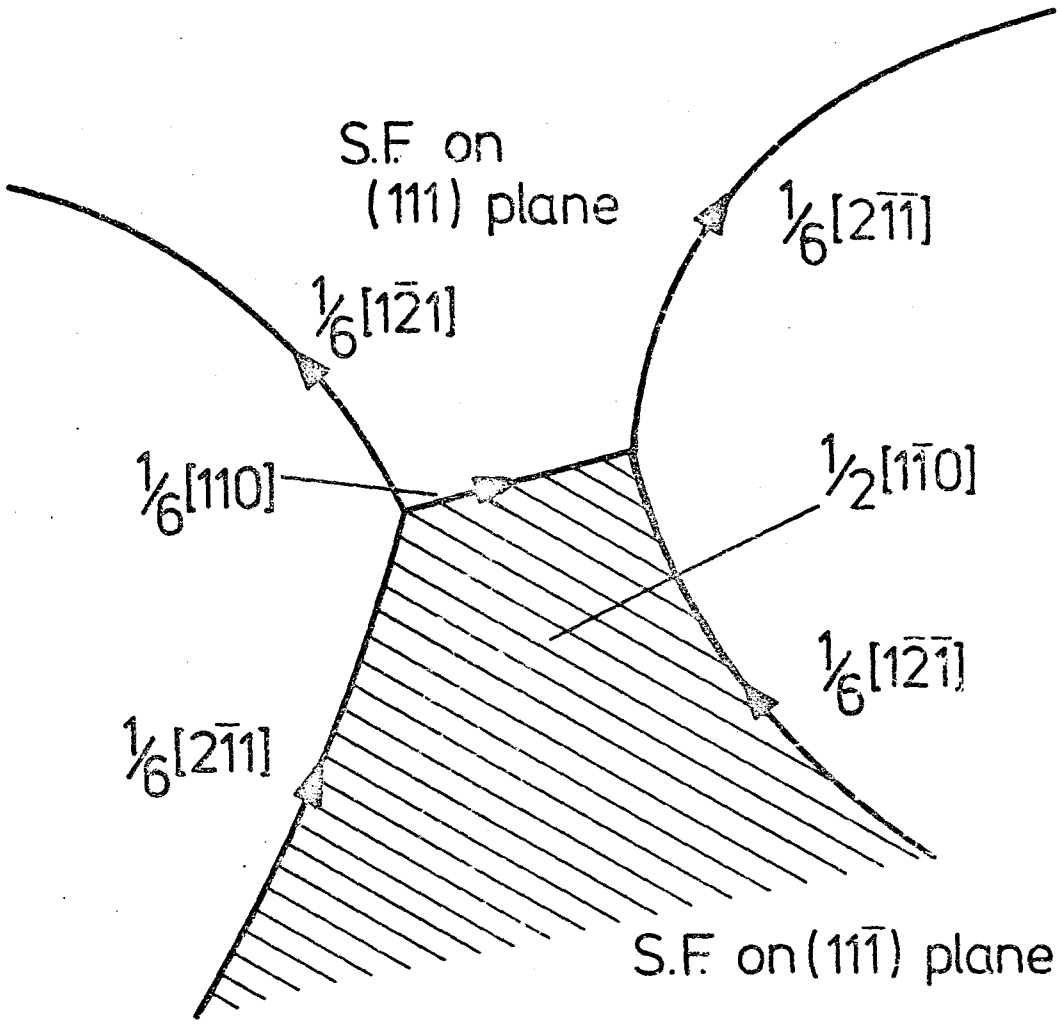
S.F. on
(111) plane
$\frac{1}{6}[2\bar{1}\bar{1}]$
$\frac{1}{6}[1\bar{2}1]$
$\frac{1}{6}[110]$
$\frac{1}{2}[1\bar{1}0]$
$\frac{1}{6}[1\bar{2}\bar{1}]$
$\frac{1}{6}[2\bar{1}1]$
S.F. on $(11\bar{1})$ plane

(A)

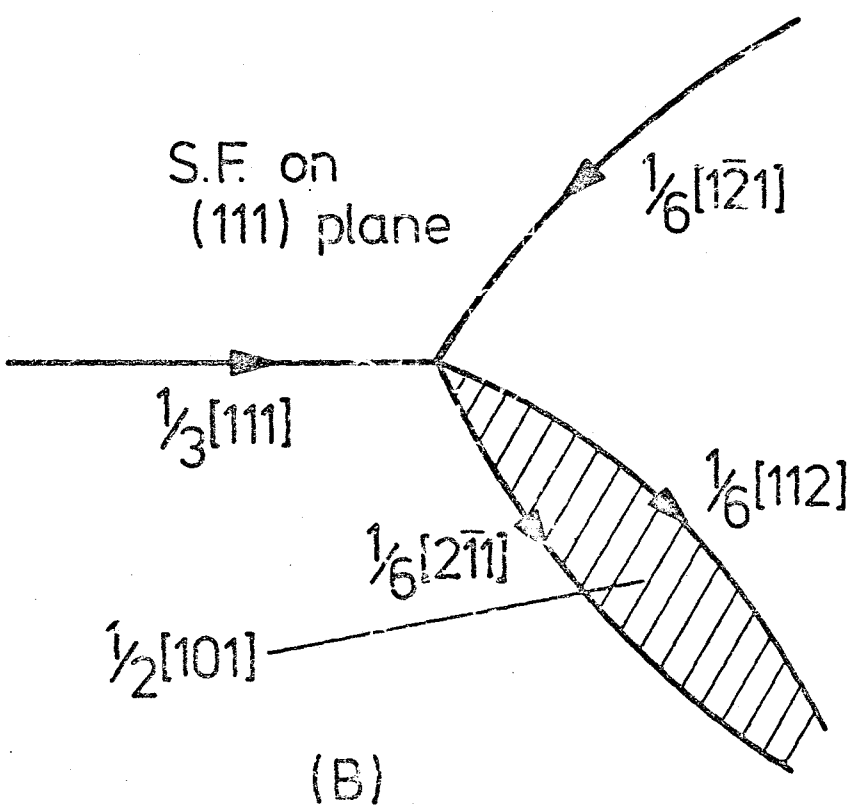
S.F. on
(111) plane
$\frac{1}{6}[1\bar{2}1]$
$\frac{1}{3}[111]$
$\frac{1}{6}[112]$
$\frac{1}{6}[2\bar{1}1]$
$\frac{1}{2}[101]$

(B)

Fig. 3/39 illustrates the possible reactions which may occur when the Shockley partial $\frac{a}{6}[2\bar{1}\bar{1}]$ joins the Frank partial $\frac{a}{3}[111]$. The dislocations observed are shown in fig. (D).

The Shockley partial dislocations were nucleated when the loop interacted with another Frank loop on an inclined plane.

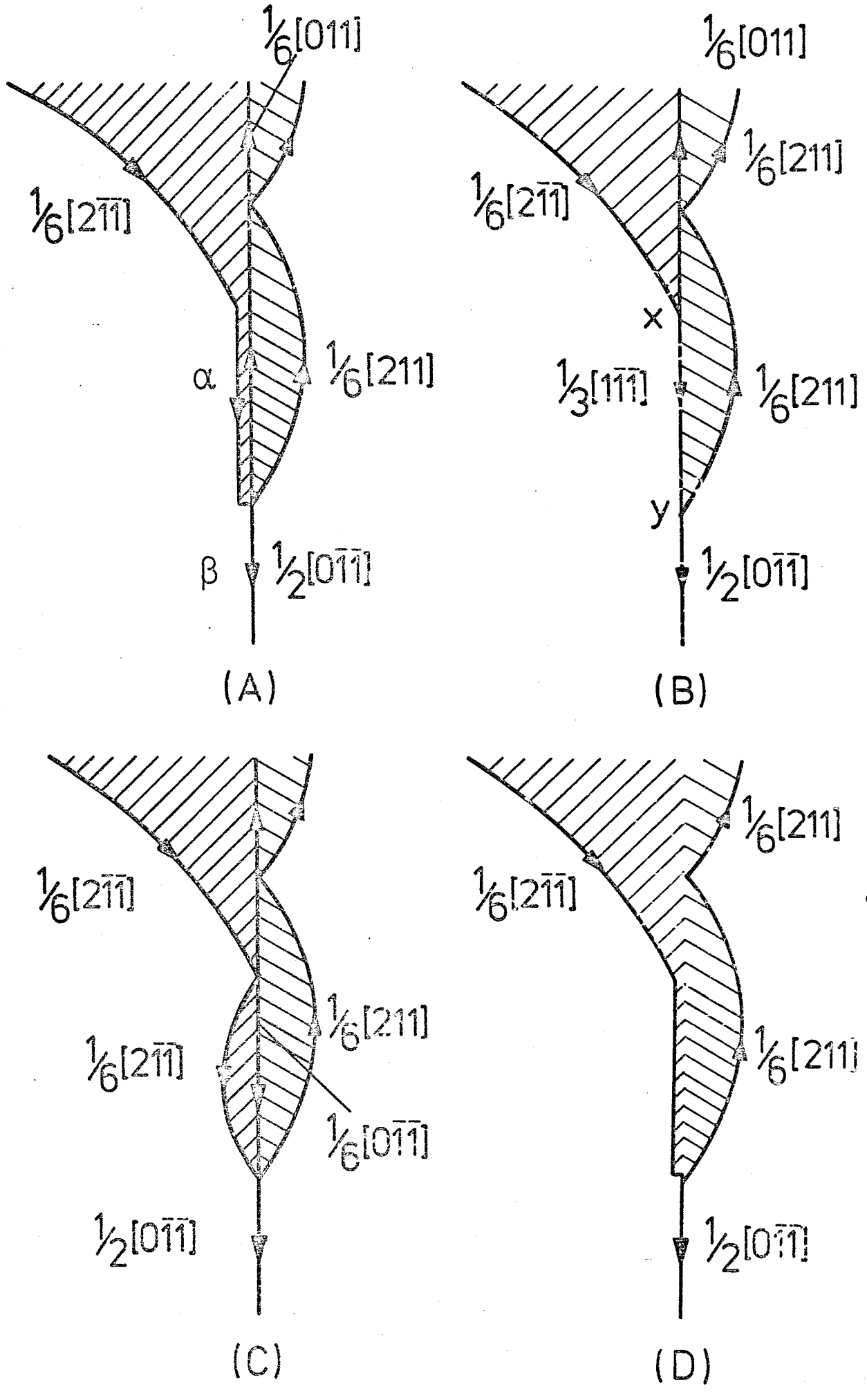
1/6[011]
1/6[2$\bar{1}\bar{1}$]
α
1/6[211]
β
1/2[0$\bar{1}\bar{1}$]
(A)
1/6[011]
1/6[211]
1/6[2$\bar{1}\bar{1}$]
x
1/3[1$\bar{1}\bar{1}$]
1/6[211]
y
1/2[0$\bar{1}\bar{1}$]
(B)
1/6[2$\bar{1}\bar{1}$]
1/6[211]
1/6[2$\bar{1}\bar{1}$]
1/6[0$\bar{1}\bar{1}$]
1/2[0$\bar{1}\bar{1}$]
(C)
1/6[211]
1/6[2$\bar{1}\bar{1}$]
1/6[211]
1/2[0$\bar{1}\bar{1}$]
(D)

Fig. 3/40 Weak beam micrographs of a partially sheared Frank loop in Cu 16% Al.

The dissociation of the Frank partial into Shockley and stair-rod dislocations is faintly visible. Also visible is the dissociation of the sheared area of the loop, with Shockley partials.

Fig. 3/41 shows schematically a Shockley partial dislocation $\frac{a}{6}[\bar{2}11]$ in the process of shearing a complete Frank (111) loop. The initial energy for the nucleation of the Shockley probably resulted from foil stresses. The micrographs of this partially sheared Frank loop are shown in fig. 3/40.

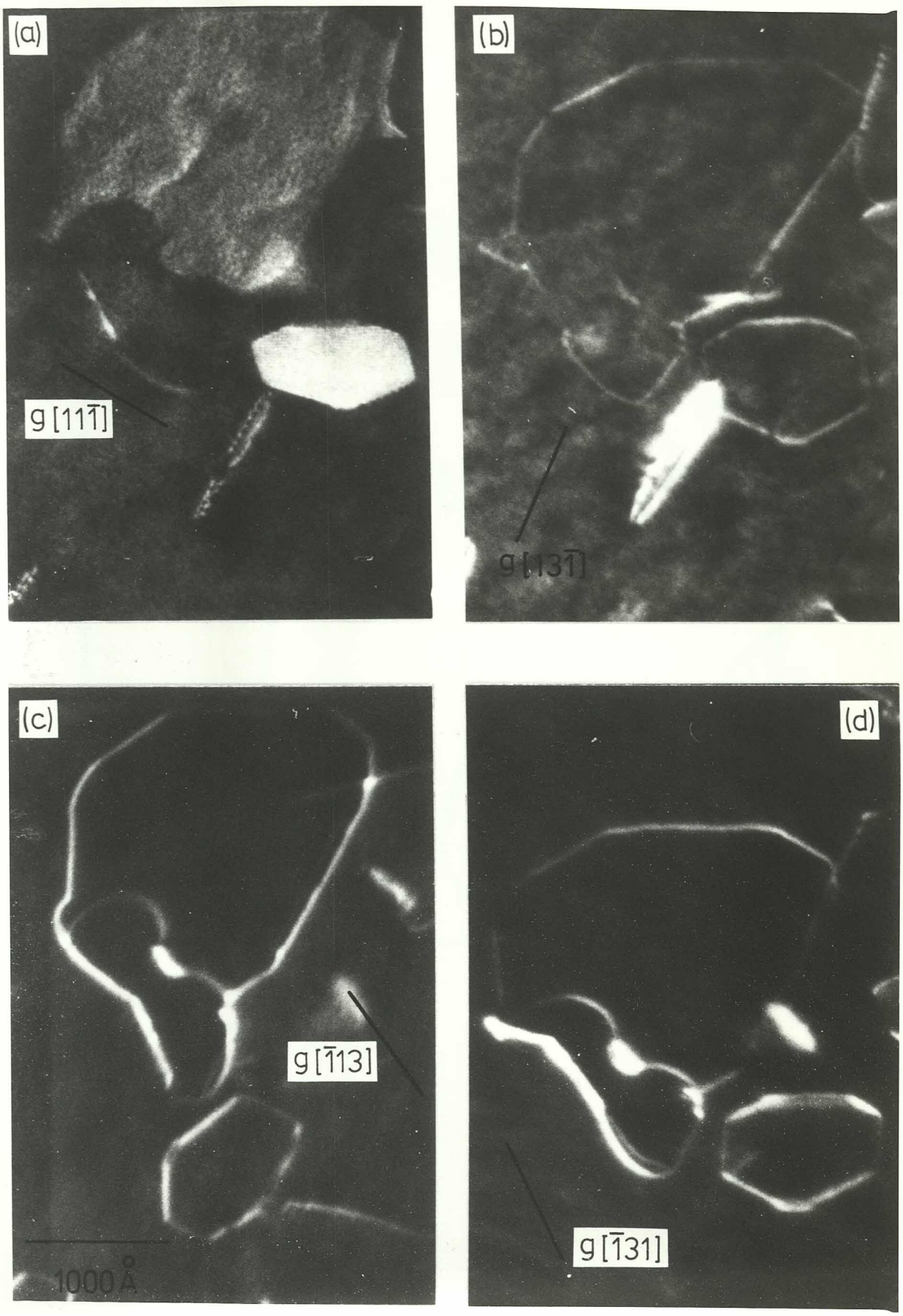

Fig. 3/40

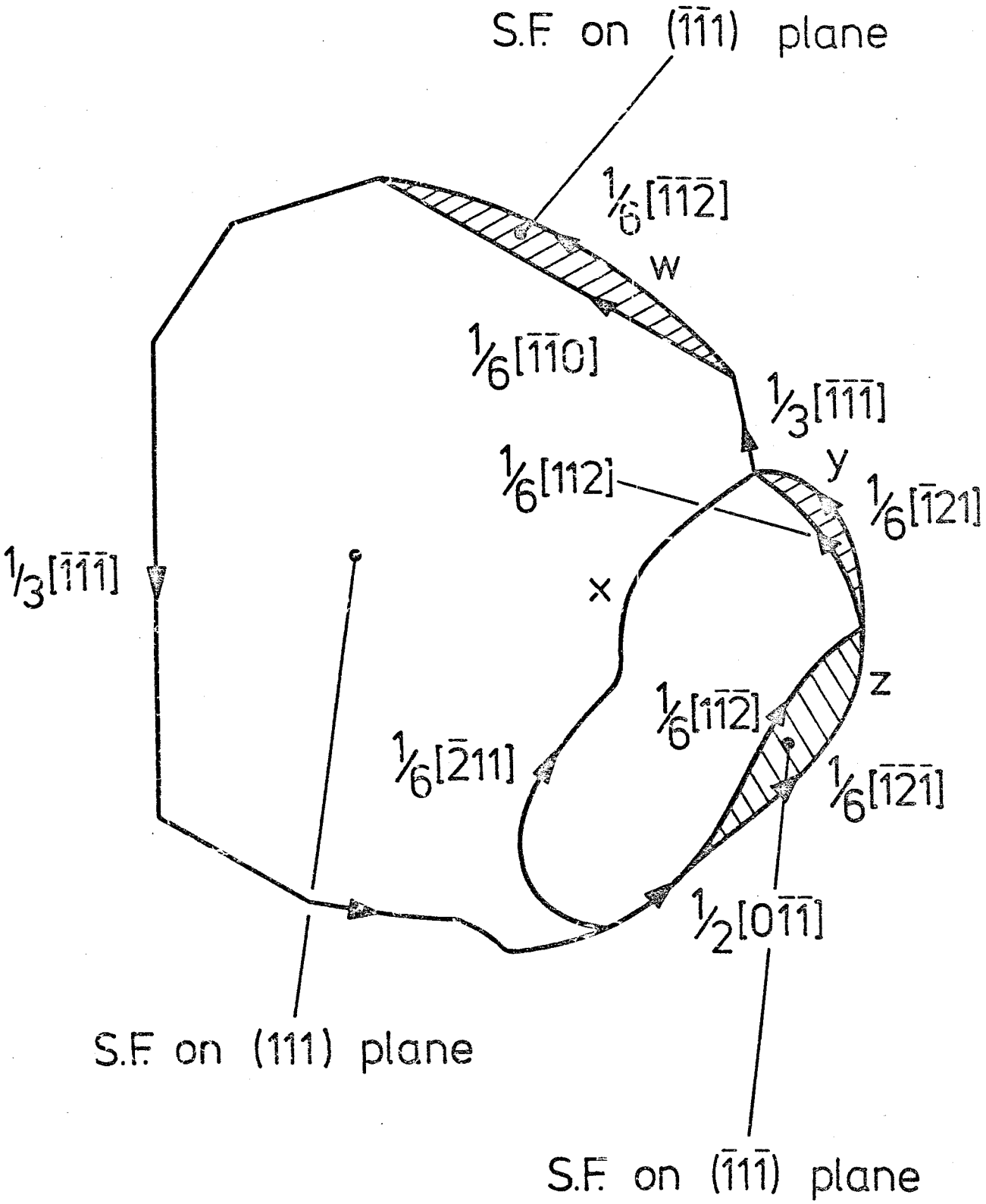
S.F. on $(\bar{1}\bar{1}1)$ plane
$\frac{1}{6}[\bar{1}\bar{1}2]$
w
$\frac{1}{6}[\bar{1}\bar{1}0]$
$\frac{1}{3}[\bar{1}\bar{1}\bar{1}]$
$\frac{1}{6}[112]$
y
$\frac{1}{6}[\bar{1}21]$
$\frac{1}{3}[\bar{1}\bar{1}\bar{1}]$
x
z
$\frac{1}{6}[1\bar{1}\bar{2}]$
$\frac{1}{6}[\bar{2}11]$
$\frac{1}{6}[\bar{1}\bar{2}1]$
$\frac{1}{2}[0\bar{1}\bar{1}]$
S.F. on (111) plane
S.F. on $(\bar{1}1\bar{1})$ plane

Fig. 3/41

Fig. 4/1 Burgers vector analysis of rhombus loops in a Cu 5% Al foil after irradiation in the H.V.E.M. (slow grown crystal).

Loop 1 $\bar{b} = \pm \frac{a}{2} [10\bar{1}]$

Loop 2 $\bar{b} = \pm \frac{a}{2} [110]$

Loop 3 $\bar{b} = \pm \frac{a}{2} [101]$

Loop 4 $\bar{b} = \pm \frac{a}{2} [1\bar{1}0]$

Loop 6 $\bar{b} = \pm \frac{a}{2} [011]$

Loop 7 $\bar{b} = \pm \frac{a}{2} [0\bar{1}1]$

Fig. 4/2 Inside outside contrast of the rhombus loops in fig. 4/1.

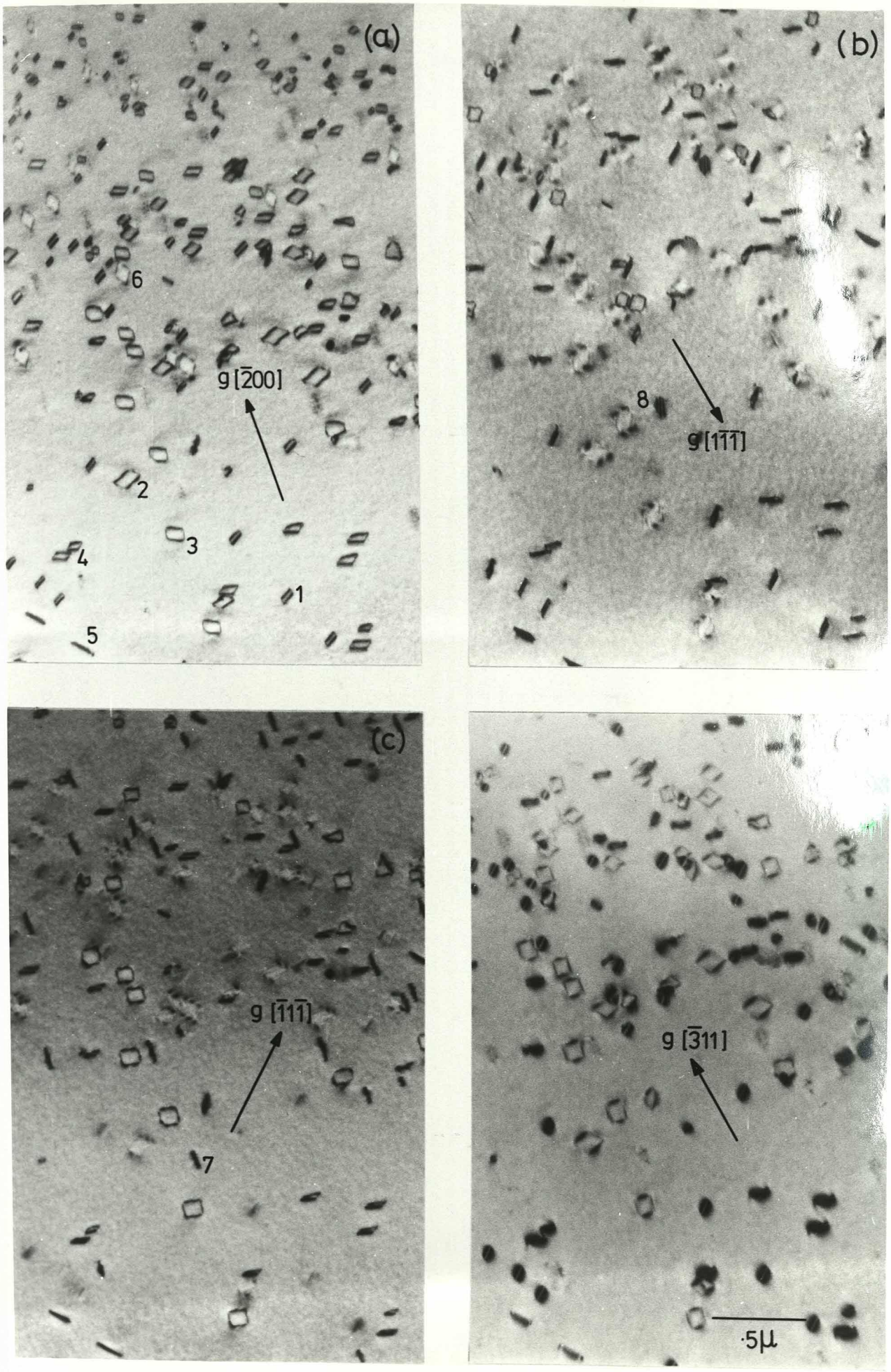

Fig.4/1

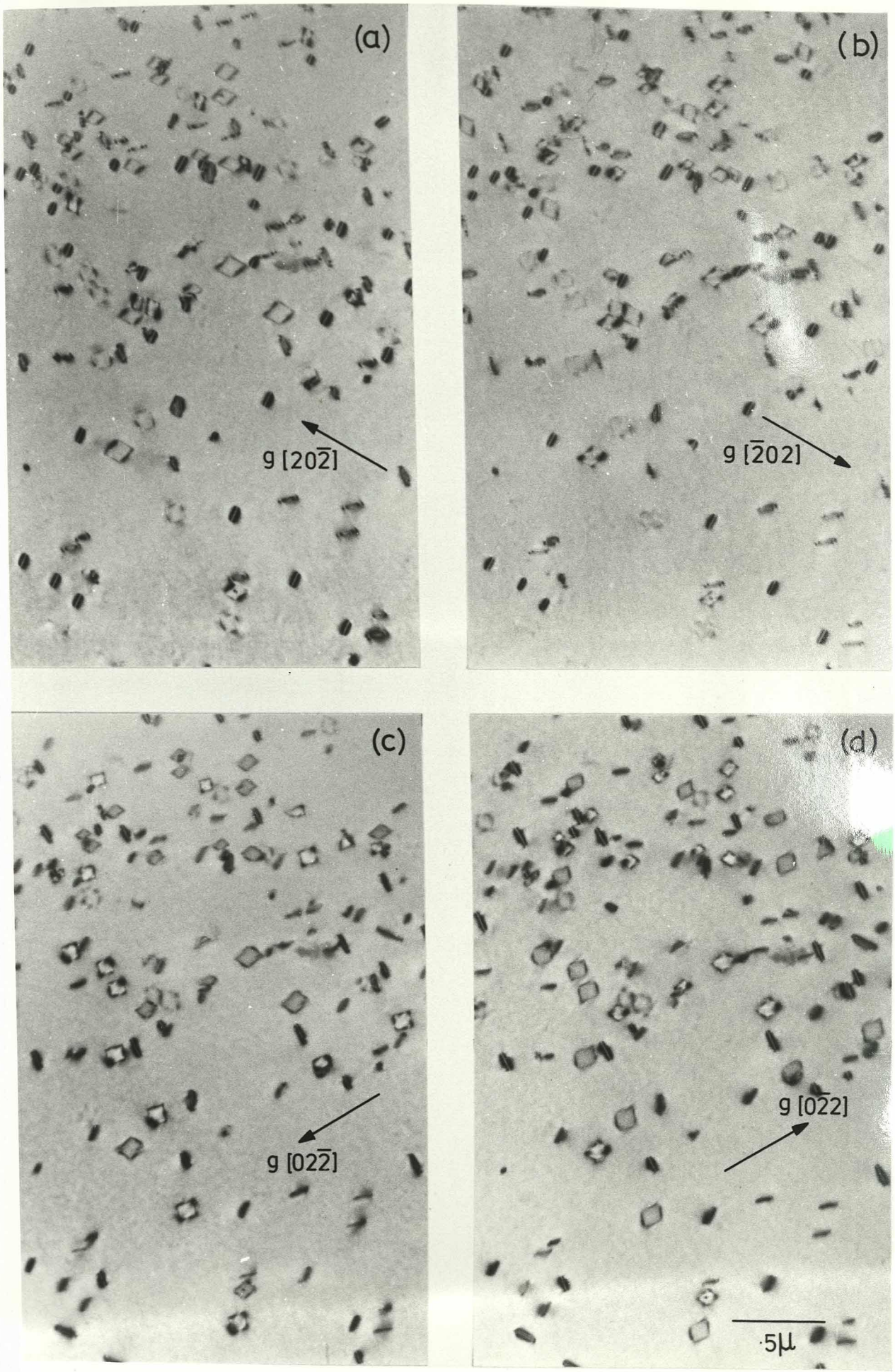

Fig.4/2

Fig. 4/3 The stereogram depicts the method used to obtain the loop normal of loop 2 figs 4/1 and 4/2.

Points A, B and C are the beam directions used in imaging the loops.

The great circles -.-.- correspond to the planes of projection for each of the beam directions labelled.

For each plane of projection, the projected direction of $\bar{u}$ is marked at a corresponding angle from $\bar{g}$ in a known sense. Thus AUα1 represents the projection of one side of the loop at the beam direction A.

The true direction of $\bar{u}$ lies in the plane containing the beam direction and the projection of $\bar{u}$. This plane was constructed for each beam direction by drawing the great circle containing the projected direction of $\bar{u}$ and the beam direction (solid line). The region of intersection defines the loop side direction, e.g. Uα1.

The vector cross product was obtained by drawing great circles (dashed line) at right angles to the loop edge directions Uα1 and Uα2. The region of intersection defines the loop normal. In this case $\bar{n} \triangleq 320$, with the loop sides along $[2\bar{3}\bar{5}]$ and $[2\bar{3}5]$.

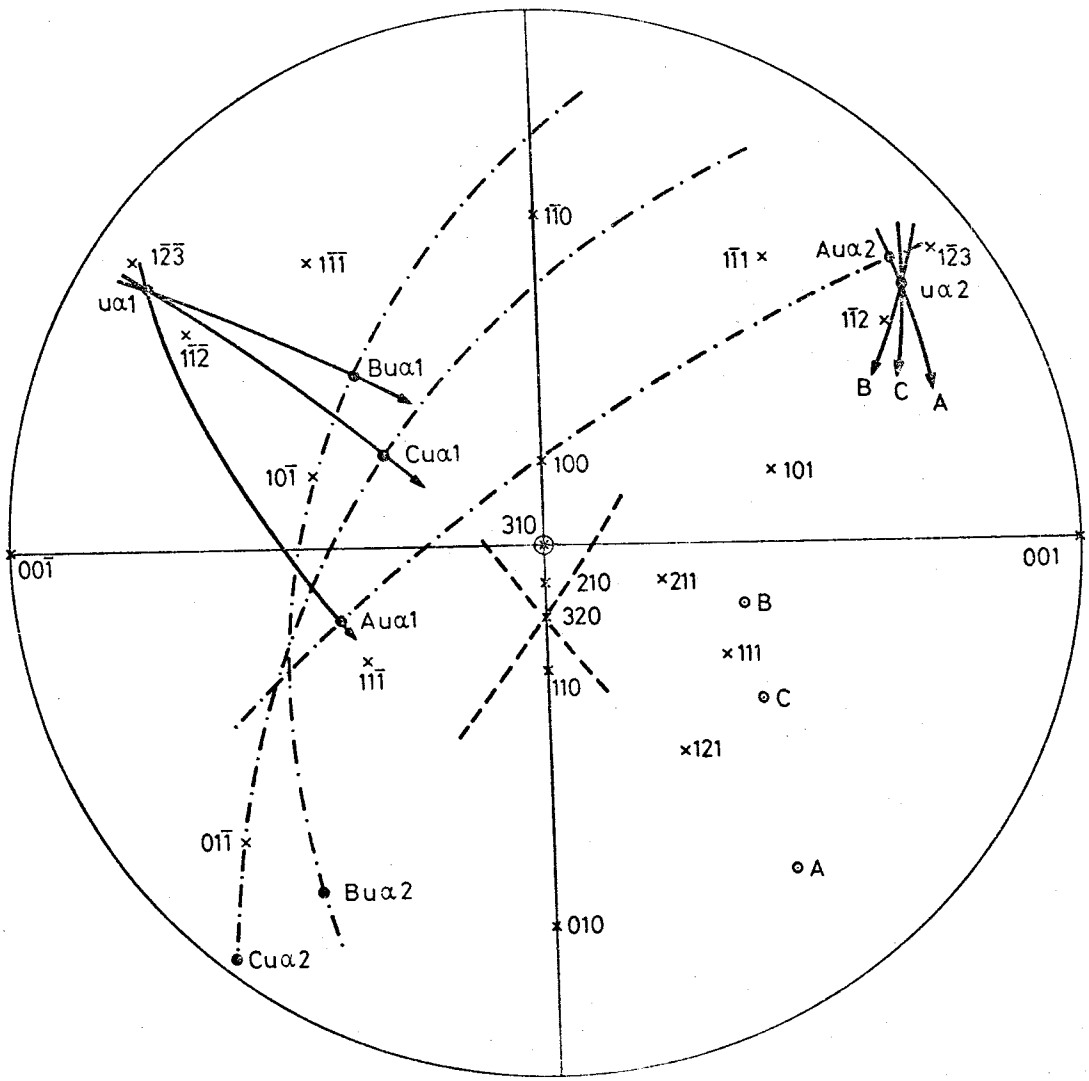
1$\bar{2}\bar{3}$
uα1
1$\bar{1}\bar{1}$
1$\bar{1}\bar{2}$
Buα1
Cuα1
10$\bar{1}$
00$\bar{1}$
Auα1
11$\bar{1}$
01$\bar{1}$
Buα2
Cuα2
1$\bar{1}$0
1$\bar{1}$1
Auα2
1$\bar{2}$3
uα2
1$\bar{1}$2
B
C
A
100
101
310
001
210
211
320
B
111
110
C
121
A
010

Fig. 4/4 The stereogram summarizes the relationship between loop plane normal $\bar{n}$ and associated Burgers vector $\bar{b}$ for the rhombus loops measured in fig. 4/1 and 4/2. In all cases, the normals lie near the Burgers vector direction.

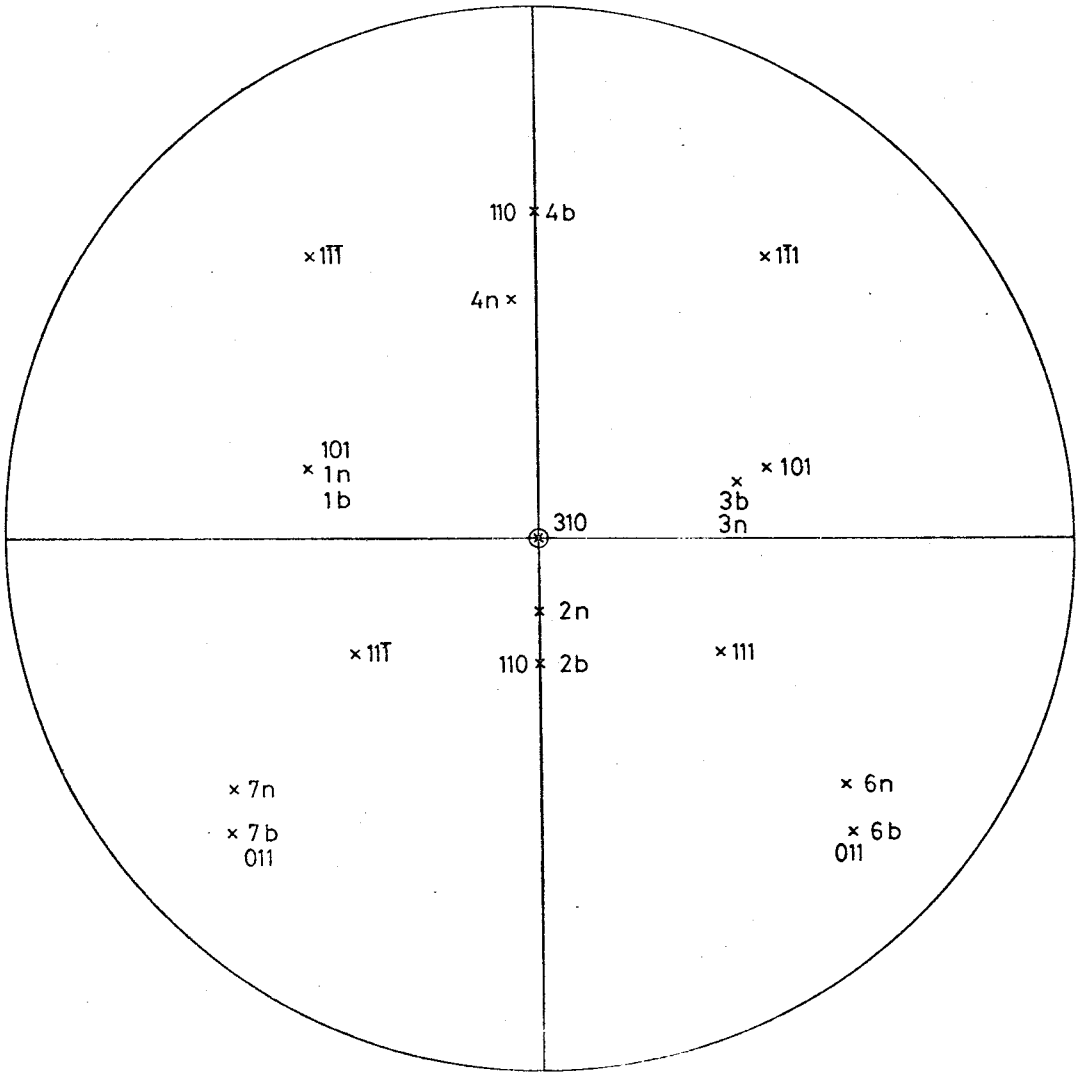
110 × 4b
× 1$\bar{1}\bar{1}$
× 1$\bar{1}$1
4n ×
101
× 1n
1b
× 101
3b
3n
310
× 2n
× 11$\bar{1}$
110 × 2b
× 111
× 7n
× 7b
011
× 6n
× 6b
011

Fig. 4/5 The diagrams illustrate the projections of rhombus loops to be expected at beam directions $\bar{z}$ = [112] and [011] using Thomson tetrahedron.

In the reflection g = $[\bar{1}\bar{1}1]$ loops 4, 5 and 6 are out of contrast, while in the reflection g = [200] loops 2 and 4 are out of contrast.

Loop 1 b = $\frac{a}{2}$ [110]

Loop 2 b = $\frac{a}{2}$ $[0\bar{1}1]$

Loop 3 b = $\frac{a}{2}$ $[\bar{1}01]$

Loop 4 b = $\frac{a}{2}$ [011]

Loop 5 b = $\frac{a}{2}$ $[1\bar{1}0]$

Loop 6 b = $\frac{a}{2}$ [101]

Side δ in (111)

α in $(\bar{1}1\bar{1})$

β in $(1\bar{1}\bar{1})$

γ in $(\bar{1}\bar{1}1)$

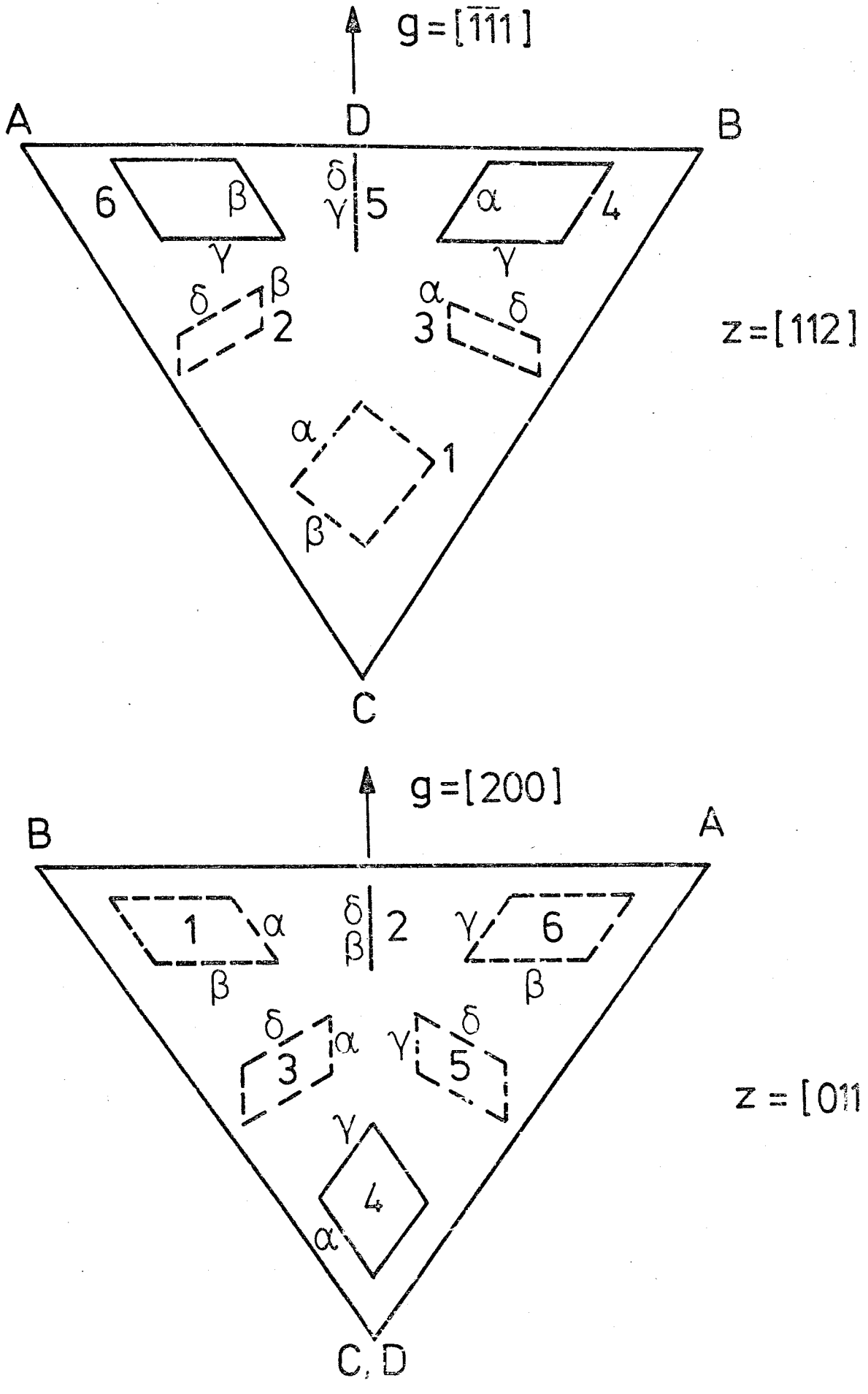
g=[1̄1̄1]
A
D
B
6
β
γ
δ
γ
5
α
4
γ
δ
β
2
α
3
δ
z=[112]
α
1
β
C
g=[200]
B
A
1
α
β
δ
β
2
γ
6
β
δ
3
α
γ
δ
5
γ
4
α
C, D
z=[011]

Fig. 4.6 Diagram (A) illustrates the prismatic character of {320} loops. The Burgers vector of the loop is along [110] and the loop sides are along the $[2\bar{3}\bar{5}]$ and $[2\bar{3}5]$ directions on the $(\bar{1}1\bar{1})$ and $(1\bar{1}\bar{1})$ planes. This loop is capable of conservative glide along [110], without shape change.

Diagram (B) shows the atomic positions on the (001) face of a F.C.C. structure. The dots correspond to atoms on the fact and the crosses to atoms displaced perpendicular to the paper by half a lattice spacing. When three adjacent $(\bar{1}20)$ planes are removed, the lattice can re-unite with a Burgers vector $\frac{a}{2}[\bar{1}10]$, leaving no stacking fault.

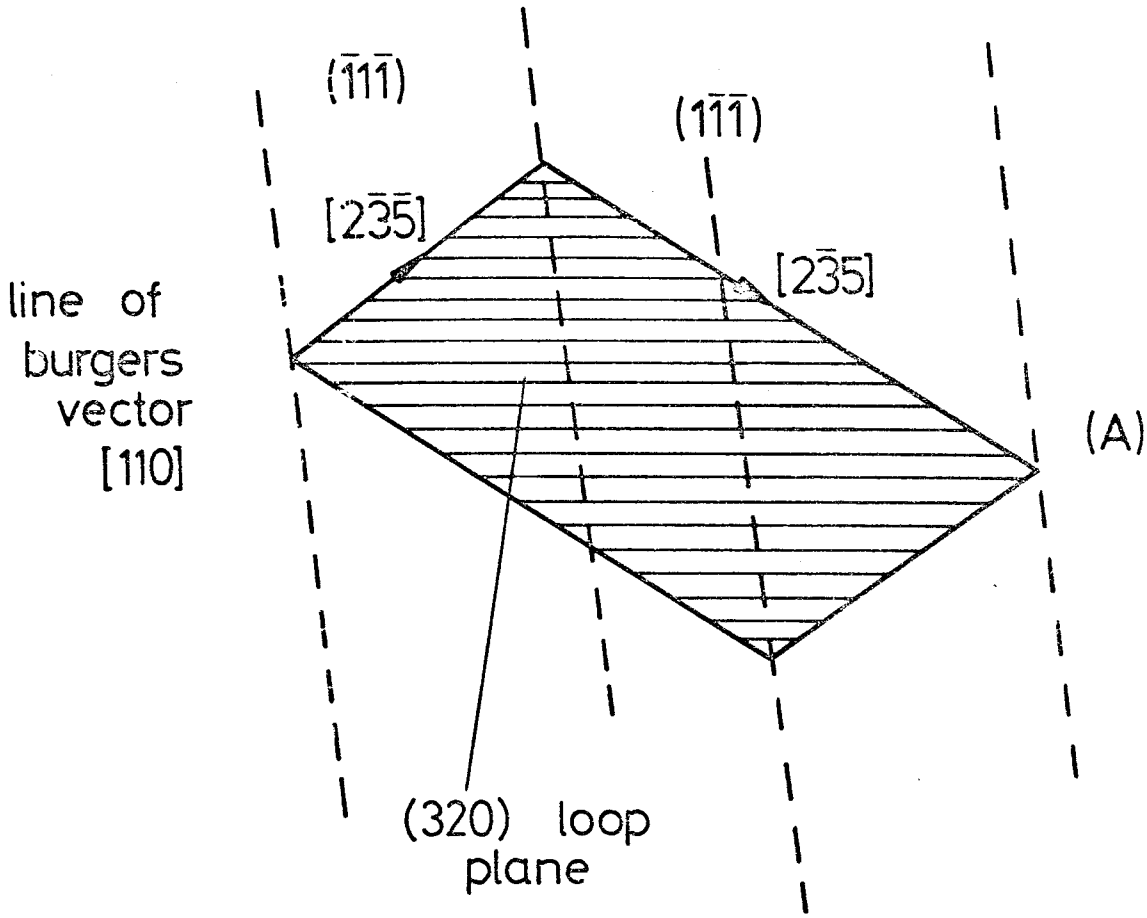
(1̄11̄)
(11̄1̄)
[2̄35̄]
[23̄5]
line of burgers vector [110]
(A)
(320) loop plane

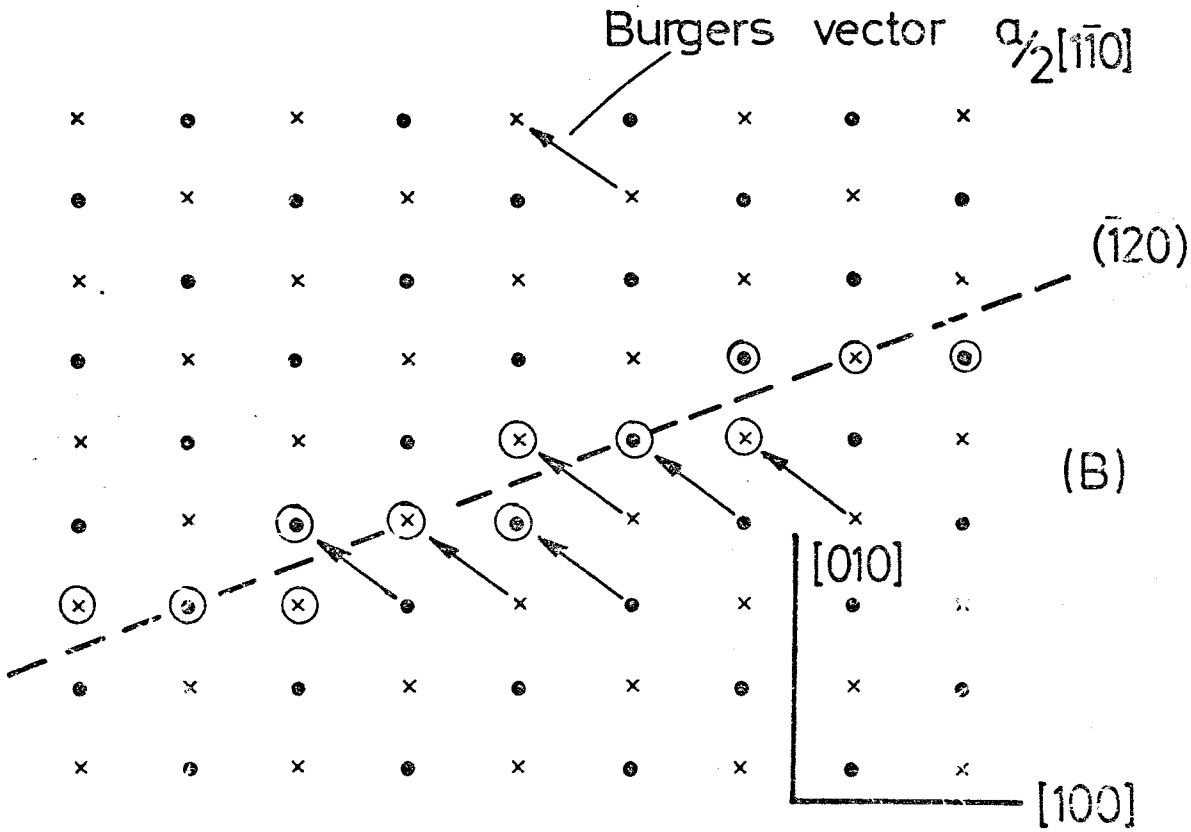
Burgers vector a/2[1̄10]
(1̄20)
(B)
[010]
[100]

Fig. 4/7 This diagram illustrates the transformation of a faulted Frank triangular loop on the (111) plane into a rhombus perfect loop on (110) plane. Diagram (A) shows the loop after the stacking fault has been removed but the sides confined to <110> directions. In Diagram (B) the $[\bar{1}01]$ and $[0\bar{1}1]$ sides have dissociated into Shockley partials on the $(\bar{1}1\bar{1})$ and $(1\bar{1}\bar{1})$ planes. Side $\bar{A}\bar{B}$ can, by a process of glide and climb transform itself into the position shown in diagram (C). Stair-rods $\alpha\beta$ and $^{\alpha\beta}/_{DC}$ join the stacking faults at the intersection of the (111) planes. By a rotation about the two areas shown, the final position of {320} can be achieved.

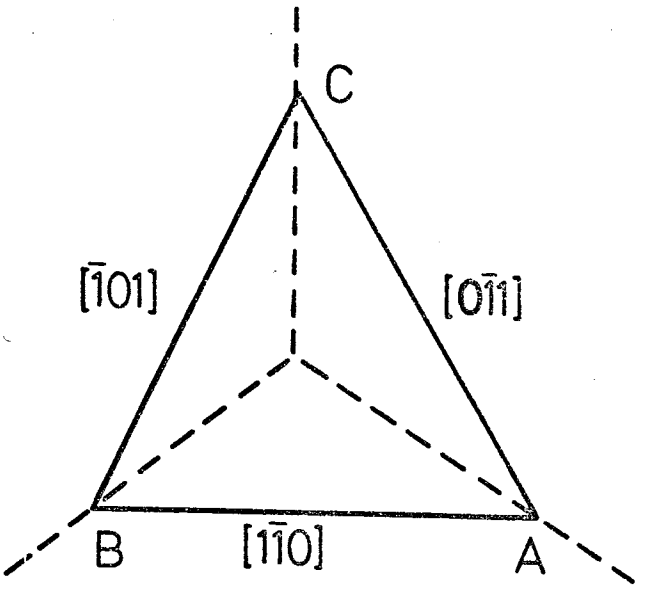

b = a/2[110]

n = (111)

(A)

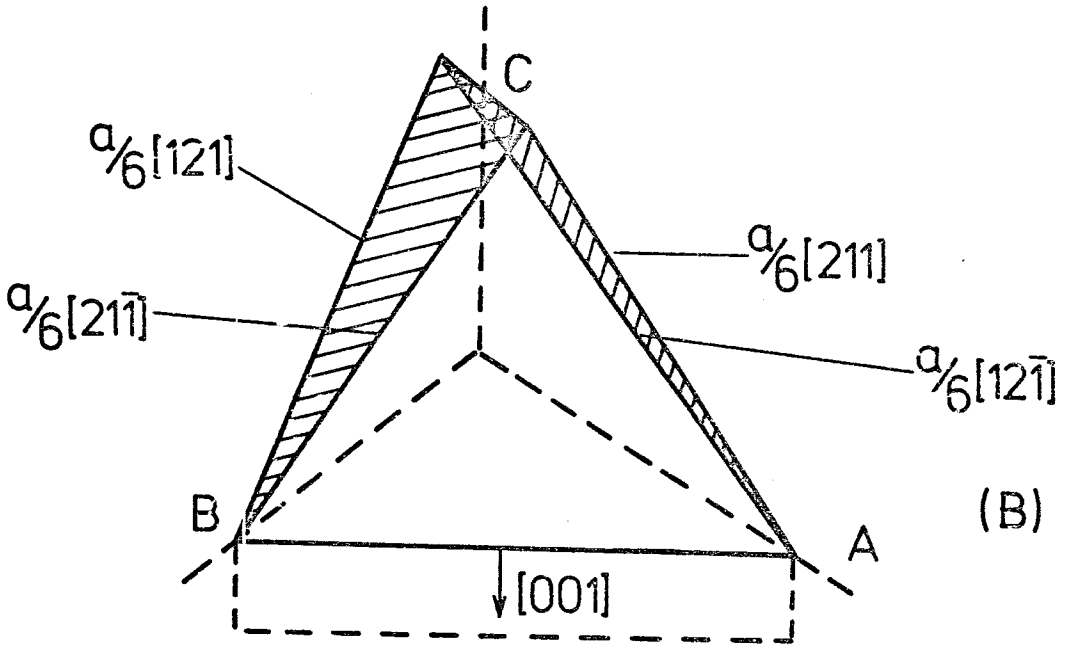

(B)

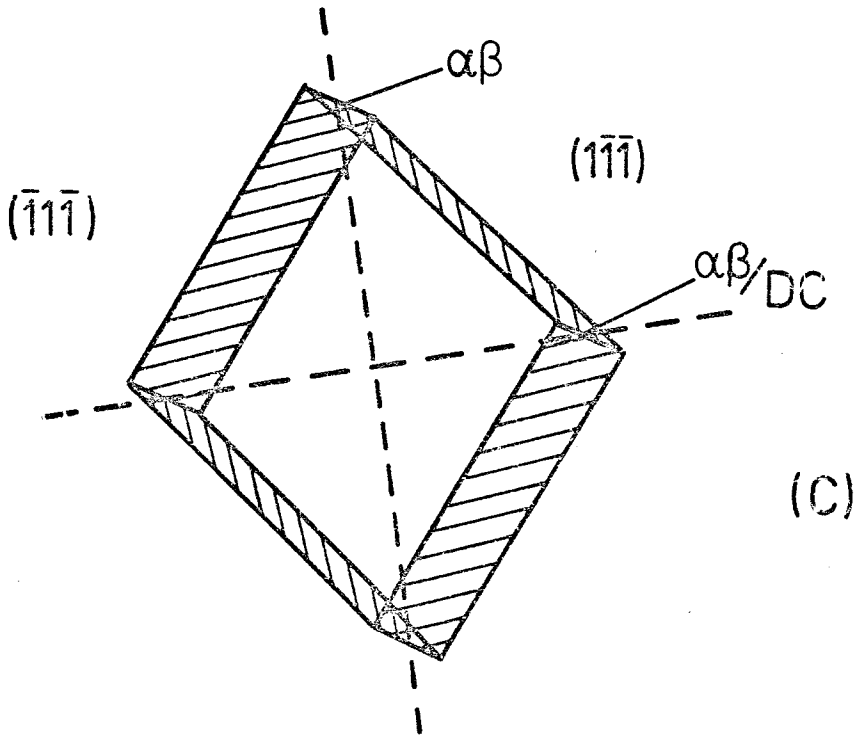

(C)

Fig. 4/8 Stereogram showing the geometry of the conversion of a (111) <110> hexagonal loop into a diamond with sides $[0\bar{1}1]$ and $[\bar{1}01]$. The loop sides can then slip on the two {111} planes shown, towards <235> directions corresponding to loops on {320} planes.

Several paths can be followed, in order to rotate from (111) to (320).

(A) The prismatic loop on the (111) plane can rotate about the $[1\bar{1}0]$ axis so that its sides lie along $[1\bar{1}2]$ and $[\bar{1}12]$. When the loop normal reaches (110), a rotation about the [001] axis (along (B)) brings theloop to its final position near (320).

Alternatively the loop can rotate directly along (C) to reach (320).

Experimental observations of the final loop normals indicate that route (D) is the one followed, in which rotation about the $[1\bar{1}0]$ and [001] axes occur simultaneously.

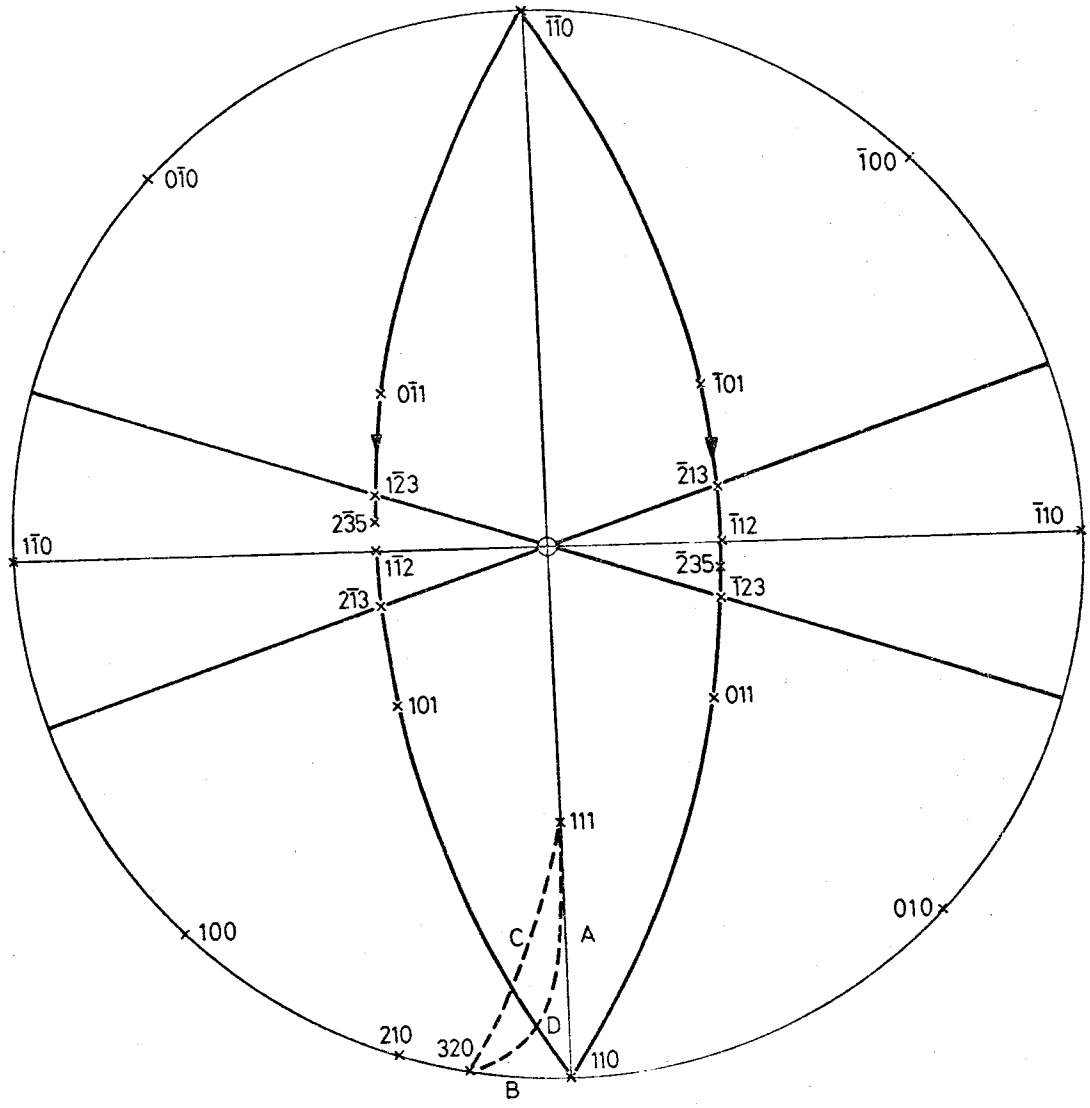
$\bar{1}\bar{1}0$
$0\bar{1}0$
$\bar{1}00$
$0\bar{1}1$
$\bar{1}01$
$1\bar{2}3$
$\bar{2}13$
$2\bar{3}5$
$\bar{1}12$
$\bar{1}10$
$1\bar{1}0$
$1\bar{1}2$
$\bar{2}35$
$2\bar{1}3$
$\bar{1}23$
101
011
111
100
010
C
A
D
210
320
110
B

Fig. 4/9 shows the total elastic energy of a rhombus loop plotted for different loop sizes in copper as a function of the angle of rotation ϕ. Rotation was about the <100> major axis and calculations showed that the energy minimum was deeper, than for rotation about the <110> minor axis.

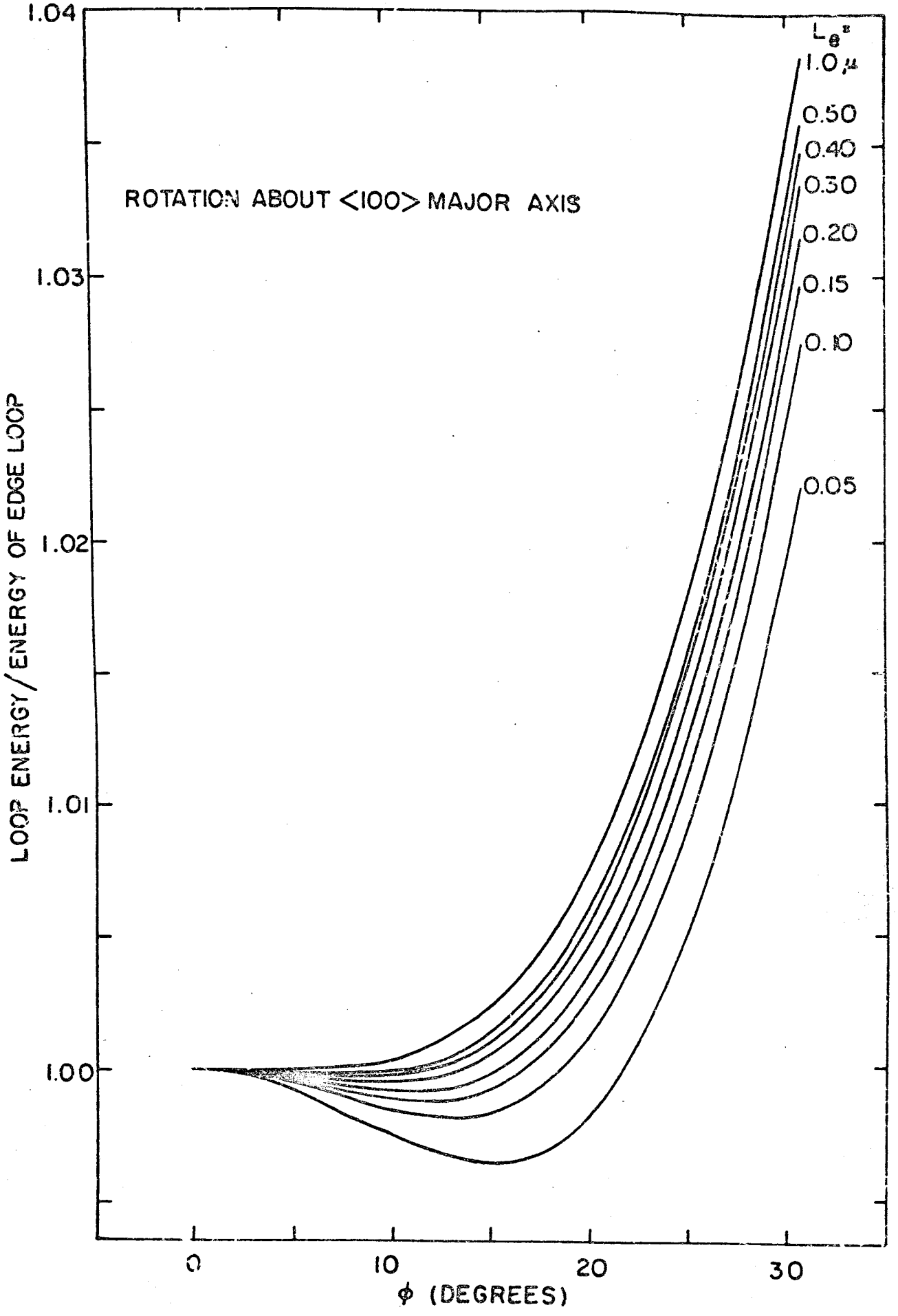

a

XBL755-6378

Fig. 4/10 Part of a growth sequence of rhombus loops in a Cu 16% Al foil during irradiation at $T_i = 235^{o}C$.

(a) 1 minute

(b) 4 minutes

(c) 7 minutes

(d) 10 minutes.

α = nucleation of new loops

β = irregular growth of loops

γ = interaction of loops with the foil surface

δ = agglomeration of rhombus loops into one large loop

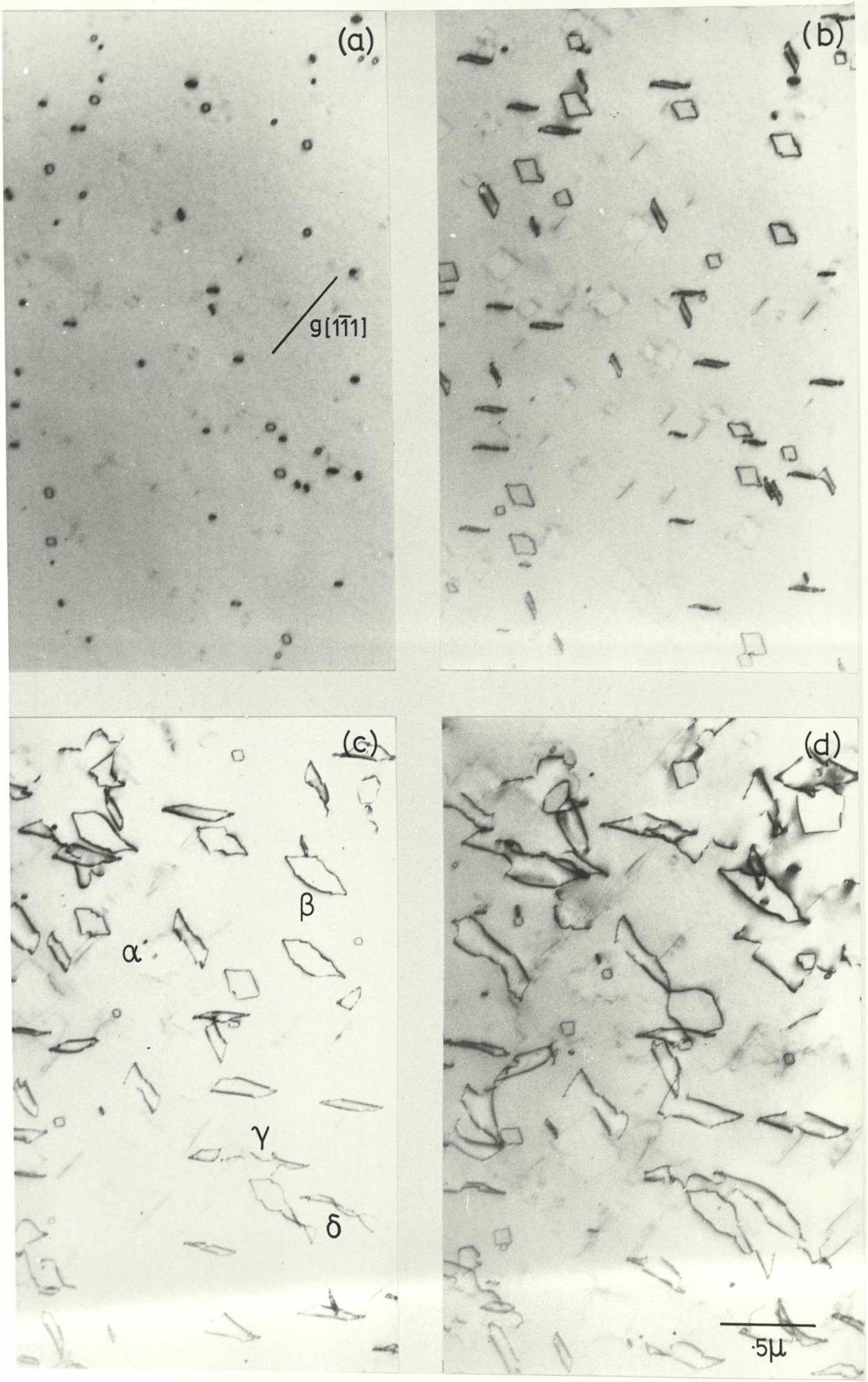
(a)
g[1$\bar{1}$1]
(b)
(c)
α
β
γ
δ
(d)
·5μ

Fig. 4/11 This graph shows a plot of corrected loop diameter versus the angle between the sides of loops in fig. 4/10, and suggests that the loop normal changes direction as the loop grows in size.

Linear growth was observed between 700 Å and 2000 Å, after which, the rate of growth decreased.

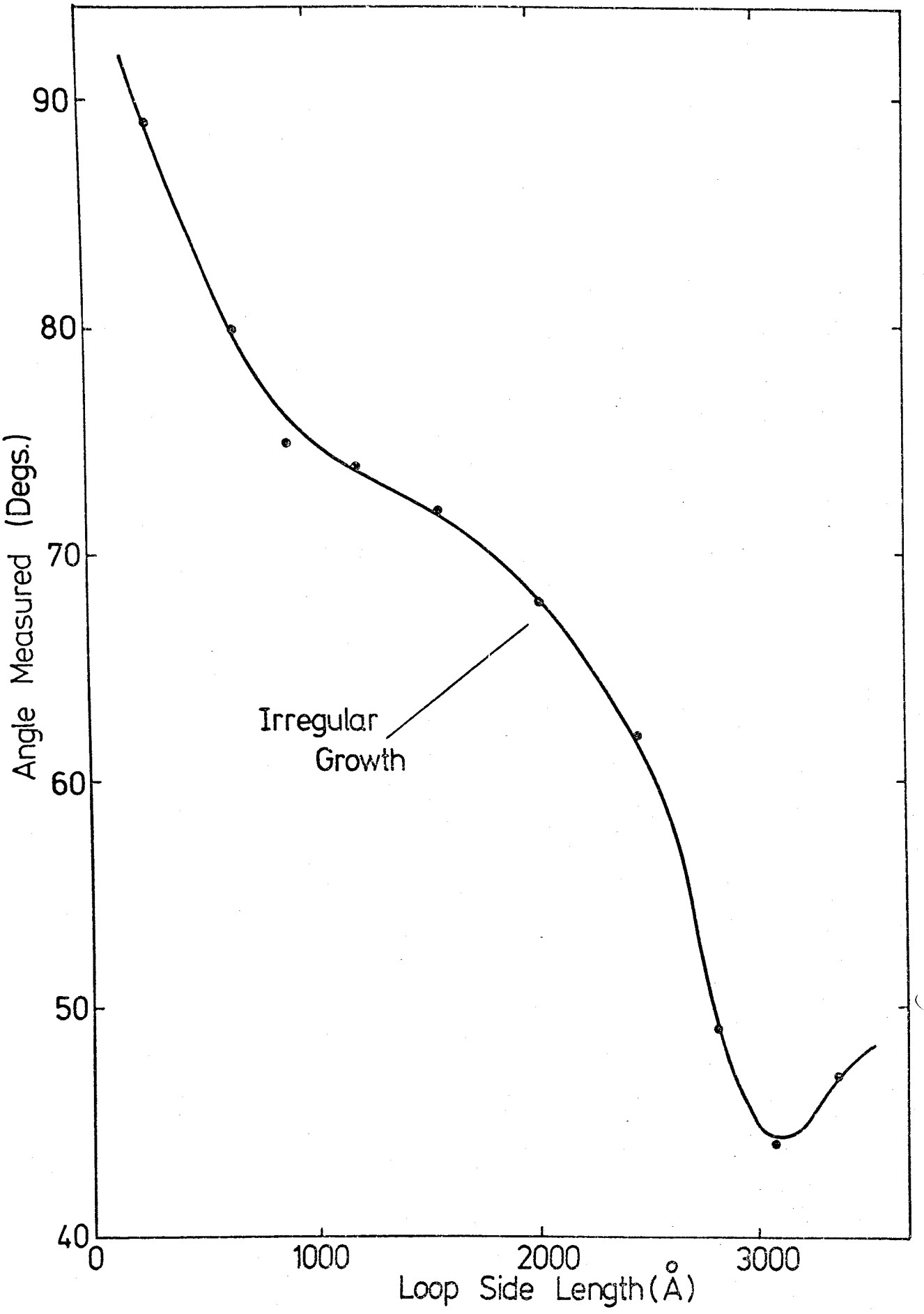
90
80
70
60
50
40
Angle Measured (Degs.)
Irregular
Growth
0
1000
2000
3000
Loop Side Length (Å)

Fig. 4/12 This diagram shows the development of irregularities at the corners of rhombus loops. Examples of this growth can be seen in fig. 10/7. Generally, these ledges tend to remain on the loops during growth and do not move along the sides in the regular manner which might be expected if they were superjogs whose passage was responsible for loop growth. Since there are no loops in the near vicinity to cause interaction it is likely that the steps develop as the loops approach the depleted zone near the foil surface. The additional ledges are still confined to the original {111} planes and it is likely that dissociation into Shockley partials occurs, with stair-rod dislocations at the intersection of the {111} planes.

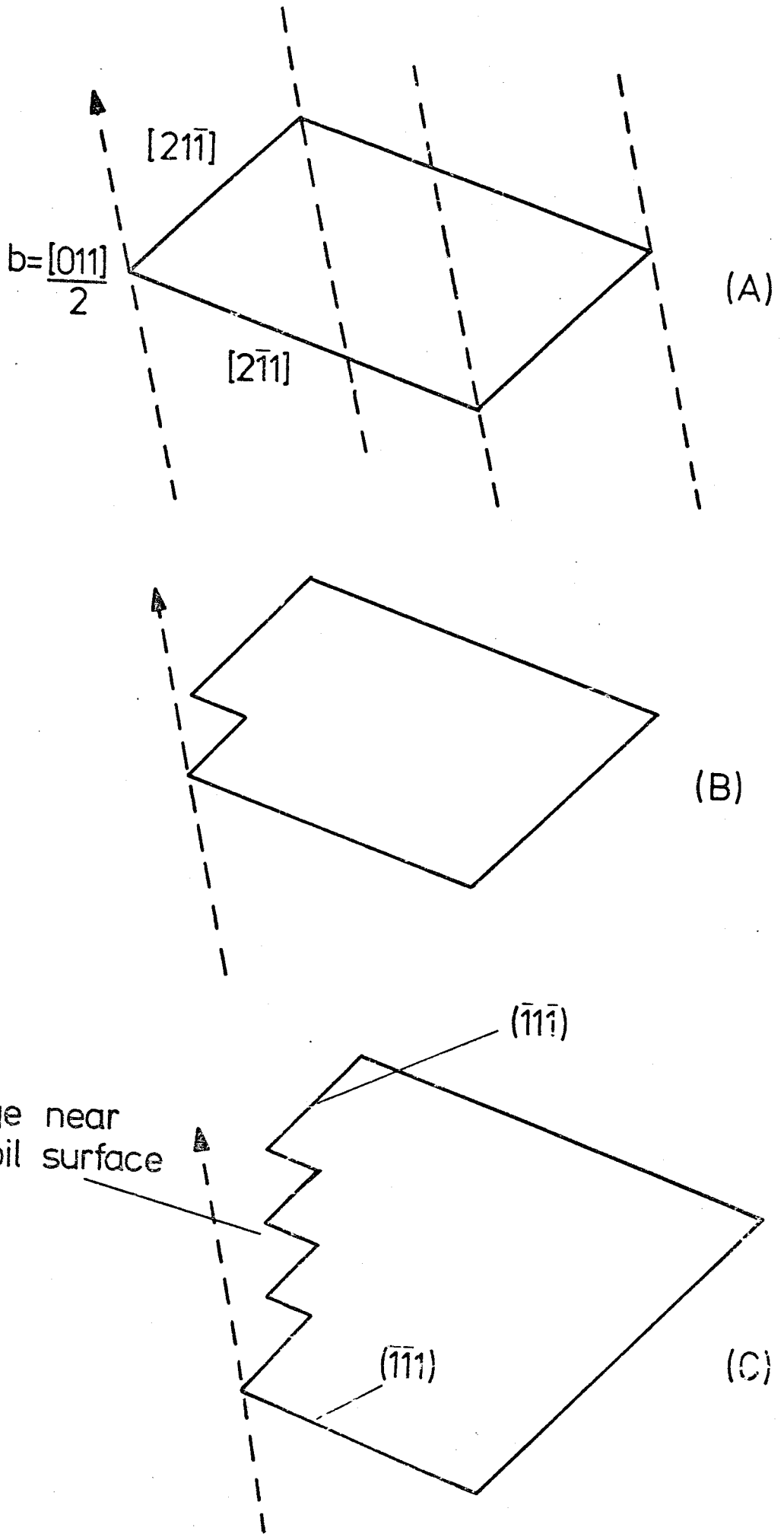
[21$\bar{1}$]
b=$\frac{[011]}{2}$
[2$\bar{1}$1]
(A)
(B)
($\bar{1}$1$\bar{1}$)
edge near
foil surface
($\bar{1}$1$\bar{1}$)
(C)

Fig. 4/13 This diagram shows the development of additional edges on a third {111} plane in a growing rhombus loop.

The Burgers vector of the loop is assumed to be $\frac{a}{2}$ [011] implying that the original loop sides are confined to the $(\bar{1}\bar{1}1)$ and $(\bar{1}1\bar{1})$ planes. However many loops have been observed to develop sides on say the (111) plane, which means that the loop is not now confined to one plane only. Examples of these loops can be seen in fig. 4/10.

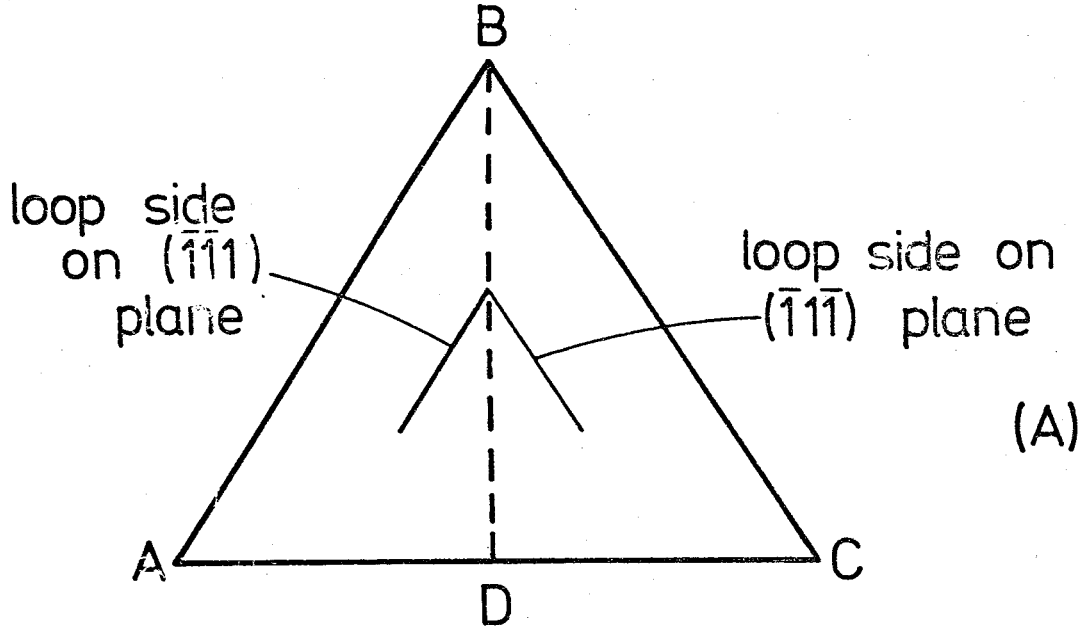
B
loop side on (1̄11) plane
loop side on (1̄11̄) plane
A
C
D

(A)

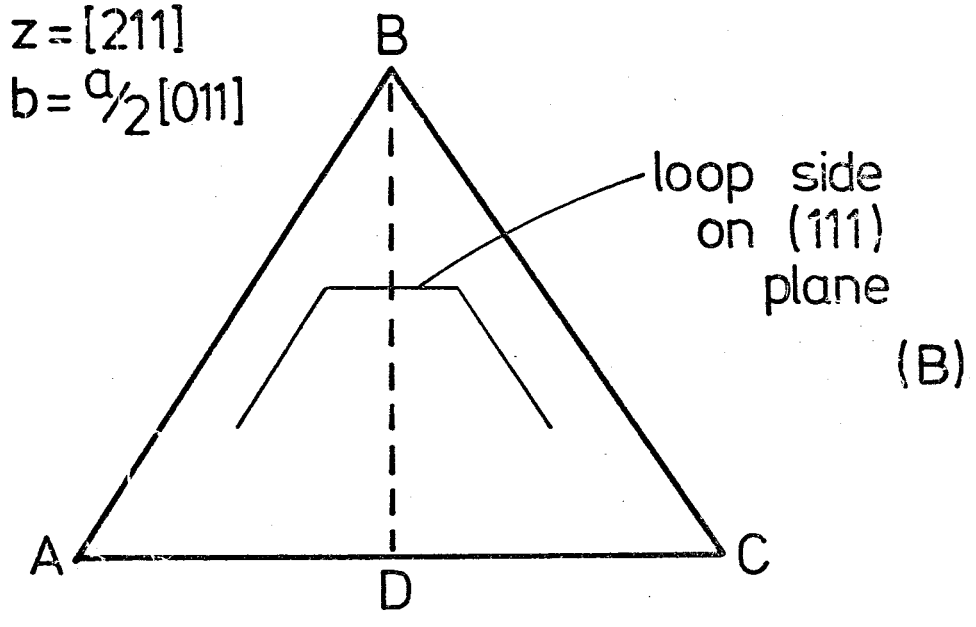
z = [211]
b = a/2 [011]
B
loop side on (111) plane
A
C
D

(B)

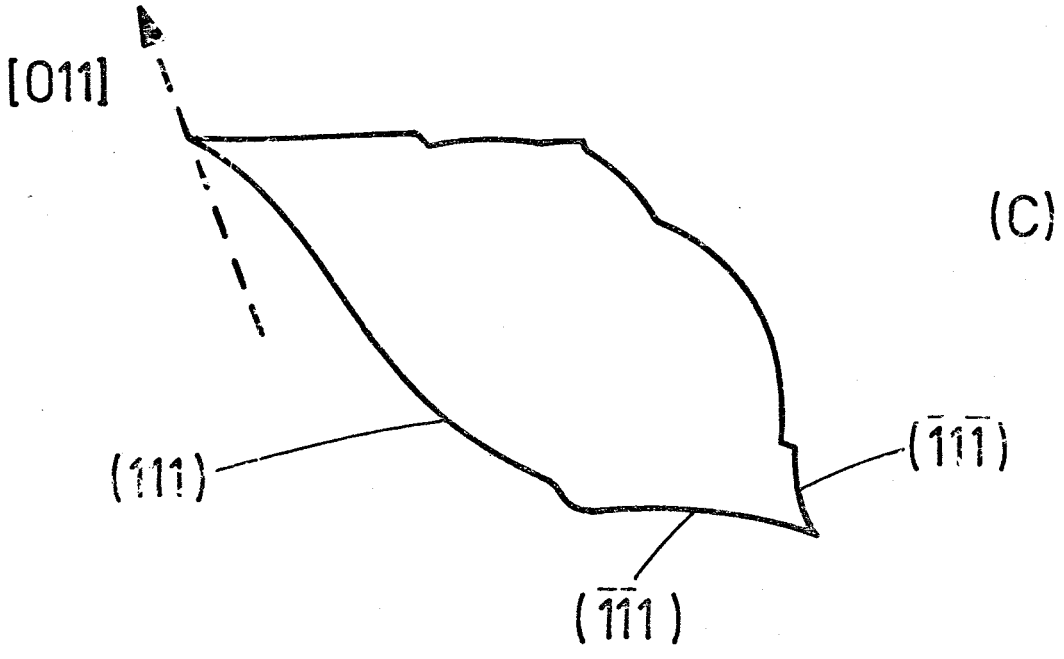
[011]
(111)
(1̄11̄)
(1̄11)

(C)

Fig. 4/14 Diagram (A) shows how loops having similar Burgers vectors and loop normals can interact when their strain fields overlap. The approaching sides will eliminate each other since their Burgers vectors are in opposite directions and amalgamation can then occur. When the loops are situated above each other, the strain fields repel.

Loops having different Burger's vectors can also interact and join together when one side of each loop has the same glide plane. Diagram (B) illustrates that interaction can occur between segments α and β, which are on the $(1\bar{1}\bar{1})$ plane.

Fig. C illustrates a third interaction which is possible but has not been experimentally observed. This occurs when none of the loop sides are in the same glide plane.

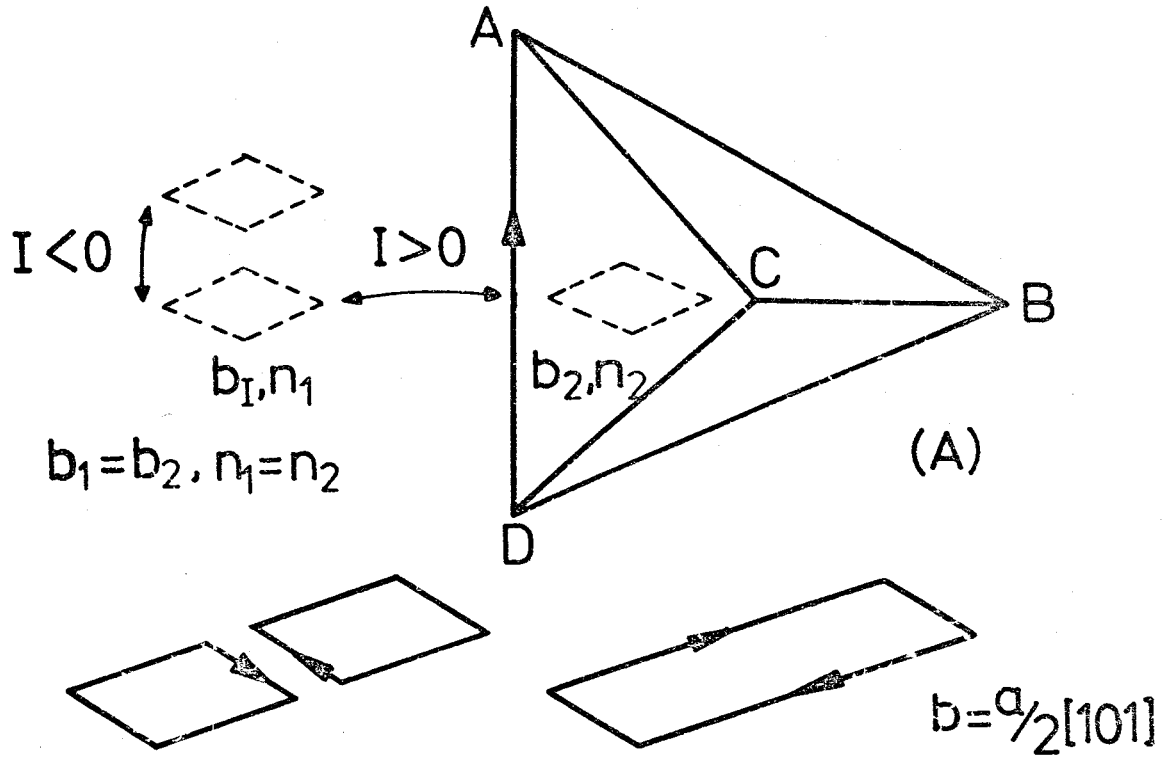
A
I<0
I>0
C
B
b_I, n_1
b_2, n_2
$b_1 = b_2$, $n_1 = n_2$
(A)
D
$b = a/2[101]$

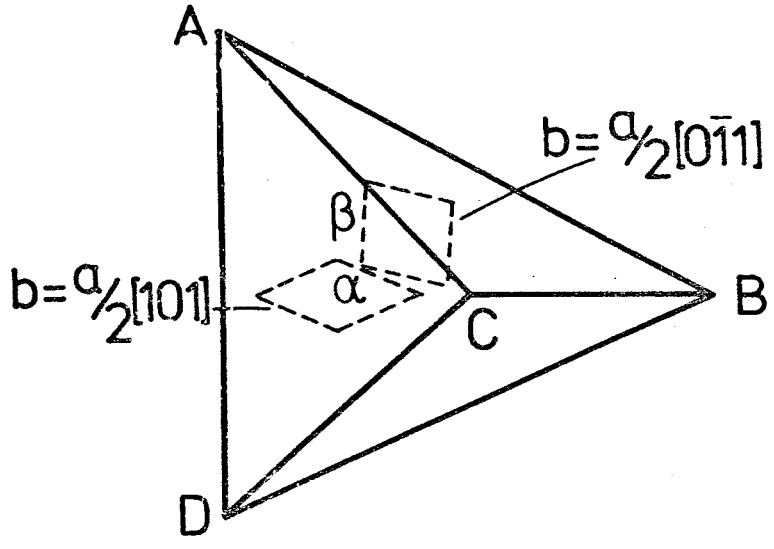
A
$b = a/2[0\bar{1}1]$
β
$b = a/2[101]$
α
B
C
(B)
D

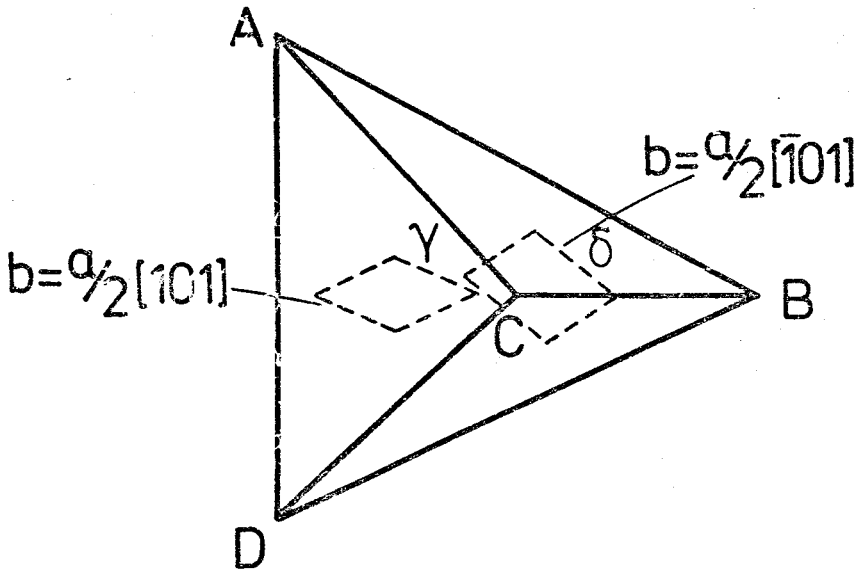
A
$b = a/2[\bar{1}01]$
γ
δ
$b = a/2[101]$
B
C
(C)
D

Fig. 4/15 Rhombus loop interactions ina Cu 16% Al foil.

(A) Interactions between loops with similar Burgers vectors and loop normals.

(B) Interactions between loops with different Burgers vectors but each loop having one side in the same glide plane.

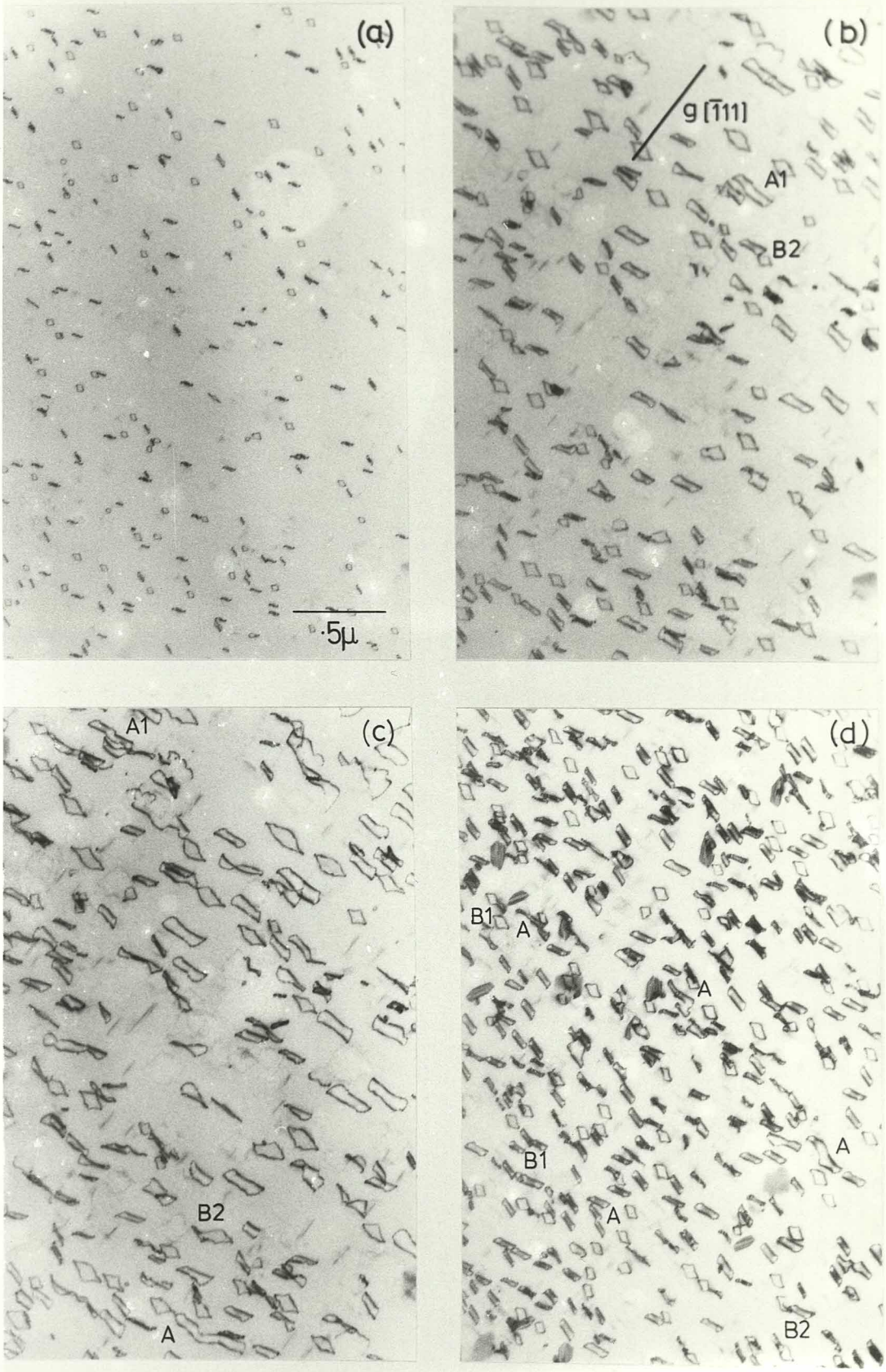
(a)
·5μ
(b)
g [1̄11]
A1
B2
(c)
A1
B2
A
(d)
B1
A
A
B1
A
A
B2

Fig. 4/16 Loops having Burgers vectors $b = \frac{a}{2}[0\bar{1}1]$ and $\frac{a}{2}[011]$, in which none of the loop sides are in the same glide plane can dissociate into Shockley partials on the δ and γ planes. If the loops approach close enough so that the leading partials join up, a Lomer-Cottrell lock will be formed. This reaction is illustrated in figure (B).

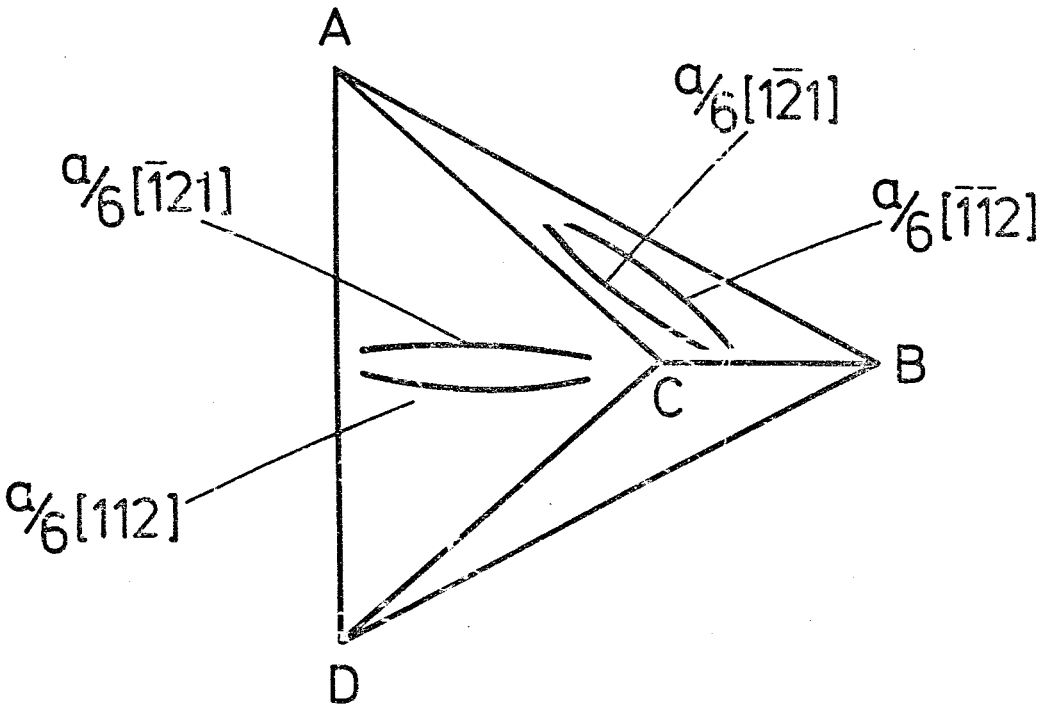
A
a/6[1̄21]
a/6[1̄21]
a/6[1̄1̄2]
B
C
a/6[112]
D

(A)

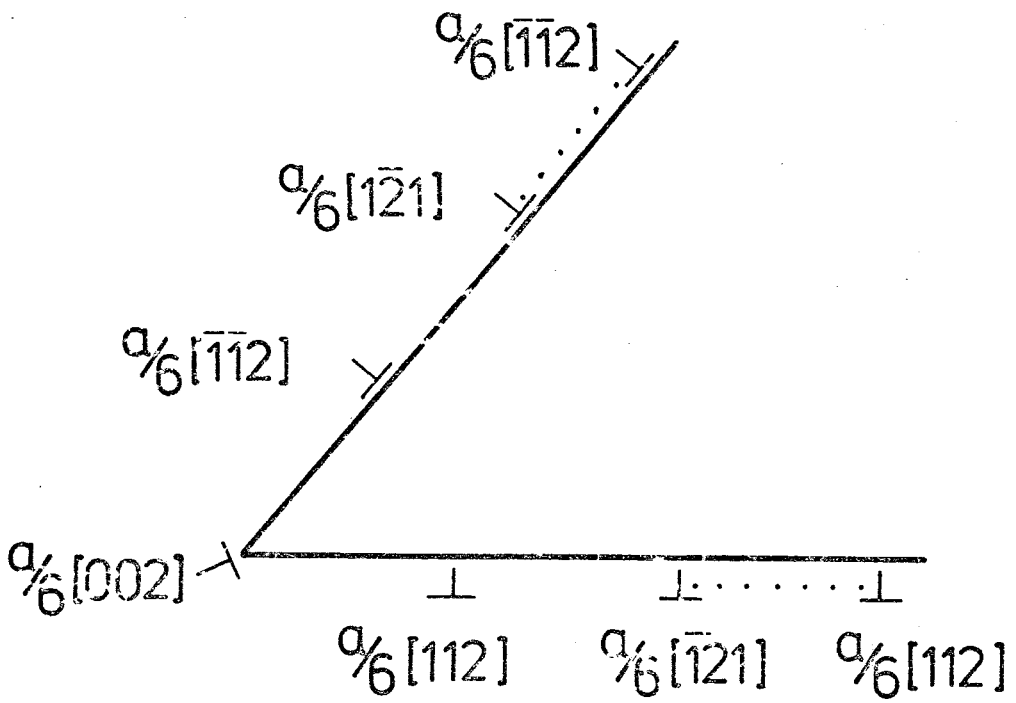
a/6[1̄1̄2]
a/6[1̄21]
a/6[1̄1̄2]
a/6[002]
a/6[112]
a/6[1̄21]
a/6[112]

(B)

Fig. 4/17 Figs (A) (B) show the movement of atoms in a {111} glide plane to produce a perfect dislocation $b = \frac{a}{2}[0\bar{1}1]$ with component Shockley partials $\frac{a}{6}[1\bar{2}1]$ and $\frac{a}{6}[\bar{1}\bar{1}2]$.

Fig. (C) shows that a loop with $\bar{b} = \frac{a}{2}[011]$ can have either of two planes (012) or (021) after rotation from (111). The {012} plane has been predicted to be near the minimum energy configuration for rhombus perfect loops

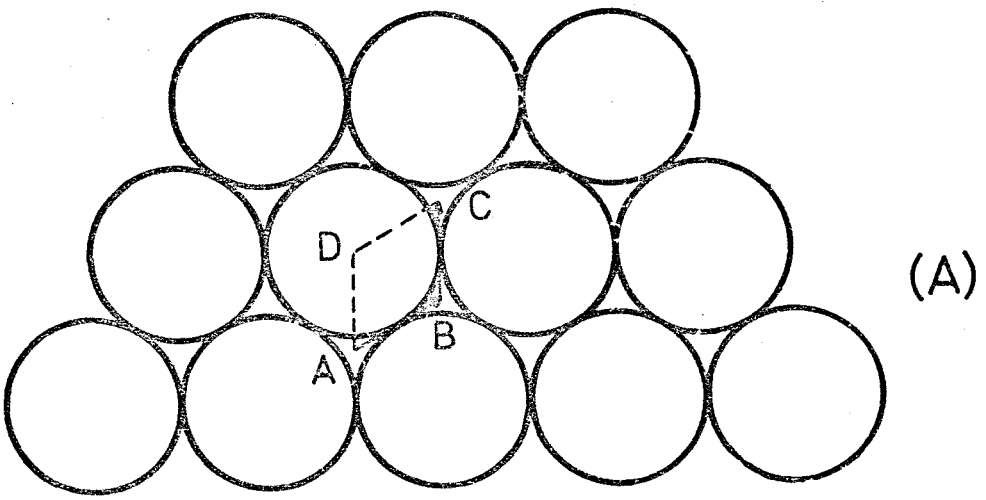

(A)

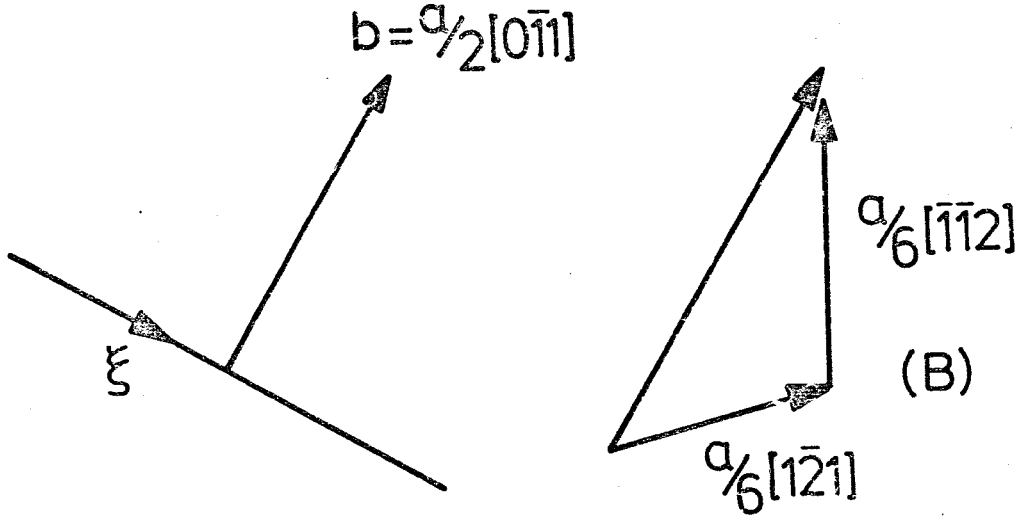

(B)

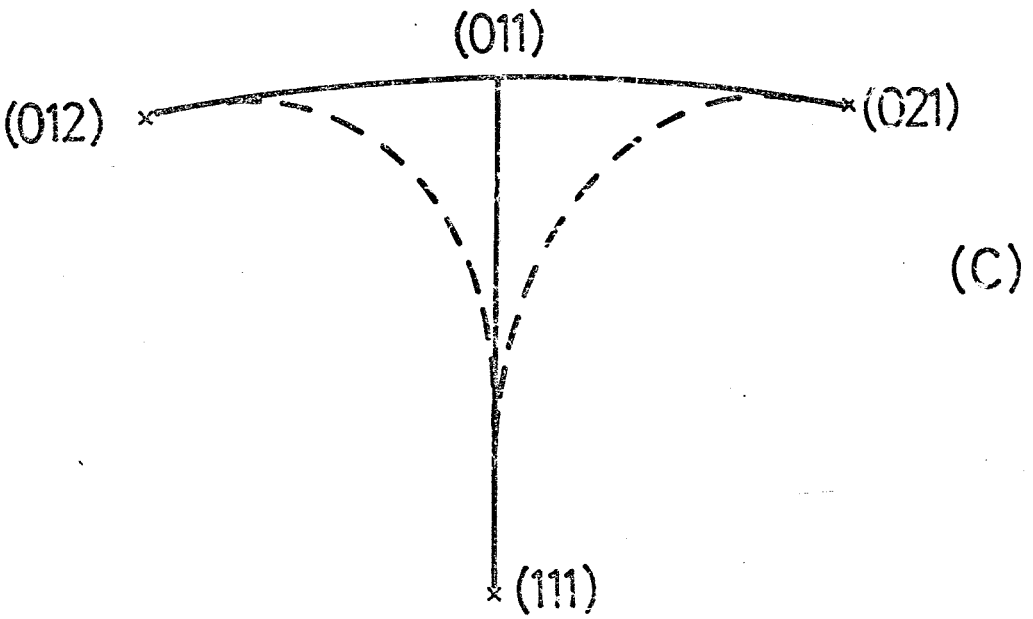

(C)

Fig. 5/1 Effect of specimen polishing temperature on the subsequent loop formation.

(A) Specimen polished at $-30^{\circ}C$ 4.4 volts

(B) Specimen polished at $-75^{\circ}C$ 4.4 volts.

$T_i = 240^{\circ}C$ Cu 16% Al (slow grown crystal).
Dose rate 6×10^{18} el./cm.^{2}/sec.
Foil thickness $\triangleq$ 2200 Å.

Specimens irradiated within 5 minutes of the electropolish.

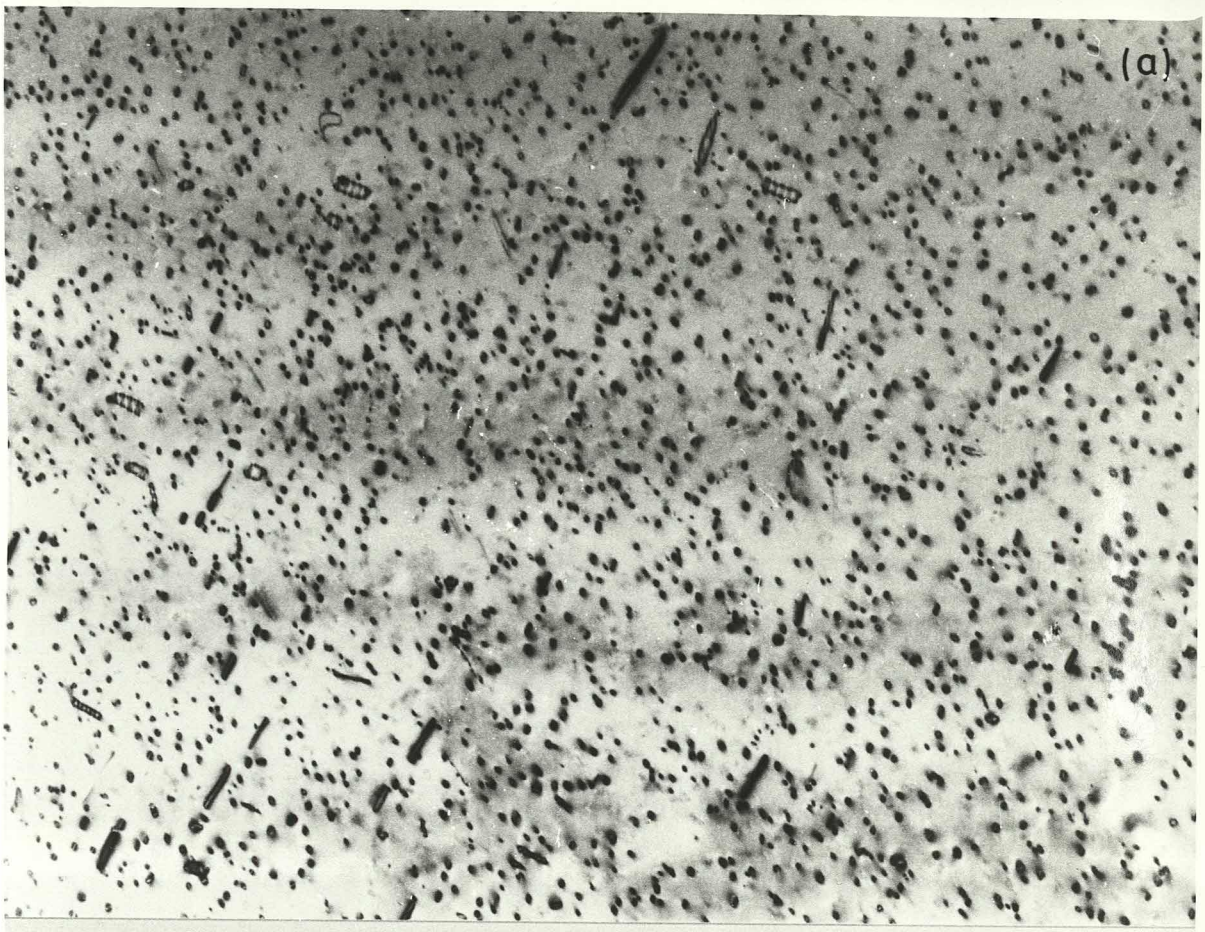
(a)

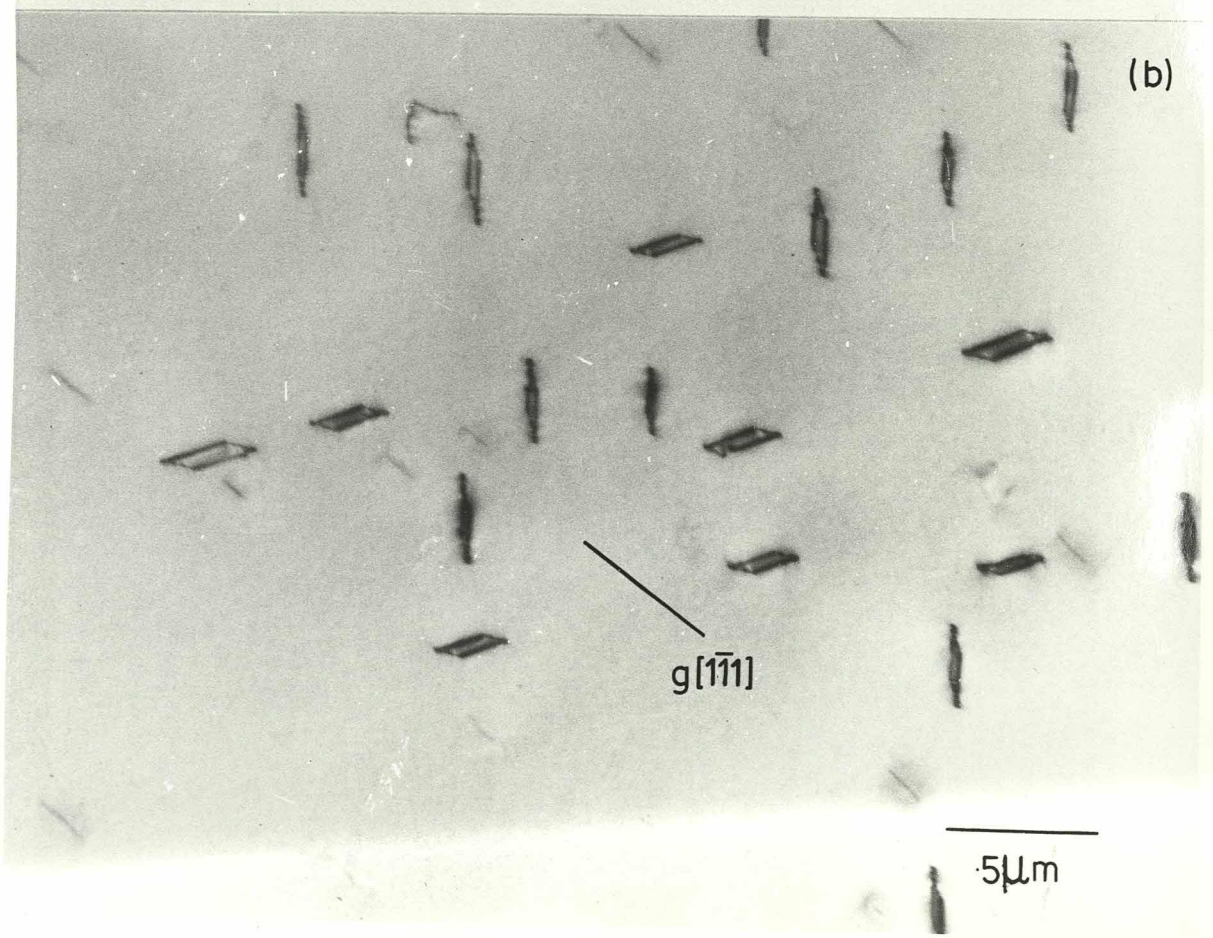
(b)
g[1$\bar{1}\bar{1}$]
5μm

Fig. 5/2 Analysis of elongated perfect loops in a Cu 16% Al foil,
5/3 imaged in various diffraction vectors.
5/4

(a) (b)	$\bar{g} \pm [11\bar{3}]$	$\bar{z}$ [211]
(c) (d)	$\bar{g} \pm [\bar{1}11]$	$\bar{z}$ [211]
(e)	$\bar{g}$ $[02\bar{2}]$	$\bar{z}$ [011]
(f)	$\bar{g}$ $[2\bar{2}0]$	$\bar{z}$ [111]
(g)	$\bar{g}$ $[1\bar{1}1]$	$\bar{z}$ [121]
(h)	$\bar{g}$ $[11\bar{3}]$	$\bar{z}$ [121]
(i) (j)	$\bar{g} \pm [02\bar{2}]$	$\bar{z}$ [111]
(k) (l)	$\bar{g} \pm [20\bar{2}]$	$\bar{z}$ [111]

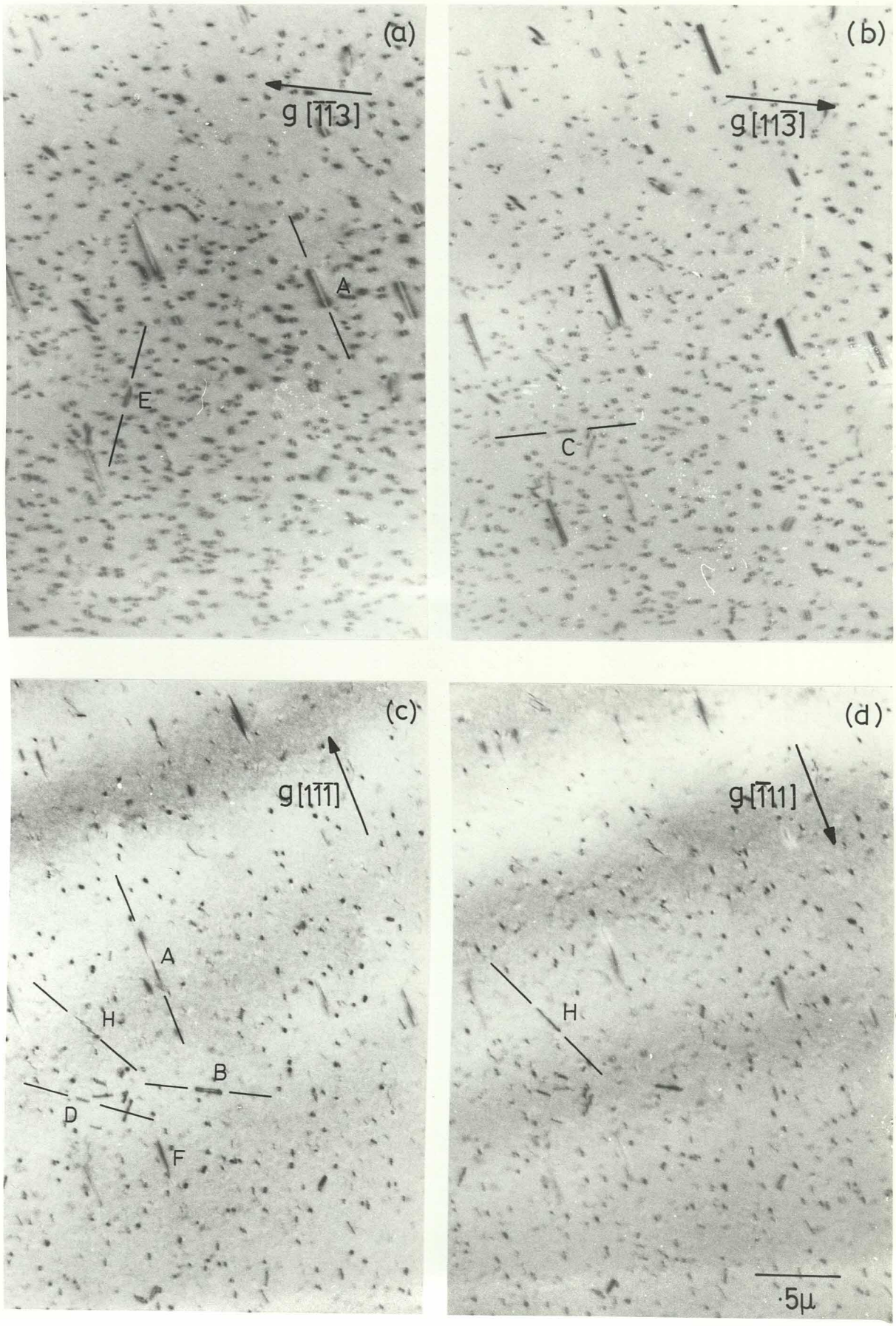

Fig.5/2

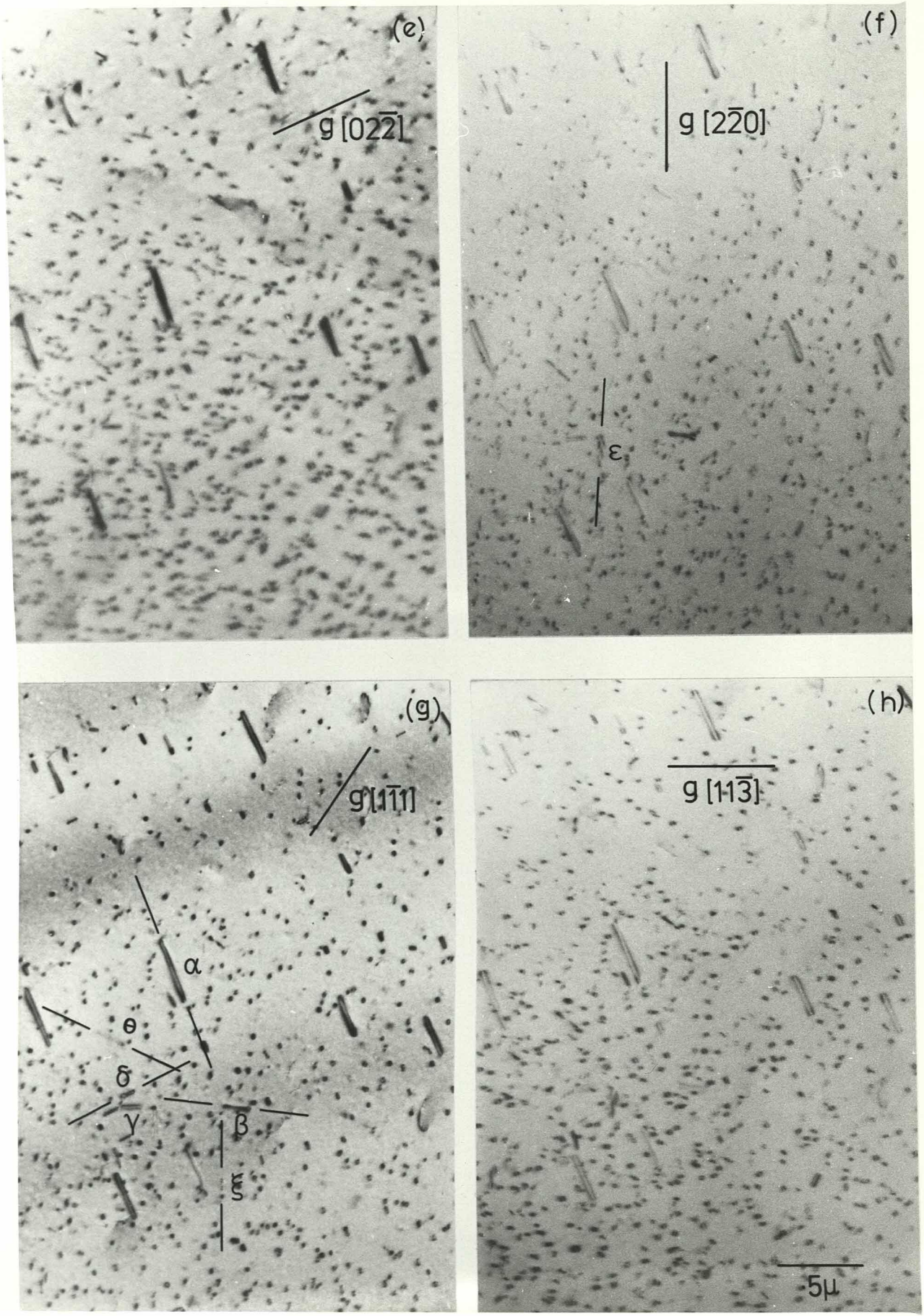

Fig.5/3

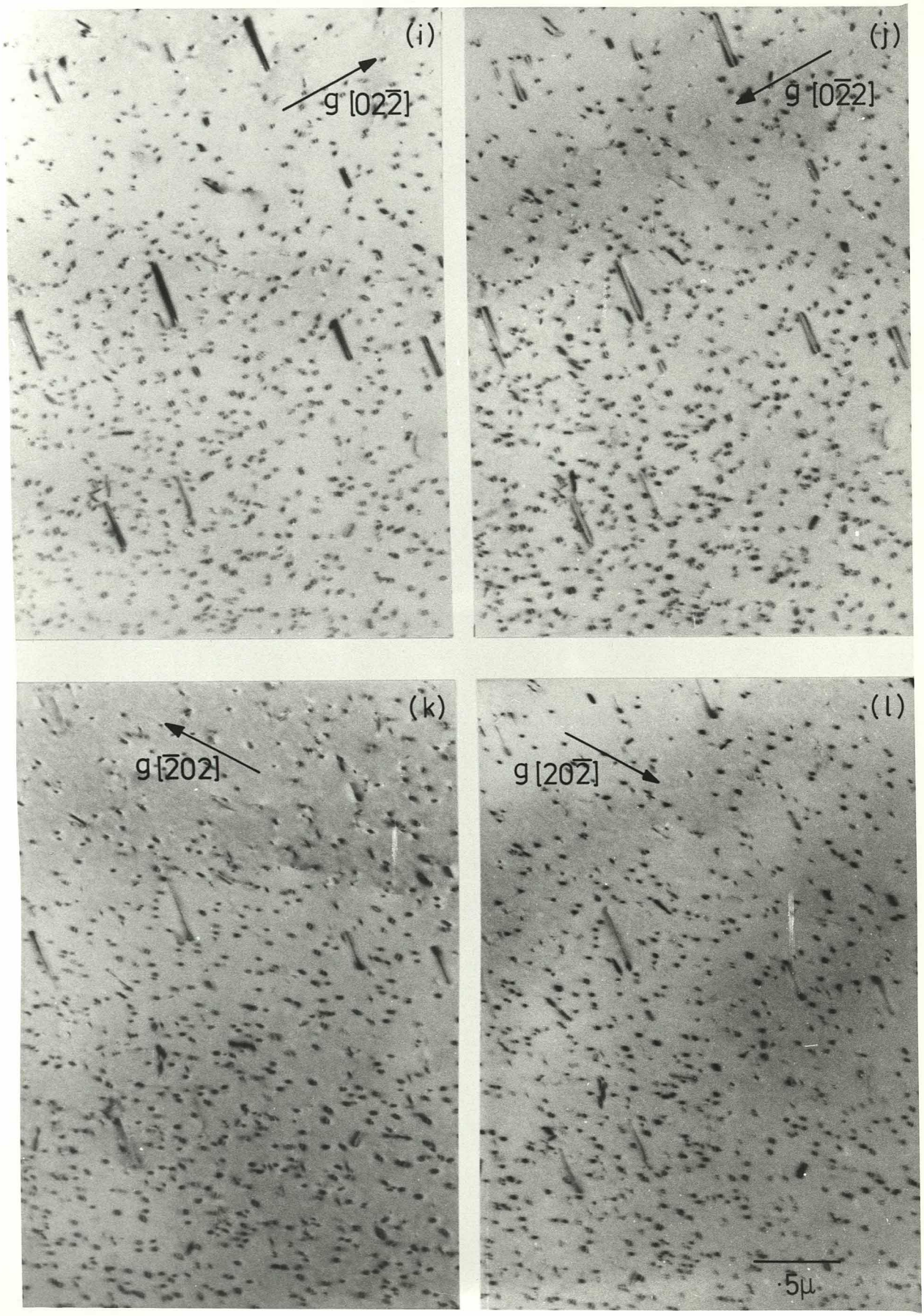

Fig.5/4

Fig. 5/5 The stereogram shows the calculation of the loop side directions of elongated loops in micrographs 5/2, 5/3, 5/4. The line directions of the loops are as follows:-

Uα	$\bar{5}32$
Uβ	$\bar{2}\bar{1}3$
Uγ	$\bar{2}\bar{3}5$
Uδ	112
Uε	$\bar{2}1\bar{1}$
Uθ	$\bar{2}13$
Uη	$\bar{2}11$

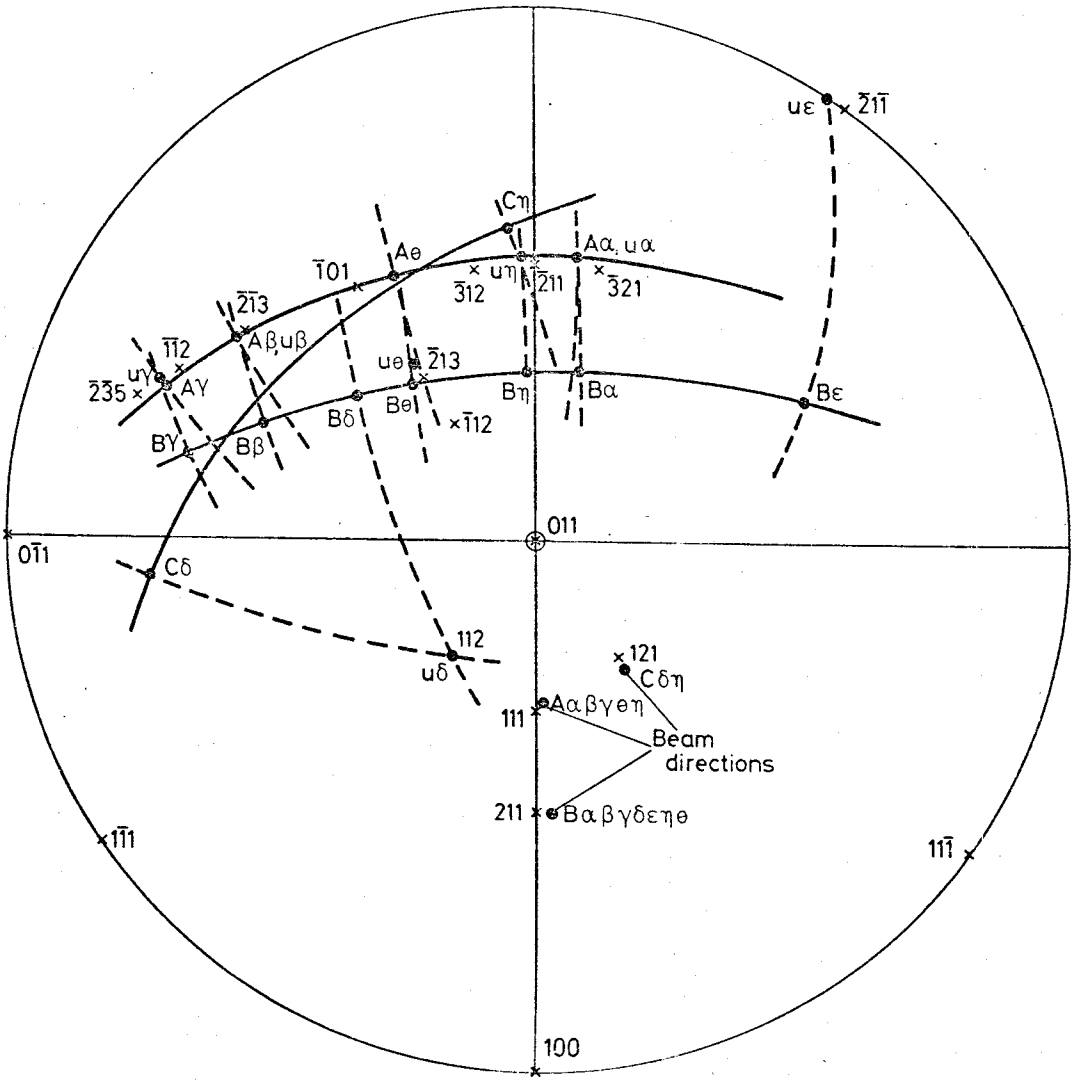
uε
2̄11̄
Cη
Aθ
Aα, uα
1̄01
ū12
1̄211
3̄21
2̄13̄
A β,uβ
1̄12
uγ
2̄35
Aγ
uθ
2̄13
Bη
Bα
Bε
Bγ
Bβ
Bδ
Bθ
×1̄12
011
0 1̄1
Cδ
112
uδ
×121
Cδη
Aαβγεη
111
Beam
directions
211
Bαβγδεηθ
1̄11
11̄
100

Figs 5/6 Burgers vector analysis of elongated loops in a Cu 16% Al
5/7 foil.

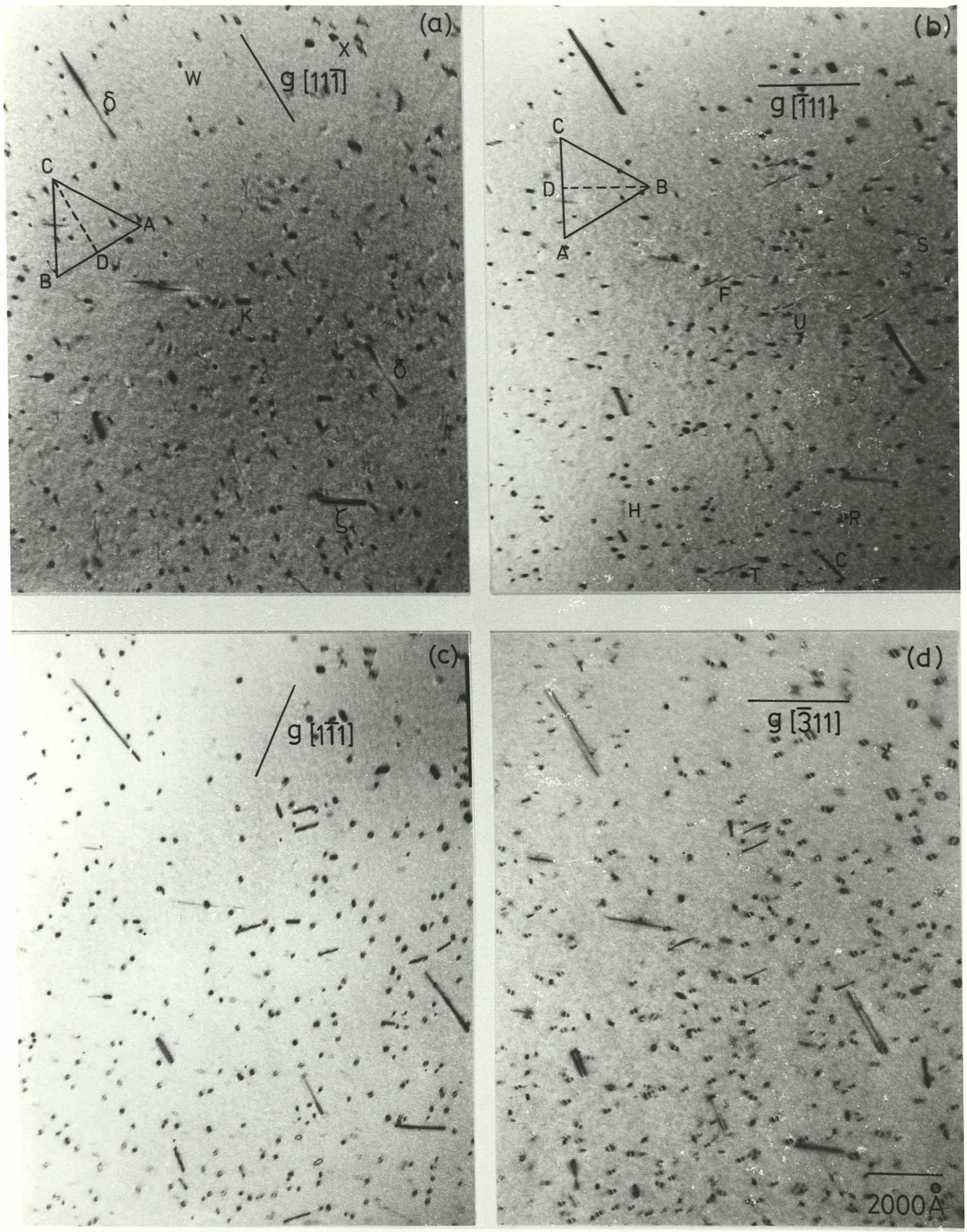
(a)
X
W
g [11$\bar{1}$]
δ
C
A
D
B
K
δ
ζ
(b)
g [$\bar{1}$11]
C
D
B
A
S
F
U
H
R
T
C
(c)
g [1$\bar{1}$1]
(d)
g [$\bar{3}$11]
2000 Å

Fig.5/6

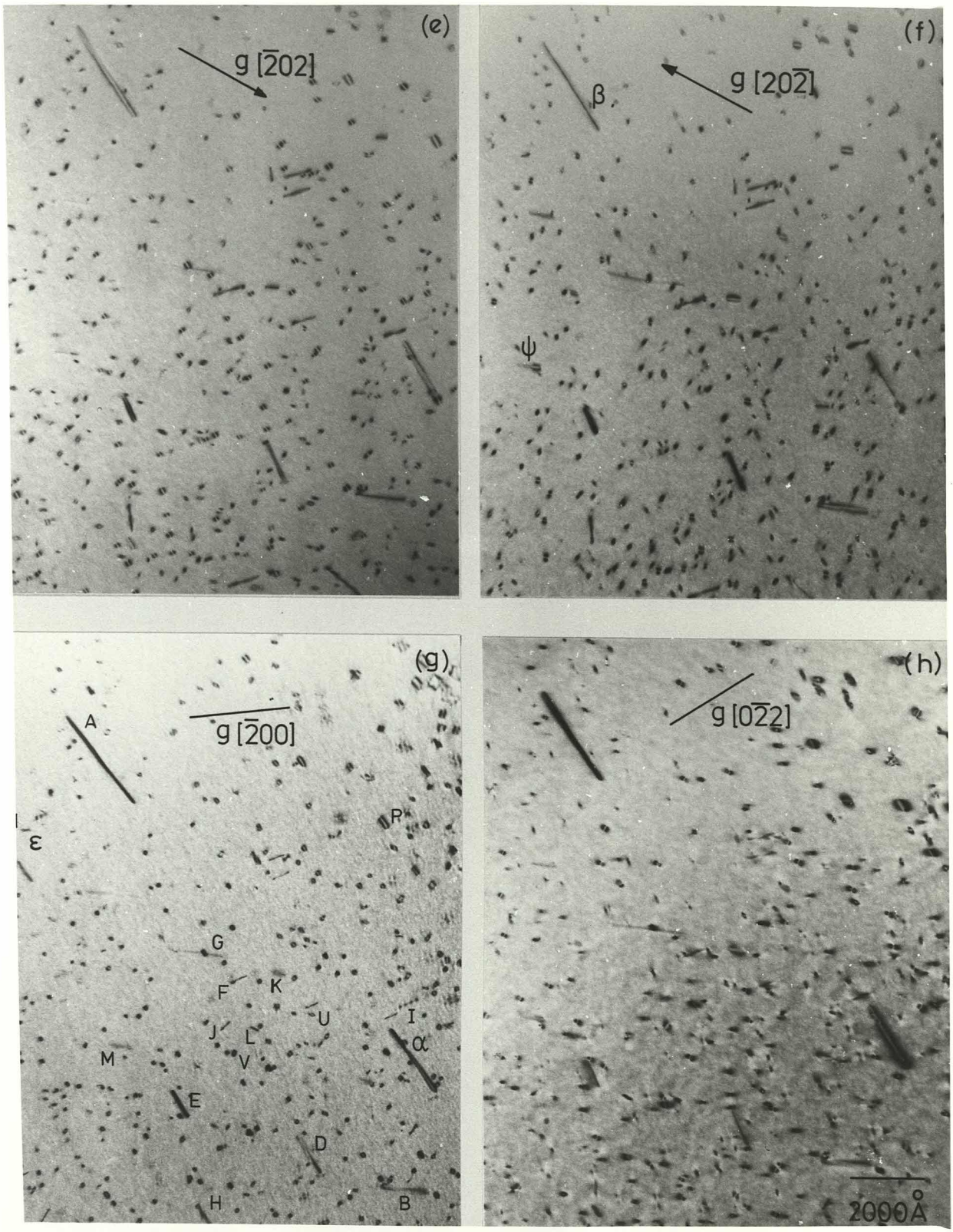
(e)
g [$\bar{2}$02]
(f)
g [20$\bar{2}$]
β
ψ
(g)
g [$\bar{2}$00]
A
ε
P
G
F
K
U
I
J
L
α
M
V
E
D
H
B
(h)
g [0$\bar{2}$2]
2000 Å

Fig.5/7

Fig. 5/8 The stereogram shows the relationship between the line direction $\bar{U}$ and Burgers vector $\bar{b}$ for elongated loops on the α, β, γ and δ planes. Since there are three elongated loops on each {111} plane, Uδ2 represents the line direction $[2\bar{1}\bar{1}]$ of loop 2 on the $\delta(111)$ plane. The Burgers vector of this loop $\frac{a}{2}[0\bar{1}1]$ is at 90° to $[2\bar{1}\bar{1}]$ and is represented by $\bar{b}\delta 2$. Similarly for the other loops.

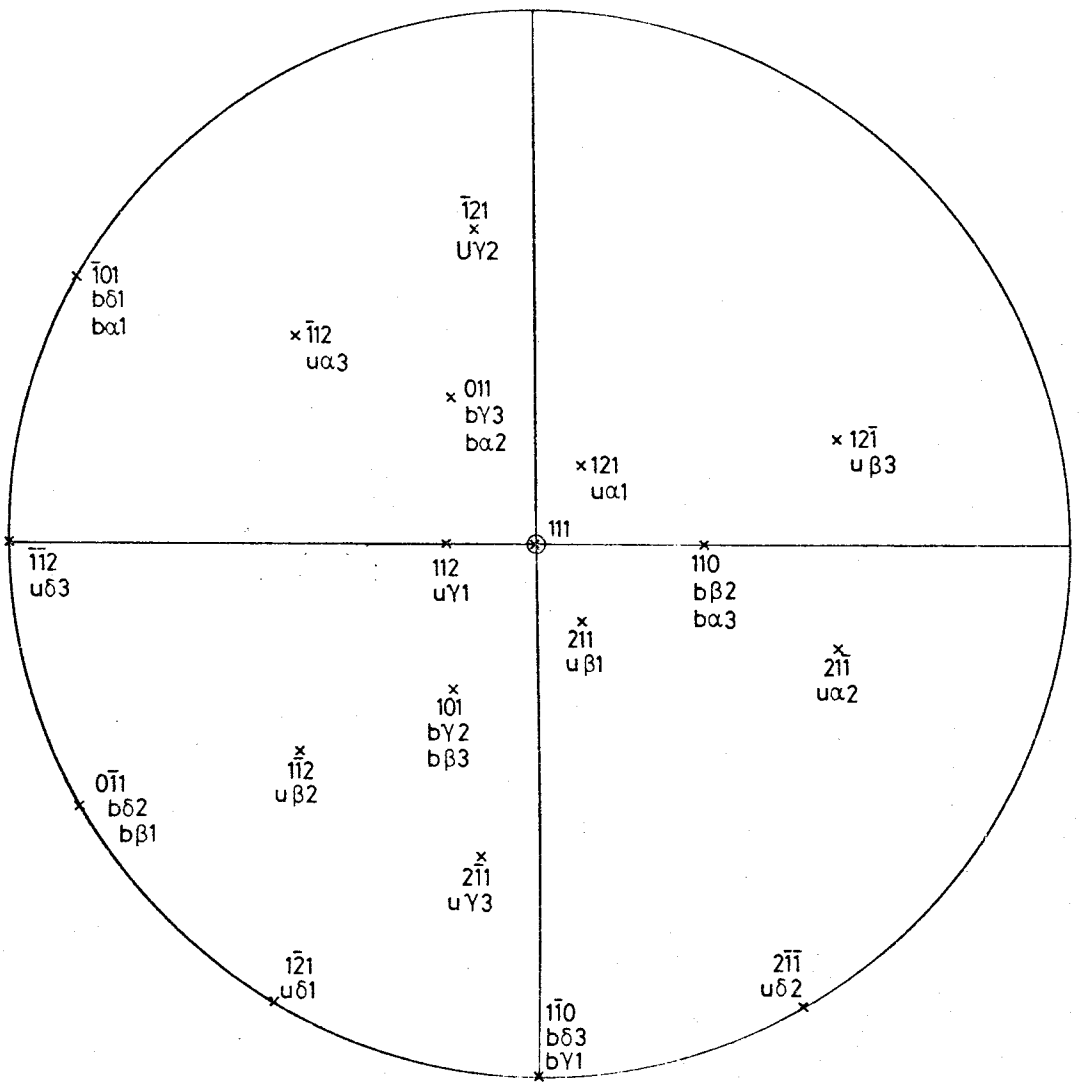
$\bar{1}21$
UY2
$\bar{1}01$
bδ1
bα1
$\bar{1}12$
uα3
011
bY3
bα2
121
uα1
$12\bar{1}$
uβ3
111
$\bar{1}\bar{1}2$
uδ3
112
uY1
110
bβ2
bα3
211
uβ1
$21\bar{1}$
uα2
101
bY2
bβ3
$1\bar{1}2$
uβ2
$0\bar{1}1$
bδ2
bβ1
$2\bar{1}1$
uY3
$1\bar{2}1$
uδ1
$2\bar{1}\bar{1}$
uδ2
$1\bar{1}0$
bδ3
bY1

Fig. 5/9 illustrates schematically the type of loops that have been considered when investigating the nature of the elongated loops observed in electron irradiated copper aluminium alloys.

(A) line of dilation

(B) Frank loop parallel to the foil surface

(C) Perfect loop inclined to the foil surface

(D) Frank loop inclined to the foil surface

(E) Loops having $b = \frac{a}{k}[010]$. When $k = 2$ the loop is faulted. This loop has been commonly observed in electron irradiated boron implanted silicon.

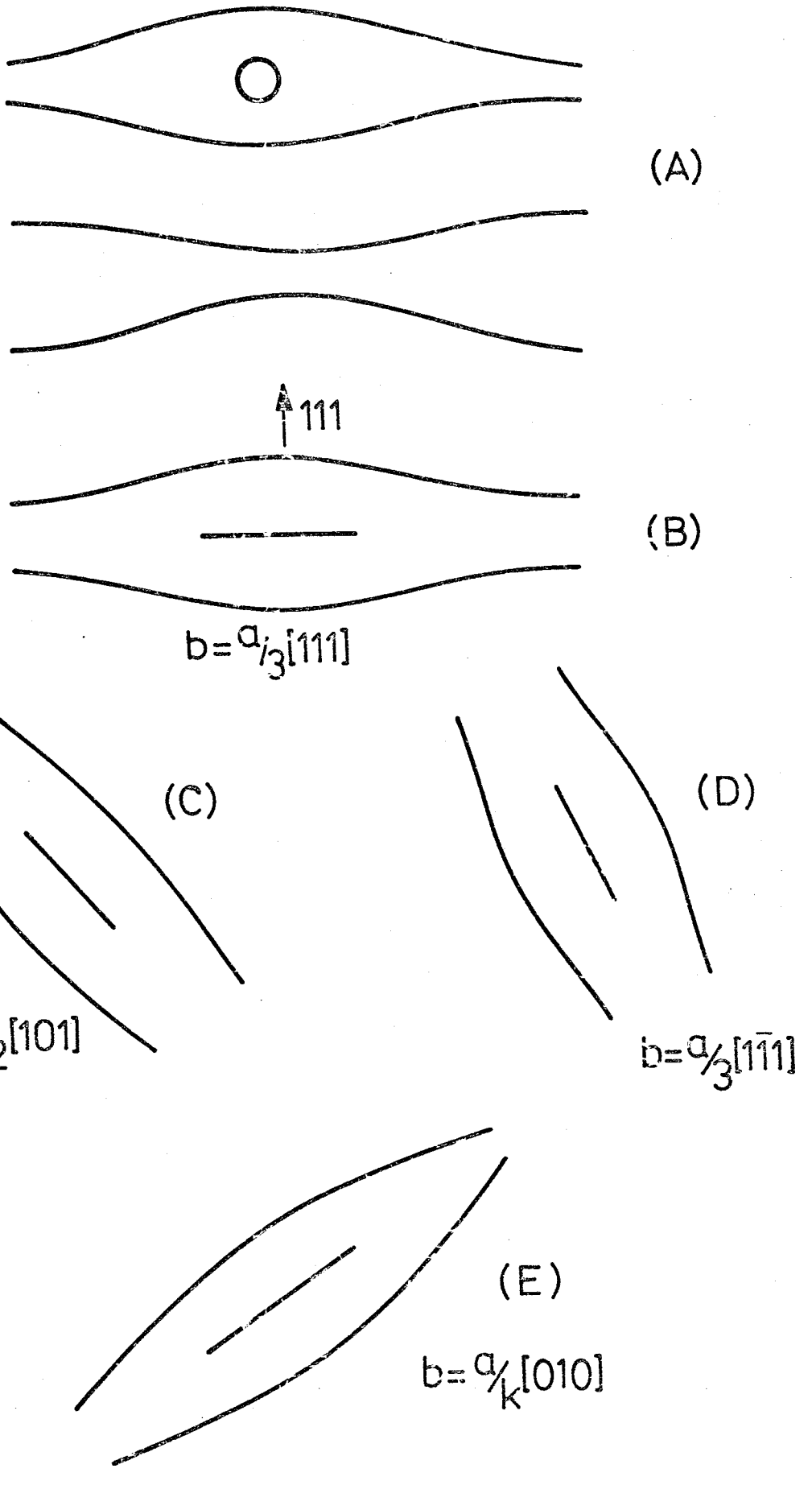
(A)
111
(B)
b=a/3[111]
(C)
b=a/2[101]
(D)
b=a/3[1$\bar{1}$1]
(E)
b=a/k[010]

Fig. 5/10 The stereogram shows the possible habit planes of elongated loops having line directions $\bar{U}$ $[2\bar{1}\bar{1}]$ and $[3\bar{2}\bar{1}]$.

Loops lying along $[2\bar{1}\bar{1}]$ have possible habit planes $(0\bar{1}1)$, $(1\bar{1}3)$, (102), (213) and (111). (line A).

When loops lie along $[\bar{3}21]$ curve B show the possible habit planes.

In general, elongated loops have directions between <211> and <321> and the likely habit planes lie between $\{011\}$ and $\{0\bar{1}2\}$.

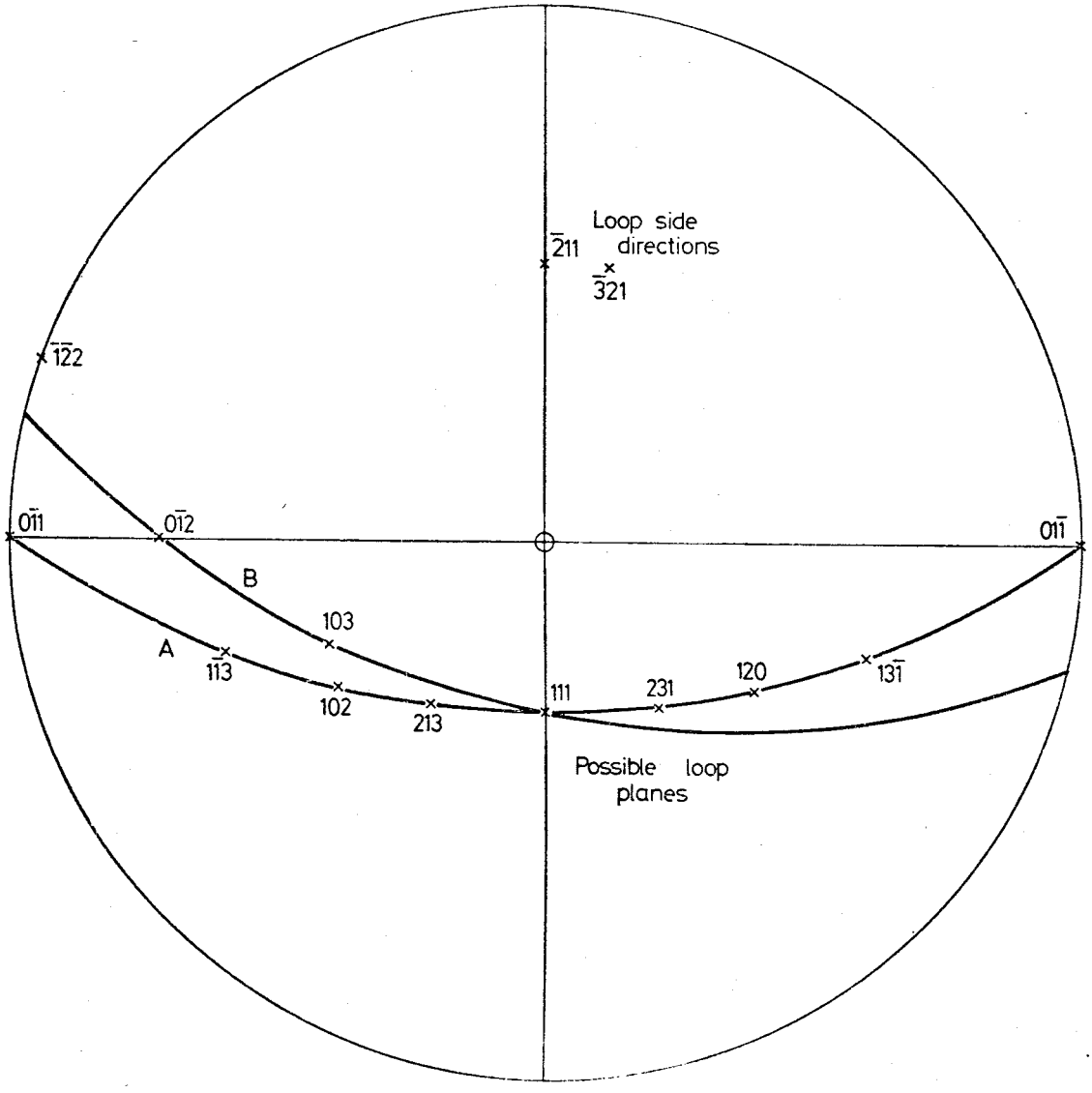
Loop side directions
$\bar{2}11$
$\bar{3}21$
$\bar{1}\bar{2}2$
$0\bar{1}1$
$0\bar{1}2$
$01\bar{1}$
B
103
A
$1\bar{1}3$
102
213
111
231
120
$13\bar{1}$
Possible loop planes

Fig. 5/11 Unusual contrast of an elongated loop of Burgers vector $\bar{b} = \frac{a}{2}[\bar{1}01]$ in a Cu 16% Al foil polished at -40°C, 5 volts.

(A) $\bar{g}$ $[02\bar{2}]$ $\bar{z}$ [111] weak beam g/3g satisfied

(B) $\bar{g}$ $[02\bar{2}]$ $\bar{z}$ [111] B.F.

(C) $\bar{g}$ $[2\bar{2}0]$ $\bar{z}$ [111] B.F.

Note the absence of contrast in the middle of the loop in $\bar{g}$ $[2\bar{2}0]$.

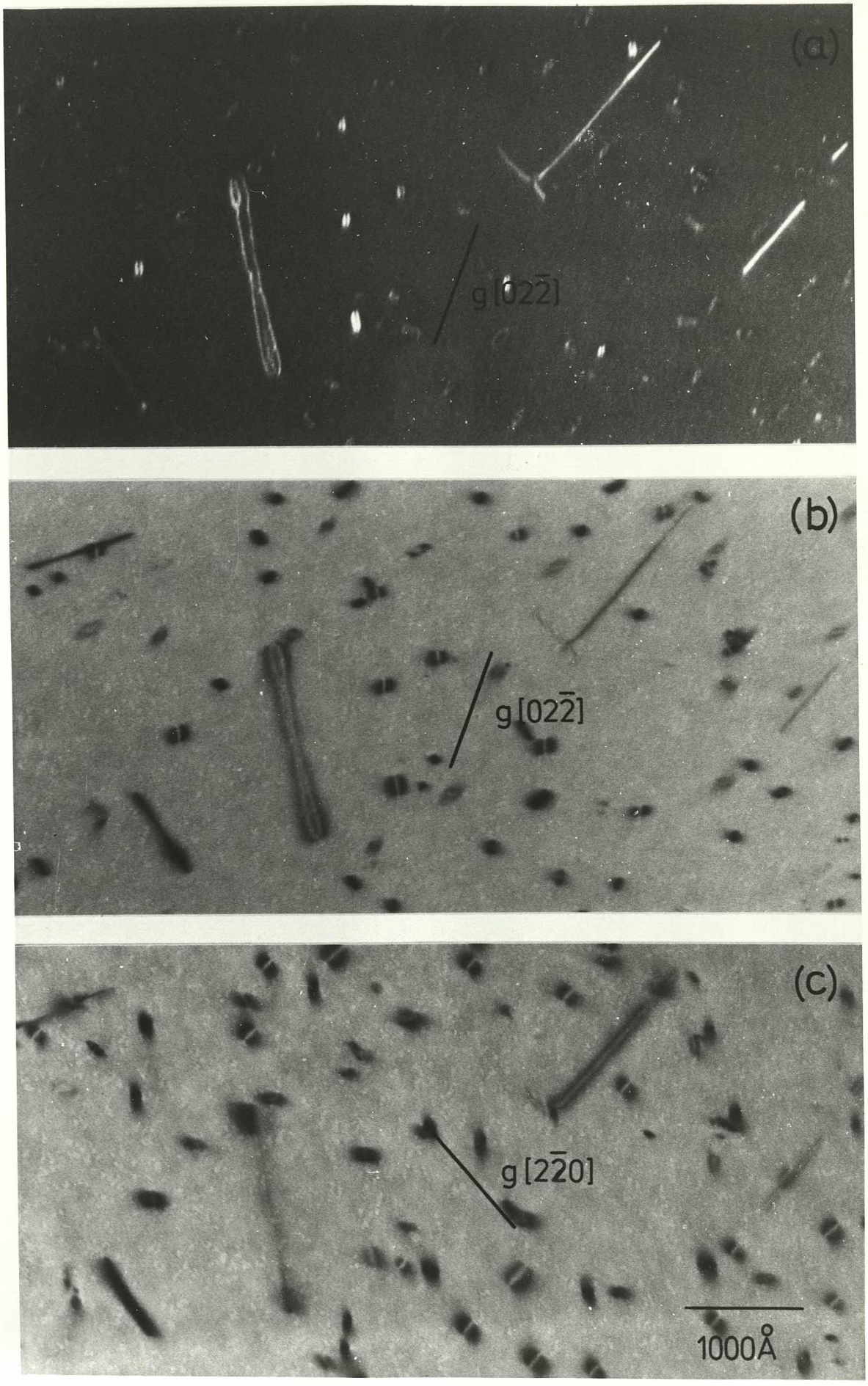
(a)
g [02$\bar{2}$]
(b)
g [02$\bar{2}$]
(c)
g [2$\bar{2}$0]
1000Å

Fig. 5/12 Weak beam analysis of elongated loops in Cu 16% Al.

5/13

5/14

(a) g $[0\bar{2}2]$ z [111] Weak beam g/3g satisfied

(b) g $[20\bar{2}]$ z [111] Weak beam g/3g satisfied

(c) g $[\bar{2}20]$ z [111] Weak beam g/3g satisfied

(d) $\bar{g}$ $[\bar{2}02]$ z [111] Weak beam g/3g satisfied

(e) g $[\bar{1}\bar{1}1]$ z [112] Strong beam

(f) g $[\bar{1}11]$ z [211] g/5g satisfied

(g) g $[\bar{1}1\bar{1}]$ z [121] Strong beam

(h) g $[\bar{1}11]$ z [211] Strong beam

(i) g $[11\bar{1}]$ z [112] g/5g satisfied

(j) g $[\bar{2}02]$ z [101] g/3g satisfied

(k) g $[\bar{2}20]$ z [113] g/3g satisfied

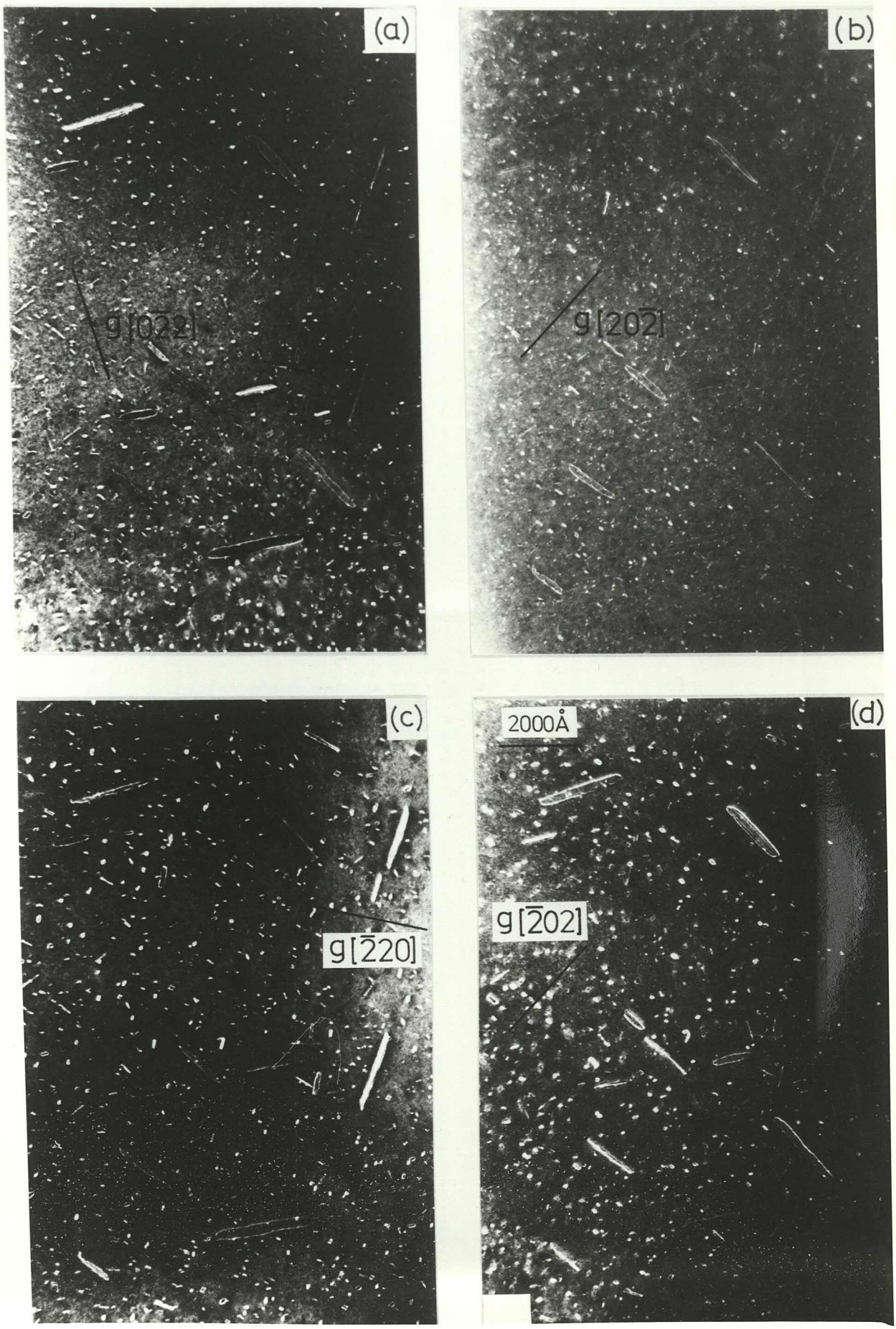

Fig.5/12

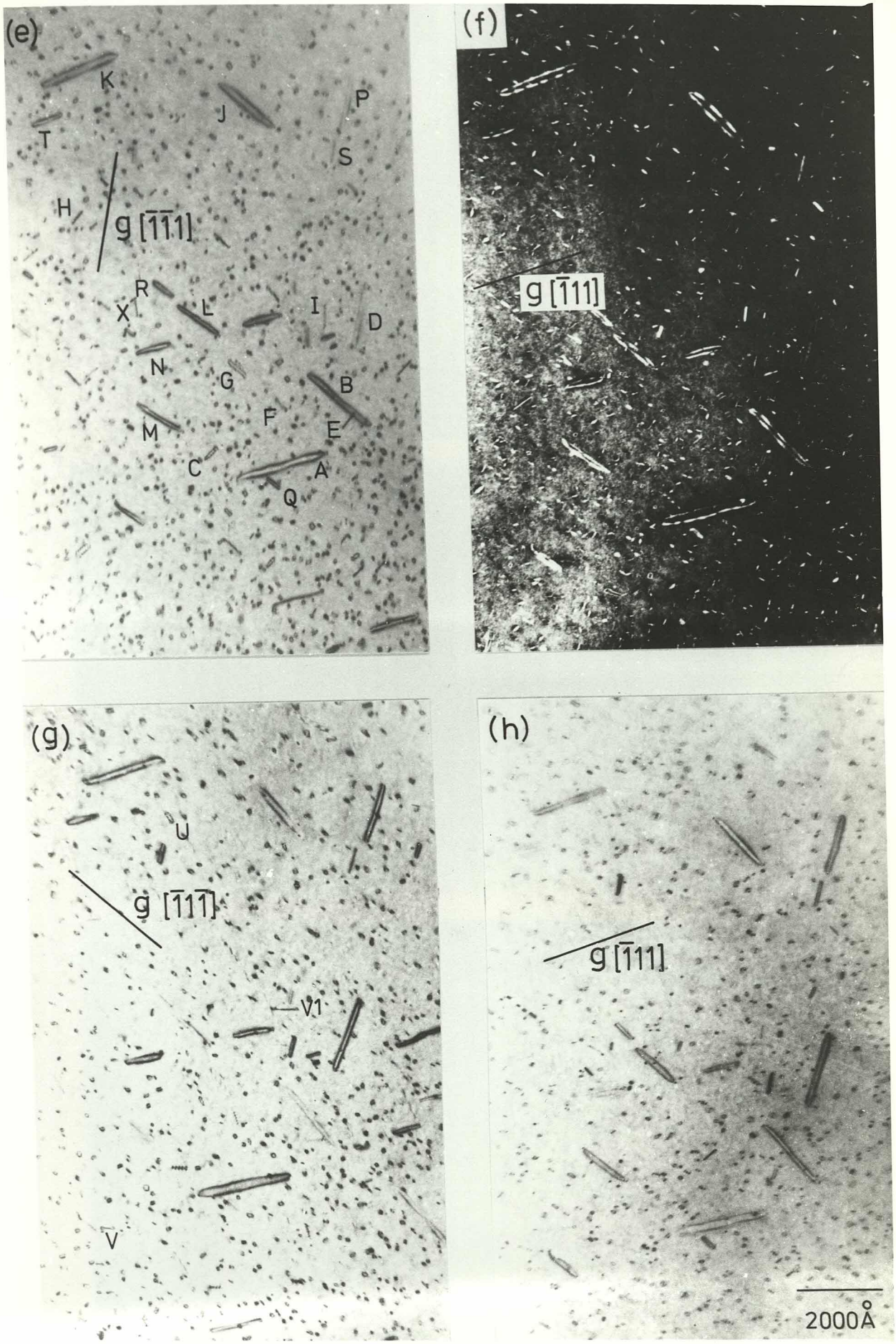

Fig.5/13

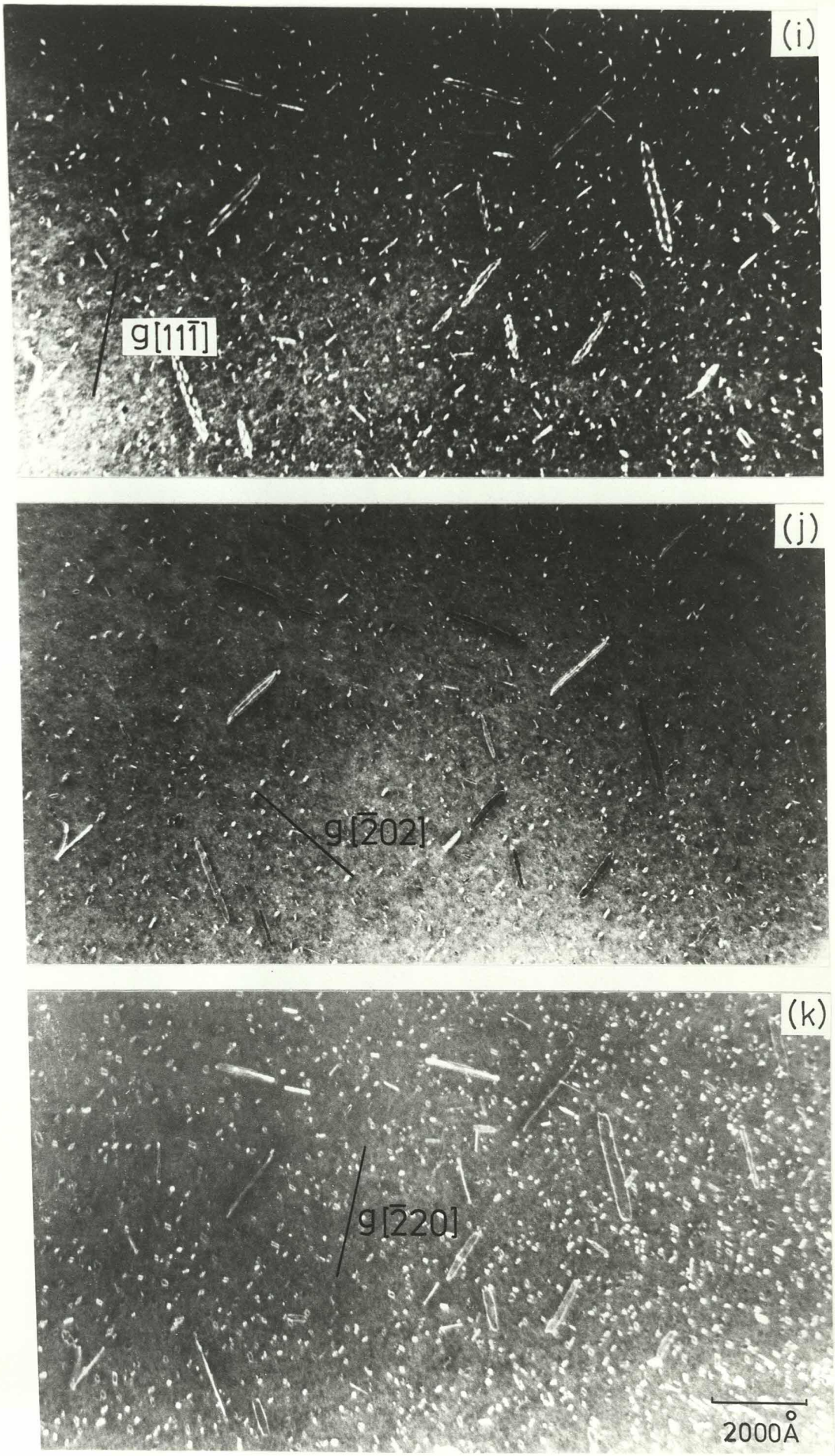

Fig.5/14

Fig. 5/15 Fig. A shows the sequential arrangement of partial dislocations to form an enclosed intrinsic stacking fault.

Fig. B illustrates how the resultant Shockley partials arrange themselves to form an extrinsic fault.

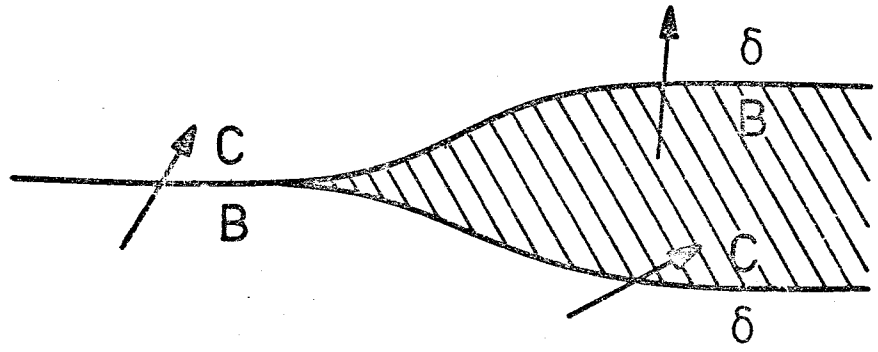

Intrinsic
fault

(A)



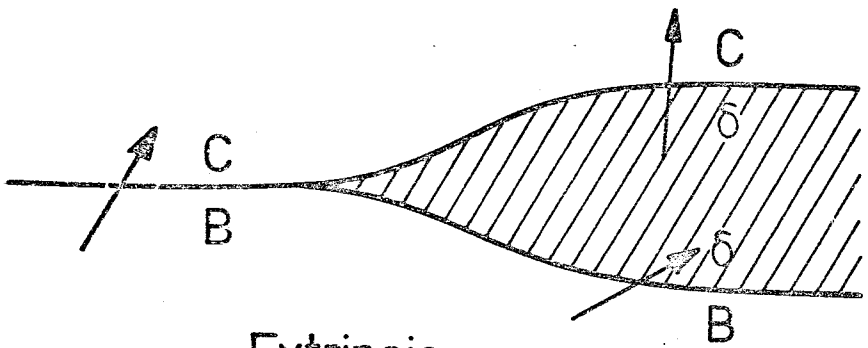

Extrinsic
fault

(B)





Fig. 5/16 The configurations of elongated loops that can form in electron irradiated Cu/Al alloys.

If the positive sense of the dislocation is defined as pointing into the paper, an intrinsic stacking fault is formed with the uppermost dislocation $\overline{\delta C}$ on the left and an extrinsic fault if $\overline{\delta C}$ is on the right. For each Burgers vector and line direction, two possible loop orientations are allowed, each rotated a few degrees on either side of the {110}.

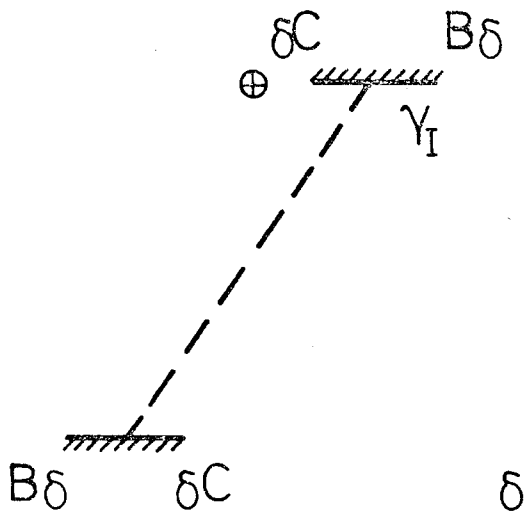

(A)

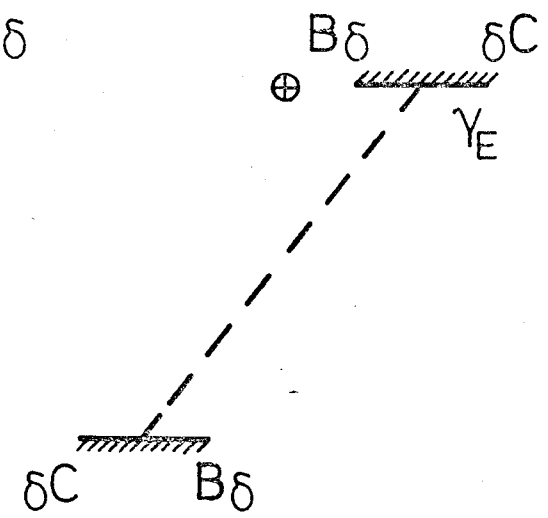

(B)

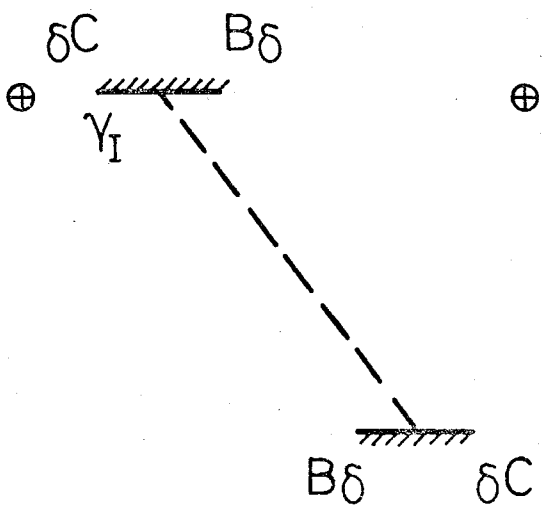

(C)

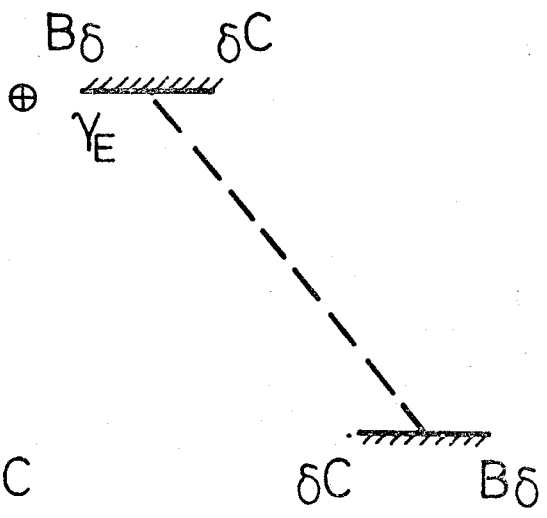

(D)

Fig. 5/17 Diagram shows the origin of the strong narrow and weak broad contrast form elongated loops.

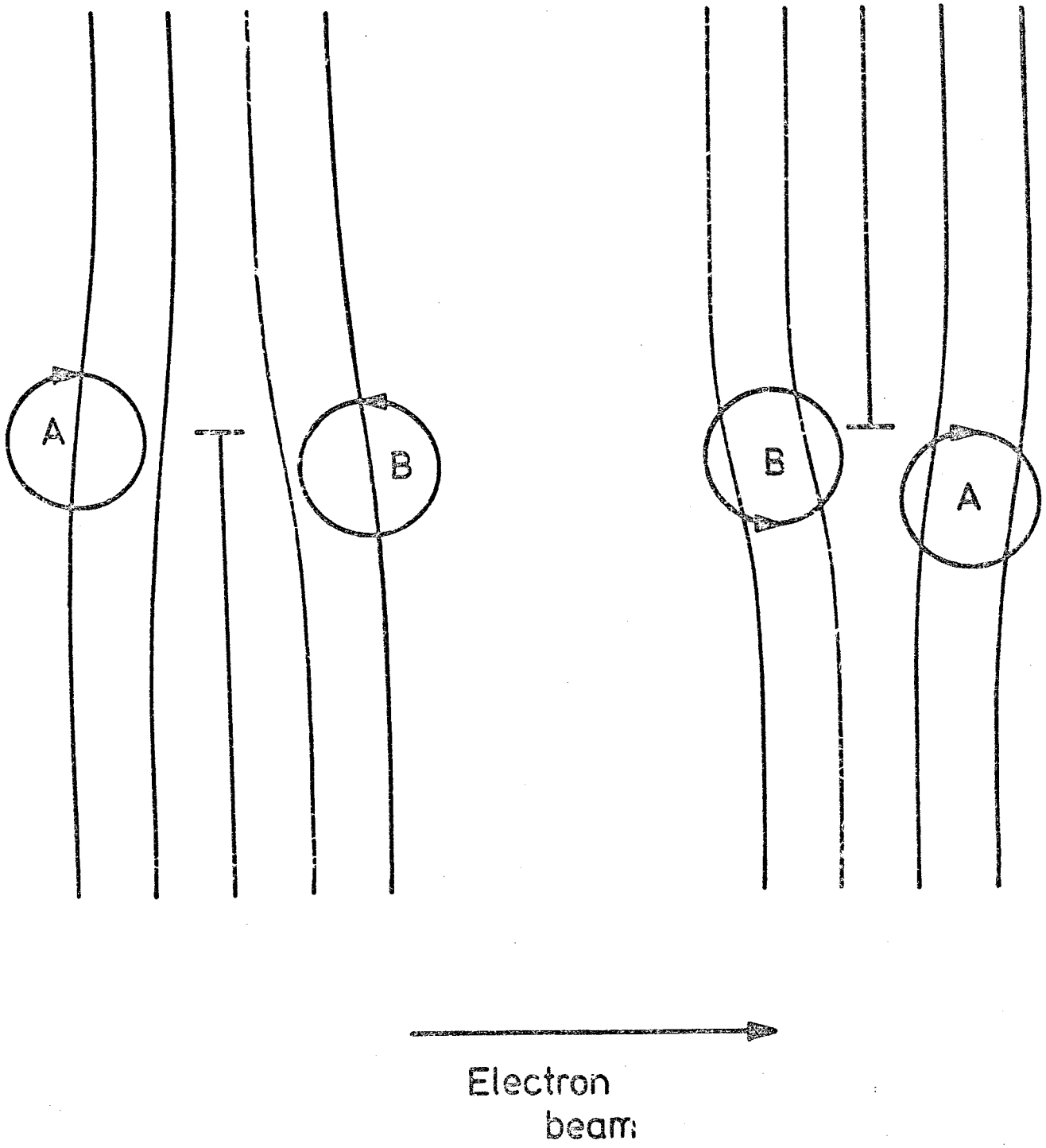
A
B
B
A
Electron
beam

Fig. 5/18 The schematic arrangement of Shockley partials as seen from the weak beam micrographs fig. 5/12 (A) and (C). The configuration giving rise to such contrast is shown below each loop.

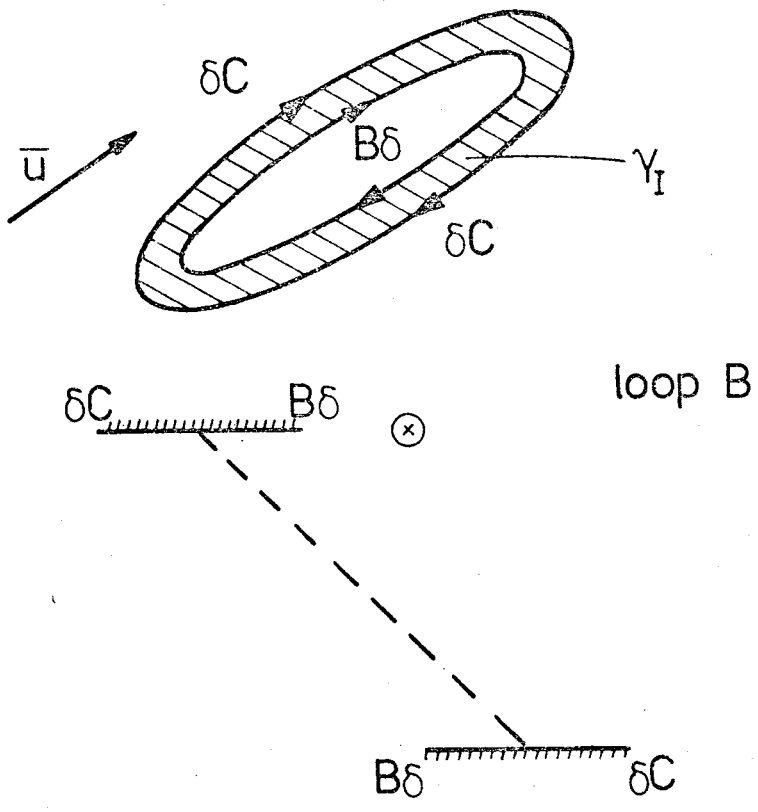
δC
Bδ
$\bar{u}$
γ_I
δC
loop B
δC
Bδ
⊗
Bδ
δC
Bδ
δC
loop L
$\bar{u}$
⊗
δC
Bδ
Bδ
δC

Fig. 5/19 Elongated loops in Cu 16% Al with similar Burgers vector $\bar{b} = \frac{a}{2}[10\bar{1}]$, but different line direction.

Note the difference in contrast between loops ψ and ξ and the transition in contrast of loop ϕ.

$\bar{z} = [111]$

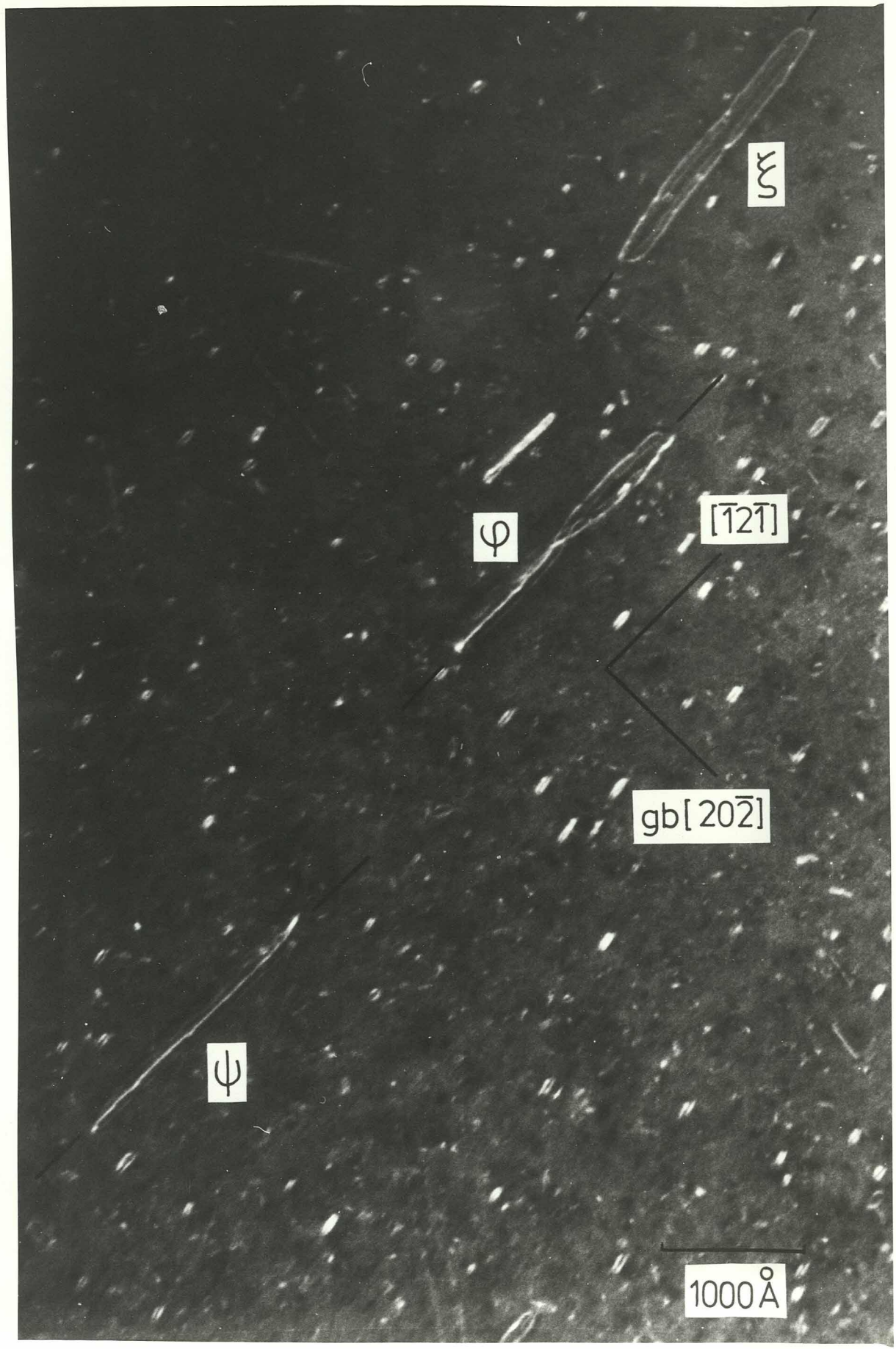
ξ
φ
[1̄21̄]
gb[20$\bar{2}$]
ψ
1000 Å

Fig. 5/20 This diagram depicts the partial configuration of loop ϕ, a linear defect on fig. 5/19, which can be explained by allowing the loop normal to change from one side of the <110> to the other. In doing so, the partials are observed to change from one side to the other.

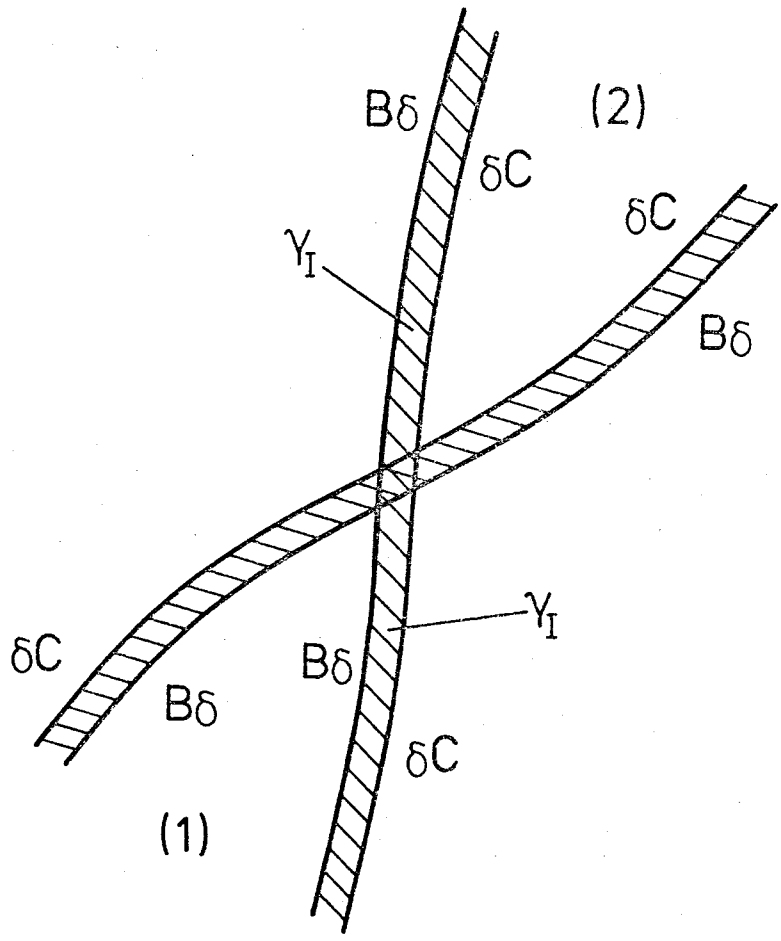
Bδ
(2)
δC
δC
γI
Bδ
γI
δC
Bδ
Bδ
δC
(1)

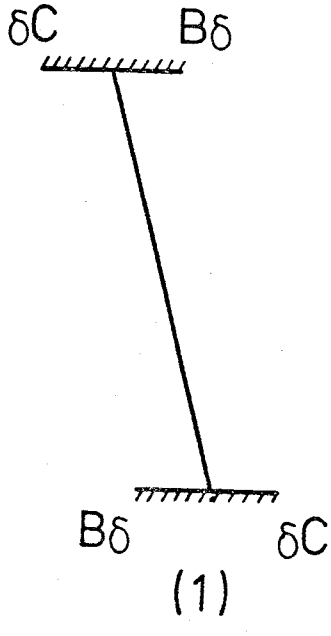
δC
Bδ
Bδ
δC
(1)

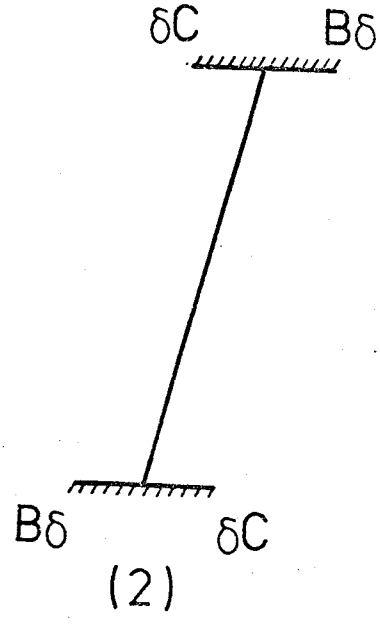
δC
Bδ
Bδ
δC
(2)

Fig. 5/21 The graph shows the effect of polishing temperature and voltage on the formation of elongated loops in Cu 16% Al irradiated at $\simeq 240^{\circ}C$ and a dose rate of 6×10^{18} el./cm.^{2}/sec., within 5 minutes of the final electropolish.

The solution consisted of 33% Nitric Acid
67% Methanol.

In region (A) no linear defects were grown and only a low density of rhombus loops nucleated.

In the narrow shaded band no linear defects grew but the density of rhombus loops increased.

Region (C) represents the conditions under which elongated defects nucleated together with a high background density of rhombus loops.

This latter condition occurred when the rate of removal of a given thickness of specimen was less than the diffusion distance of hydrogen under these polishing temperature and voltage conditions.

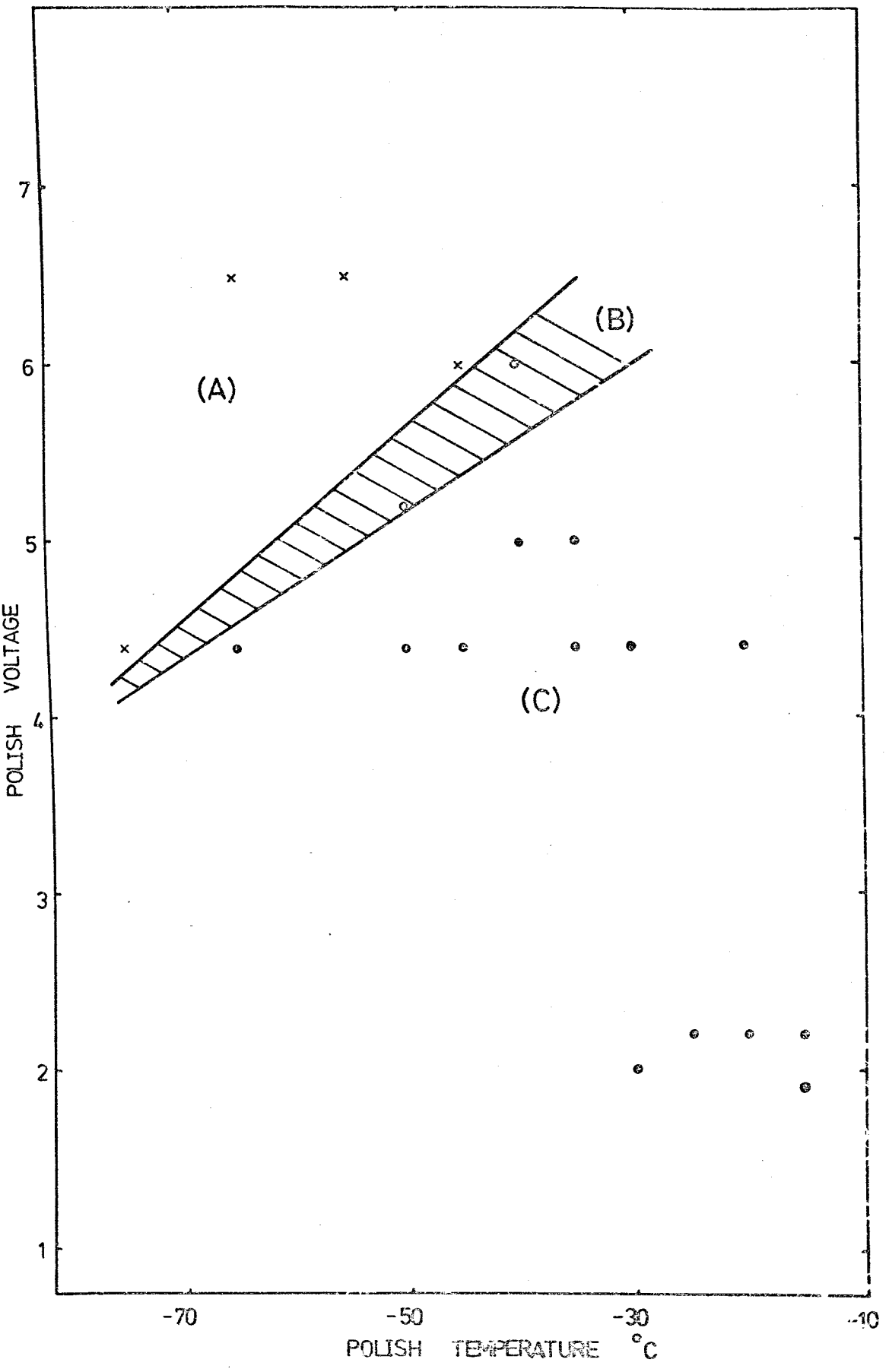
7
6
5
4
3
2
1
POLISH VOLTAGE
(A)
(B)
(C)
-70
-50
-30
-10
POLISH TEMPERATURE °C

Fig. 5/22 (A) shows the specimen polishing rate as a function of temperature, together with the hydrogen diffusion distances

(A) drift velocity of H in Cu 5% Al

(B) drift velocity of H in Cu

(C) drift velocity of H in Cu 16% Al

(D) Surface removal rate in copper foils

Though extrapolation of the diffusion constants for Cu and Cu/Al alloys were made from high temperature measurements of Mokaram (1974) the curves suggest that hydrogen will not penetrate the specimens at temperatures $< -70^{\circ}C$.

(B) Graph shows a plot of elongated loop density of loops on the (111) plane, against background rhombus loop density in foils of Cu 16% Al.

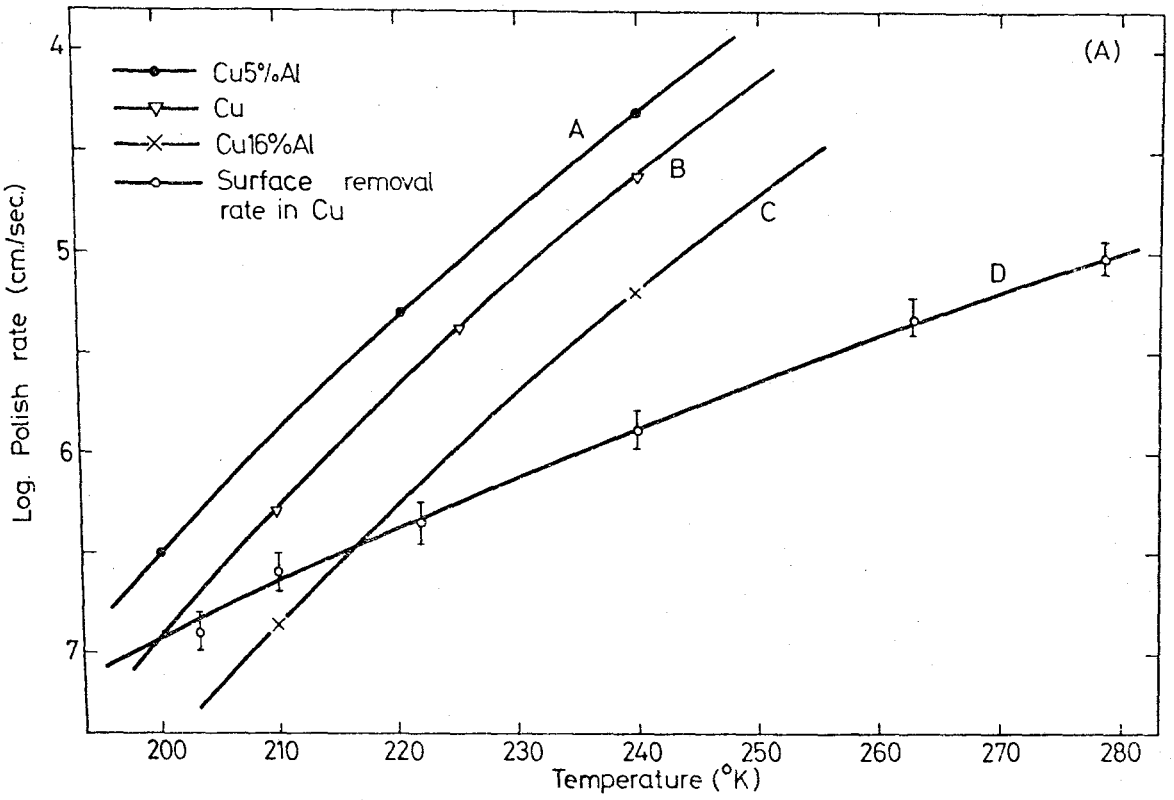
(A)
Cu5%Al
Cu
Cu16%Al
Surface removal rate in Cu
A
B
C
D
Log. Polish rate (cm./sec.)
4
5
6
7
200
210
220
230
240
250
260
270
280
Temperature (°K)

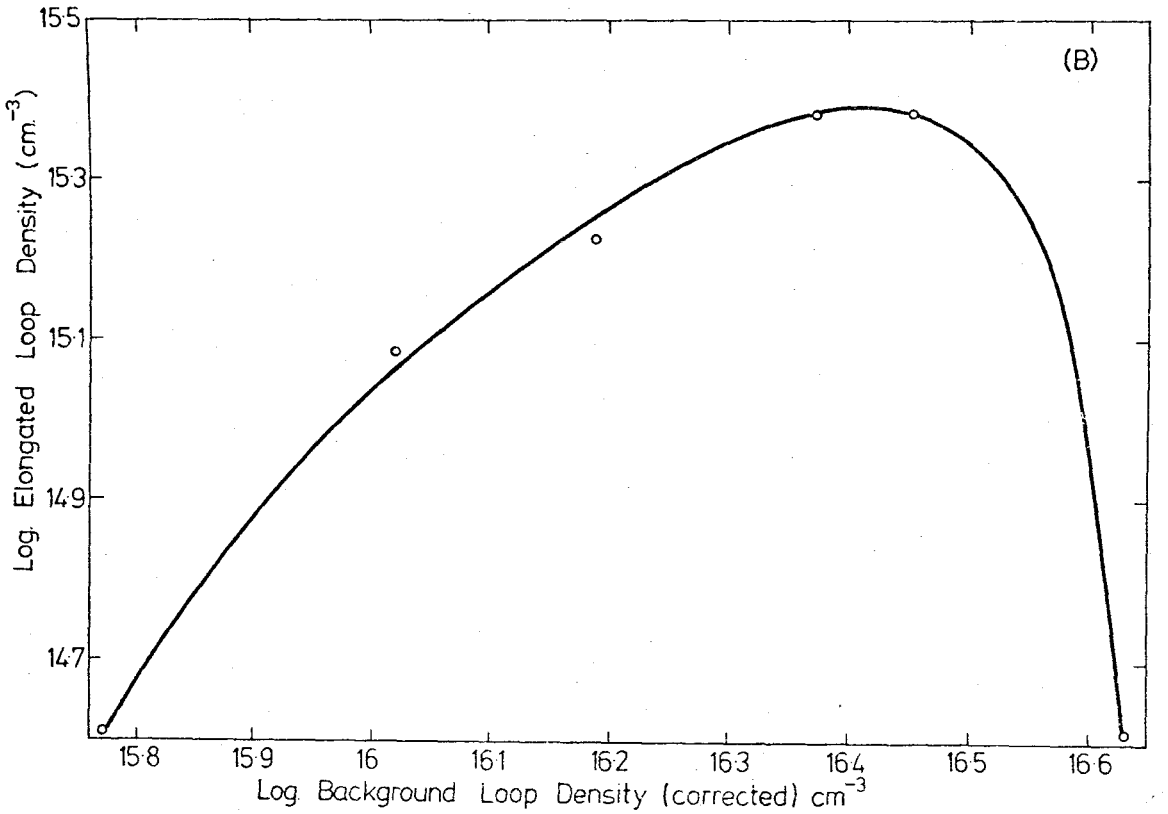
(B)
Log. Elongated Loop Density (cm.$^{-3}$)
15·5
15·3
15·1
14·9
14·7
15·8
15·9
16
16·1
16·2
16·3
16·4
16·5
16·6
Log. Background Loop Density (corrected) cm^{-3}

Fig. 5/23 Elongated loop density as a function of alloy concentration, after foils have been irradiated at T_i = 240°C. Specimens polished -35°C, 4.4 volts.

(A) Cu .15% Al. Low background rhombus or Frank loop density, and no elongated loops.

(B) Cu 2% Al. High background rhombus loop density, but no elongated loops.

(C) Cu 16% Al. High density of elongated loops.

g <111> z <112>

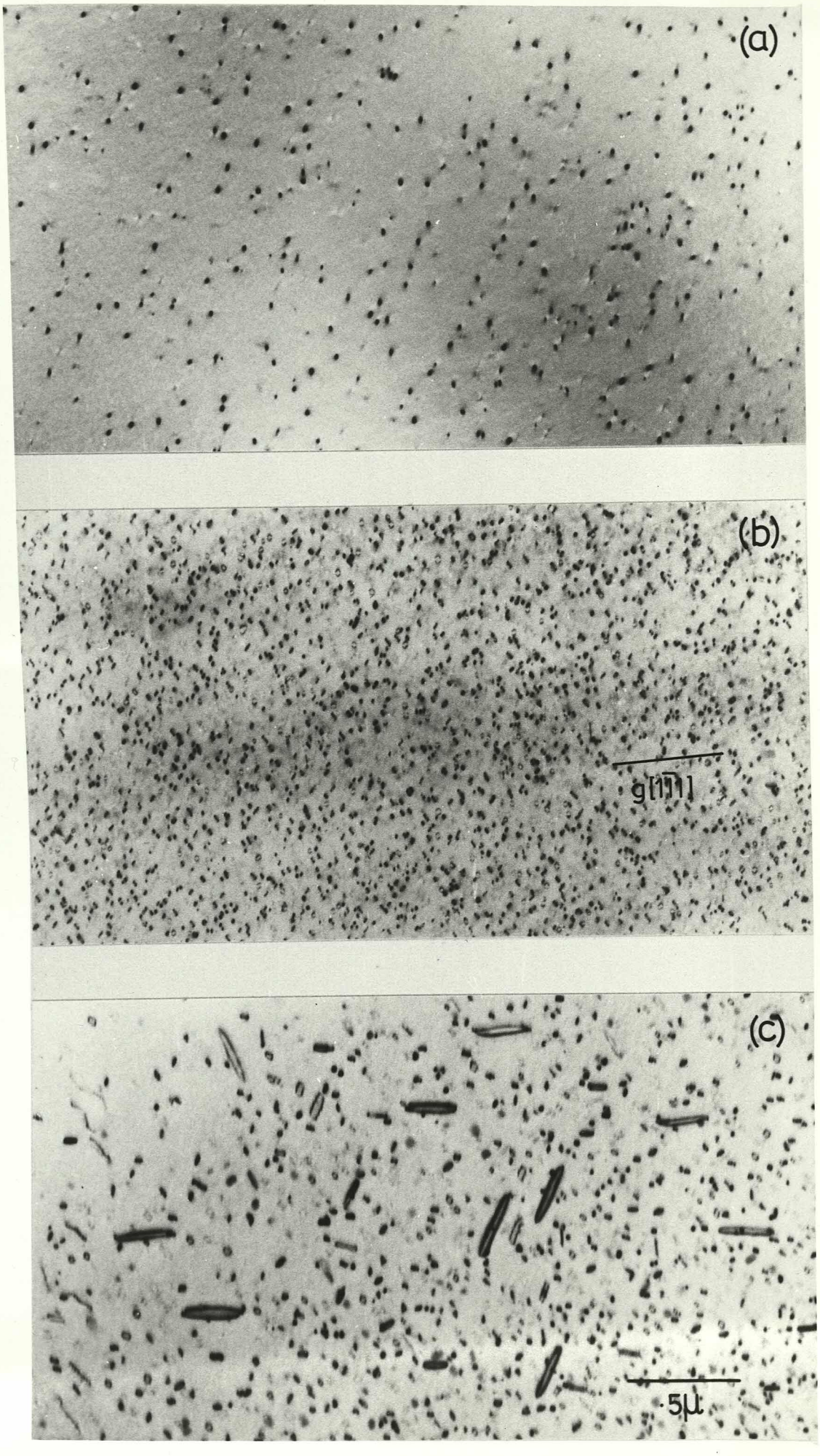
(a)
(b)
g[111]
(c)
5μ

Fig. 5/24 Effect of foil thickness on the formation of elongated perfect loops in a Cu 16% Al specimen.

Similar irradiation dose rates and temperatures were used for both areas.

(A) Thin area, high density of elongated loops

(B) Thick area, very low density of elongated loops.

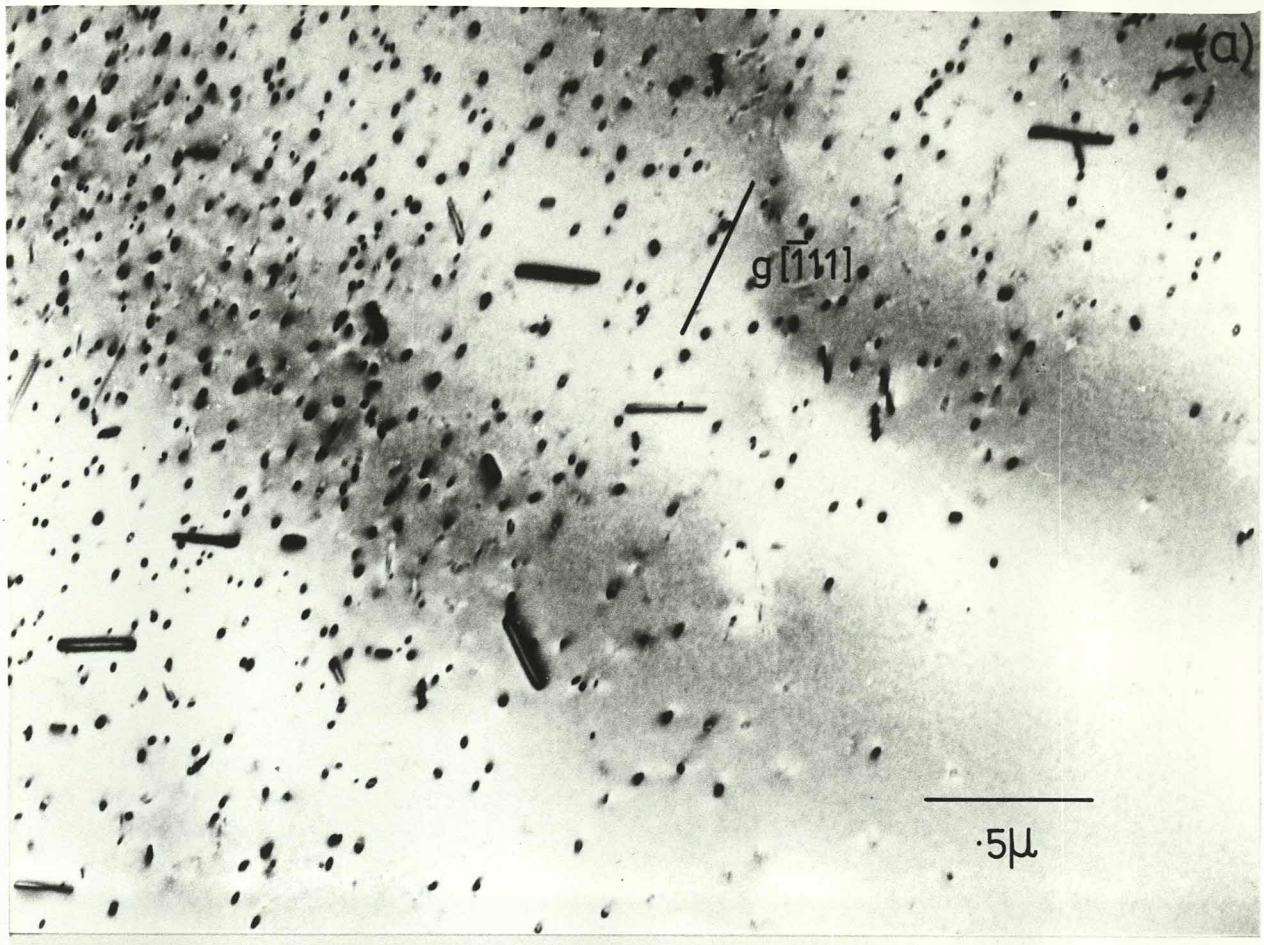
(a)
g[$\bar{1}$11]
·5μ

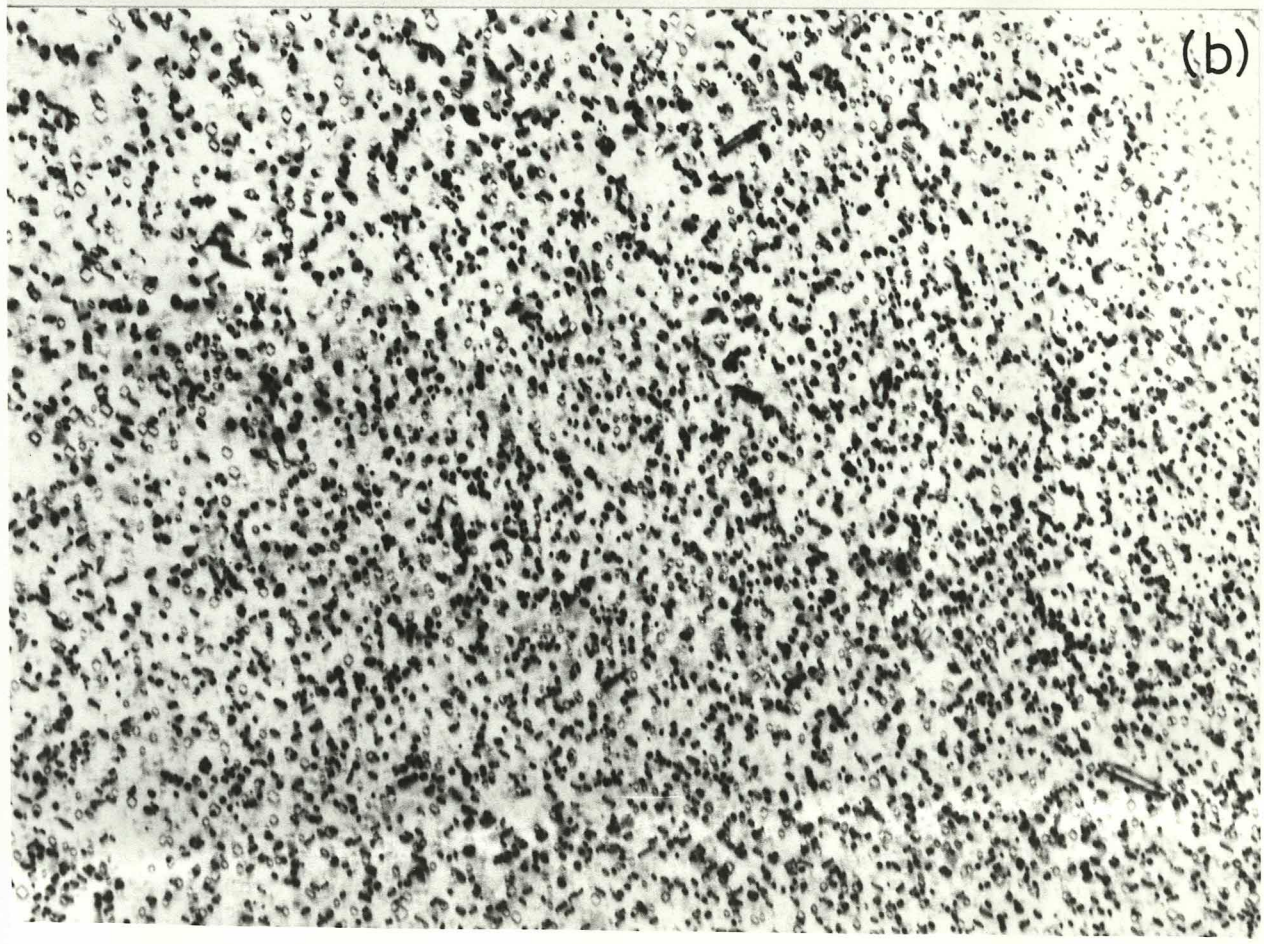
(b)

Fig. 5/25 Effect of dose rate on the formation of elongated loops in Cu 16% Al foils.

(A) dose rate $g = 7 \times 10^{18}$ cm.$^{-3}$ sec.$^{-1}$

(B) dose rate $g = 3.8 \times 10^{19}$ cm.$^{-3}$ sec.$^{-1}$.

The areas were irradiated under similar thickness and temperature conditions.

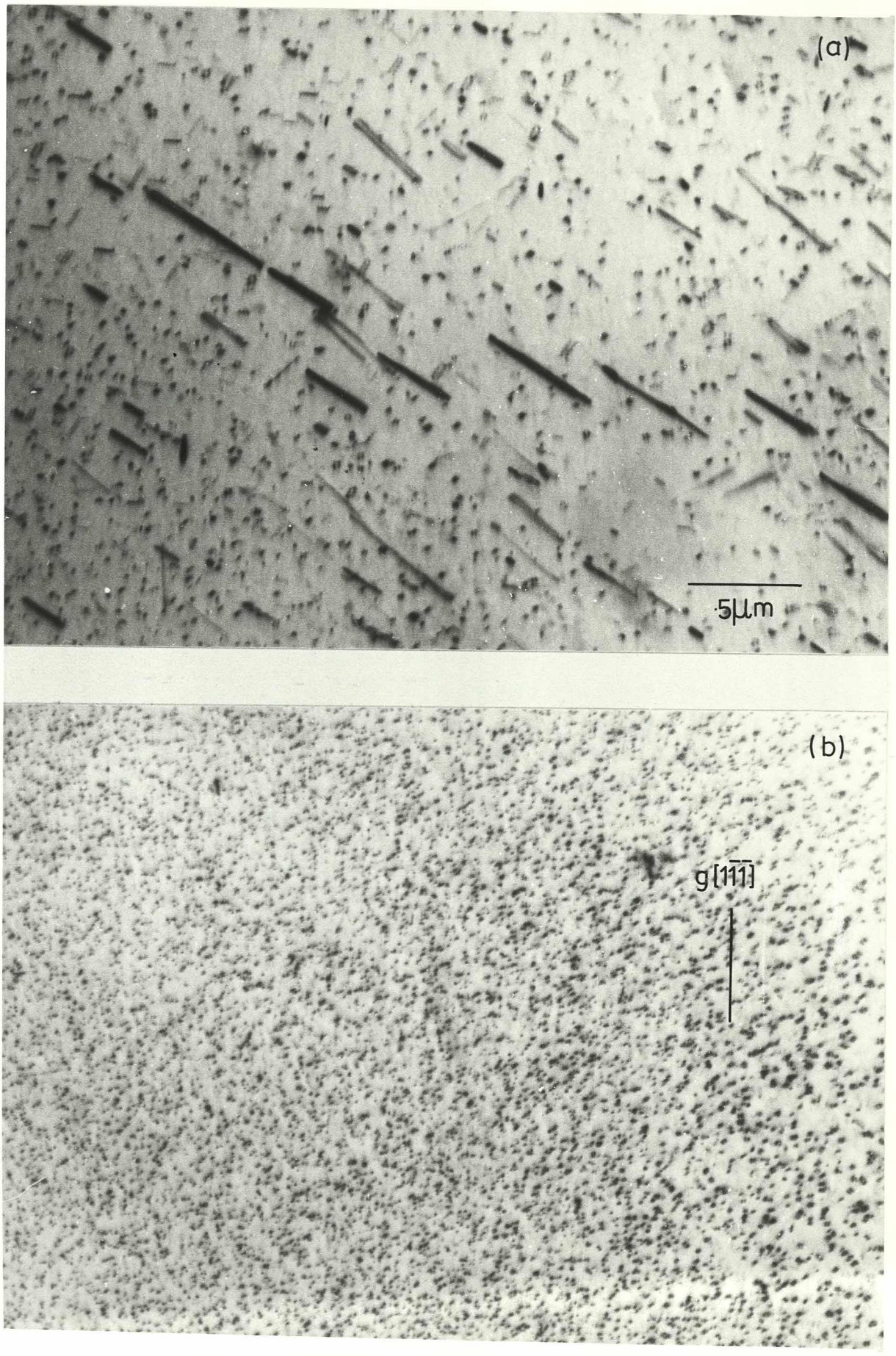
(a)
5μm
(b)
g[11̄1̄]

Fig. 5/26 The graph shows the variation of elongated loop size as a function of irradiation temperature in foils of Cu 16% Al.

dose rate $\triangleq 6 \times 10^{18}$ el./cm.^{2}/sec.

foil thickness $\triangleq 2200$ Å.

Curve (A) represents the results obtained by a stepwise increase in irradiation temperature on the same specimen, from 135°C. Some annealing of the irradiation area has already taken place and the size of the elongated defects is consequently reduced.

Curve (B):- irradiations carried out as initial irradiations on different specimens, but using the same conditions.

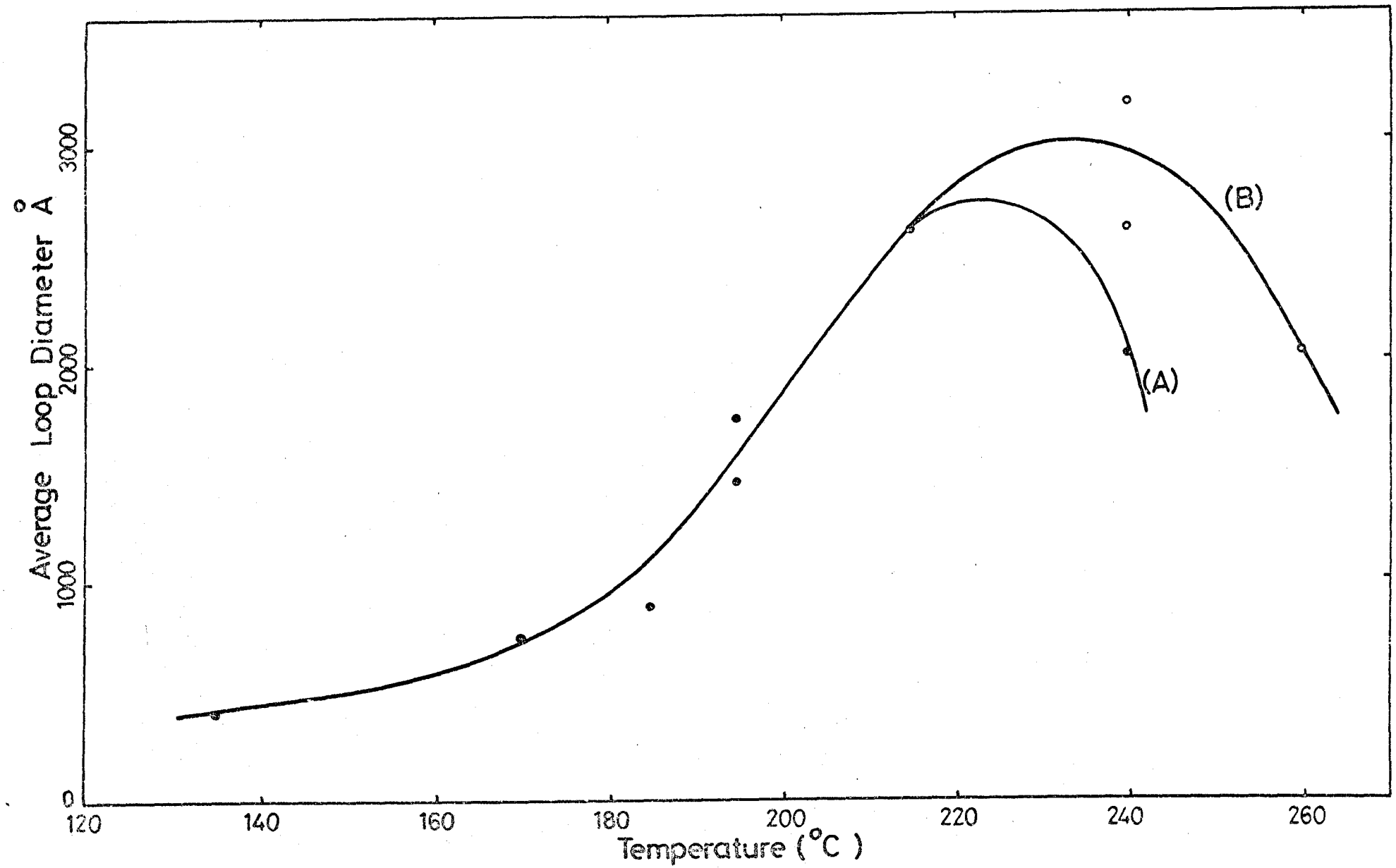
Average Loop Diameter Å
0
1000
2000
3000
120
140
160
180
200
220
240
260
Temperature (°C)
(A)
(B)

Fig. 5/27 demonstrates the differences in growth rates between elongated loops and small background rhombus loops, in the same area.

Cu 16% Al specimen polished at $-25^{o}C$ and 2.2 volts.

Elongated loops grow rapidly for the first minute of irradiation, then reduce their velocity and stop growing. In the plateau region, the defects are still absorbing interstitials, but increase in width only.

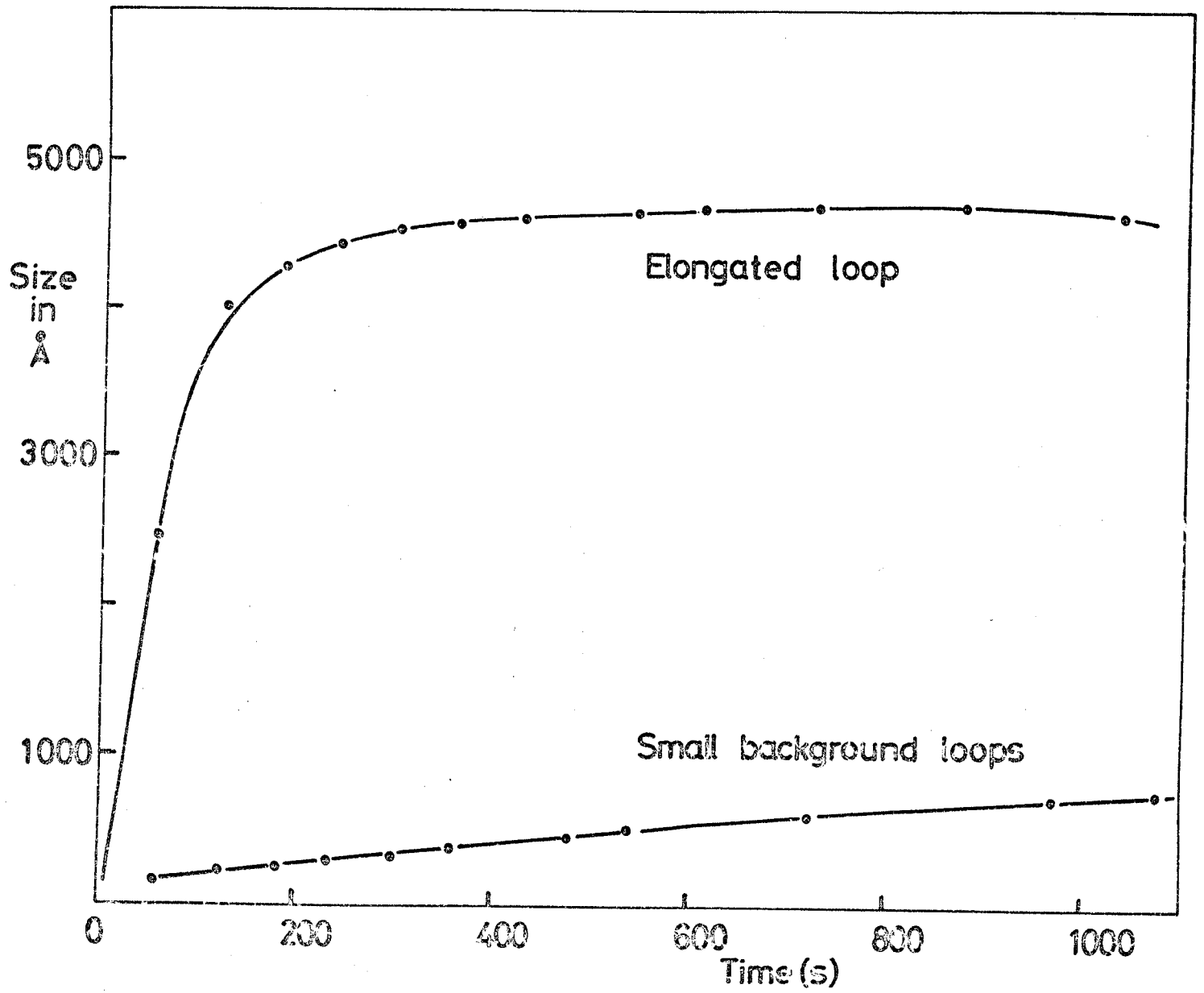
5000
3000
1000
Size in Å
Elongated loop
Small background loops
0
200
400
600
800
1000
Time (s)

Fig. 5/28 Elongated loop growth in a Cu 16% Al foil irradiated at T_i = 210°C. Specimen polished at -25°C, 2.2 volts.

$g\ [1\bar{1}\bar{1}]\quad \bar{z}\ [211]$

The main characteristics of elongated loops are an extremely rapid growth rate in the initial minute of irradiation and then subsequent broadening without further extension.

The loop contrast and direction also changes during growth.

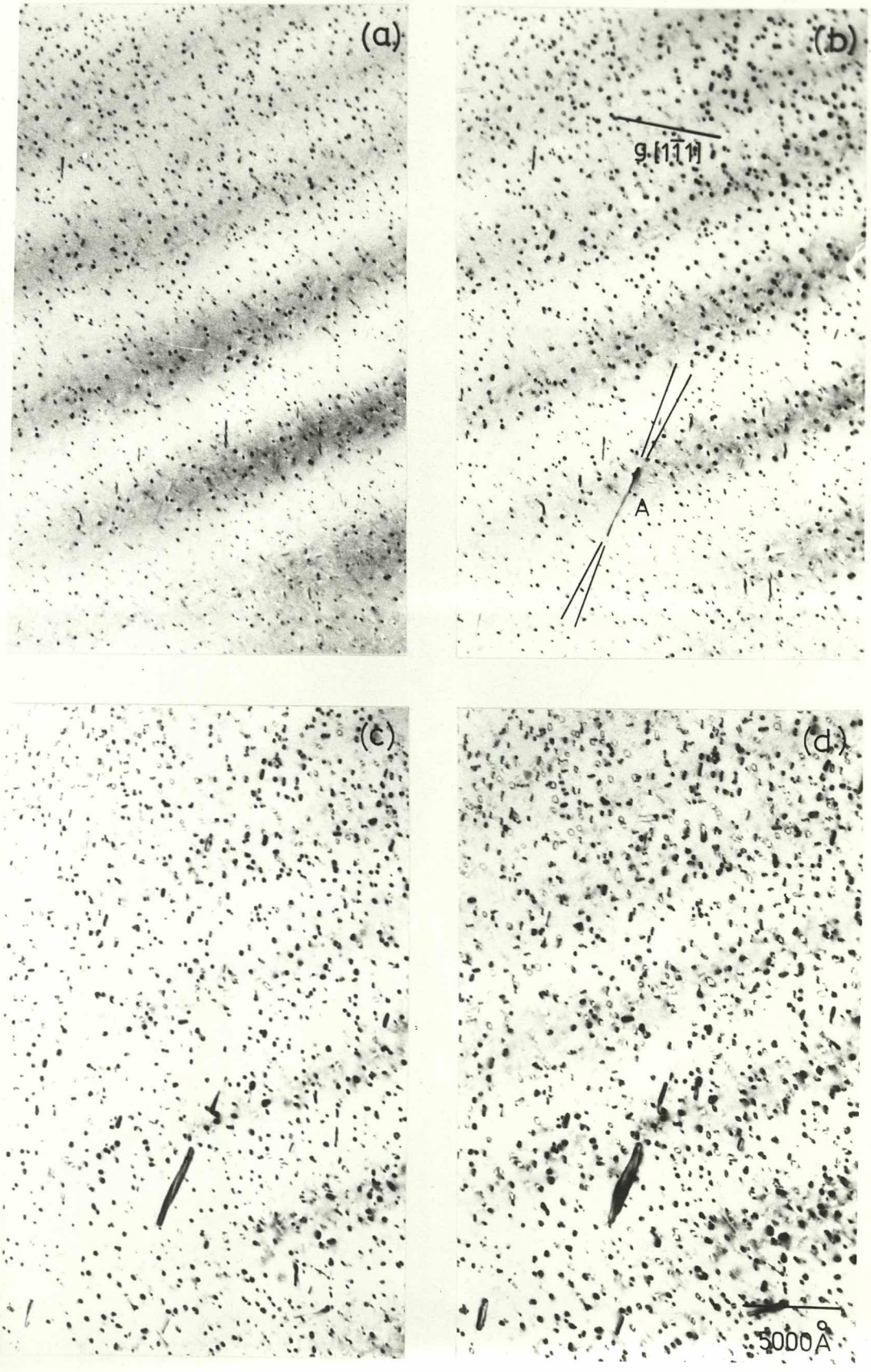
(a)
(b)
g 1 1 1
A
(c)
(d)
5000 Å

Fig. 5/29 The diagram shows schematically the possible mechanisms of elongated loop growth. A rod like defect appears with very weak contrast in the initial stages of irradiation. Fig. (A) and (B) represents a line of dilation. In the intermediate stages of growth the contrast becomes stronger. The loop with a Burgers vector $\frac{a}{2}$ <110> can dissociate into Shockley partials, though the short end segment is undissociated. Fig. (C). As the loop grows larger the end segment can climb onto the {111} plane where it can dissociate. Fig. (D). At this time, stair-rods $\bar{\alpha}\bar{\beta}$ and $\bar{\alpha}\bar{\beta}/\bar{A}\bar{B}$ develop at the corners

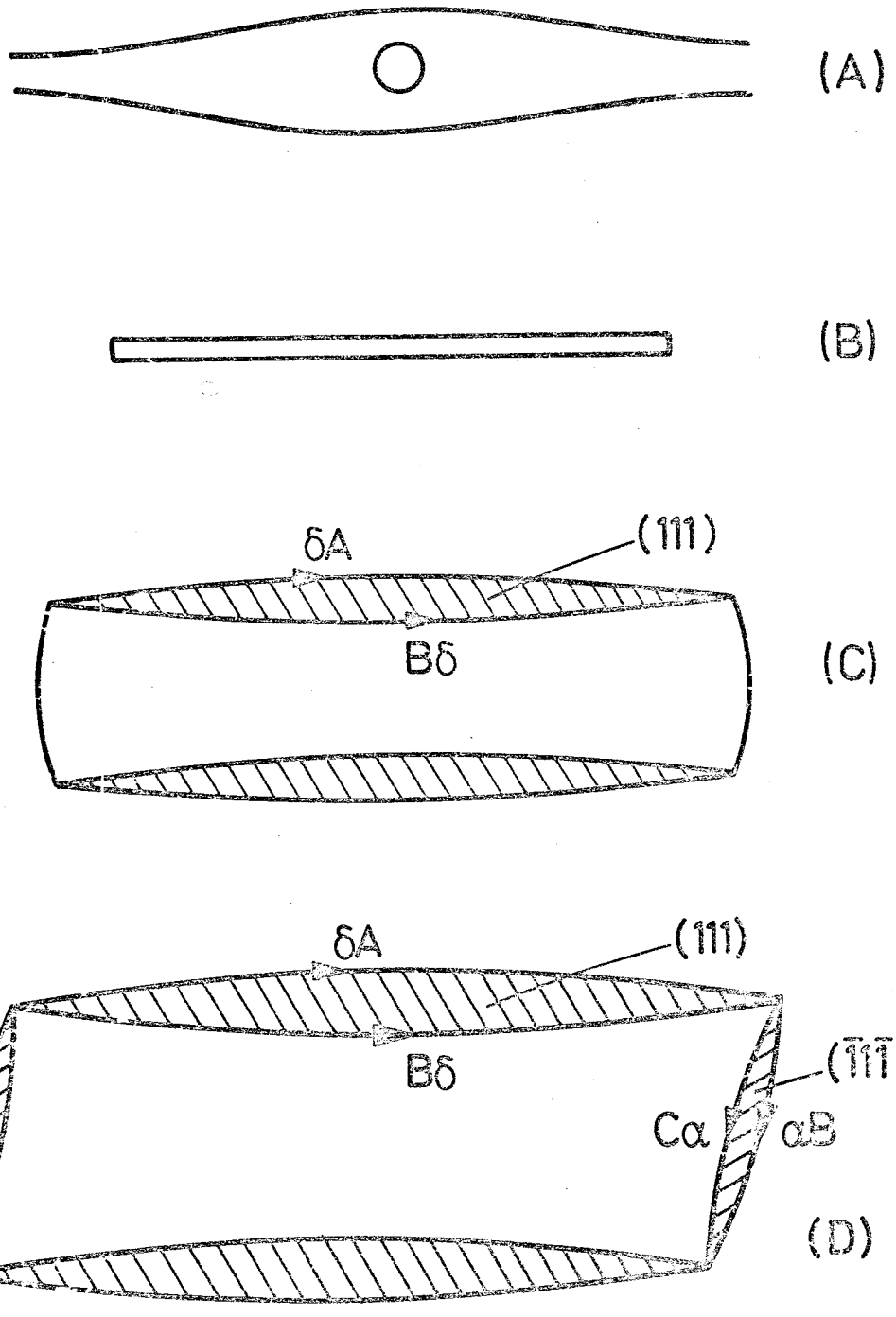
(A)
(B)
δA
(111)
Bδ
(C)
δA
(111)
Bδ
(1̄1̄1̄)
Cα
αB
(D)

Fig. 5/30 Micrographs illustrating the agglomeration of several small elongated loops after irradiation at T_i = 210°C.

g [$\bar{1}\bar{1}1$]

$\bar{z}$ [112]

generation rate = 4×10^{19} cm.$^{-3}$ sec.$^{-1}$

electropolish -15°C 2.2 volts.

Cu 16% Al specimen.

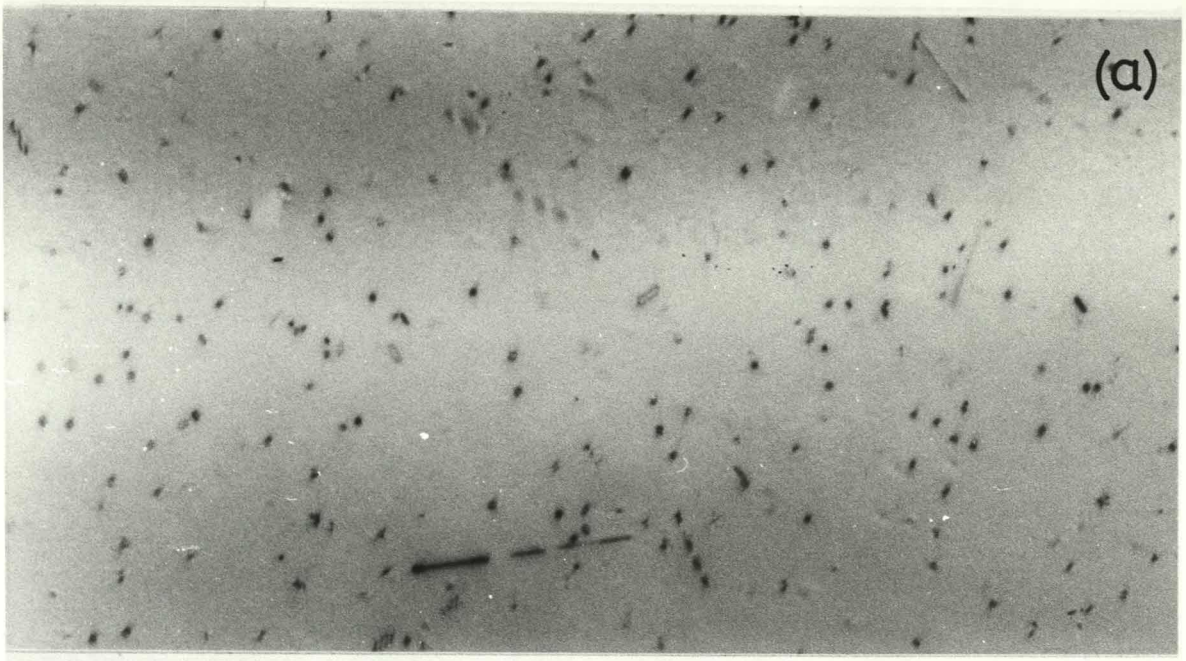
(a)

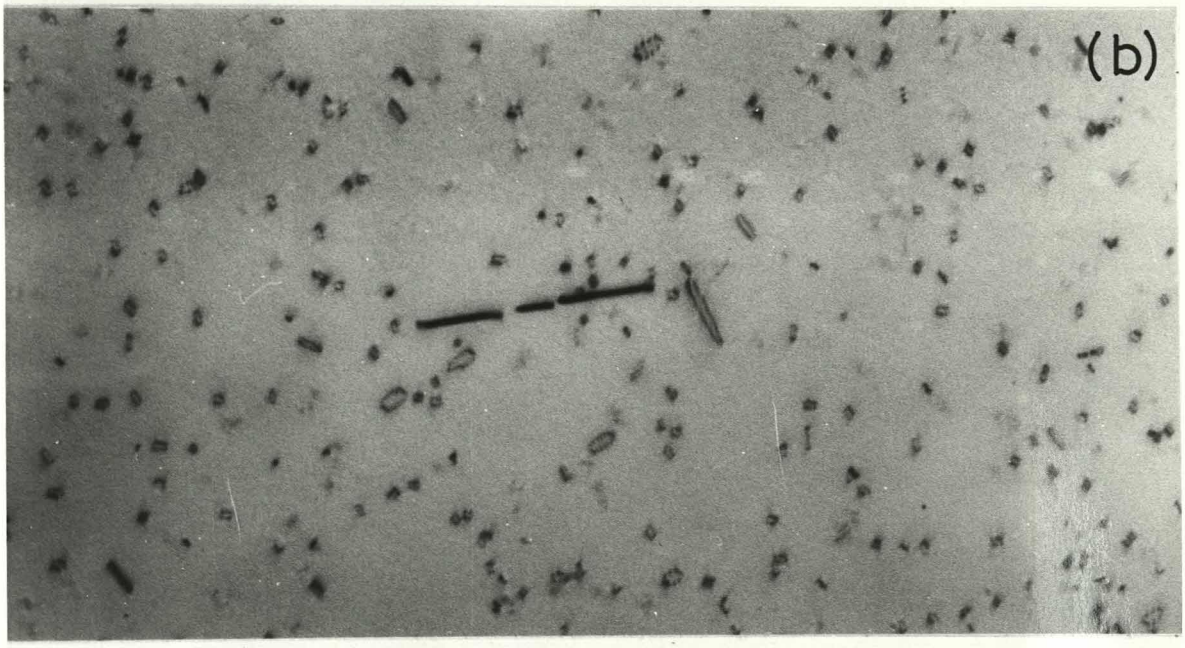
(b)

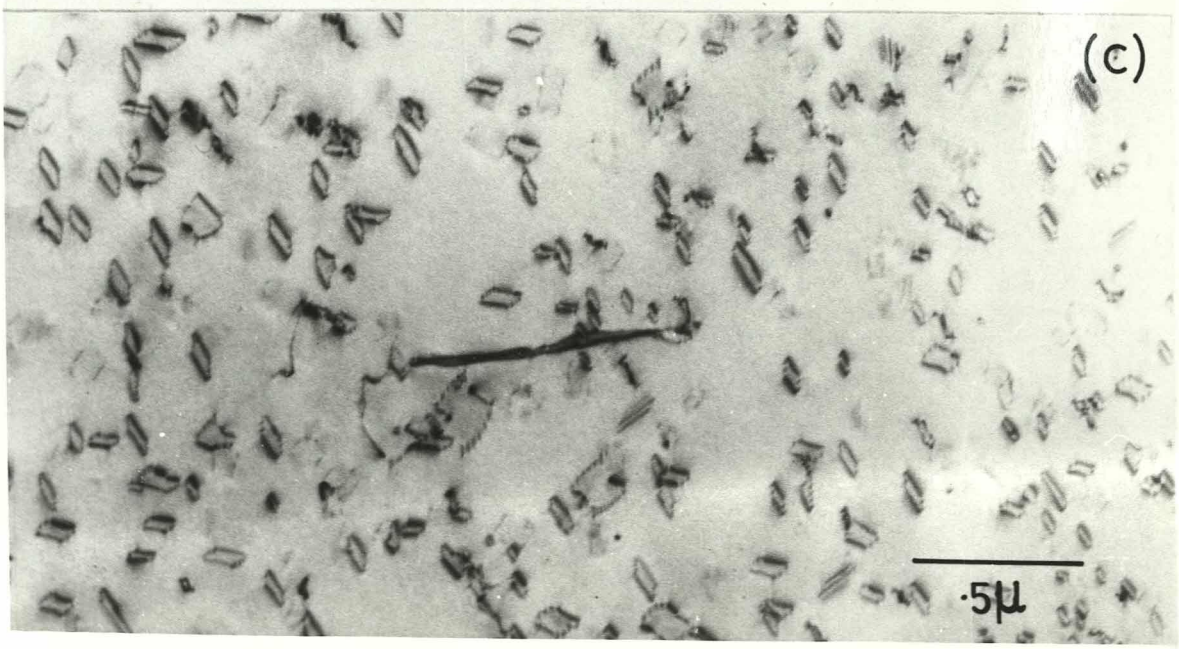
(c)
·5μ

Fig. 5/31 Early growth sequence of elongated loops in a Cu 16% Al foil during irradiation at 240°C, after an electropolish at -15°C 2.2 volts.

(A) 40 seconds irradiation
(B) 80 seconds irradiation
(C) 120 seconds irradiation
(D) 260 seconds irradiation

Loop A appears as a series of loops after about 80 seconds.
Loop C appears rapidly after ≏ 120 seconds.
Loop F appears as a series of small loops in weak contrast after 80 seconds.

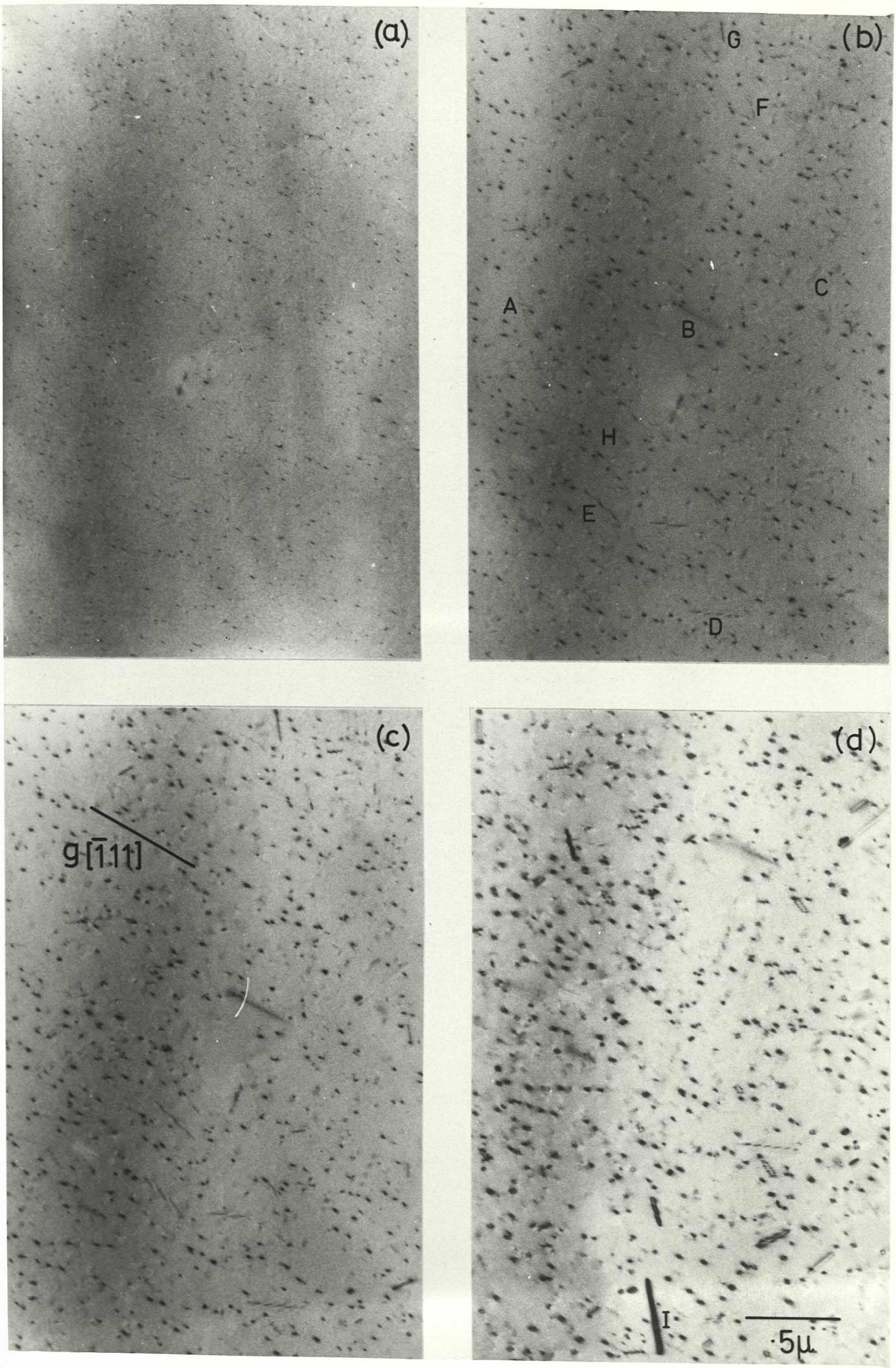
(a)
(b)
G
F
C
A
B
H
E
D
(c)
g[1̄11]
(d)
I
5μ

Fig. 5/32 Dissociation of a large elongated loop, in the later stage of growth, after it has interacted with the foil surface.
Cu 16% Al.

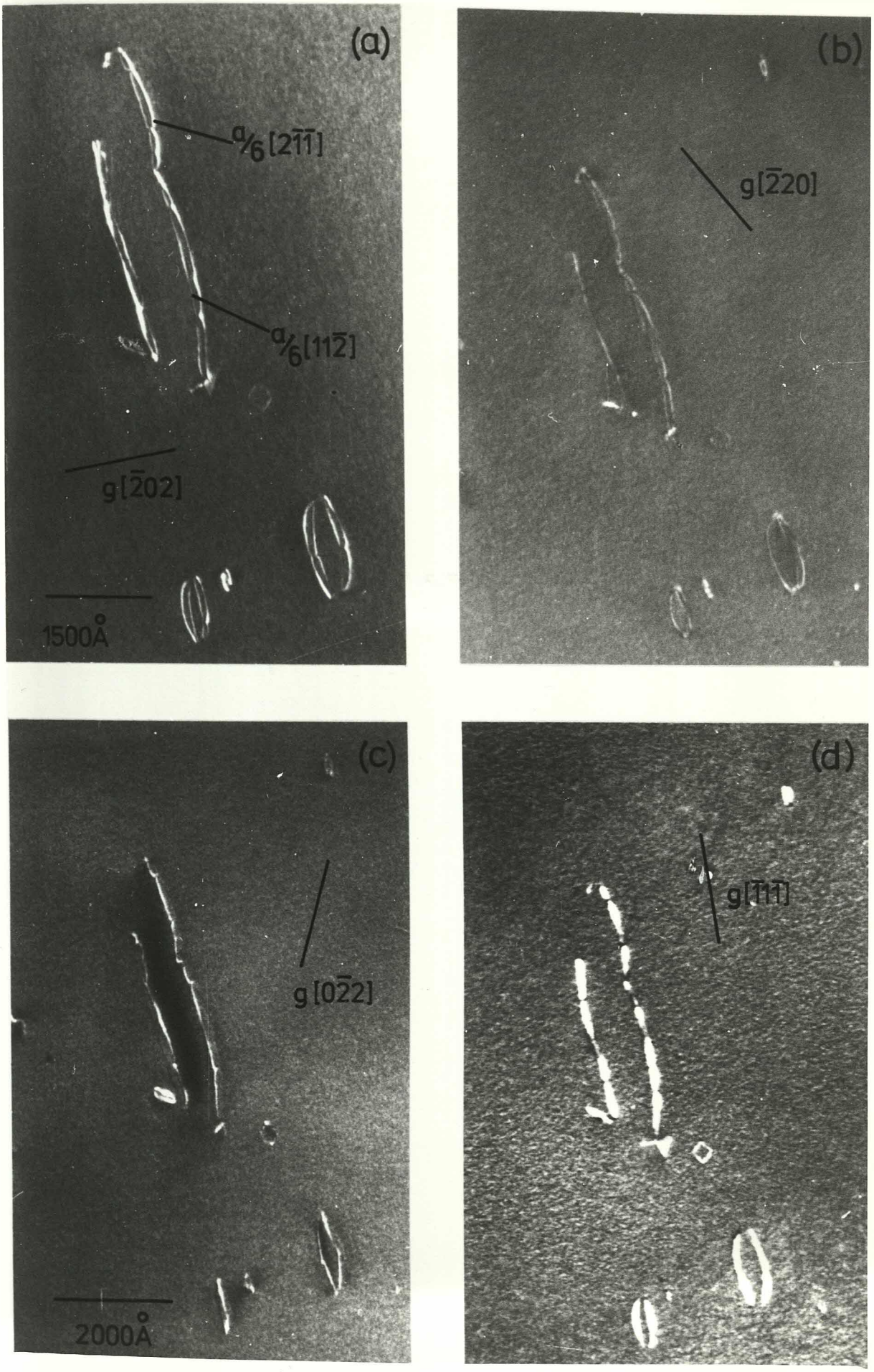
(a)
a/6 [2$\bar{1}\bar{1}$]
a/6 [11$\bar{2}$]
g[$\bar{2}$02]
1500Å
(b)
g[$\bar{2}\bar{2}$0]
(c)
g[0$\bar{2}\bar{2}$]
2000Å
(d)
g[$\bar{1}$1$\bar{1}$]

Fig. 5/33 Elongated loops in a thin foil of Cu 16% Al
The line direction of loops α and $\beta \triangleq [11\bar{2}]$
The Burgers vector of loop $\alpha = \frac{a}{2}[1\bar{1}0]$, but as a consequence of the peculiar contrast of loop β, an exact determination of the Burgers vector of this loop was not possible.

The cause of the puzzling contrast inside loop α (micrograph C) is also unknown.

Micrograph (D) indicates that loop α is growing by the passage of superjogs as constrictions from the lower right to upper left hand corner of the loop.

The small loops in the background, are rhombus in shape with Burgers vectors $\frac{a}{2}\langle 110\rangle$.

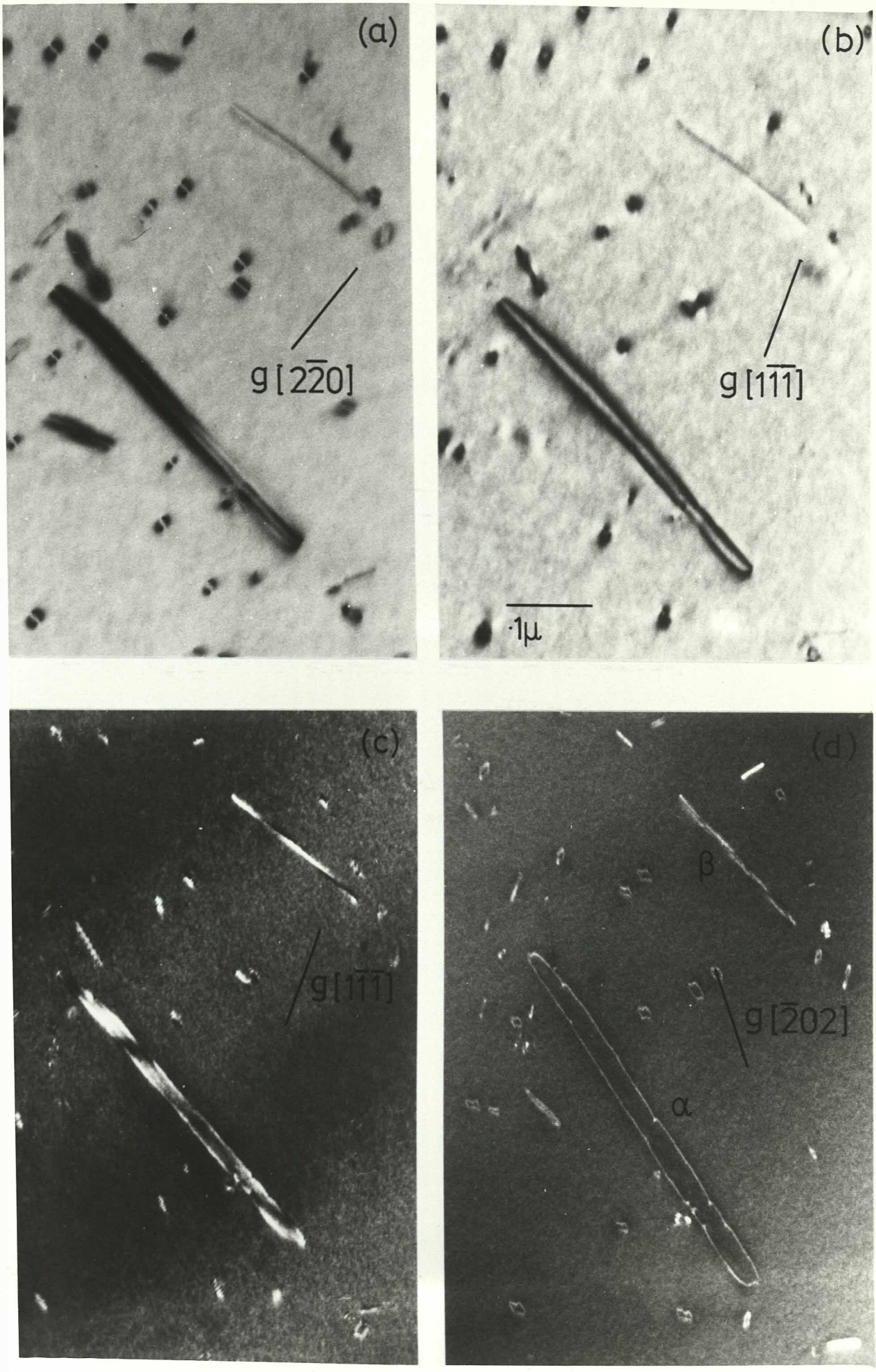
(a)
g [2$\bar{2}$0]
(b)
g [1$\bar{1}\bar{1}$]
·1μ
(c)
g [1$\bar{1}\bar{1}$]
(d)
β
g [$\bar{2}$02]
α

Fig. 5/34 This graph shows the reduction in loop density as a function of anneal time in minutes. The short anneals of the foil took place between each irradiation. Since different areas of the specimens were being irradiated great care was taken to ensure similar irradiation conditions.

Specimen polished at $-15^{\circ}C$ at 2.2 volts and generation rate = 4×10^{19} cm.$^{-3}$ sec.$^{-1}$.

(A) Many elongated loops nucleated in this region. After a 10 minute anneal at $240^{\circ}C$ a slight reduction in loop density occurred.

(B) After two minutes anneal at $290^{\circ}C$.

(C) After two minutes anneal at $315^{\circ}C$, the rhombus and elongated loop density was dramatically reduced.

(D) After two minutes anneal at $340^{\circ}C$, no elongated loops nucleated during irradiation.

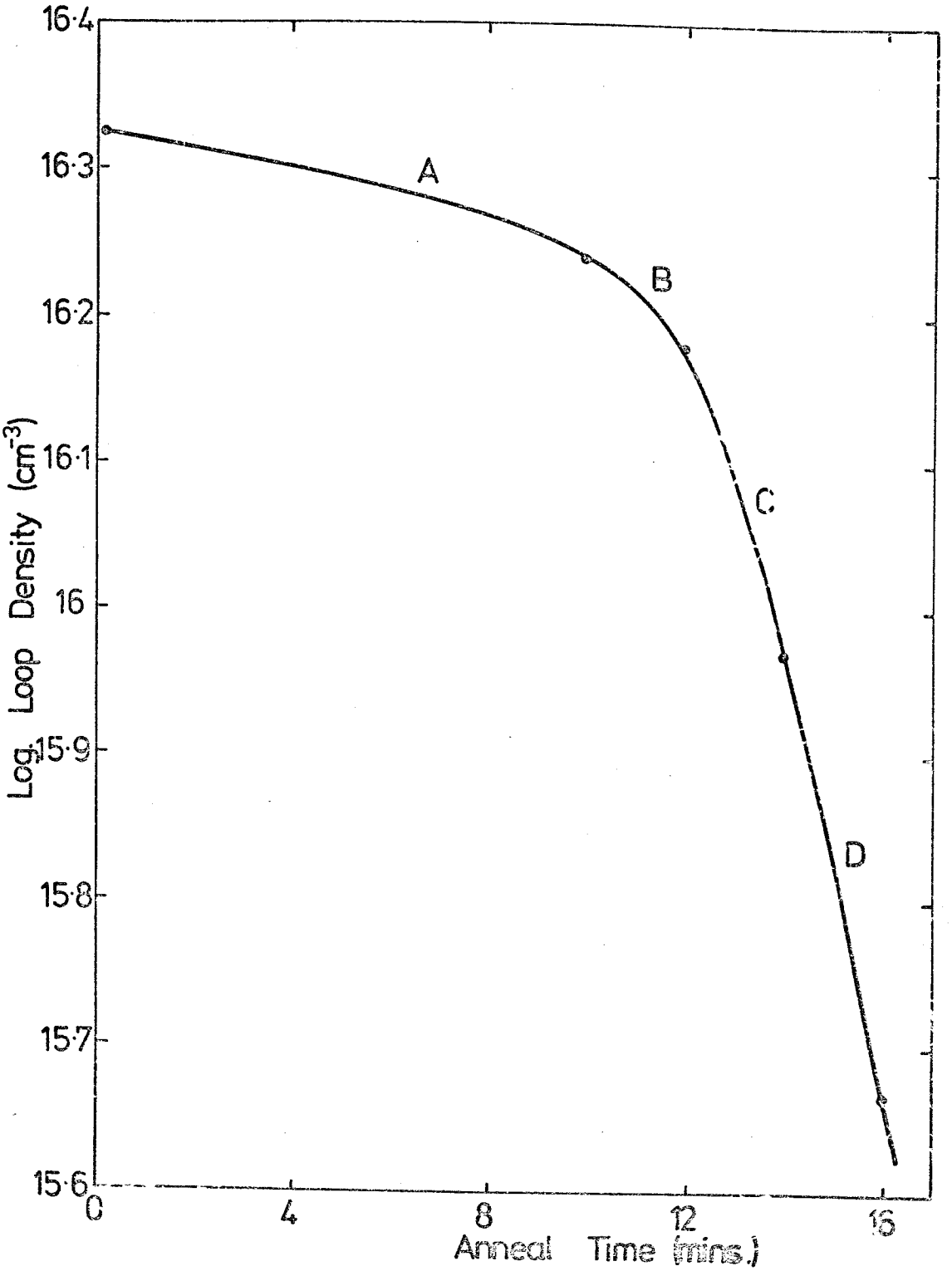
16·4
16·3
16·2
16·1
16
15·9
15·8
15·7
15·6
Log. Loop Density (cm⁻³)
A
B
C
D
0
4
8
12
16
Anneal Time (mins.)

Fig. 5/35 Affect of an in-situ annealing treatment on the nucleation of elongated loops, in a Cu 16% Al foil electropolished at -15°C 2.2 volts.

(A) initial irradiation at 240°C

(B) irradiation at 240°C after 13 minutes anneal at 240°C

(C) irradiation at 240°C after 2 minutes anneal at 295°C

(D) irradiation at 240°C after 2 minutes anneal at 315°C

Similar foil thicknesses and dose rates were used.

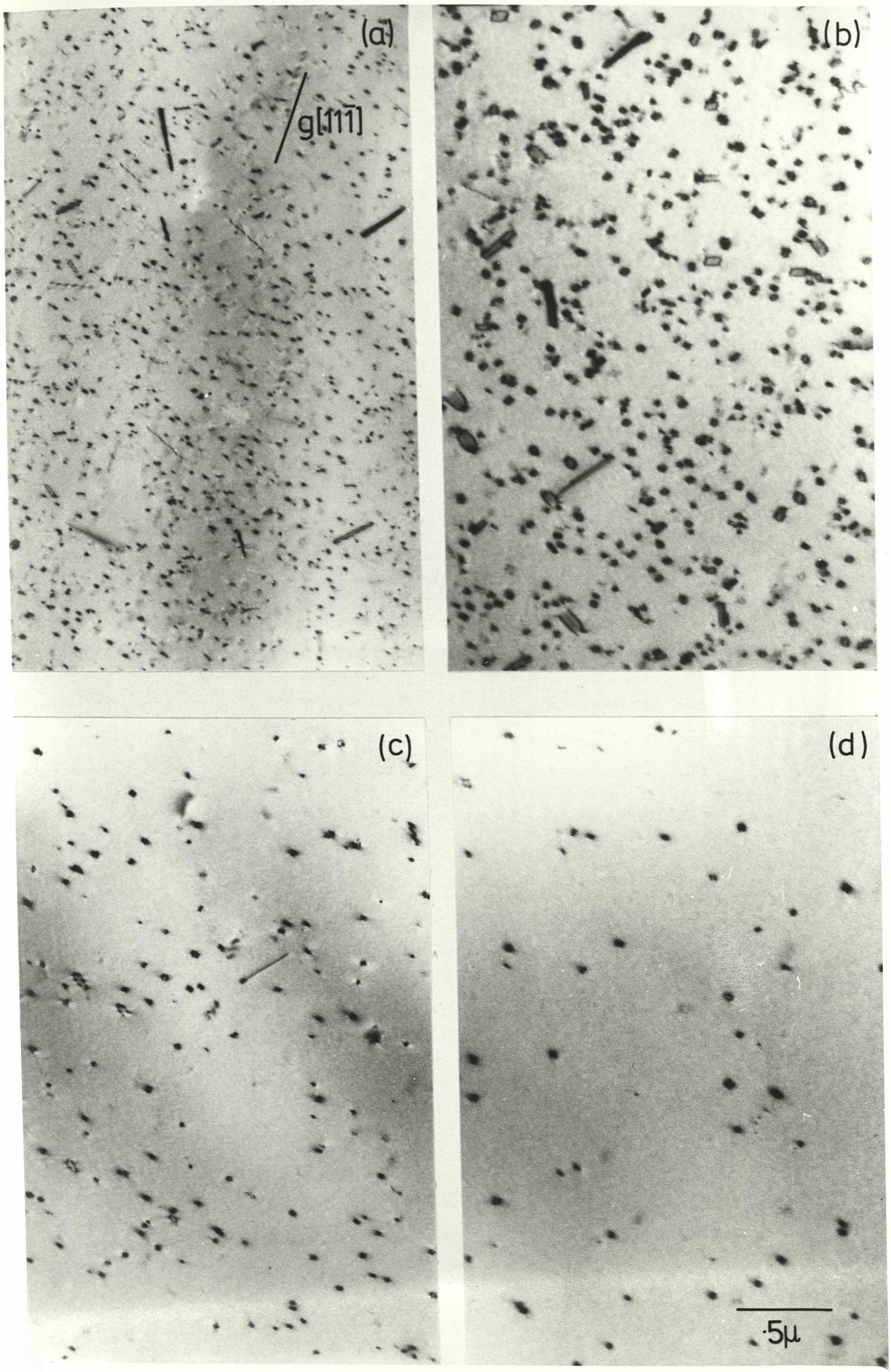
(a)
g[111]
(b)
(c)
(d)
·5μ

Fig. 5/36 Weak beam micrographs of elongated Frank loops in Cu 16% Al

(A) g $[1\bar{1}1]$ z [110] g/5g

(B) g $[1\bar{1}1]$ z [011] g/5g

Loop plane of T in (A) and (B) is (111) and parallel to the foil surface.

(C) g $[20\bar{2}]$ z [111] g/3g

Fig. 5/37 (A) g $[0\bar{2}2]$ z [011] g/3g

(B) g $[0\bar{2}2]$ z [111] g/3g

(C) g $[\bar{2}20]$ z [110] g/3g

(D) g $[20\bar{2}]$ z [010] g/3g

The loops in contrast are Frank loops on the inclined planes, but dissociating onto the (111) plane.

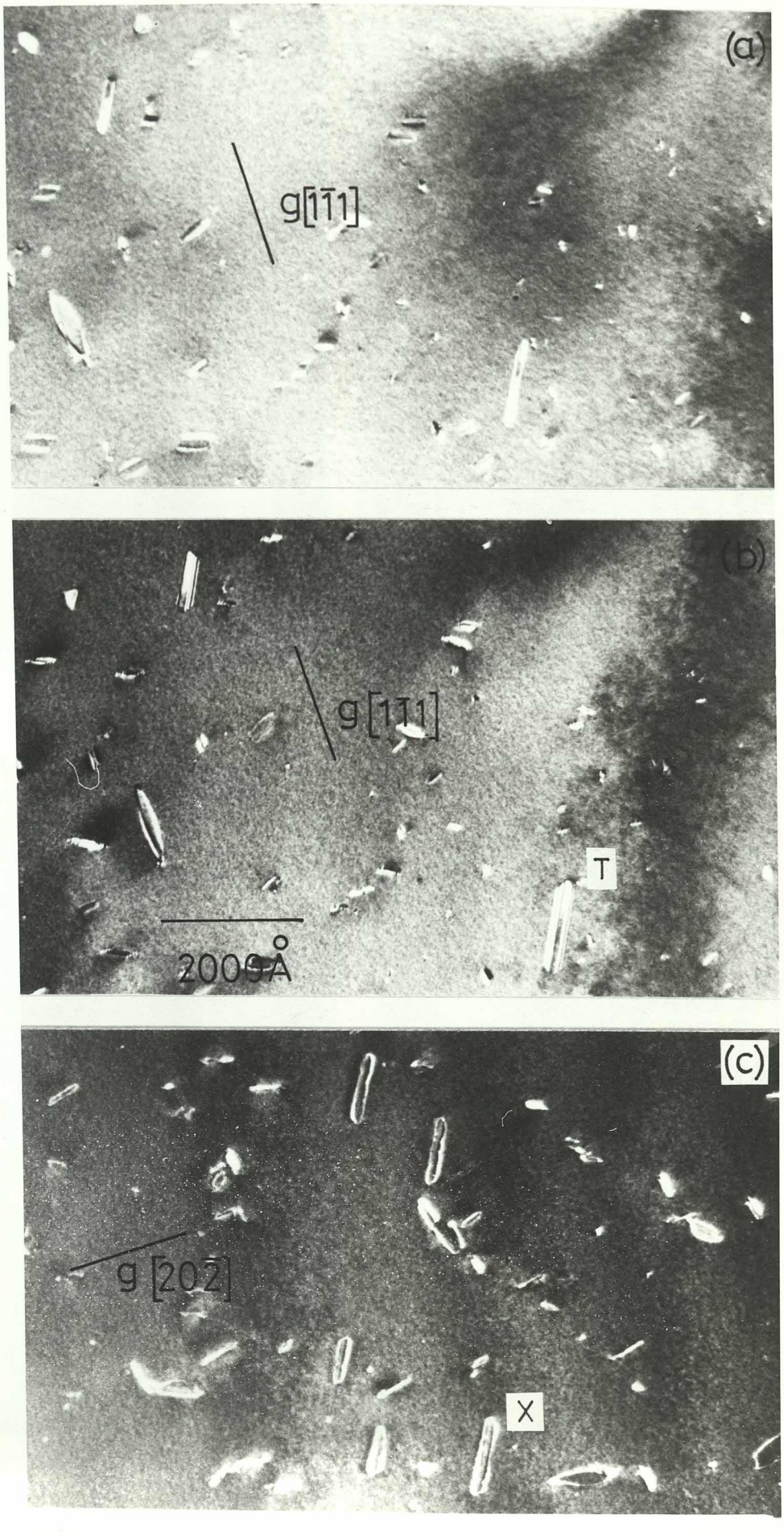

Fig.5/36

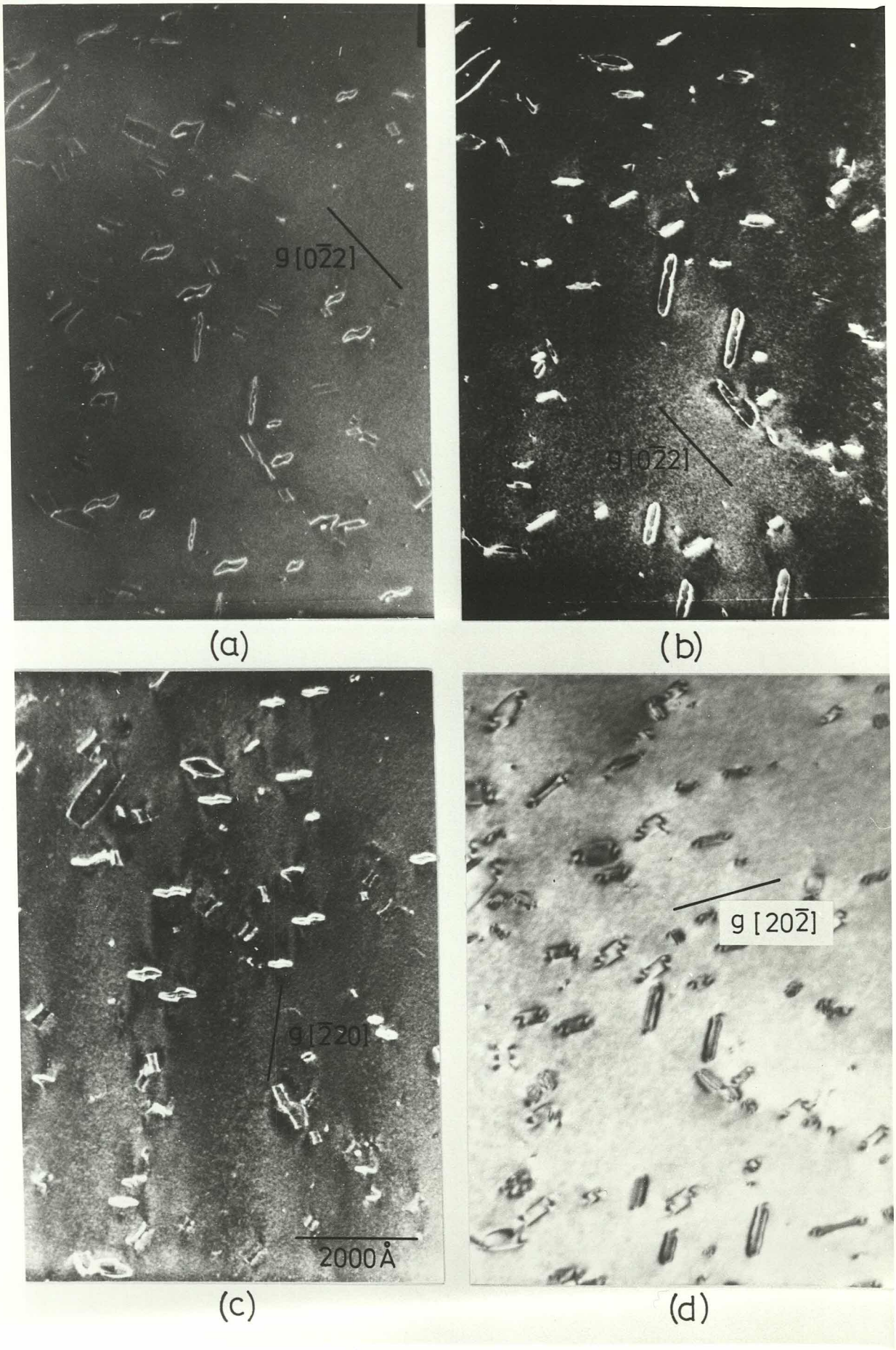

Fig.5/37

Fig. 6/1 Illustration of the differences in loop nature as a function of crystal growth rate for specimens of Cu 10% Al.

(A) A mixture of Frank and perfect loops during irradiation of a foil cut from a crystal grown at 2.2 cm./hr.

(B) Rhombus perfect loops as a result of irradiation of a foil cut from a crystal grown at 3 mm./hr.

Specimens polished at $-40^{\circ}C$ 4.4 volts
Irradiation temperature $\simeq 250^{\circ}C$
Dose rate $\simeq 6 \times 10^{18}$ el./cm.^{2}/sec.
Foil thickness $\simeq 2200\text{Å}$.

The parameters of the crystal growing furnace were unaltered, except for the change in pulling speed.


(a)
g[1$\bar{1}\bar{1}$]

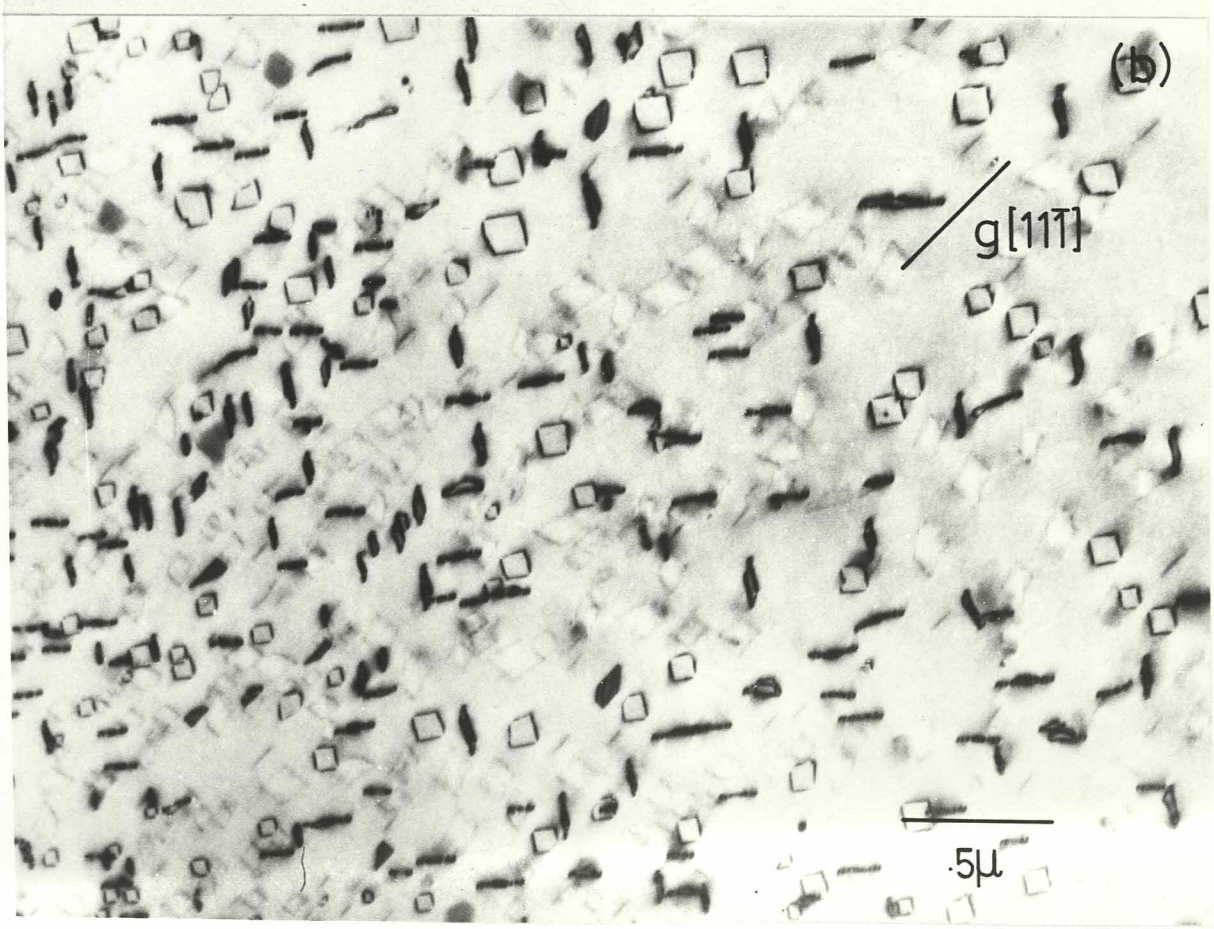
(b)
g[11$\bar{1}$]
.5μ

Fig. 7/1 shows the loop density measurements from an irradiated foil of Cu 16% Al. The lower graph illustrates the measured densities at the foil centre as a function of temperature, without taking into account the specimen surfaces.

The upper curve shows the bulk density calculated taking into account diffusion of point defects to the foil surfaces.

$g = 3.79 \times 10^{19}$ cm.$^{-3}$sec.$^{-1}$

$z = \langle 532 \rangle$

$\bar{g} = \langle 111 \rangle$

$t \simeq 6\xi_g$ (300 keV)

The specimens were annealed in the H.V.E.M. for 300 seconds at 380°C, prior to irradiation.

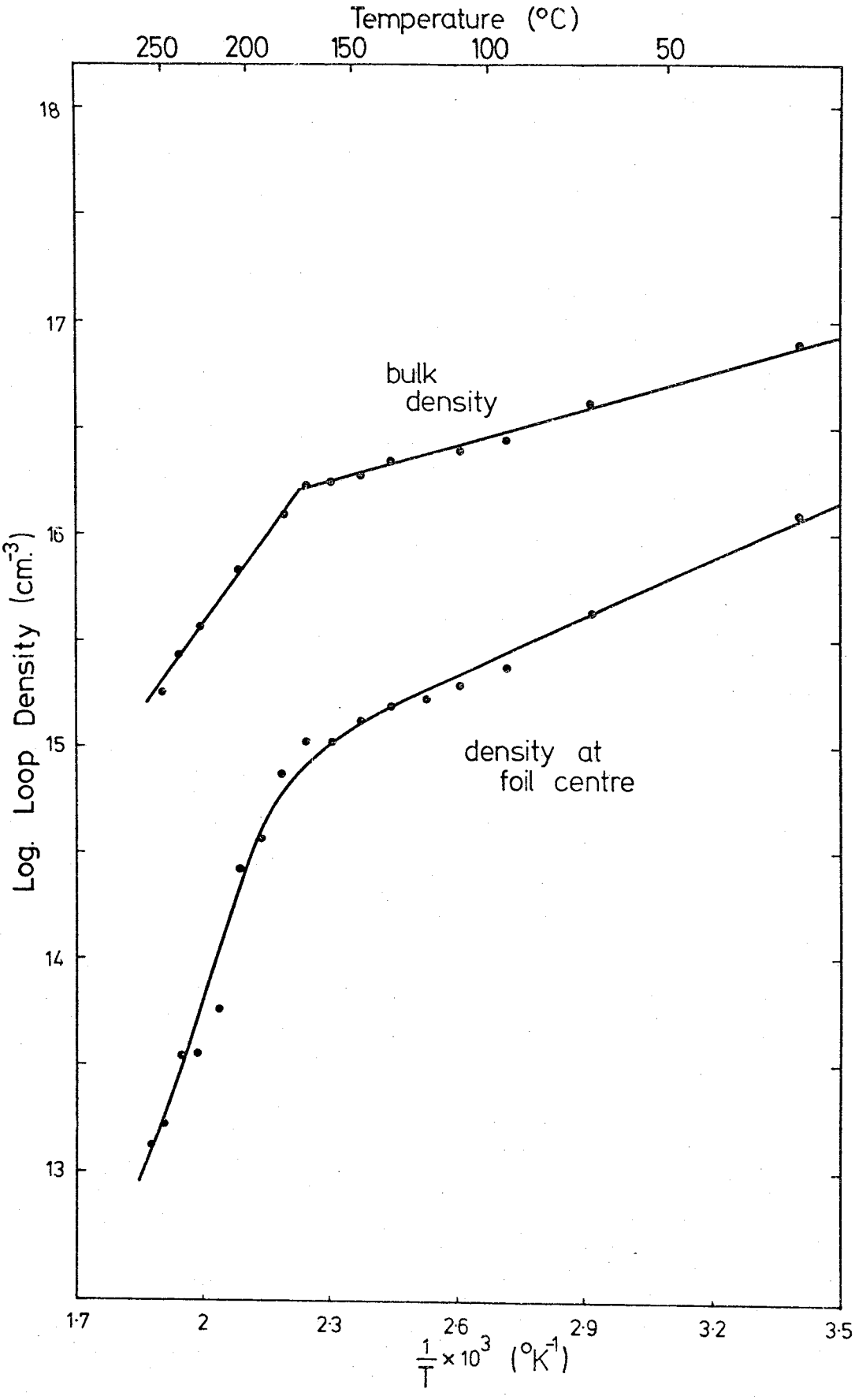
Temperature (°C)
250
200
150
100
50
18
17
16
15
14
13
Log. Loop Density (cm.$^{-3}$)
bulk
density
density at
foil centre
1·7
2
2·3
2·6
2·9
3·2
3·5
$\frac{1}{T} \times 10^3$ (°K^{-1})

Fig. 7/2 Ratios of loop densities $L(\infty, {}^{h}/2)$ and $L(\infty, av)$ at the centre of the foil and averaged throughout the foil respectively to $L(\infty, bulk)$, the corresponding value for bulk material, as a function of surface diffusion parameter P.

$$\text{Curve (A)} = \frac{\text{L Centre}}{\text{L Bulk}}$$

$$\text{Curve (B)} = \frac{\text{L Mean}}{\text{L Bulk}}$$

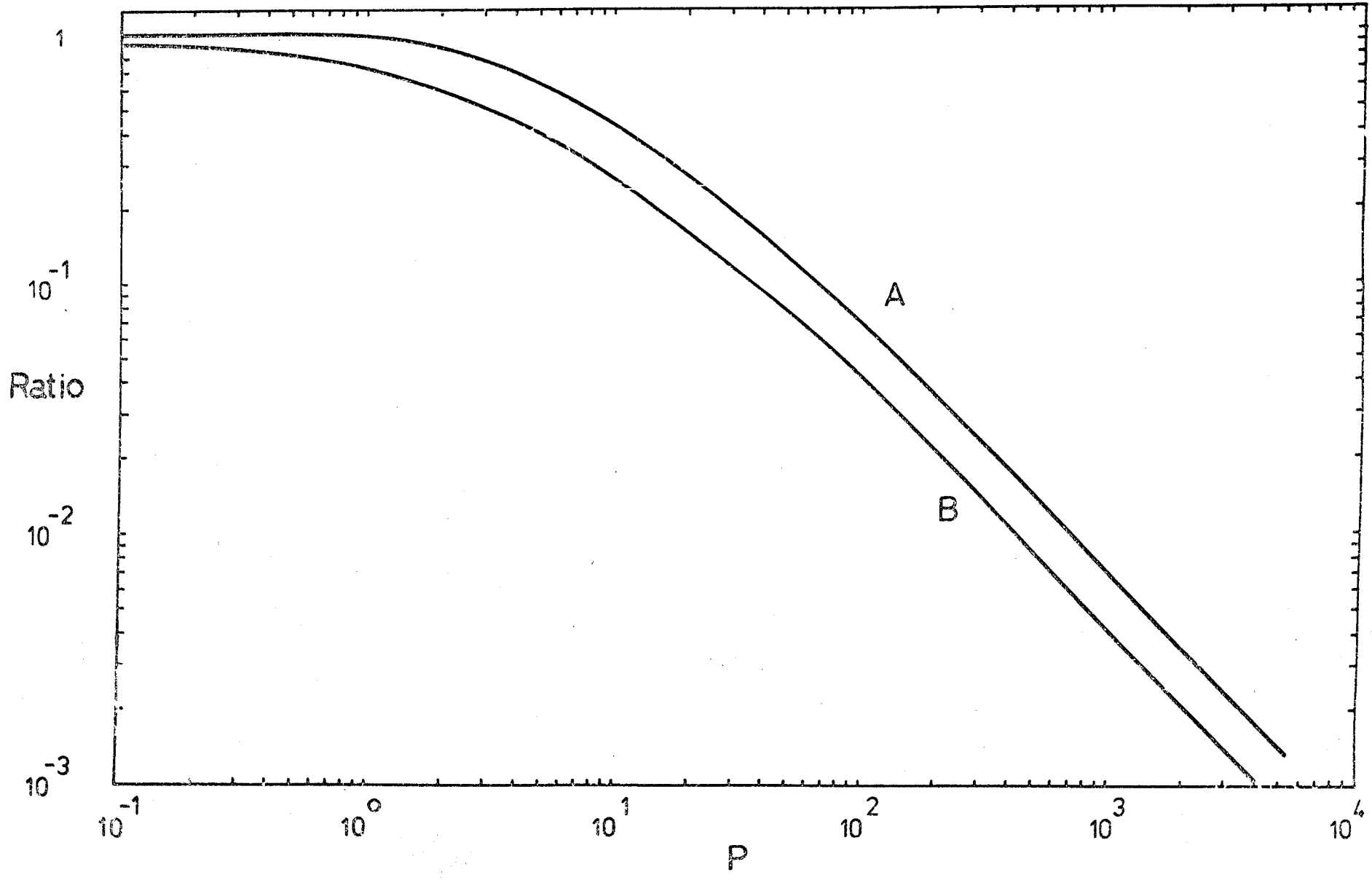
1
10^{-1}
10^{-2}
10^{-3}
Ratio
A
B
10^{-1}
10^{0}
10^{1}
10^{2}
10^{3}
10^{4}
P

Fig. 7/3 Graph shows the corrected and uncorrected loop densities as a function of specimen thickness, to test the validity of the Goringe correction factor.

(A) corrected loop density taking into account diffusion to the foil surface.

(B) uncorrected loop densities.

ξ_{111} = 340 Å measured at 300 keV.

All irradiations were performed at a temperature of 210°C and a dose rate of $g = 5.69 \times 10^{19}$ cm.$^{-3}$sec.$^{-1}$. The foil thickness was measured by counting 111 thickness fringes at 300 keV.

At foil thicknesses <1500 Å statistical error in counting causes fluctuations in the corrected loop densities.

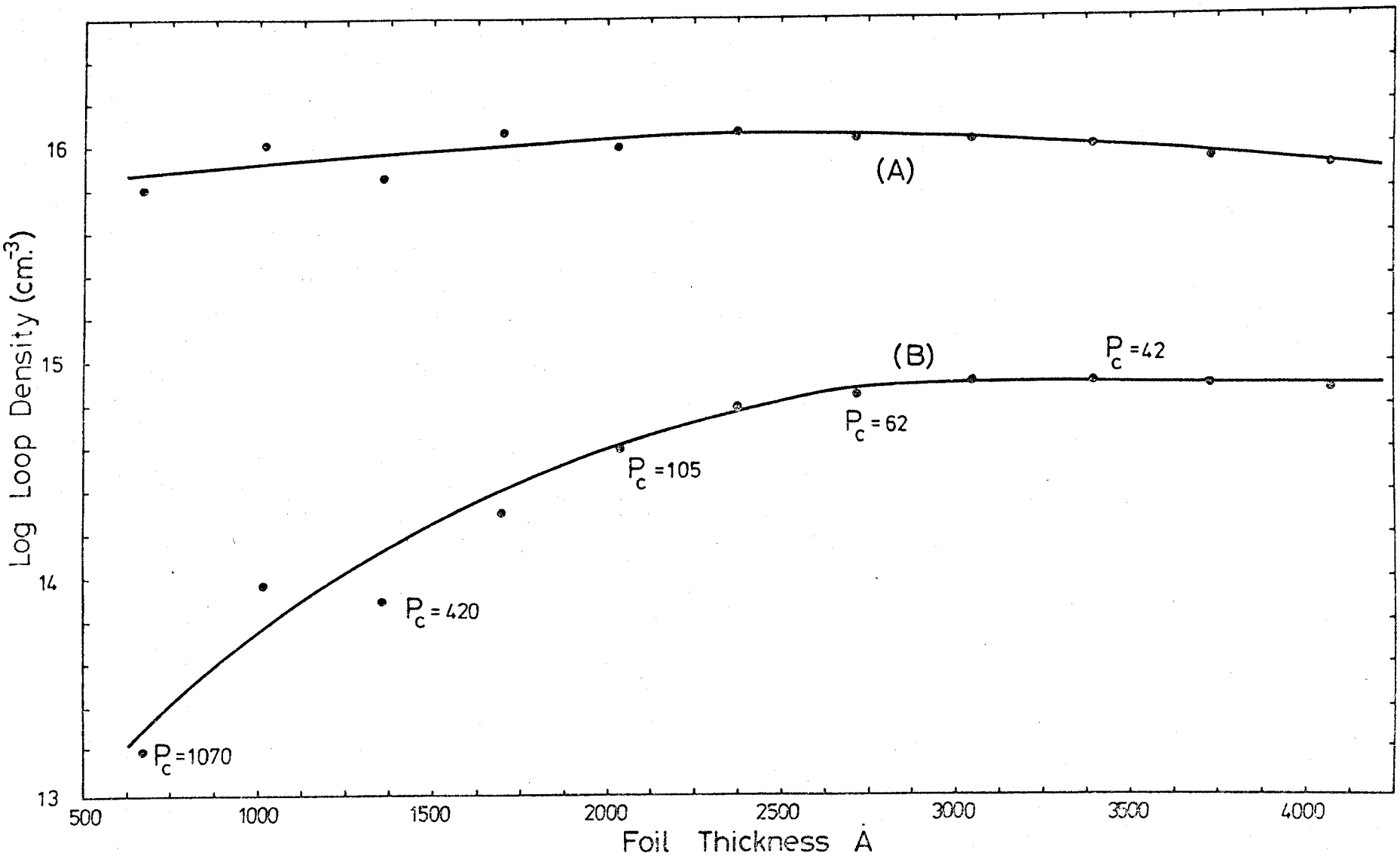
Log Loop Density (cm.$^{-3}$)
16
15
14
13
500
1000
1500
2000
2500
3000
3500
4000
Foil Thickness Å
(A)
(B)
P_c =42
P_c = 62
P_c =105
P_c = 420
P_c =1070

Fig. 7/4 Shows the relationship between loop density and diffusion parameter P.

The $L^{\infty} \alpha P^{-1}$ relationship is observed for bulk densities, while $L^{\infty} \alpha P^{-2}$ for loop densities at the foil centre.

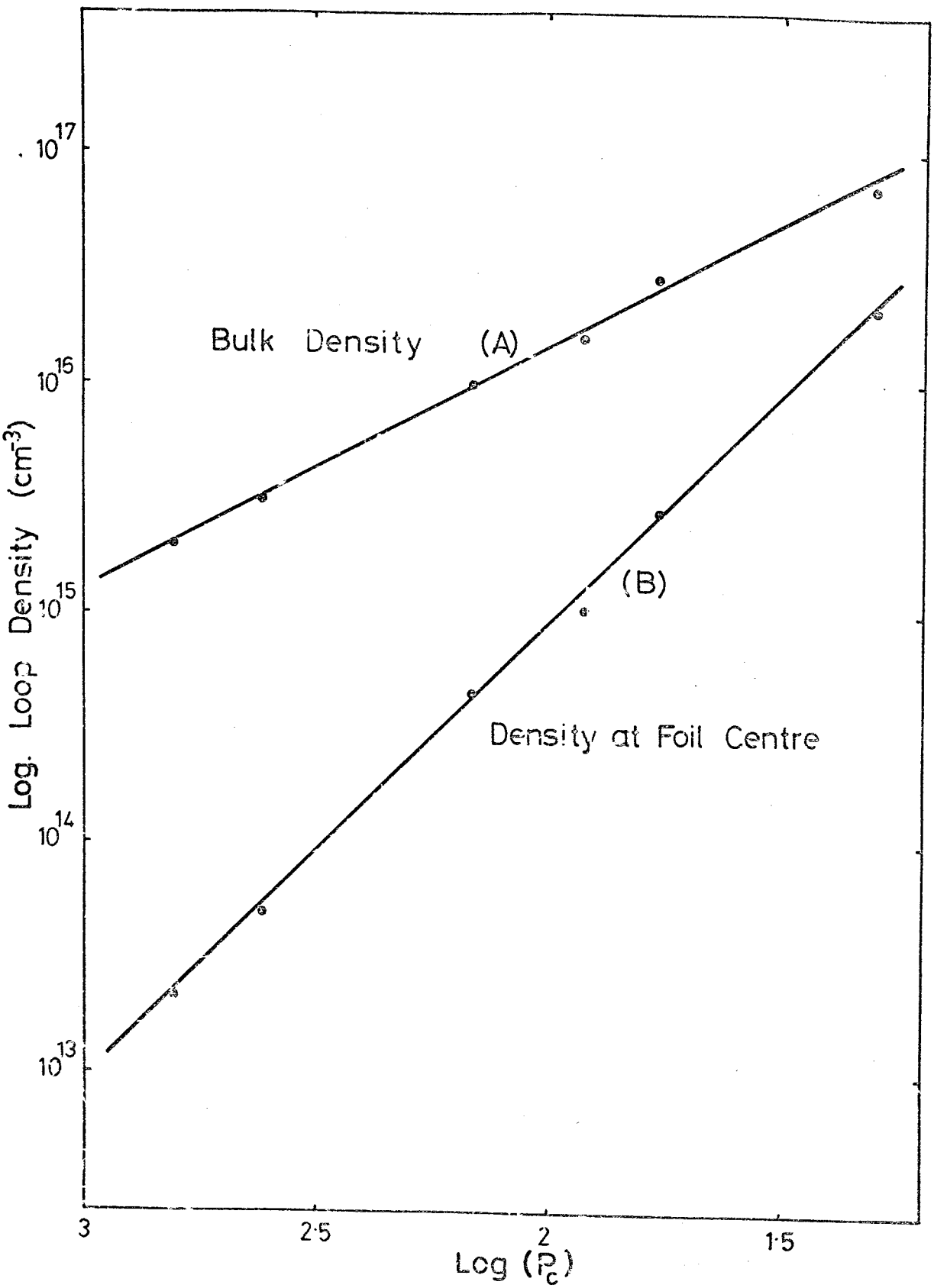
Bulk Density (A)
(B)
Density at Foil Centre
Log. Loop Density (cm⁻³)
10¹⁷
10¹⁶
10¹⁵
10¹⁴
10¹³
3
2·5
2
1·5
Log (Pc)

Fig. 7/5 Graph shows the relationship between loop density at the foil centre and foil thickness in order to achieve bulk conditions.

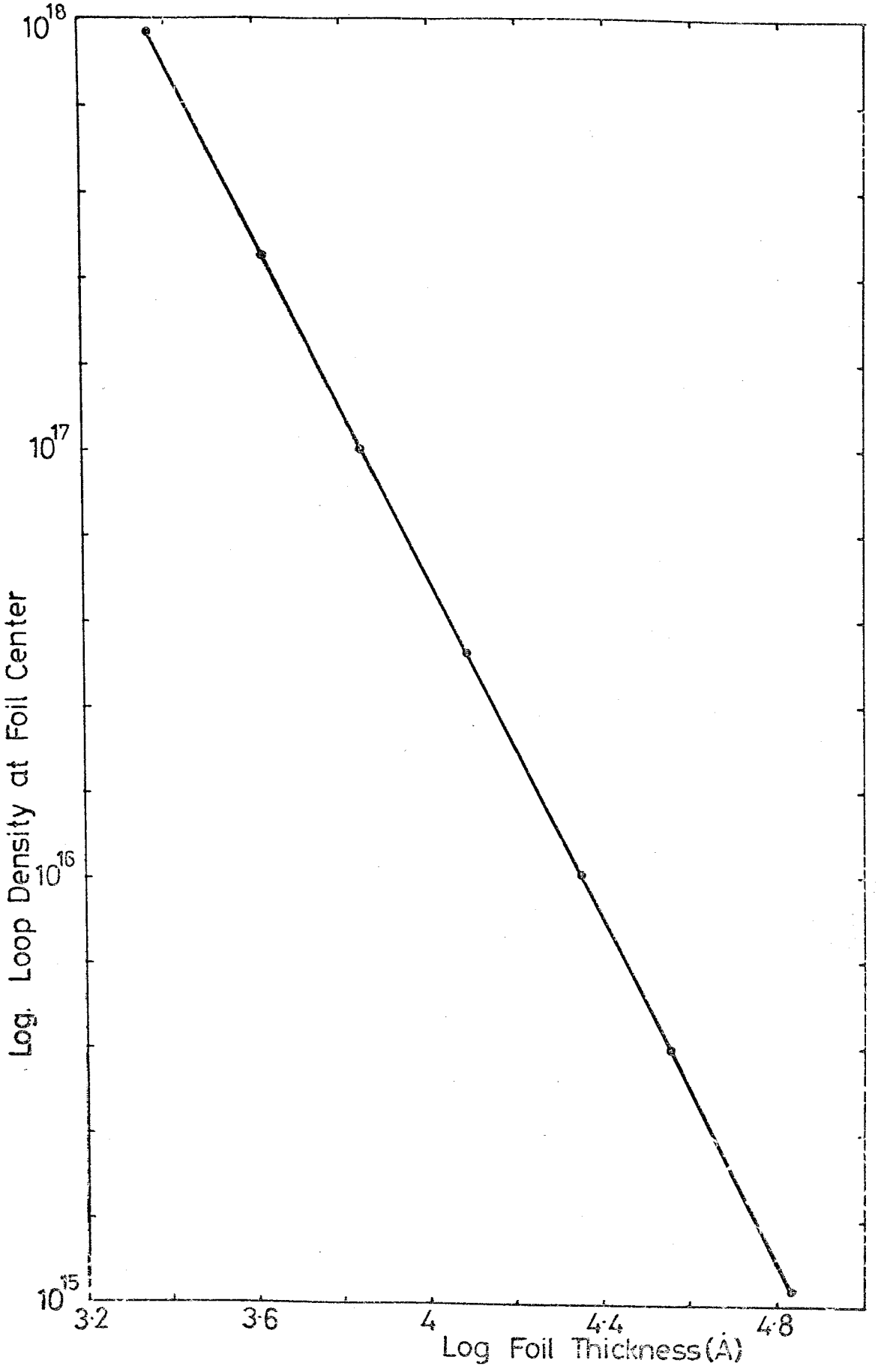
10^{18}
10^{17}
10^{16}
10^{15}
Log. Loop Density at Foil Center
3·2
3·6
4
4·4
4·8
Log Foil Thickness (Å)

Fig. 7/6 Irradiation temperature dependence of cluster density in copper and Cu·98% Al foils irradiated in the H.V.E.M.

The density measurements of Spring et al. are much lower and examination of their micrographs suggests the presence of a thick contamination layer, stressing the foil, and causing loop slippage to the foil surface.

The Cu.98% Al results do not appear to be impurity controlled.

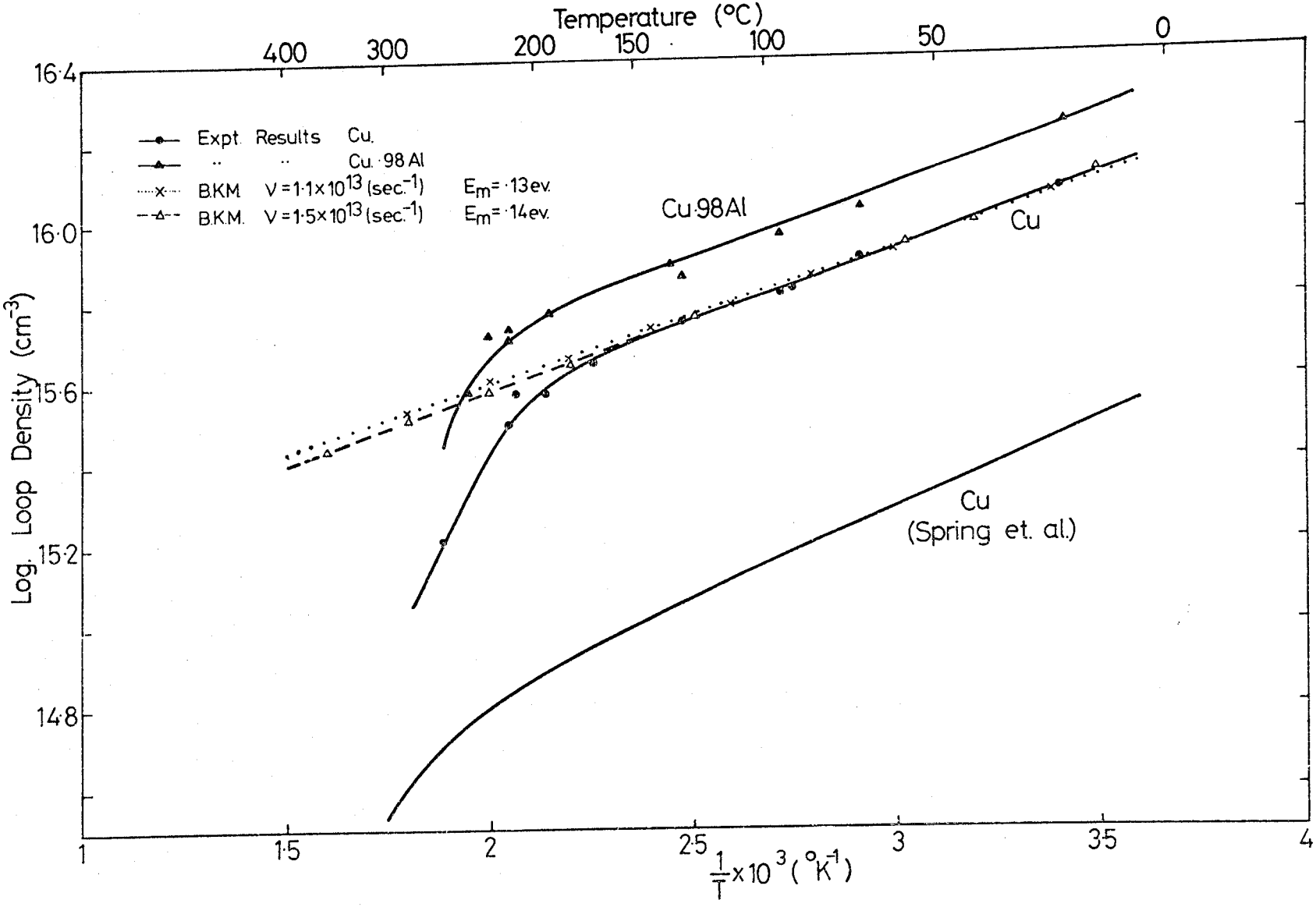
Temperature (°C)
400
300
200
150
100
50
0
16·4
16·0
15·6
15·2
14·8
Log. Loop Density (cm⁻³)
Expt. Results Cu.
" " Cu. ·98 Al
B.K.M. V = 1·1 × 10¹³ (sec.⁻¹) Em = ·13 ev.
B.K.M. V = 1·5 × 10¹³ (sec.⁻¹) Em = ·14 ev.
Cu·98Al
Cu
Cu
(Spring et. al.)
1
1·5
2
2·5
3
3·5
4
1/T × 10³ (°K⁻¹)

Fig. 7/7 Loop density as a function of temperature for foils of Cu 2% Al, after an in-situ anneal for 5 minutes at 380°C.

Results averaged over four specimens, with two separate runs on each.

Best theoretical B.K.M. fit + $\nu = 8.5 \times 10^{12}$ sec.$^{-1}$ $E_m = .13$ eV. $E_b = .11$ eV.

Best theoretical Bourret fit ∇ $\nu = 8.5 \times 10^{12}$ sec.$^{-1}$ $E_m + E_b = .24$ eV $E_{11} = .68$ eV.

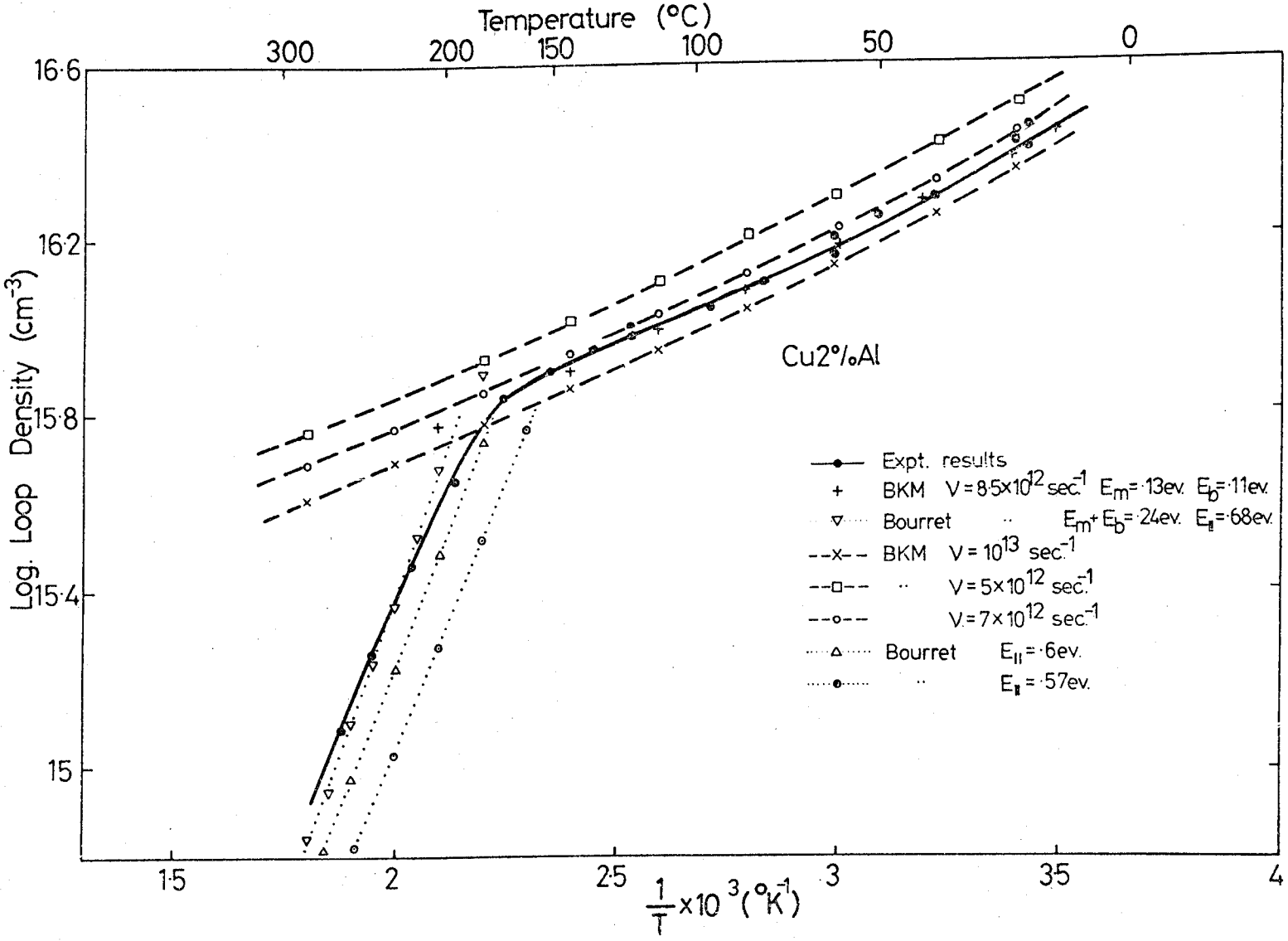
Temperature (°C)
300
200
150
100
50
0
16·6
16·2
15·8
15·4
15
Log. Loop Density (cm⁻³)
Cu2%Al
Expt. results
BKM V = 8·5×10¹² sec⁻¹ Em = ·13ev. Eb = ·11ev.
Bourret " Em + Eb = ·24ev. Eii = ·68ev.
BKM V = 10¹³ sec⁻¹
" V = 5×10¹² sec⁻¹
V = 7×10¹² sec⁻¹
Bourret Eii = ·6ev.
" Eii = ·57ev.
1·5
2
2·5
3
3·5
4
1/T ×10³ (°K⁻¹)

Fig. 7/8 Relationship of loop density to temperature for foils of Cu 5% Al showing the effects of hydrogen gas on the nucleation of defects.

(A) foils polished at $-50^{\circ}C$ 5.2 volts with no anneal.

(B) foil polished $-45^{\circ}C$ 4.4 volts with no anneal, first irradiation at $240^{\circ}C$.

(C) foils annealed for 5 minutes at $380^{\circ}C$ in the H.V.E.M.

(D) dramatic reduction in loop density due to diffusion to the foil surface and the dissociation of di-interstitials.

(E) specimen polished at $-50^{\circ}C$ 5.2 volts and annealed for 8 minutes at $290^{\circ}C$.

- ⊛ experimental results
- × best B.K.M. theoretical fit $\nu = 5 \times 10^{12}$ sec.$^{-1}$ $E_m + E_b = .24$ eV.
- □ Bourret theoretical fit $\nu = 5 \times 10^{12}$ sec.$^{-1}$ $E_{11} = .6$ eV.
- ∇ Bourret theoretical fit $\nu = 5 \times 10^{12}$ sec.$^{-1}$ $E_{11} = .57$ eV.
- Δ Bourret theoretical fit $\nu = 5 \times 10^{12}$ sec.$^{-1}$ $E_{11} = .52$ eV
- o best Bourret theoretical fit $\nu = 5 \times 10^{12}$ sec.$^{-1}$ $E_m + E_b = .24$ $E_{11} = .66$ eV.

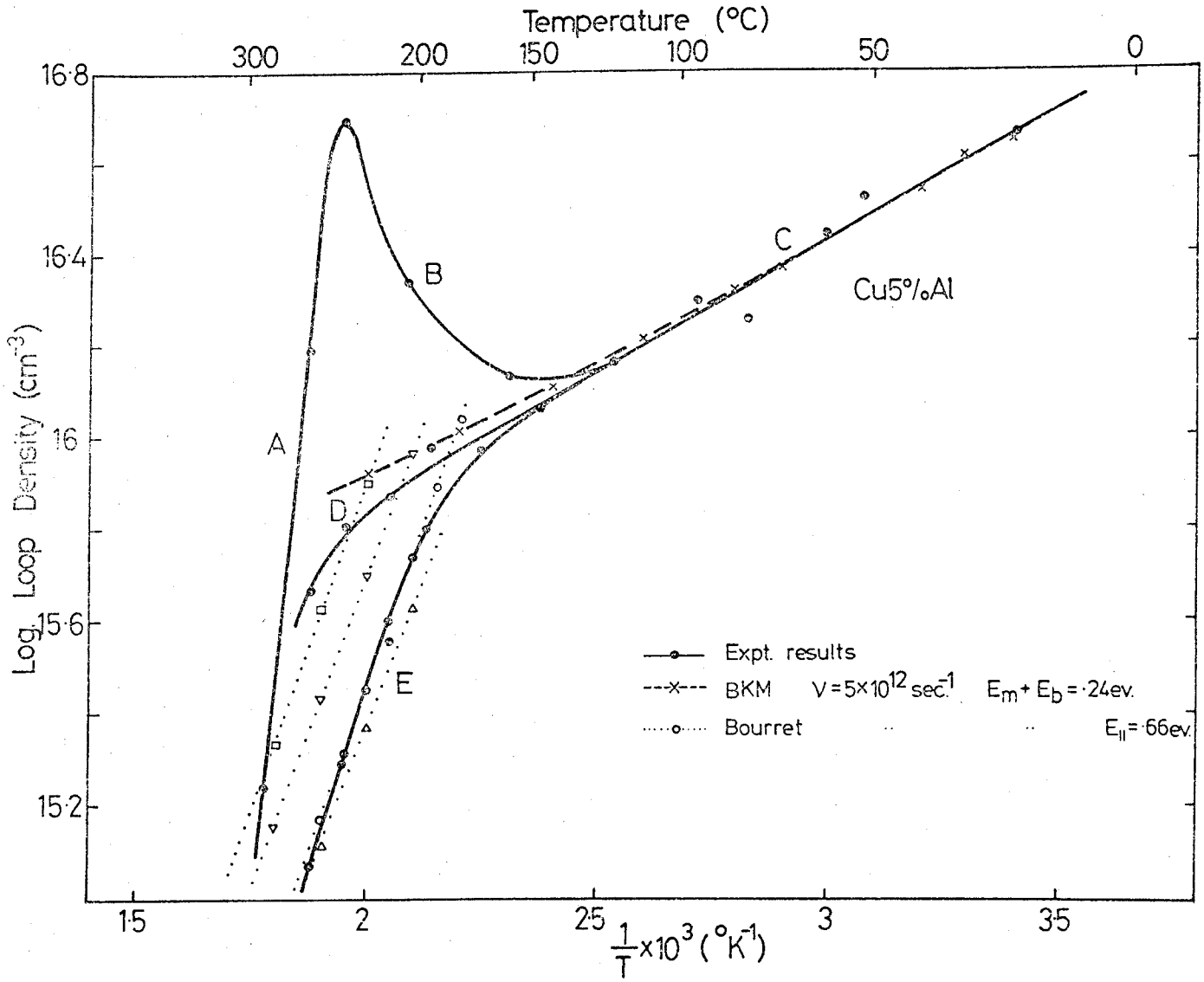
Temperature (°C)
300
200
150
100
50
0
16·8
16·4
16
15·6
15·2
Log Loop Density (cm⁻³)
A
B
C
D
E
Cu5%Al
Expt. results
BKM V=5×10¹² sec⁻¹ Em+Eb=·24ev.
Bourret Eii=·66ev.
1·5
2
2·5
3
3·5
1/T ×10³ (°K⁻¹)

Fig. 7/9 Plot of loop density versus anneal time at an anneal temperature of 240°C.

Cu 16% Al foil polished at -35°C 4.4 volts.

Adjacent areas of foil were irradiated under similar conditions. The reduction in loop density was due to the diffusion of hydrogen gas out of the specimen during the anneals between irradiations.

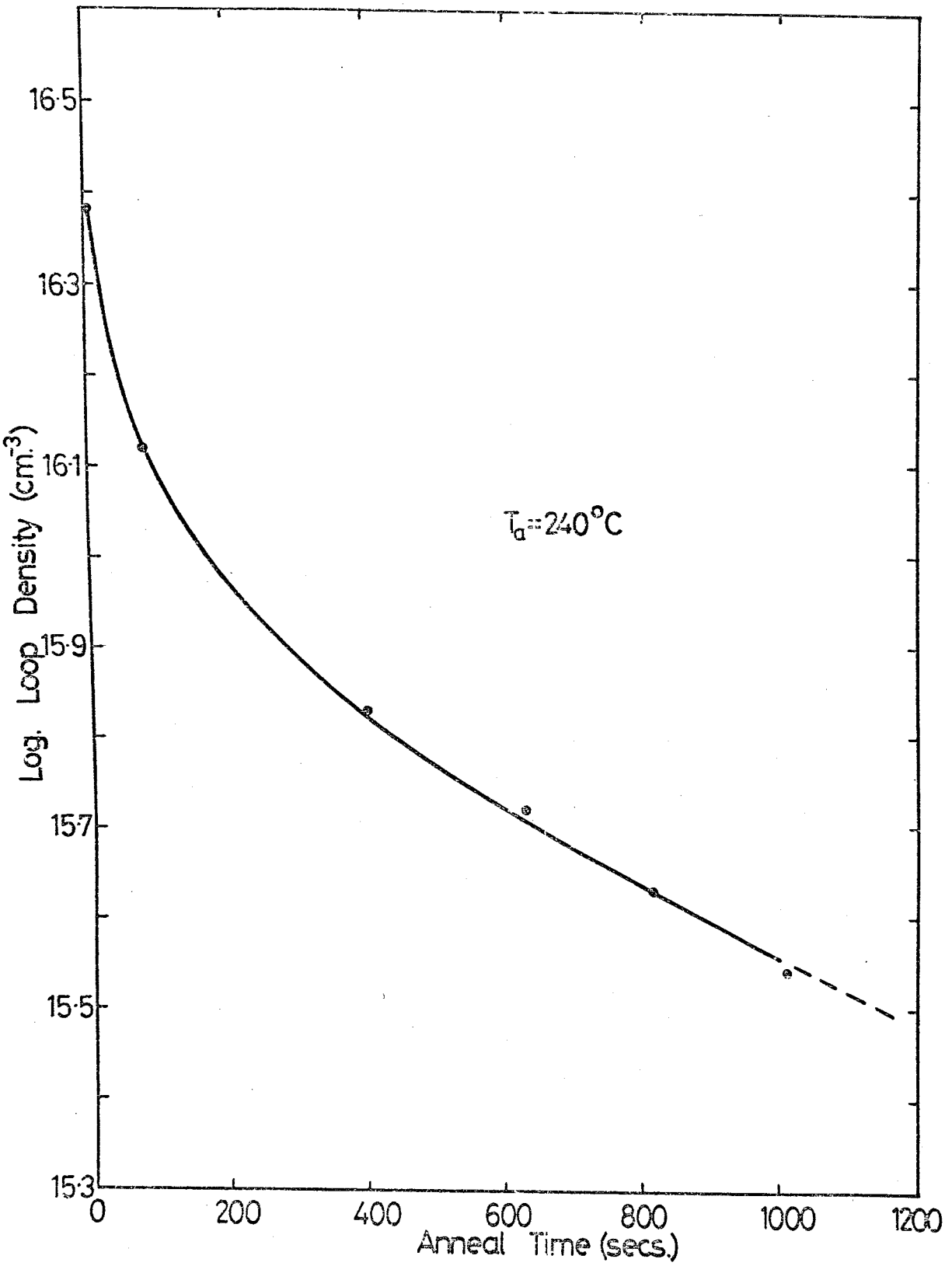
16·5
16·3
16·1
15·9
15·7
15·5
15·3
Log. Loop Density (cm.$^{-3}$)
T_a=240°C
0
200
400
600
800
1000
1200
Anneal Time (secs.)

Fig. 7/10 Graph shows loop densities versus temperature for foils of Cu 16% Al after having been annealed for 5 minutes at 380° in the H.V.E.M. generation rate $\simeq 3.8 \times 10^{19}$ cm.$^{-3}$ sec.$^{-1}$.

Measured gradient $E_{11} = .63$ eV.

$E_m + E_b = .23$ eV.

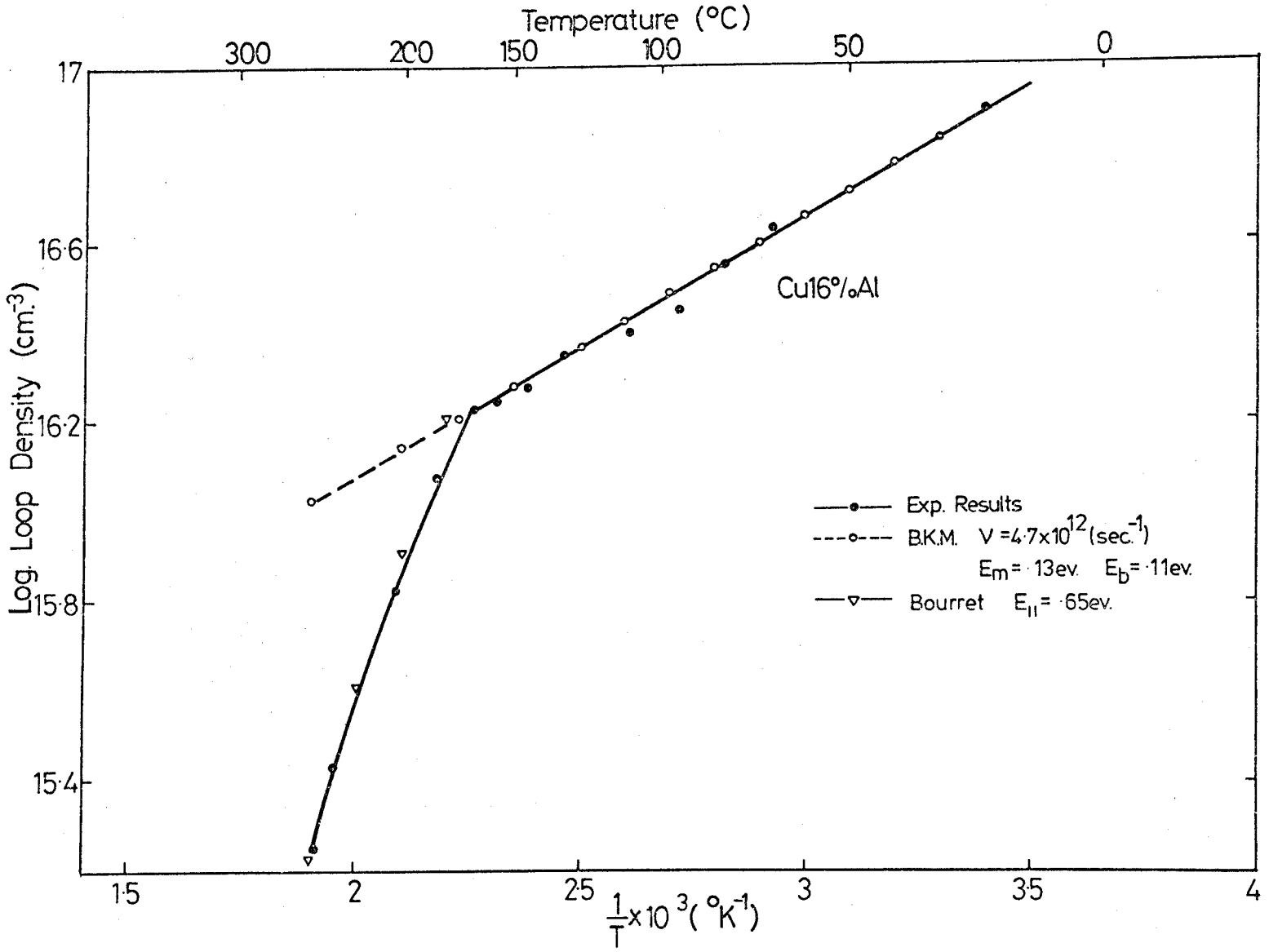
Temperature (°C)
300
200
150
100
50
0
17
16·6
16·2
15·8
15·4
Log. Loop Density (cm.⁻³)
Cu16°/₀Al
Exp. Results
B.K.M. V =4·7x10¹² (sec.⁻¹)
Em = ·13ev. Eb = ·11ev.
Bourret E11 = ·65ev.
1·5
2
2·5
3
3·5
4
1/T x 10³ (°K⁻¹)

Fig. 7/11 Graph demonstrates the relationship of loop density to square root of impurity concentration, to verify the equation

$$\frac{dl^{\infty}}{d(n^{\frac{1}{2}})} = 2.9 \left(\frac{g}{2\nu}\right)^{\frac{1}{2}} \exp\left(\frac{E_m + E_b}{2kT}\right)$$

ν measured as 3.95×10^{12} sec.$^{-1}$ at T = 293°K.
ν measured as 4.82×10^{12} sec.$^{-1}$ at T = 393°K.

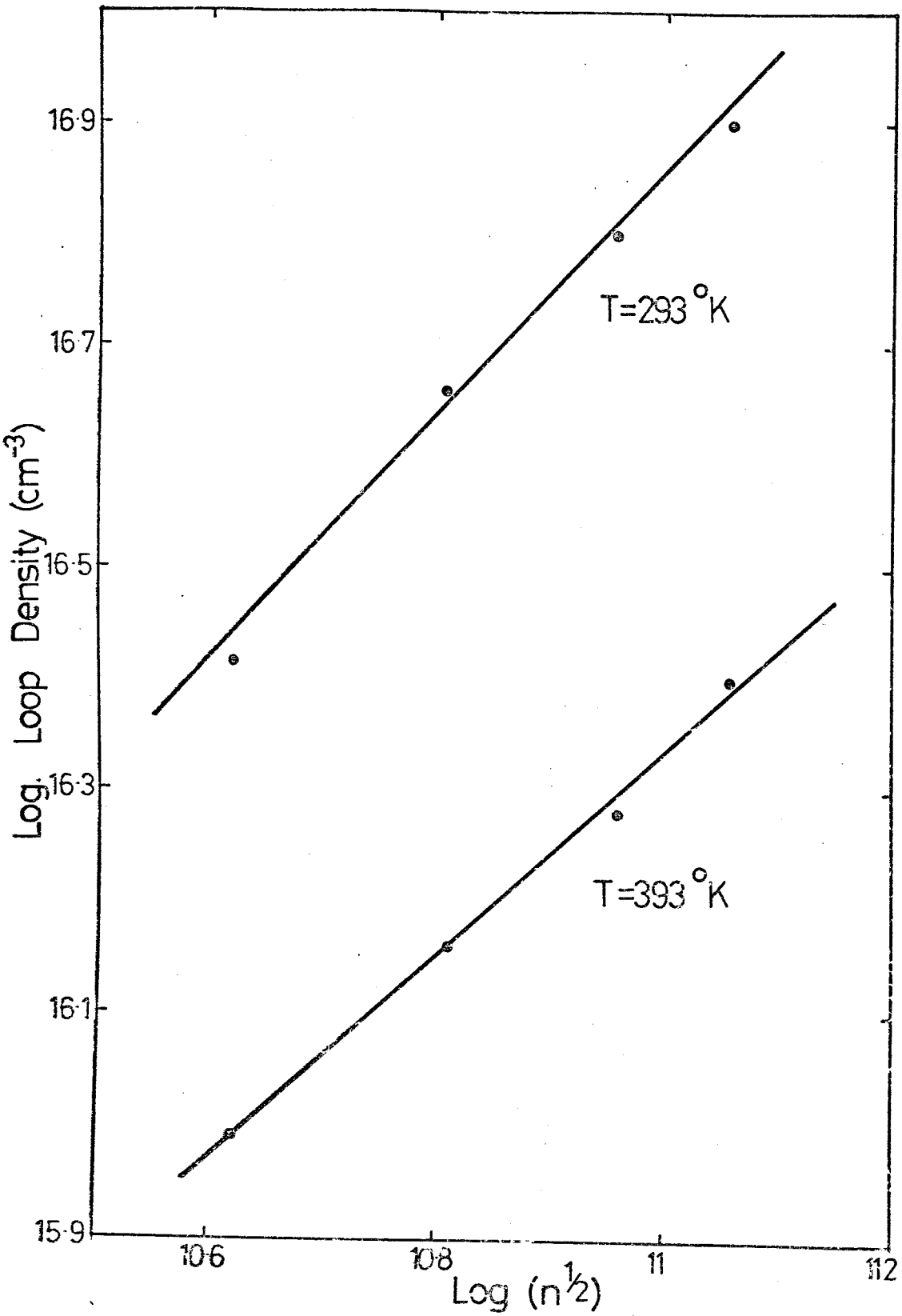
16·9
16·7
16·5
16·3
16·1
15·9
Log. Loop Density (cm⁻³)
T=293 °K
T=393 °K
10·6
10·8
11
11·2
Log (n½)

Fig. 7/12 Graph shows the corrected interstitial speed as a function of temperature, and alloy concentration.

Foils of Cu, Cu 2% Al and Cu 16% Al annealed at 380°C for five minutes, before irradiation.

Cu 5% Al curve (A) -50°C 5.2 volts. 8 minutes anneal at 290°C.

(B) -45°C 4.4 volts annealed for 5 minutes at 380°C

(C) -50°C 5.2 volts no anneal.

(D) -45°C 4.4 volts no anneal.

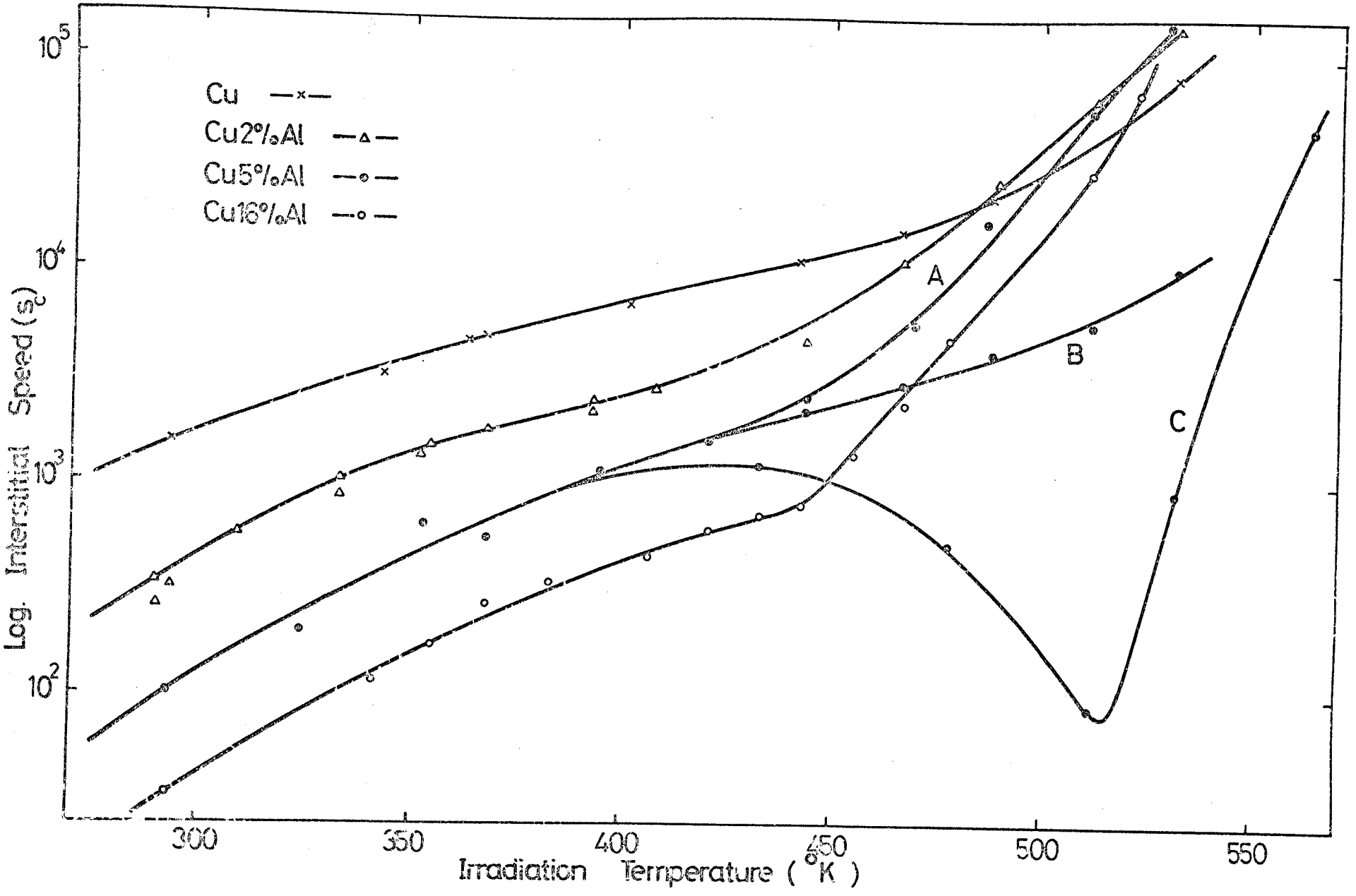
Cu —×—
Cu2%Al —△—
Cu5%Al —⊙—
Cu16%Al —○—
A
B
C
10^5
10^4
10^3
10^2
Log. Interstitial Speed (s_c)
300
350
400
450
500
550
Irradiation Temperature (°K)

Fig. 7/13 Graphs shows a plot $\ln\sqrt{S}$ versus $\frac{1}{T}$. An average of many results has been used to make up each curve. All specimens annealed in the H.V.E.M. at 380°C for 5 minutes. Generation rate $\simeq 3.79 \times 10^{19}$ cm.$^{-3}$ sec.$^{-1}$.

The gradients are $\simeq \frac{1}{2}$, except in copper 2% aluminium.

where region (A) is impurity controlled

(B) as for copper (not impurity controlled)

(C) di-interstitial dissociation.

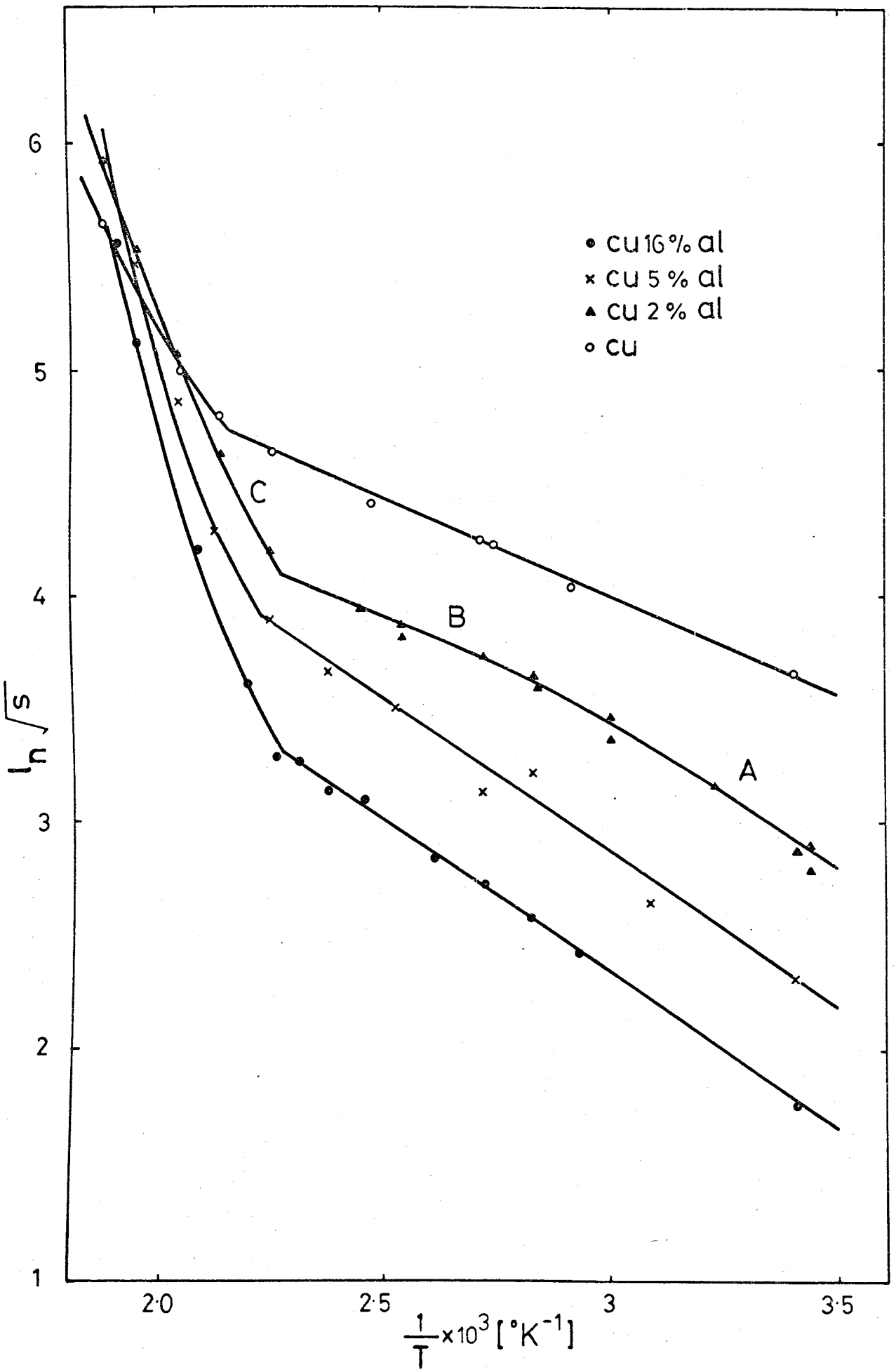
• cu 16 % al
× cu 5 % al
▲ cu 2 % al
○ cu
A
B
C
6
5
4
3
2
1
2·0
2·5
3
3·5
ln √S
1/T x10³ [°K⁻¹]

Fig. 7/14 Graph shows the loop density versus alloy concentration.

(A) loop density not impurity controlled

(B) transition from intrinsic to extrinsic behaviour

(C) impurity controlled.

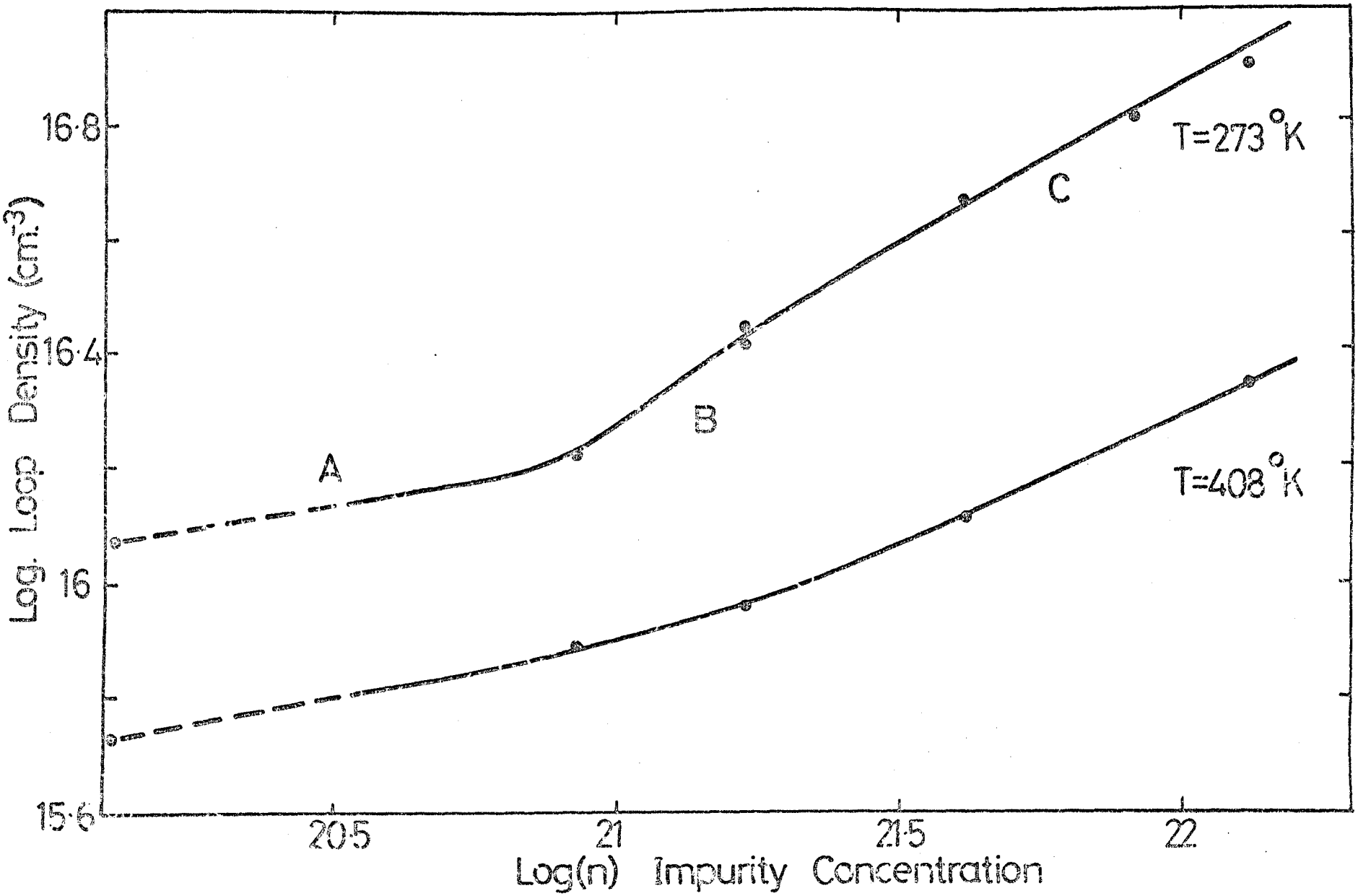
16·8
16·4
16
15·6
Log. Loop Density (cm⁻³)
A
B
C
T=273°K
T=408°K
20·5
21
21·5
22
Log(n) Impurity Concentration

Fig. 7/15 Relationship of loop density to generation rate for an annealed Cu 10% Al foil irradiated at $383^{o}K$.

(A) high density caused by nucleation on impurities

(B) $l^{\infty} \alpha g^{\frac{1}{2}}$.

(C) saturation due to (1) loop agglomeration

(2) temperature rise of specimen caused by beam

(3) effect of objective aperture

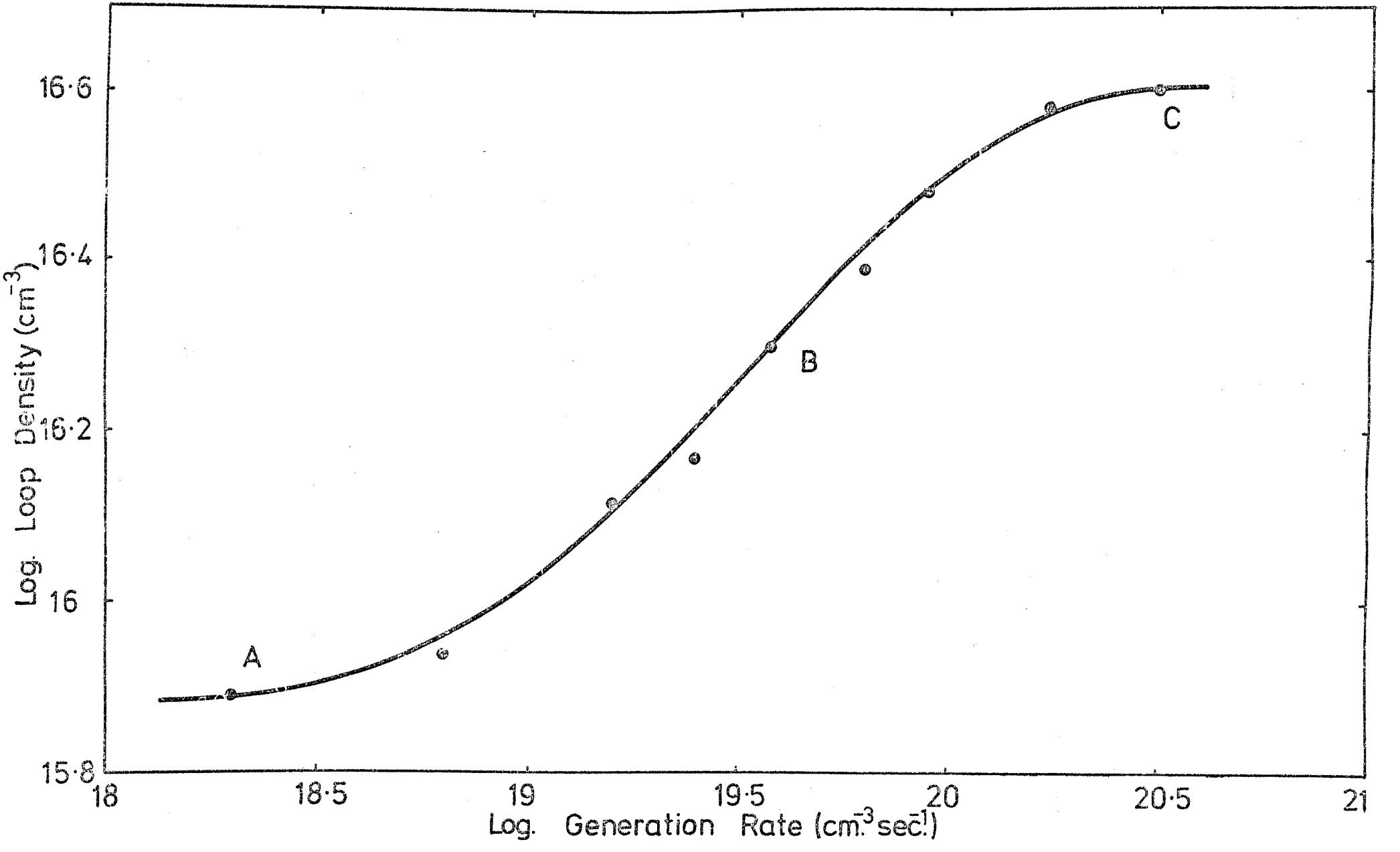
16·6
16·4
16·2
16
15·8
Log. Loop Density (cm^{-3})
A
B
C
18
18·5
19
19·5
20
20·5
21
Log. Generation Rate ($cm^{-3} sec^{-1}$)

Fig. 7/16 Dependence of loop density on irradiation temperature for foils of Cu 16% Al.

Specimens were cut from slow grown crystals and annealed for 300 seconds at 380°C in the H.V.E.M. prior to irradiation.

(A) $T_i = 20^{\circ}C$
(B) $T_i = 90^{\circ}C$
(C) $T_i = 200^{\circ}C$
(D) $T_i = 250^{\circ}C$

Only rhombus loops with $b = \frac{a}{2}\langle 110\rangle$ were observed

(a)
g[1$\bar{1}$1]

(b)

(c)

(d)
·5μ

Fig. 7/17 Loop density dependence on impurity concentration at a constant temperature of irradiation ($T_i \simeq 210^{\circ}C$) dose rate $\simeq 6 \times 10^{18}$ el./cm.^{2}/sec.

(a) Copper

(b) Cu 2% Al

(c) Cu 5% Al

(d) Cu 16% Al.

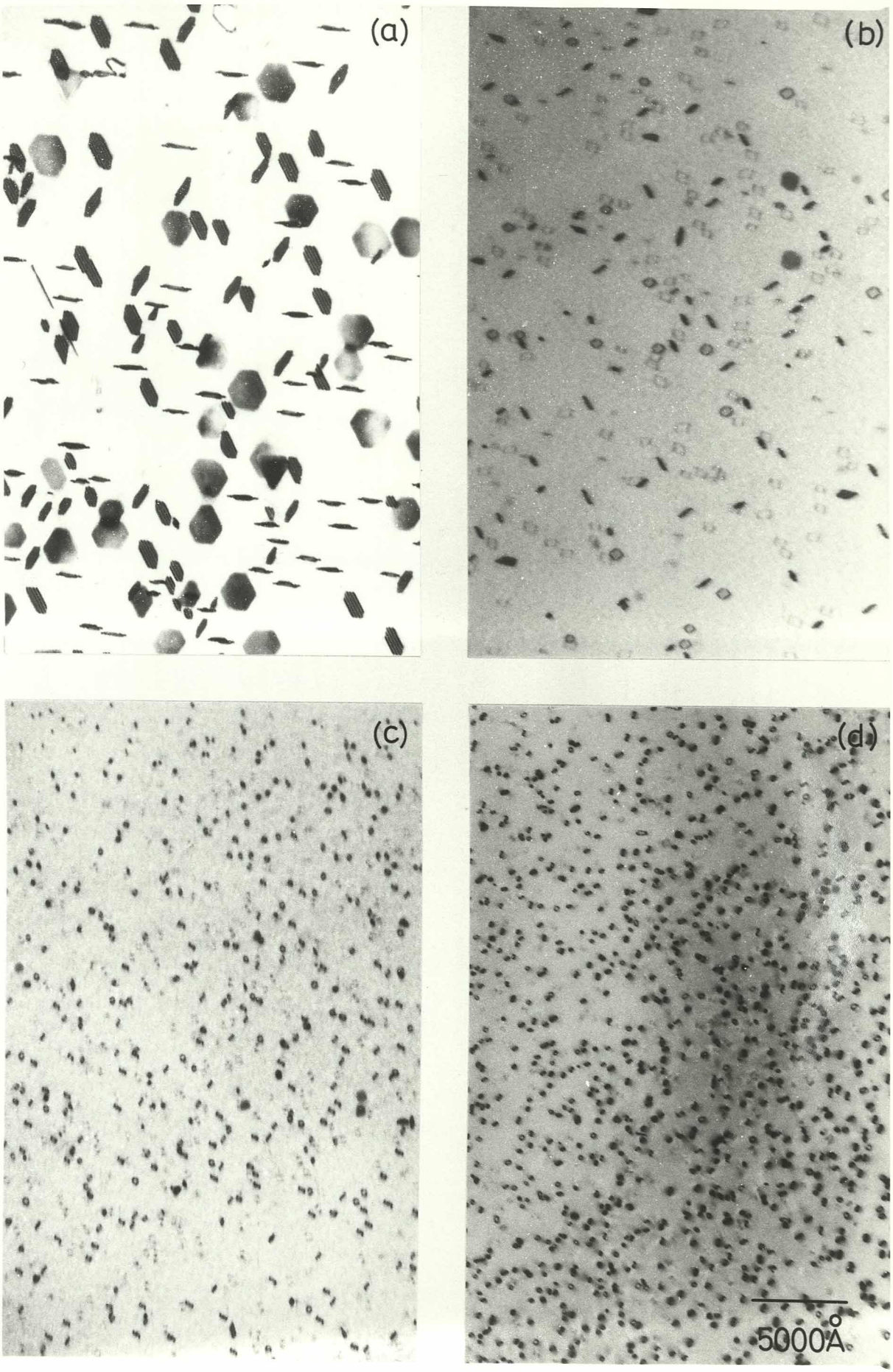
(a)
(b)
(c)
(d)
5000Å

Fig. 7/18 gives information on the asymptotic depth distribution of loops $l(\infty,z)$ with surface diffusion coefficient P as parameter.

From this figure, it may be seen that the shape of the curve is sensitive to the value of P when the latter has a value near unity and is relatively insensitive elsewhere.

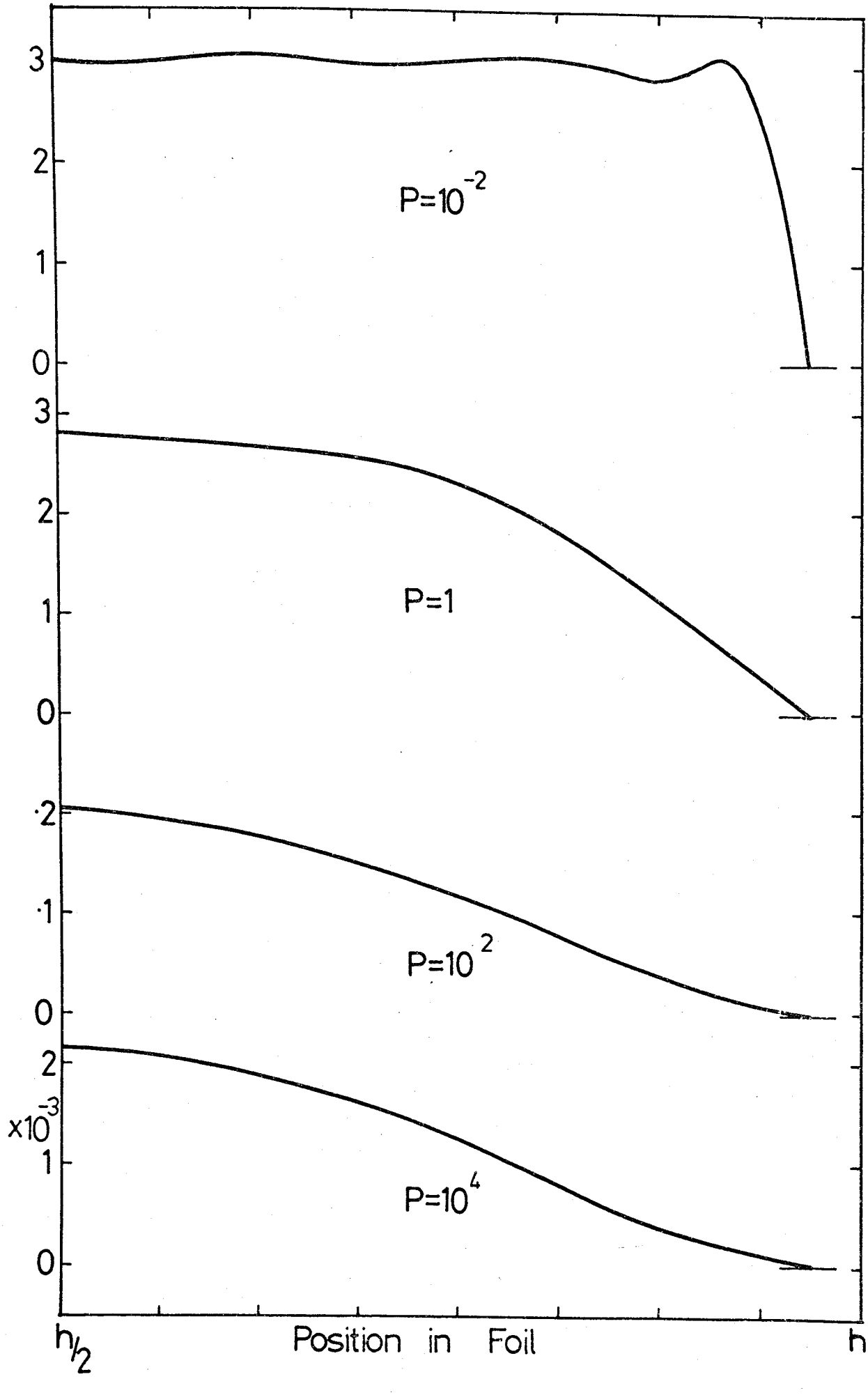
3
2
1
0
P=10^-2
3
2
1
0
P=1
·2
·1
0
P=10^2
2
x10^-3
1
0
P=10^4
h/2
Position in Foil
h

Fig. 7/19 Graphs shows the denuded zone (defined as the region at the foil surface containing 5% of the total number of loops) as a function of temperature, for Cu/Al alloys. Theoretical denuded zones obtained by comparison of mean density and density at foil centre from Goringe's diffusion calculations are also included.

o × are experimental values from stereo measurements.

● ▲ are the denuded zones used to obtain equal loop densities using l_{mean} and l_{centre}.

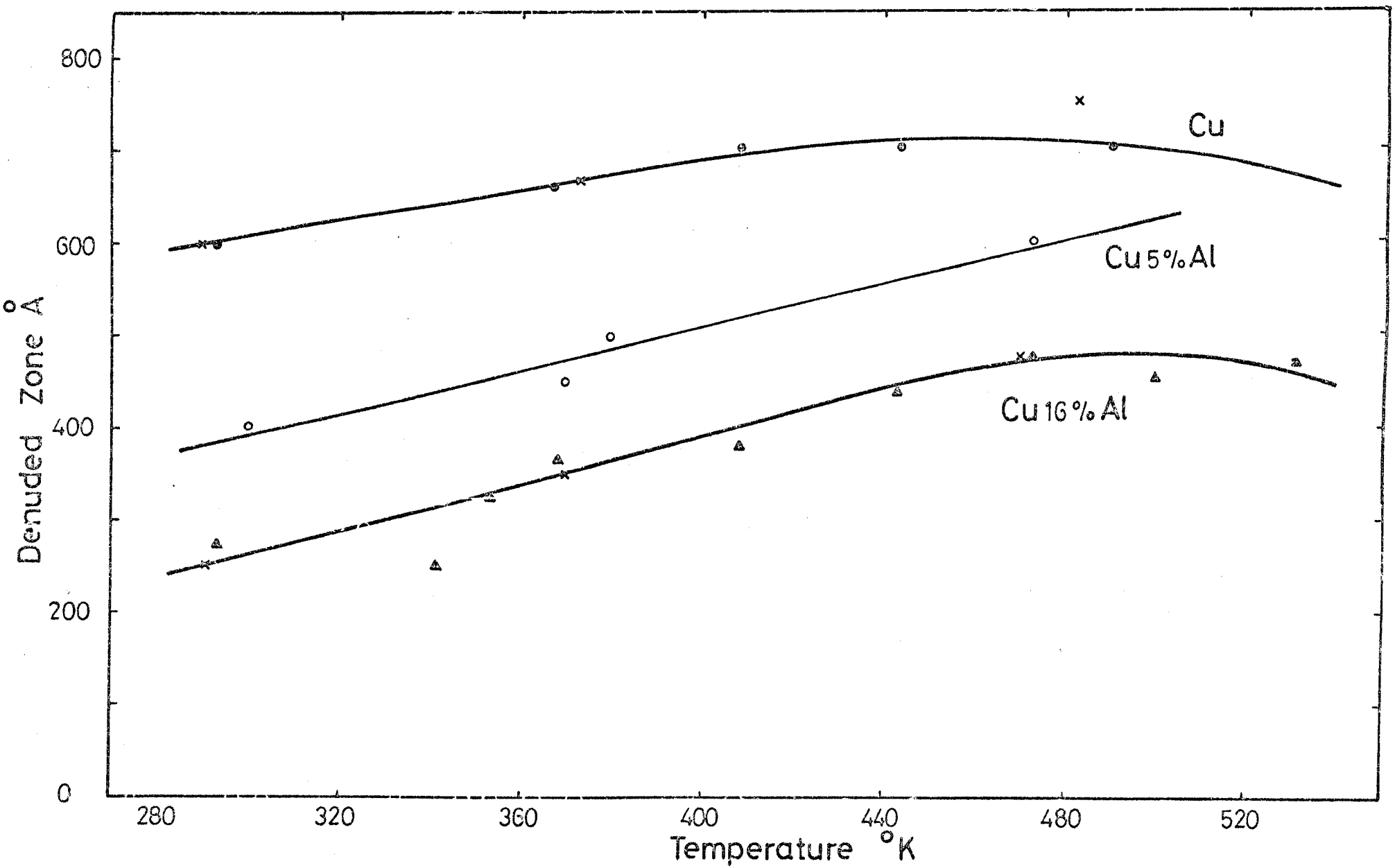
800
600
400
200
0
Denuded Zone °A
280
320
360
400
440
480
520
Temperature °K
Cu
Cu 5% Al
Cu 16% Al

Fig. 7/20 Large time (θ) solutions for the loop density l at the centre of the foil for different values of P, showing the lowered density and increased nucleation time at large values of P.

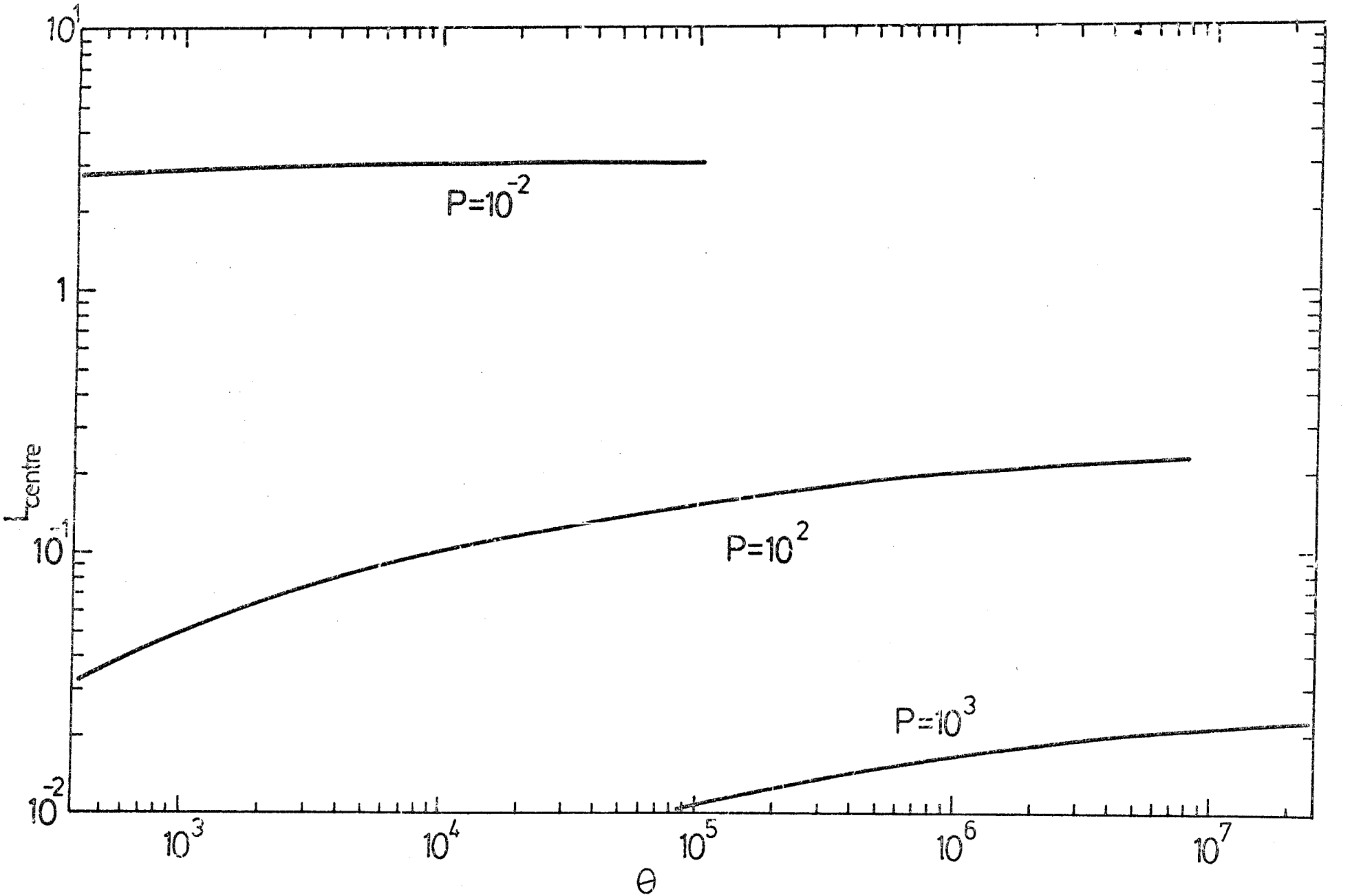
10^1
1
10^{-1}
10^{-2}
L_{centre}
$P=10^{-2}$
$P=10^{2}$
$P=10^{3}$
10^3
10^4
10^5
10^6
10^7
θ

Fig. 7/21 Measured loop density plotted against nucleation time (θ).

(A) Zone refined Cu P = 200 T = 210°C

(B) Zone refined Cu P = 41 T = 20°C

(C) Cu 16% Al P = 230 T = 235°C

(D) Cu 16% Al P = 28 T = 20°C

(α) gradual increase in loop density

(β) dislocation interaction and rapid nucleation of loops

(γ) some small loops shrink while others grow

(δ) small vacancy loops present

(ε) loop interaction and slip to the specimen surface.

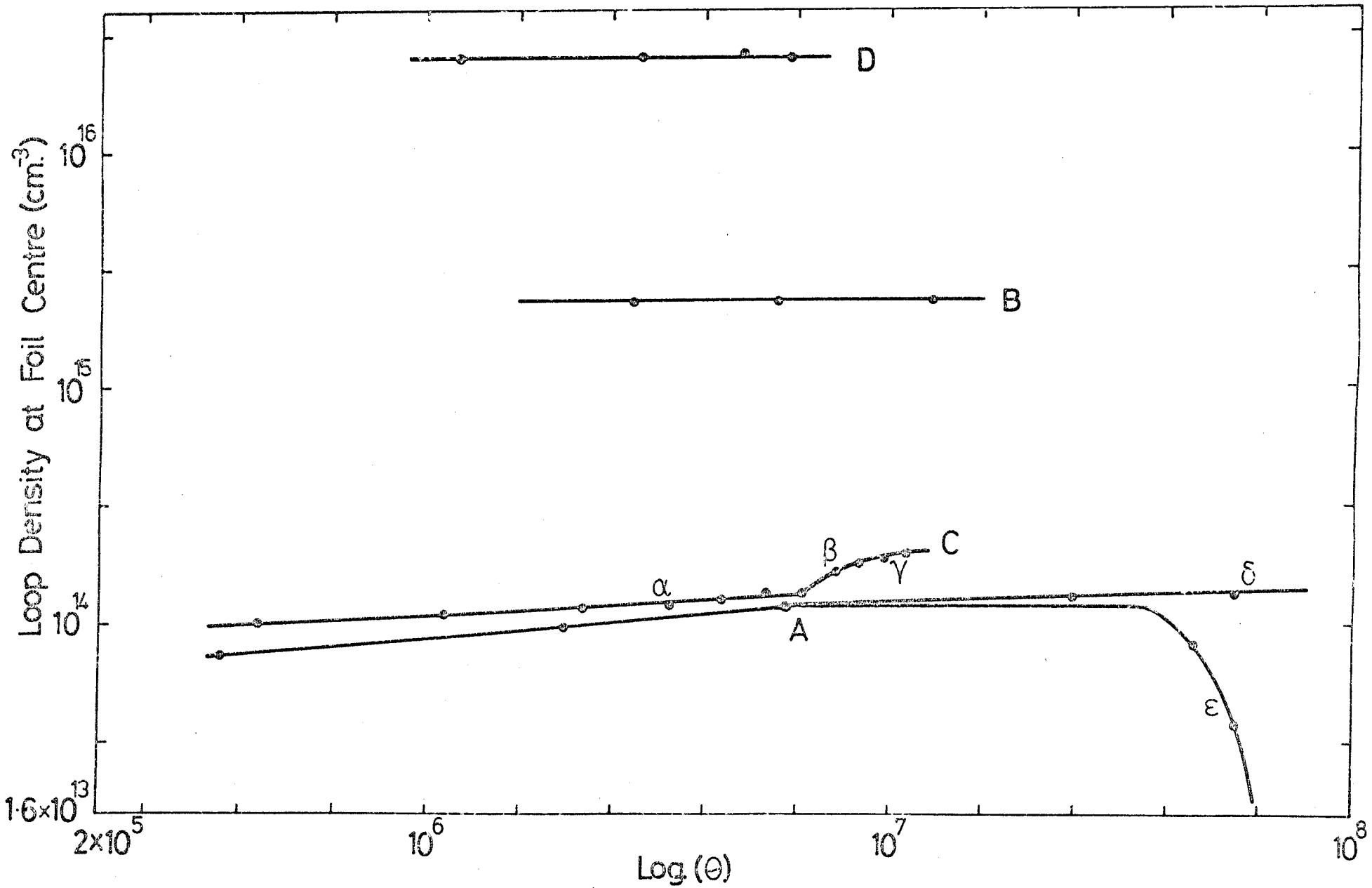
Loop Density at Foil Centre (cm.$^{-3}$)
10^{16}
10^{15}
10^{14}
$1{\cdot}6\times10^{13}$
D
B
C
A
α
β
γ
δ
ε
2×10^{5}
10^{6}
10^{7}
10^{8}
Log. (θ)

Fig. 7/22 Loop density (uncorrected) as a function of time for a Cu 16% Al foil irradiated at t = 235°C

$g = 4.68 \times 10^{19}$ cm.$^{-3}$ sec.$^{-1}$

(A) original loops plus all the loops nucleated since.

(B) total density (including new loops).

(C) density of original loops, illustrating the effects of slippage to the surface and interaction.

(D) density of new loops only.

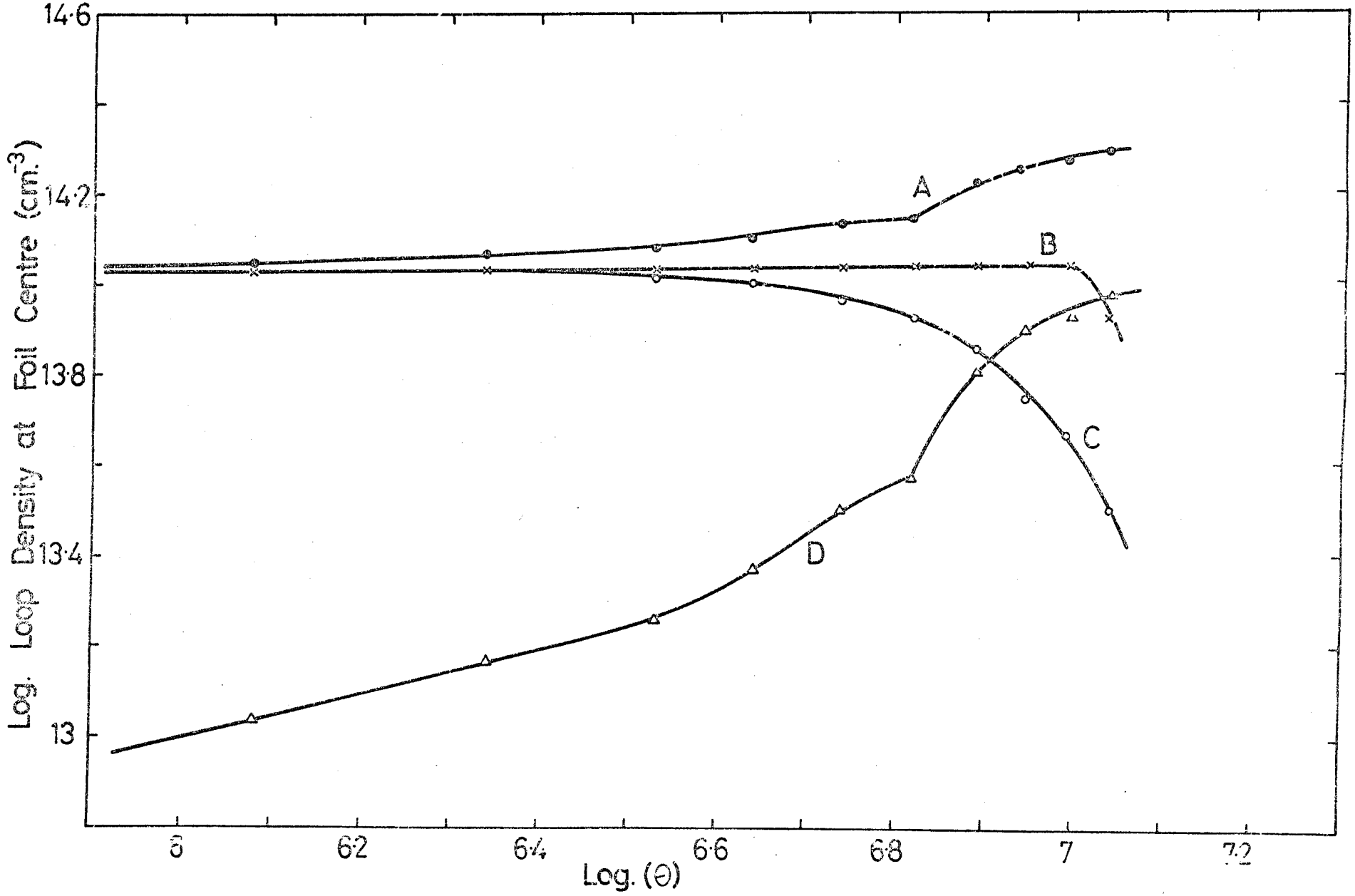
14·6
14·2
13·8
13·4
13
Log. Loop Density at Foil Centre (cm.$^{-3}$)
A
B
C
D
6
6·2
6·4
6·6
6·8
7
7·2
Log. (θ)

Fig. 7/23 illustrates the changes in uncorrected loop density as a function of fose for various temperatures, in foils of Cu 16% Al.

(A) irradiated at 120°C
(B) irradiated at 170°C
(C) irradiated at 210°C
(D) irradiated at 235°C
(E) irradiated at 275°C

For each curve:-

α includes the small loops which have nucleated after the original nucleation.

β original loop density.

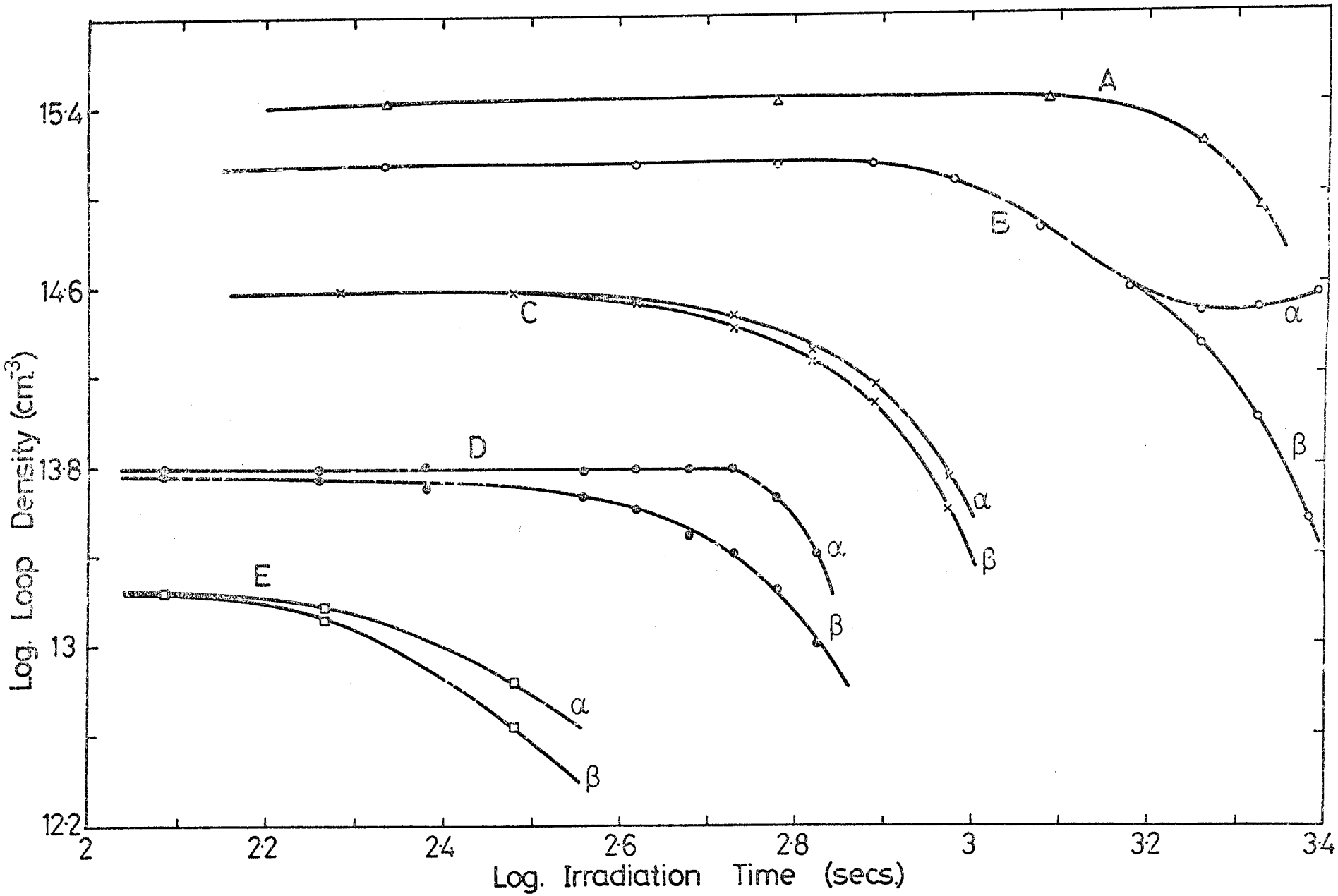
15·4
14·6
13·8
13
12·2
Log. Loop Density (cm⁻³)
2
2·2
2·4
2·6
2·8
3
3·2
3·4
Log. Irradiation Time (secs.)
A
B
C
D
E
α
β

Fig. 7/24 Graph shows the interstitial defect retention at the foil centre $P = 1 \rightarrow 10^3$. Theory and experimental results for Cu and Cu 16% Al.

Solid lines:- Theoretical calculations

× experimental results Cu 16% Al

o corrected to bulk Cu 16% Al

▲ experimental results Cu

□ corrected to bulk Cu

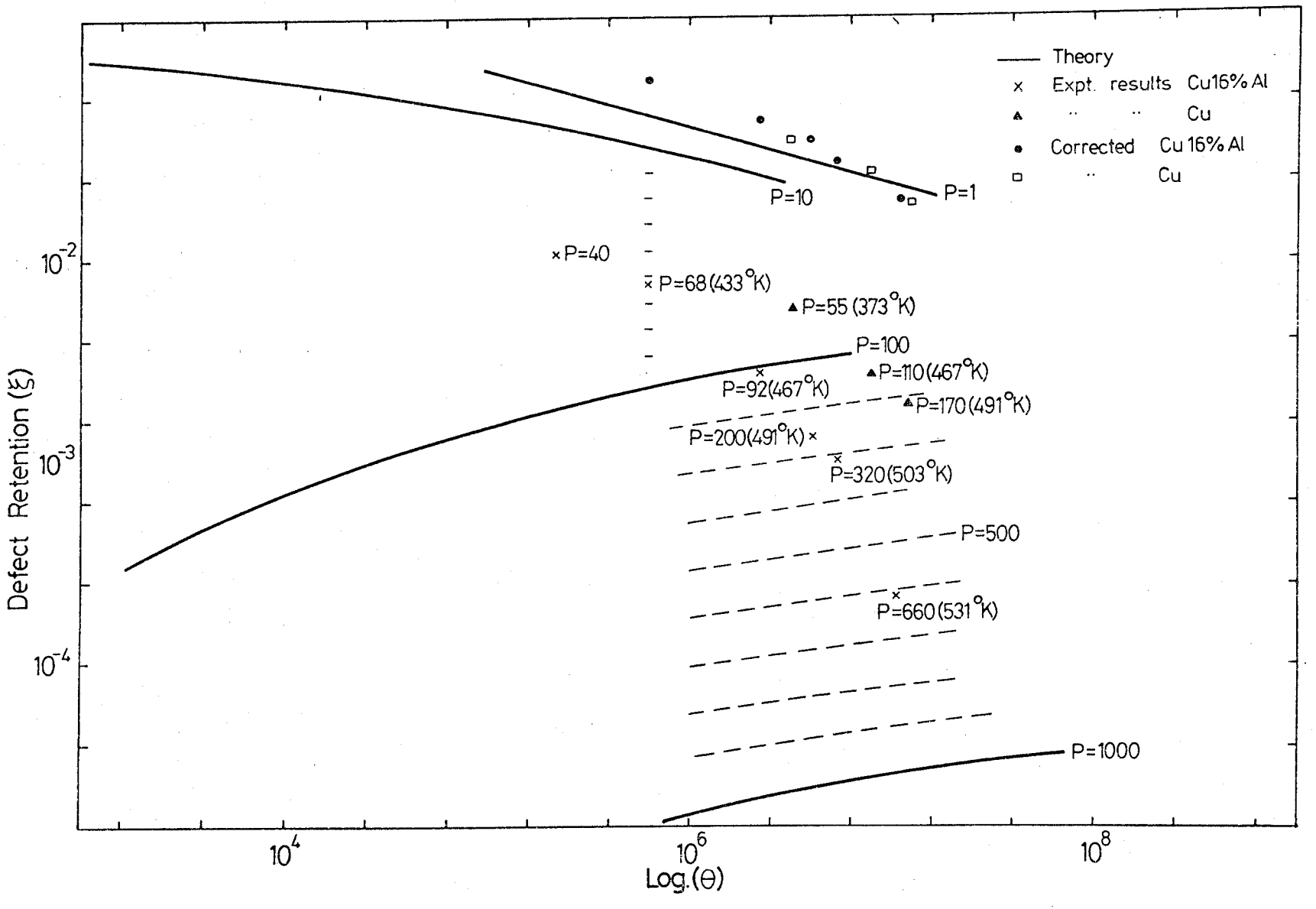
Theory
Expt. results Cu16% Al
·· ·· Cu
Corrected Cu 16% Al
·· Cu
P=1
P=10
P=40
P=68 (433°K)
P=55 (373°K)
P=100
P=92 (467°K)
P=110 (467°K)
P=170 (491°K)
P=200 (491°K)
P=320 (503°K)
P=500
P=660 (531°K)
P=1000
Defect Retention (ξ)
Log.(θ)
10^{-2}
10^{-3}
10^{-4}
10^{4}
10^{6}
10^{8}

Fig. 7/25 illustrates the loop size distribution as a function of dose for a foil of Cu 16% Al irradiated at 240°C.

(A) 1 min. irradiation
(B) 2 mins. irradiation
(C) 3 mins. irradiation
(D) 4 mins. irradiation
(E) 5 mins. irradiation.

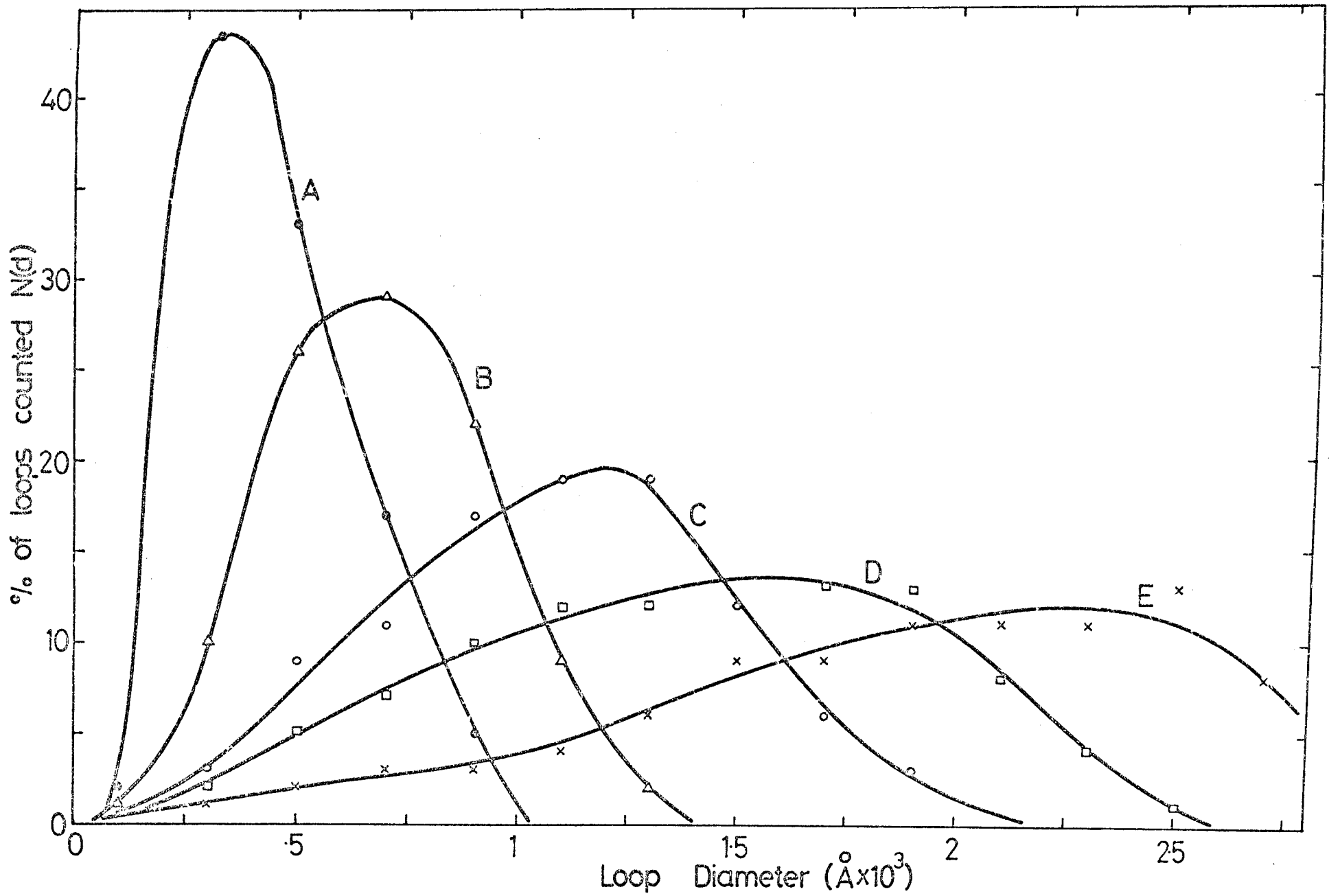
% of loops counted N(d)
40
30
20
10
0
A
B
C
D
E
0
·5
1
1·5
2
2·5
Loop Diameter (Å×10³)

Fig. 7/26 Results to show that area measurements converted to diameter gives a narrower distribution than that for loops on all planes, when one diameter is chosen as representative of loop size.

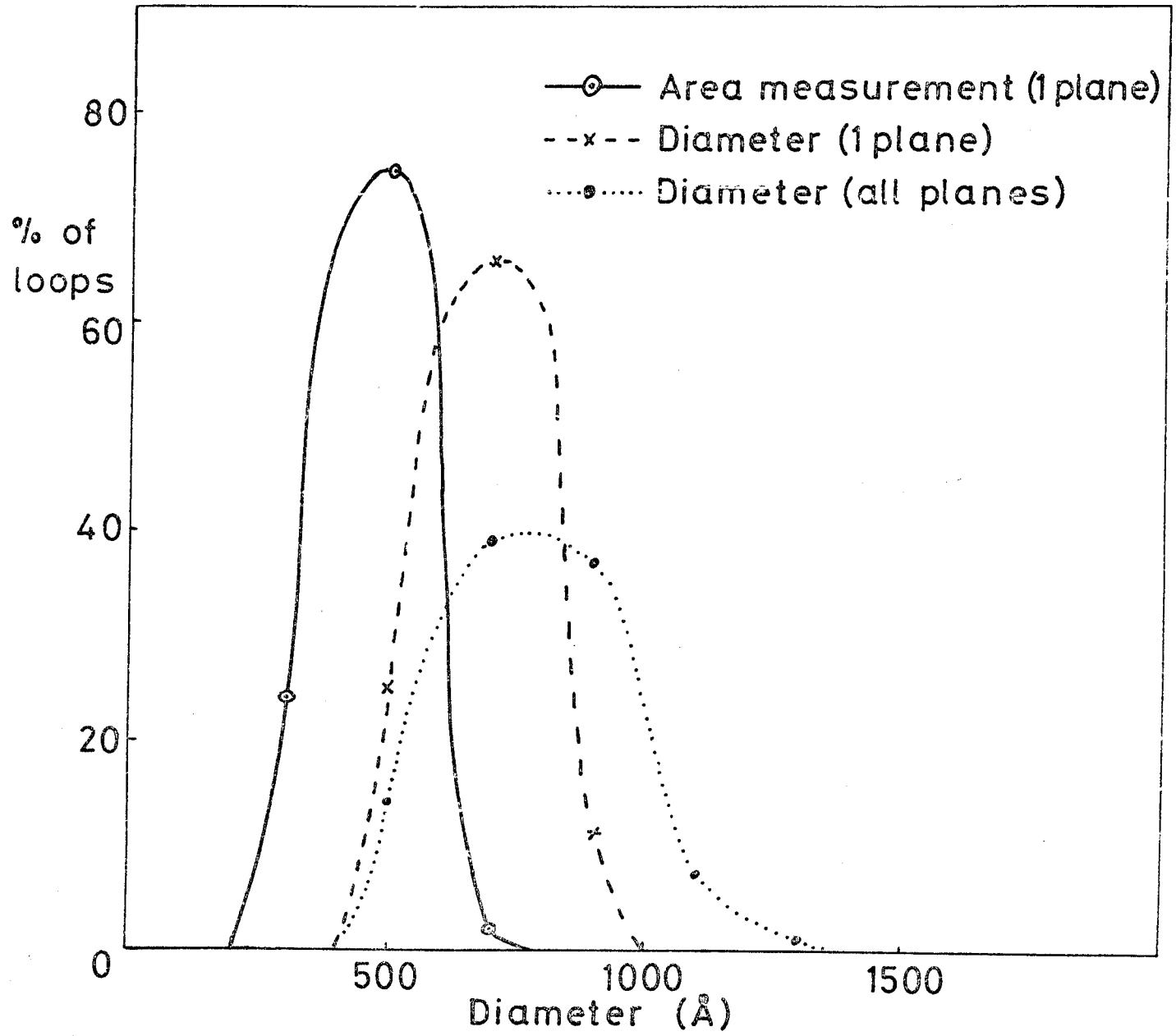
Area measurement (1 plane)
Diameter (1 plane)
Diameter (all planes)
% of loops
80
60
40
20
0
500
1000
1500
Diameter (Å)

Fig. 7/27 Size distribution plotted by counting 500 loops, in:-

(A) g <220> weak beam condition

(B) conventional bright field image.

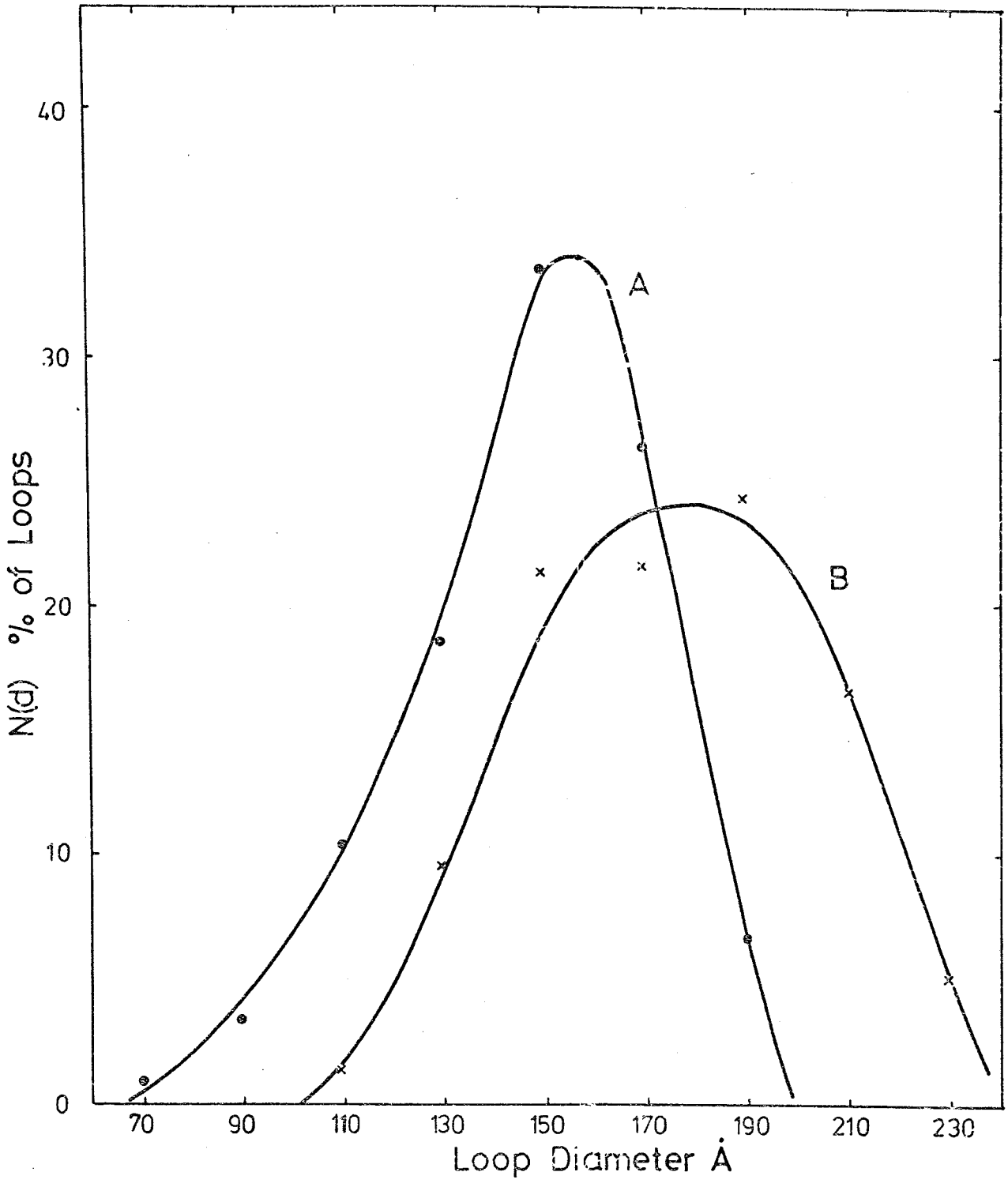
40
30
20
10
0
N(d) % of Loops
A
B
70
90
110
130
150
170
190
210
230
Loop Diameter Å

Fig. 7/28 Plot to show N(D) as a function of corrected loop diameter for different projections of perfect loops. When this correction is applied, the size distributions peak at the same diameter.

$\bar{g} = [\bar{1}1\bar{1}]$

$\bar{z} = [121]$

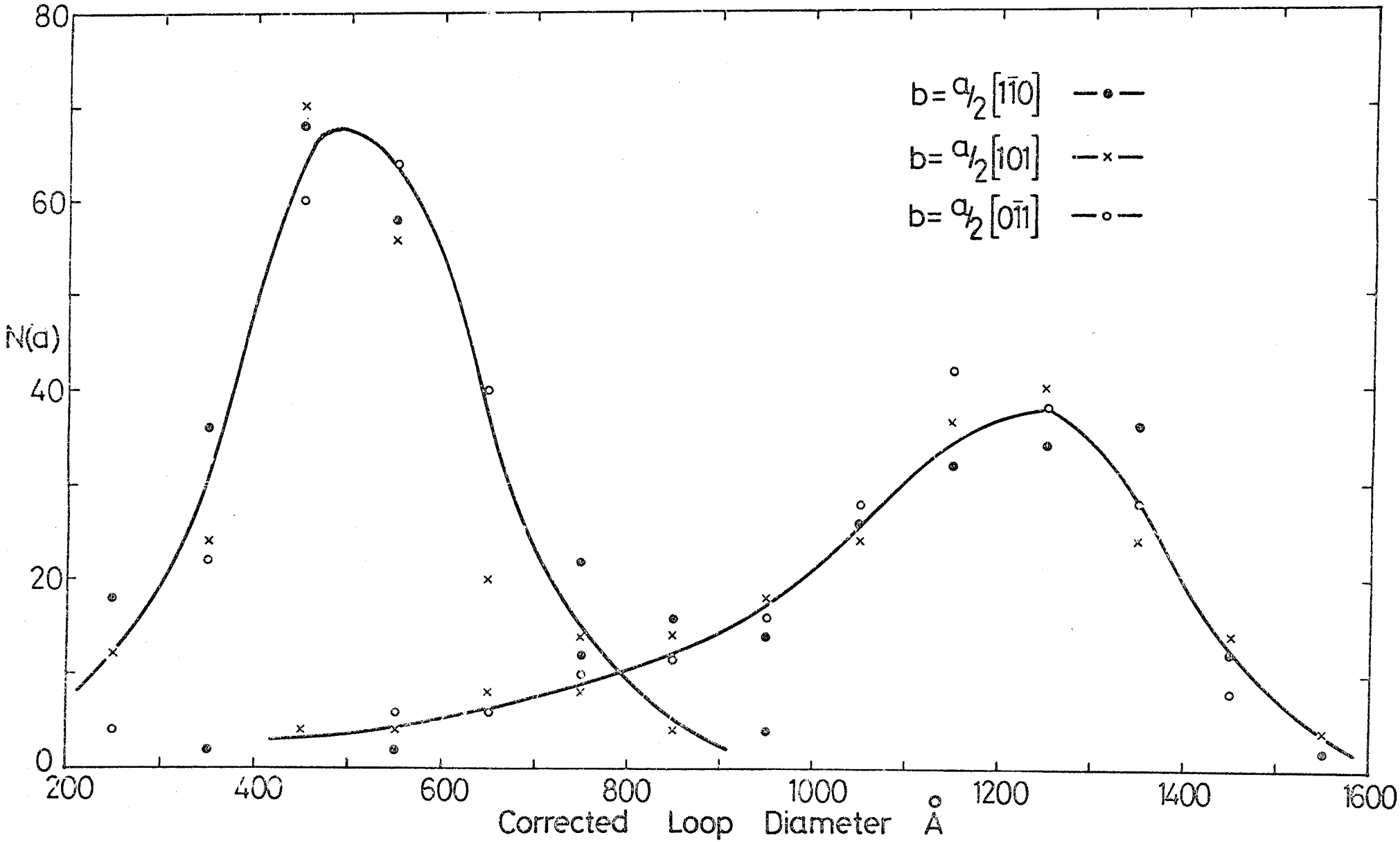
80
60
40
20
0
N(a)
200
400
600
800
1000
1200
1400
1600
Corrected Loop Diameter Å
b= a/2[1$\bar{1}$0]
b= a/2[101]
b= a/2[0$\bar{1}$1]

Fig. 7/29 shows the variation of growth rate of Frank loops as a function of depth in a foil of zone refined copper, after an irradiation at 210°C.

The areas of the loops were measured and the equivalent radius calculated. The depths of the loops were measured by using stereo techniques.

Foil thickness ≏ 2600 Å.

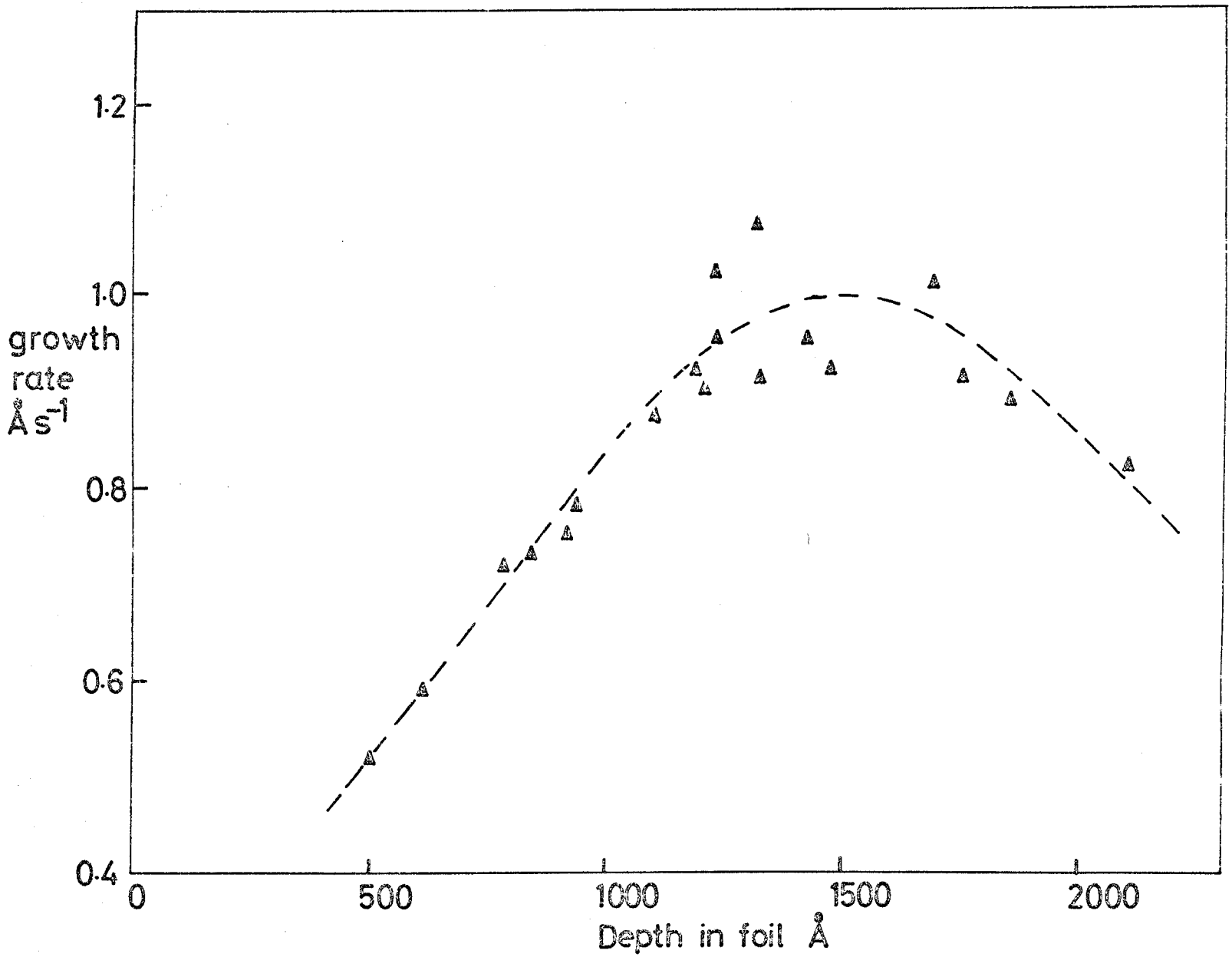
1·2
1·0
0·8
0·6
0·4
growth rate Å s⁻¹
0
500
1000
1500
2000
Depth in foil Å

Fig. 7/30 Typical size distribution in a thin foil of Cu 16% Al irradiated for six minutes at 235°C.

(A) In this area containing 13% of total loop population, nucleation has occurred since the initial nucleation. Some of these loops may be vacancy in nature.

(B) The broad spectrum is caused by surface effects.

(C) Loop interaction by two or even three loops accounts for 10% of the total loop population.

g $[1\bar{1}\bar{1}]$

z [211]

Generation rate $\triangleq 5 \times 10^{19}$ cm.$^{-3}$ sec.$^{-1}$.

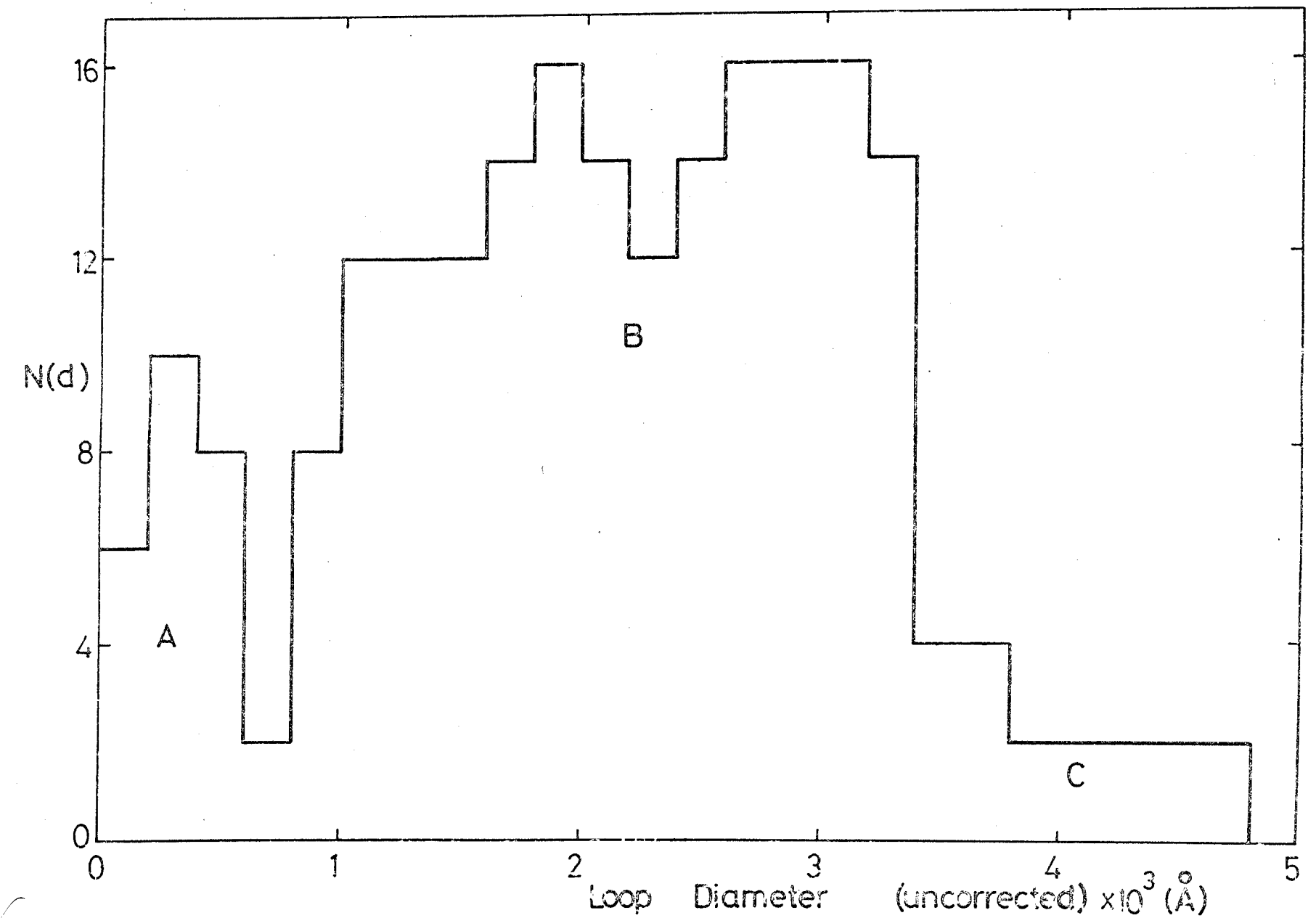
16
12
8
4
0
N(d)
A
B
C
0
1
2
3
4
5
Loop Diameter (uncorrected) x10³ (Å)

Fig. 7/31 Rhombus loop growth rates in a thin foil of Cu 16% Al irradiated at 170°C. The growth rates of some individual loops have been plotted in fig. 10/6.

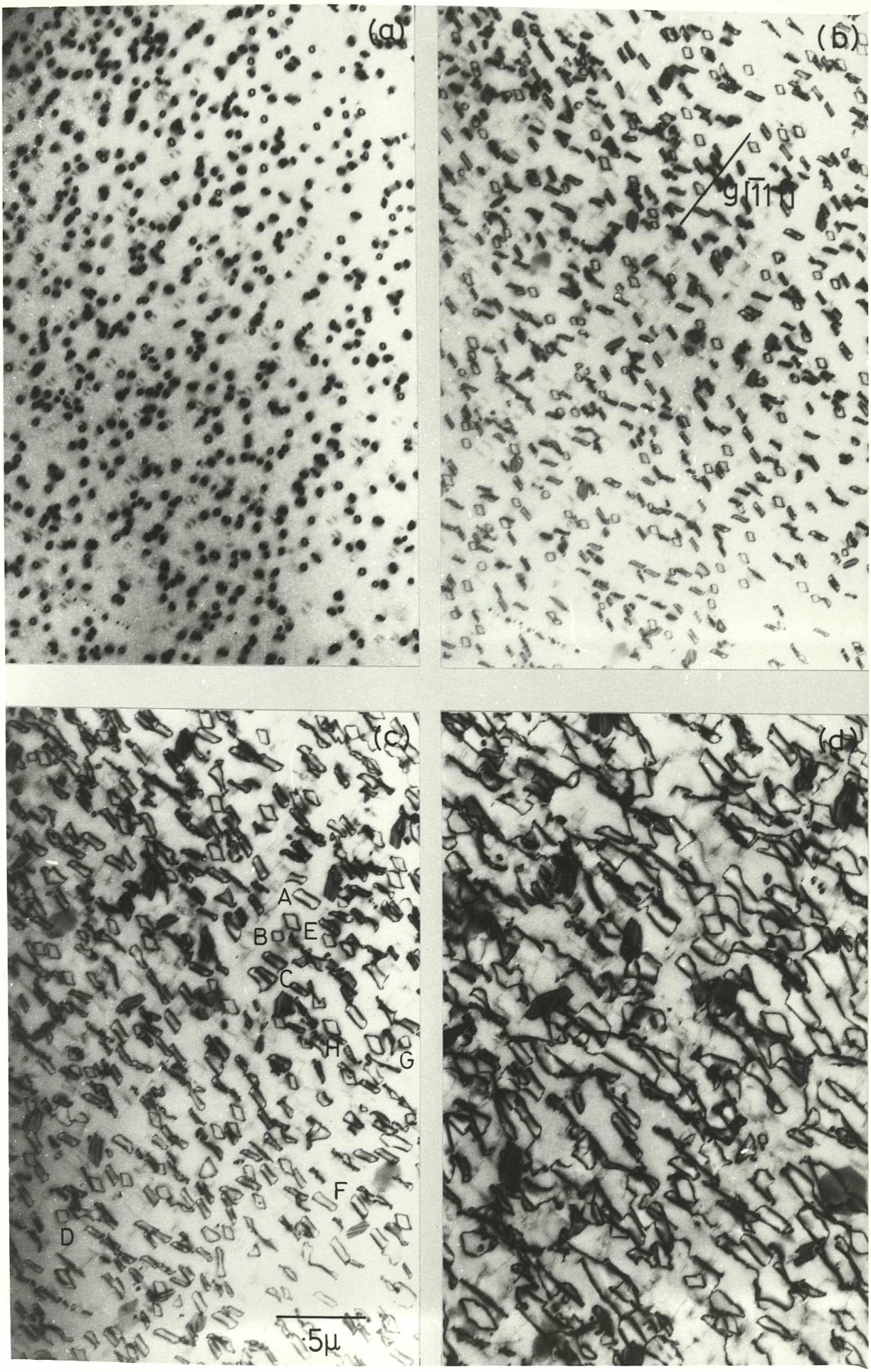
(a)
(b)
g[11̄]
(c)
A
B
C
D
E
F
G
H
.5μ
(d)

Fig. 7/32 Diagram summarizing the various factors contributing to the broadening of loop size distributions observed in electron irradiated thin foils.

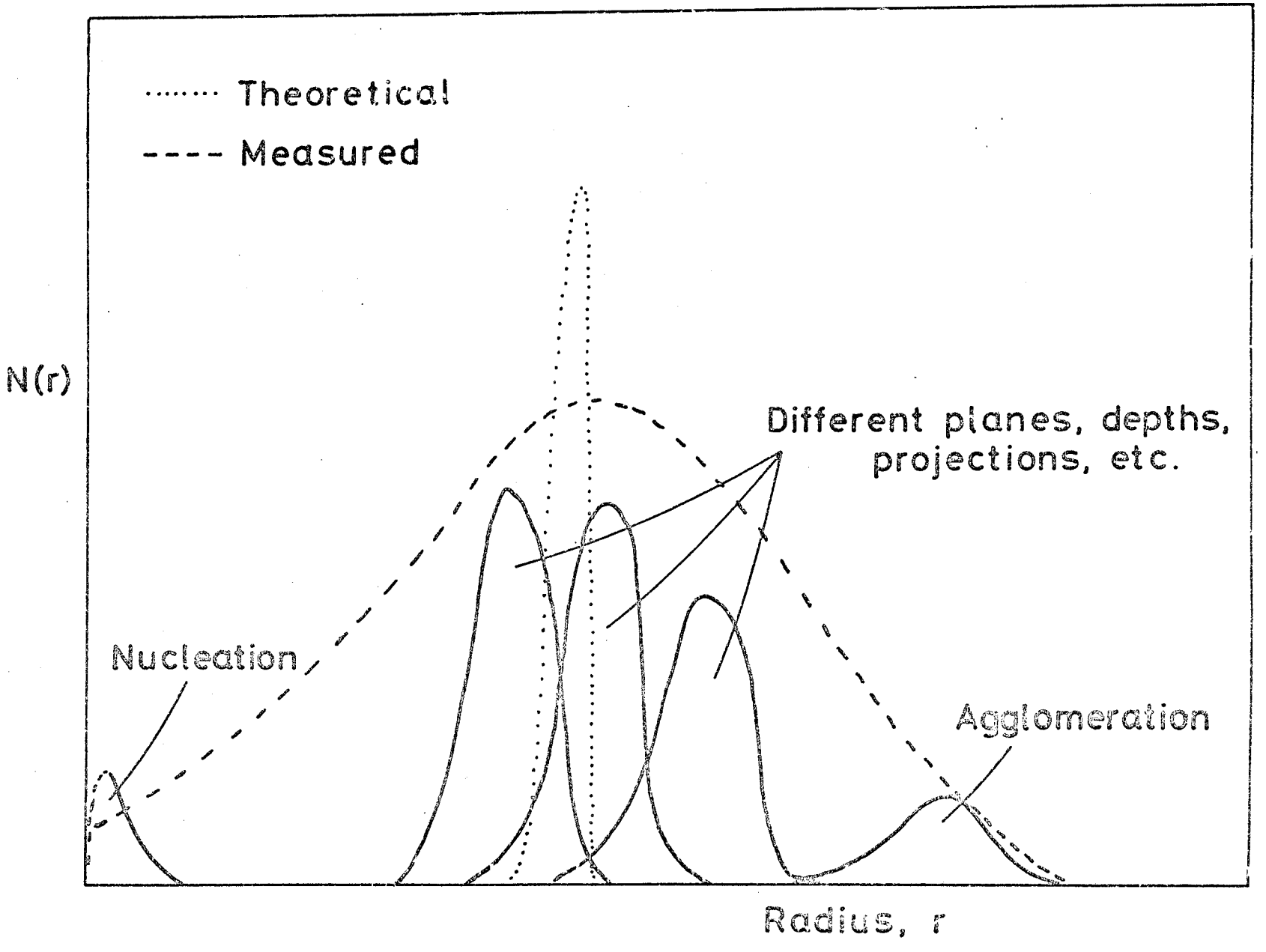
..... Theoretical
---- Measured
N(r)
Different planes, depths, projections, etc.
Nucleation
Agglomeration
Radius, r

Fig. 7/33 Effect of foil thickness on the loop size after 300 seconds irradiation at a generation rate $g = 5.7 \times 10^{19}$ cm.$^{-3}$ sec.$^{-1}$.

(A) foil thickness 2040 Å

(B) foil thickness 2720 Å

(C) foil thickness 4080 Å

Temperature of irradiation $T_i = 215^{\circ}C$ Cu 16% Al.

(Note the increase in number of Frank loops in the thick foil).

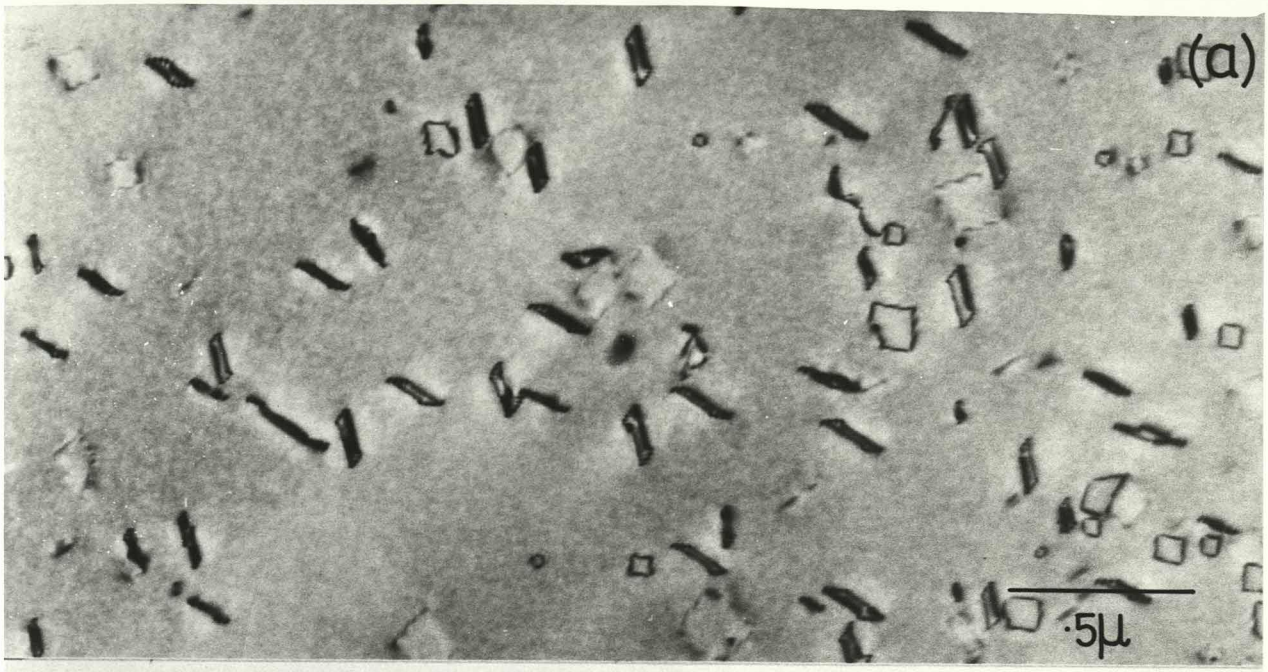
(a)
.5μ


(b)
g[1̄11]

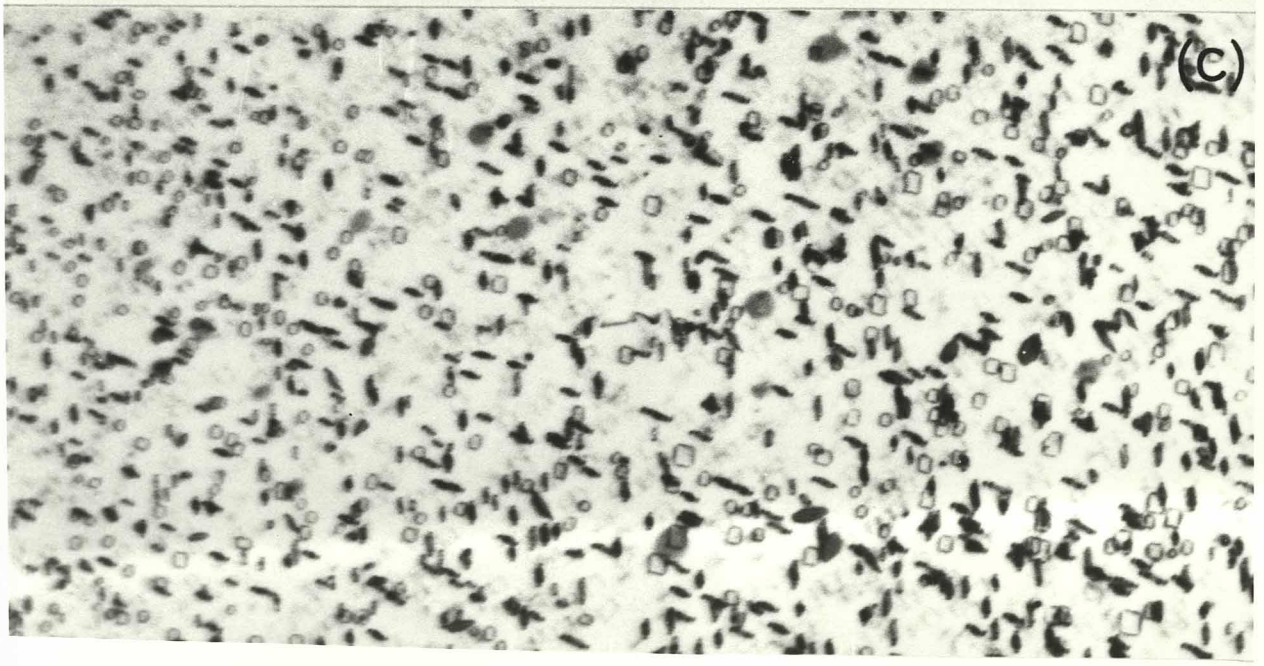
(c)

Fig. 7/34 Size distribution of interstitial rhombus loops as a function of foil thickness and loop normal.

Cu 16% Al $\bar{g} = [\bar{1}1\bar{1}]$ $z = [121]$ $T = 215^{\circ}C$ $g = 5.7 \times 10^{19}$ cm.$^{-3}$ sec.$^{-1}$.

Loop 1 $\bar{b} = \frac{a}{2}[101]$. In A represents 25% of loops, in B 32% of loops.

Loop 2 $\bar{b} = \frac{a}{2}[0\bar{1}1]$. In A represents 35% of loops, in B 34% of loops.

Loop 3 $\bar{b} = \frac{a}{2}[1\bar{1}0]$. In A represents 40% of loops, in B 33% of loops.

Foil thickness A 4080 Å
B 2720 Å
C 2040 Å

Curve A $P_c = 36$
$\theta = 6.24 \times 10^6$

Curve B $P_c = 62$
$\theta = 4.5 \times 10^6$

Curve C $P_c = 110$
$\theta = 4.95 \times 10^6$

where P_c = corrected diffusion parameter
$\theta = t\sqrt{gs\Omega}$ (irradiation time)

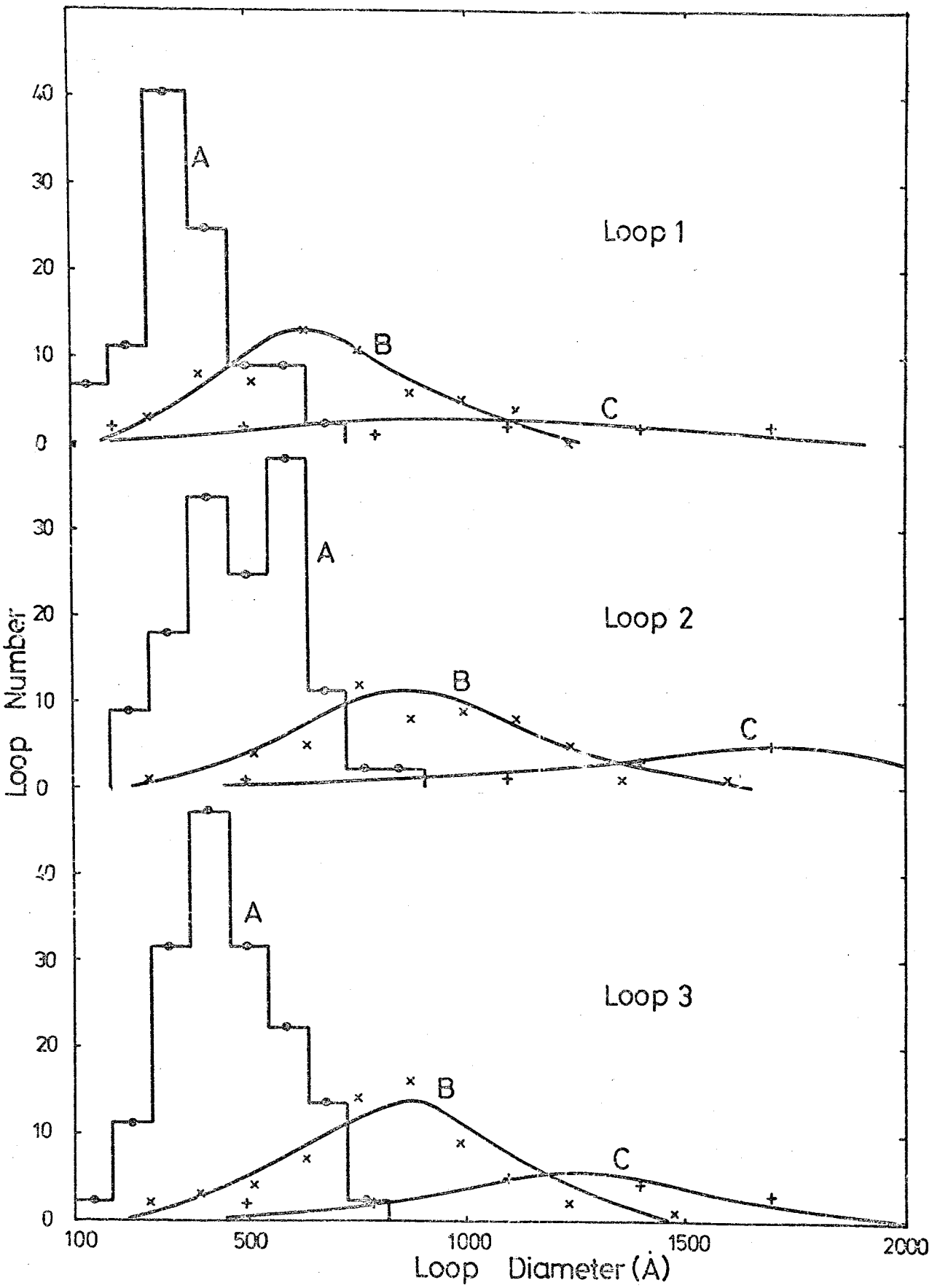
Loop 1
Loop 2
Loop 3
A
B
C
Loop Number
Loop Diameter (Å)
0
10
20
30
40
100
500
1000
1500
2000

Fig. 7/35 Plot of the size distribution as a function of depth for a foil of Cu 5% Al irradiated at 205°C, until the loops were visible. Gold on the electron exit surface.

P_c = 85 mean density 4.87×10^{14} loops/cm.^{3}
foil centre density 9.74×10^{15} loops/cm.^{3}

(1) Few loops nucleate near the foil surfaces.
(2) Distribution peaks in diameter between 250 and 300 Å irrespective of depth.
(3) The widths of each distribution are approximately equal.
(4) The thickness near the foil centre has the highest number of loops.

The defect position in the foil was measured using the stereo technique.

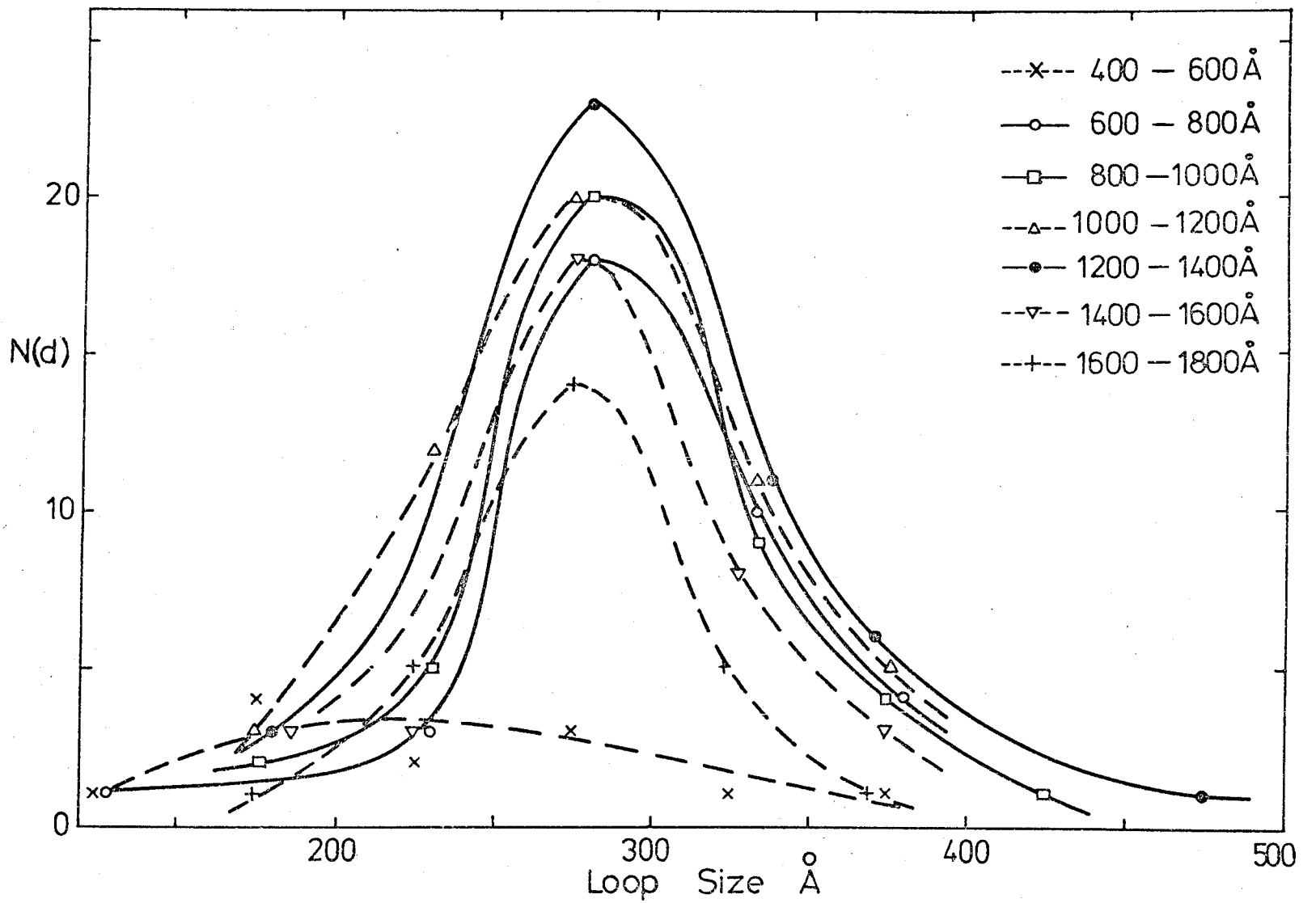
400 — 600 Å
600 — 800 Å
800 — 1000 Å
1000 — 1200 Å
1200 — 1400 Å
1400 — 1600 Å
1600 — 1800 Å
N(d)
20
10
0
200
300
400
500
Loop Size Å

Fig. 7/36 Loop size distribution as a function of depth in a foil of Cu 5% Al irradiated at 205°C for a time sufficient to grow the loops to large sizes, but not to interact.

× 400 - 600 Å
o 600 - 800 Å
□ 800 - 1000 Å
Δ 1000 - 1200 Å
● 1200 - 1400 Å
∇ 1400 - 1600 Å
+ 1600 - 1800 Å
⊙ 1800 - 2000 Å

This graph confirms that loop size distributions at given foil depths are broadened and displaced when the loops grow to a sufficient size, giving rise to broad total size distributions.

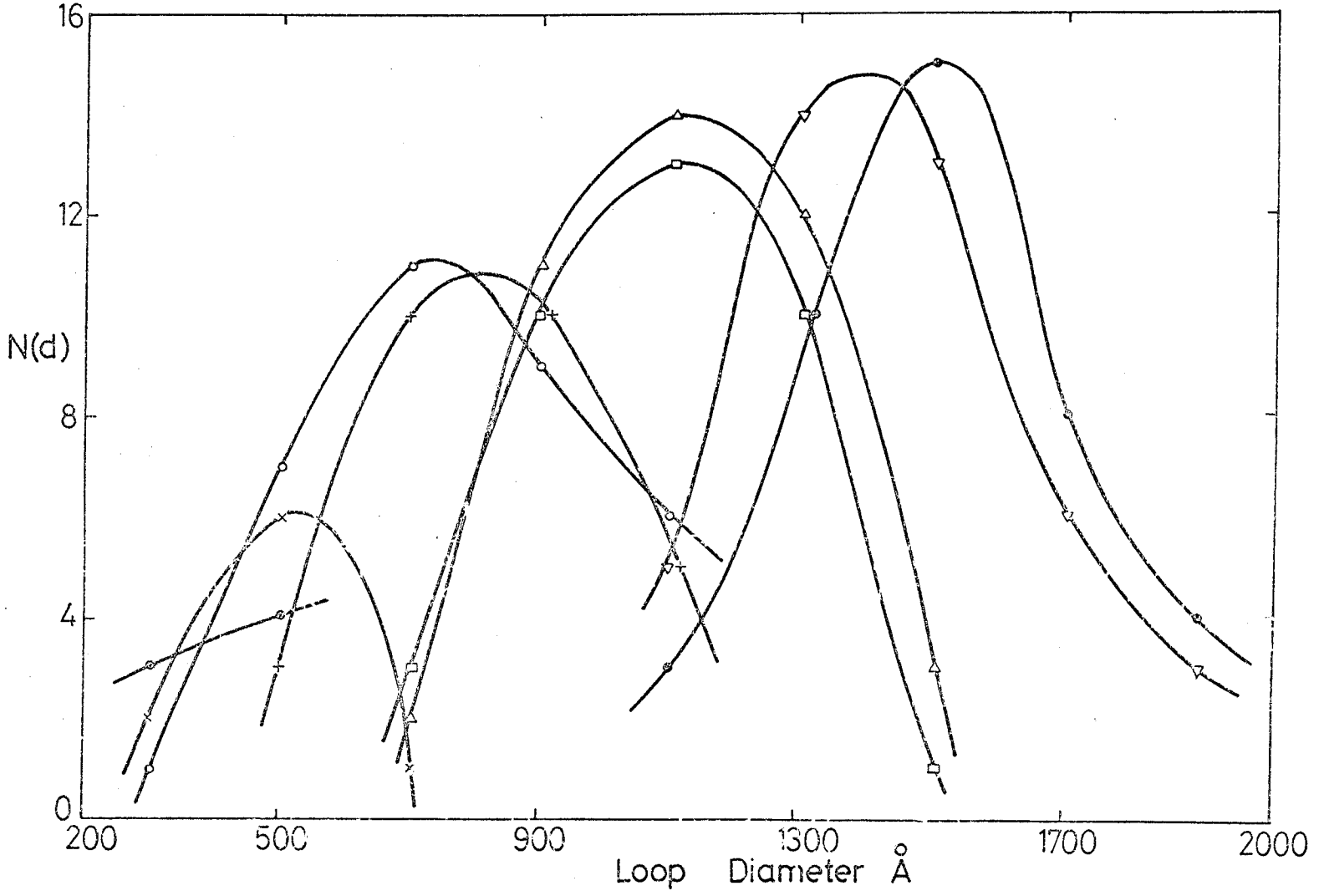
16
12
8
4
0
N(d)
200
500
900
1300
1700
2000
Loop Diameter Å

Fig. 7/37 shows the summation of the distributions taken from different depths of (A) fig. 7/35
(B) fig. 7/36

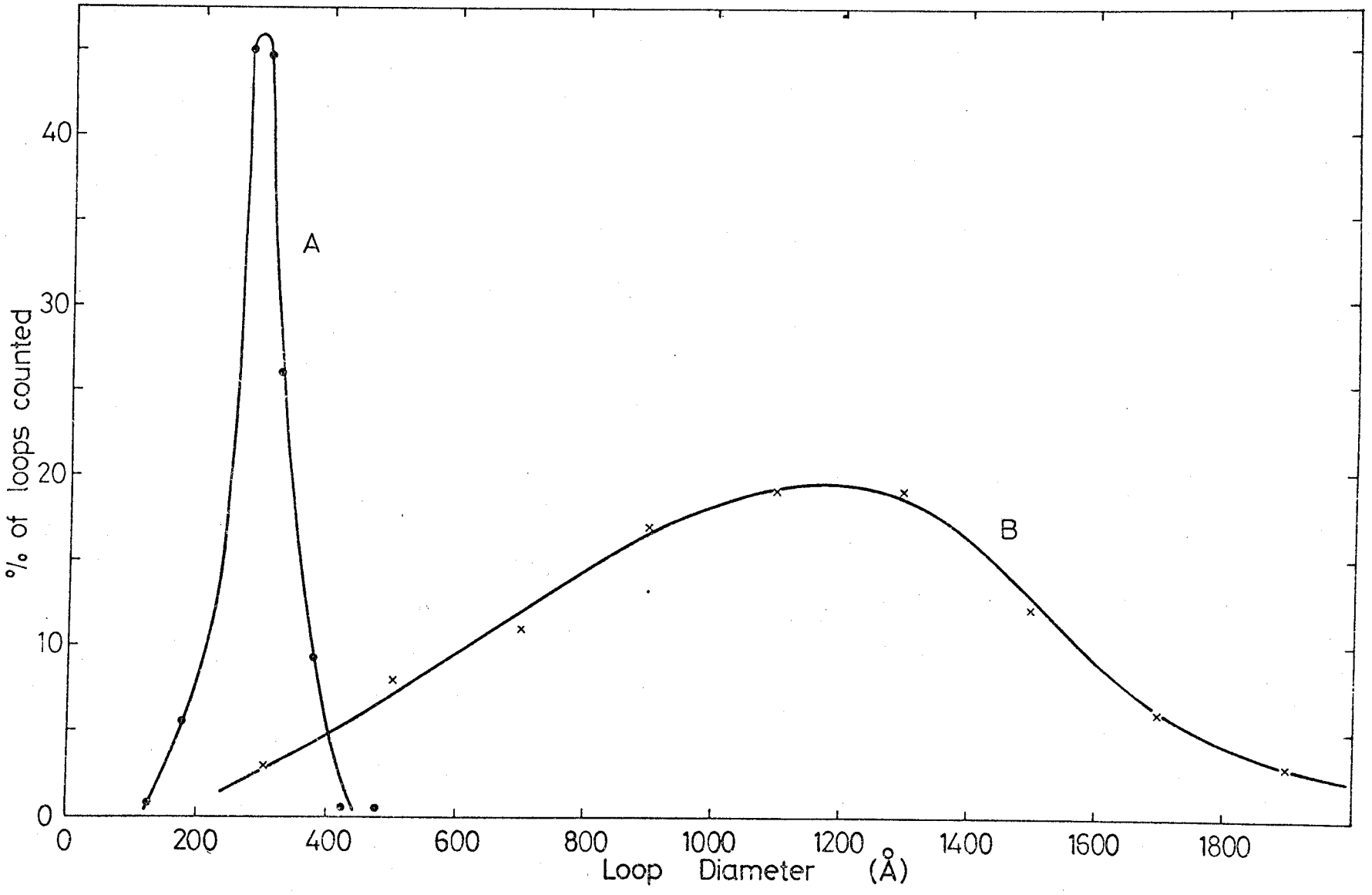
% of loops counted
0
10
20
30
40
A
B
0
200
400
600
800
1000
1200
1400
1600
1800
Loop Diameter (Å)

Fig. 7/38 Calculations showing the effect that different P values and foil depths have on loop size distributions.

(A) $P = 10^{-2}$. $R_{max} = 6.80$. $\theta = 1060$

This is representative of bulk condition and the curves for all depth positions coincide. Curve 4 is the mean of the size distributions and is displaced for clarity at each P value.

(B) $P = 1$

(1) position at foil centre 1_0 $R_{max} = 7$ $\theta = 998$

(2) position 600 Å from foil 1_6 centre $R_{max} = 7.20$

(3) position 1200 Å from foil 1_{12} centre $R_{max} = 6.05$

The mean curve was obtained by weighting (1), (2) and (3) as

$$\frac{41_0 + 21_6 + 1_{12}}{7}$$

(C) $P = 10^2$

(1) position foil centre 1_0 $R_{max} = 1.79$ $\theta = 980$

(2) position 600 Å from foil centre 1_6 $R_{max} = 1.53$

(3) position 1200 Å from foil centre $R_{max} = .70$

In the H.V.E.M. experiments the values of P were $\triangleq 10^2$.

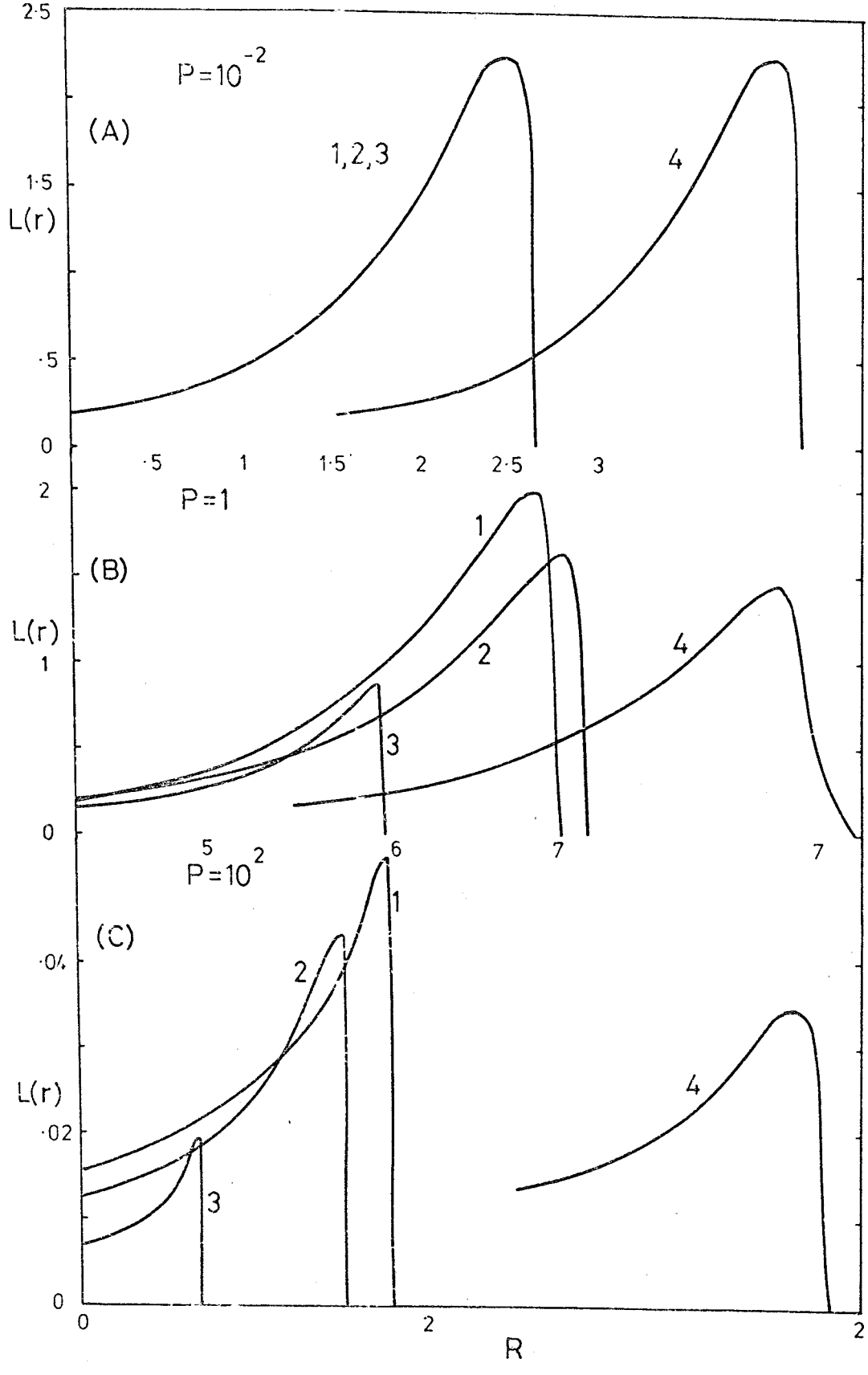
2·5
P=10^-2
(A)
1,2,3
4
1·5
L(r)
·5
0
·5
1
1·5
2
2·5
3
2
P=1
(B)
1
2
3
4
L(r)
1
0
6
7
7
P=10^5/2
(C)
1
2
3
4
·04
L(r)
·02
0
0
2
2
R

Fig. 7/39 illustrates typical size distributions at various temperatures in a foil of Cu 5% Al irradiated at a generation rate of 3.79×10^{19} cm.$^{-3}$ sec.$^{-1}$

Gold surface and electron entrance on the left hand side of the graph.

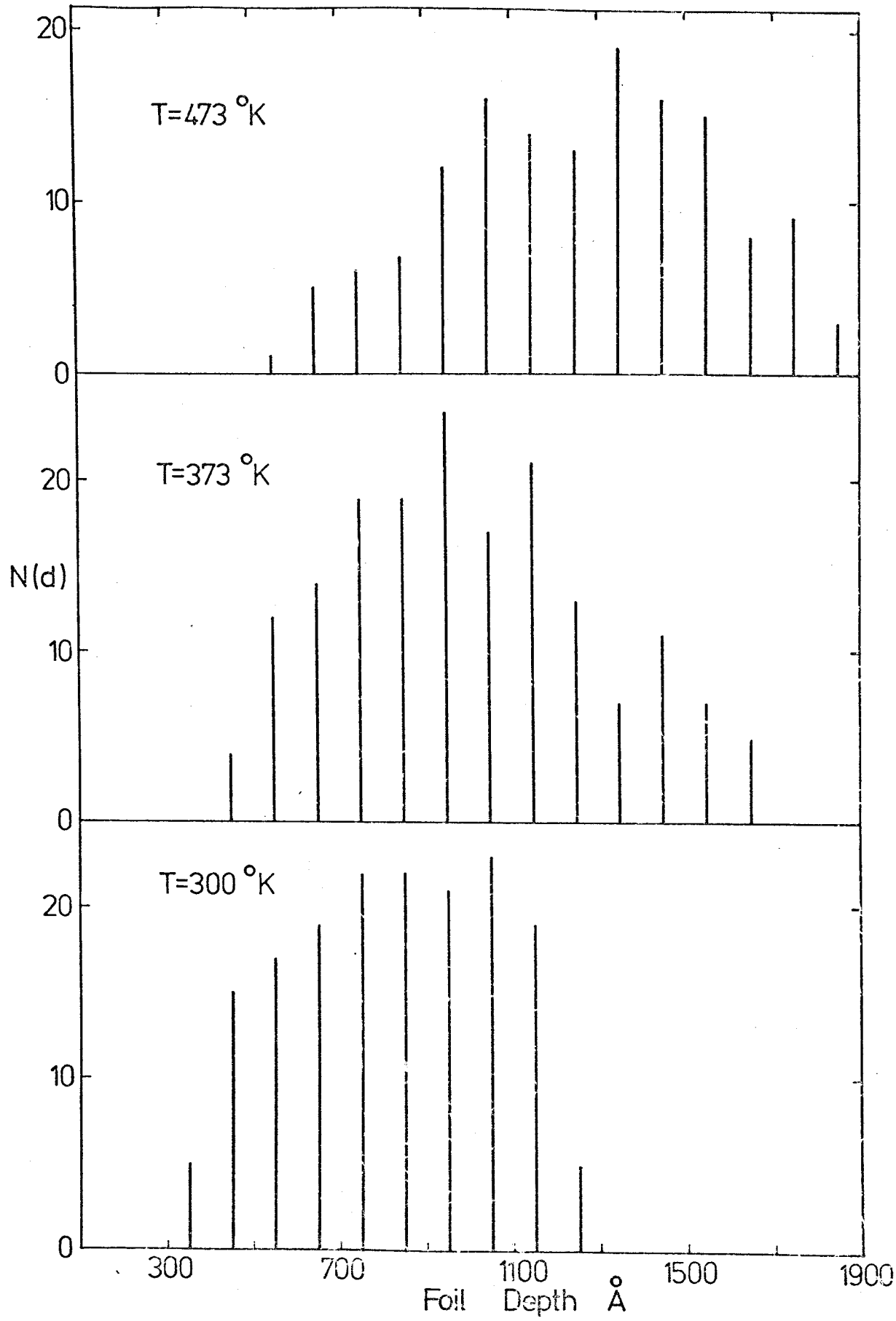
T=473 °K
T=373 °K
T=300 °K
N(d)
20
10
0
300
700
1100
1500
1900
Foil Depth Å

Fig. 7/40 Results of an experiment to test the asymmetry of size distributions in a Cu 5% Al foil irradiated at 100°C. Gold on electron entrance surface of the specimen. In the Hilger-Watts stereoviewer, the prints can be reversed giving the impression of the gold surface nearest the viewer, or away from the viewer. Since personal preference decides which method to use, the same loops were measured by both techniques to see how the results differed.

Solid line: gold away from viewer
Dotted Line: gold nearest viewer.

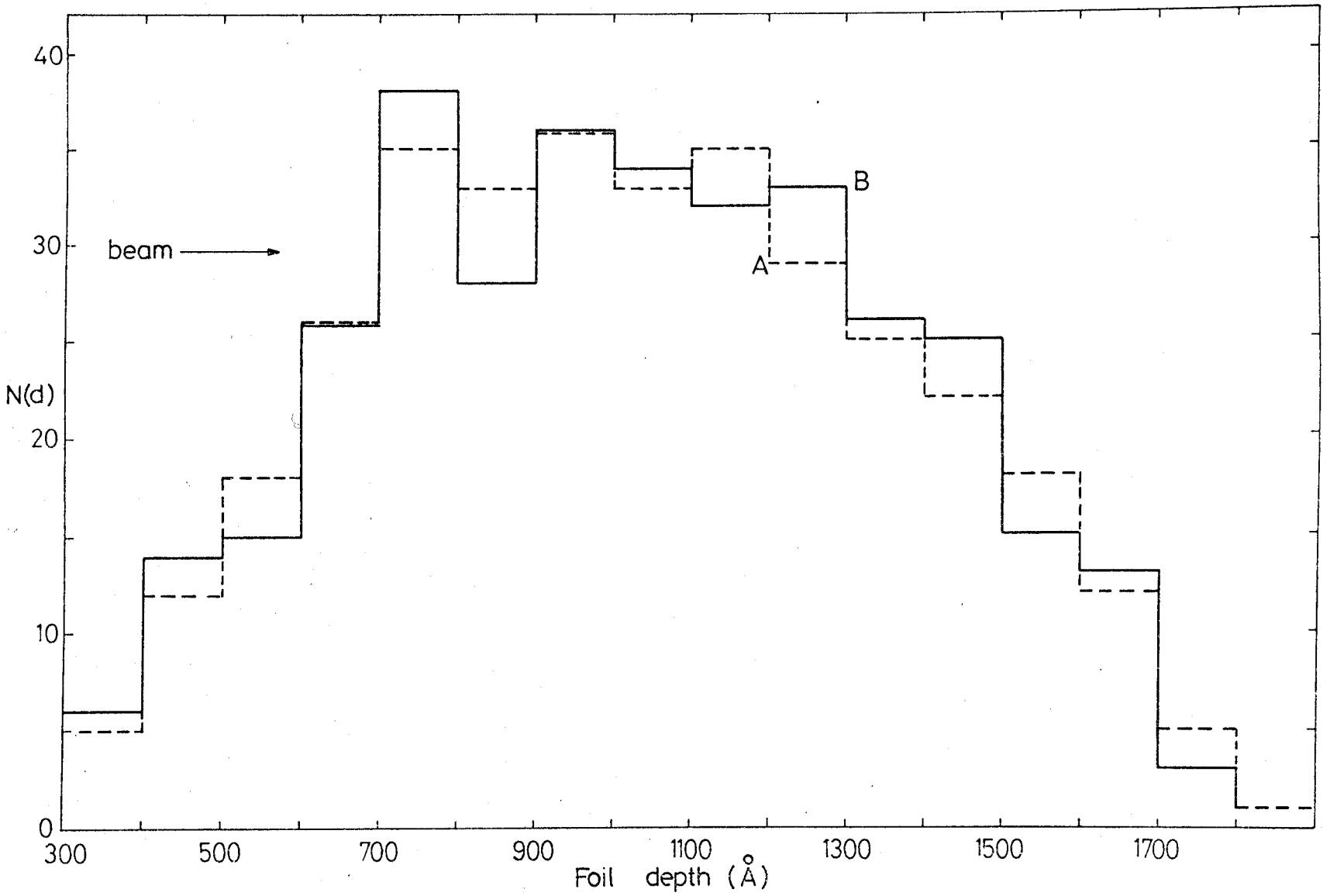
40
30
20
10
0
N(d)
beam
A
B
300
500
700
900
1100
1300
1500
1700
Foil depth (Å)

Fig. 7/41 Graph shows the effect of the objective aperture and the choice of measuring area on the loop size distribution of a Cu 5% Al specimen irradiated at 100°C.

Solid line represents results from stereomeasurements of loops measured along the same thickness contour. The symmetry of the profile contrasts with other size distributions measured for this thesis which were not taken from the same thickness contour.

Dotted line represents results taken from an area adjacent to the above, with the objective aperture in position. Measurements were made along the thickness contour. No difference in specimen temperature was observed when the aperture was inserted.

The profile indicates that in the loop growth experiments performed for this thesis, the objective aperture causes little effect on the depth distributions and densities. However, at the high doses used for void formation (generation rates in excess of 5×10^{19} cm.$^{-3}$ sec.$^{-1}$ insertion of the objective aperture causes the specimen temperature to rise between 30 and 60°C.

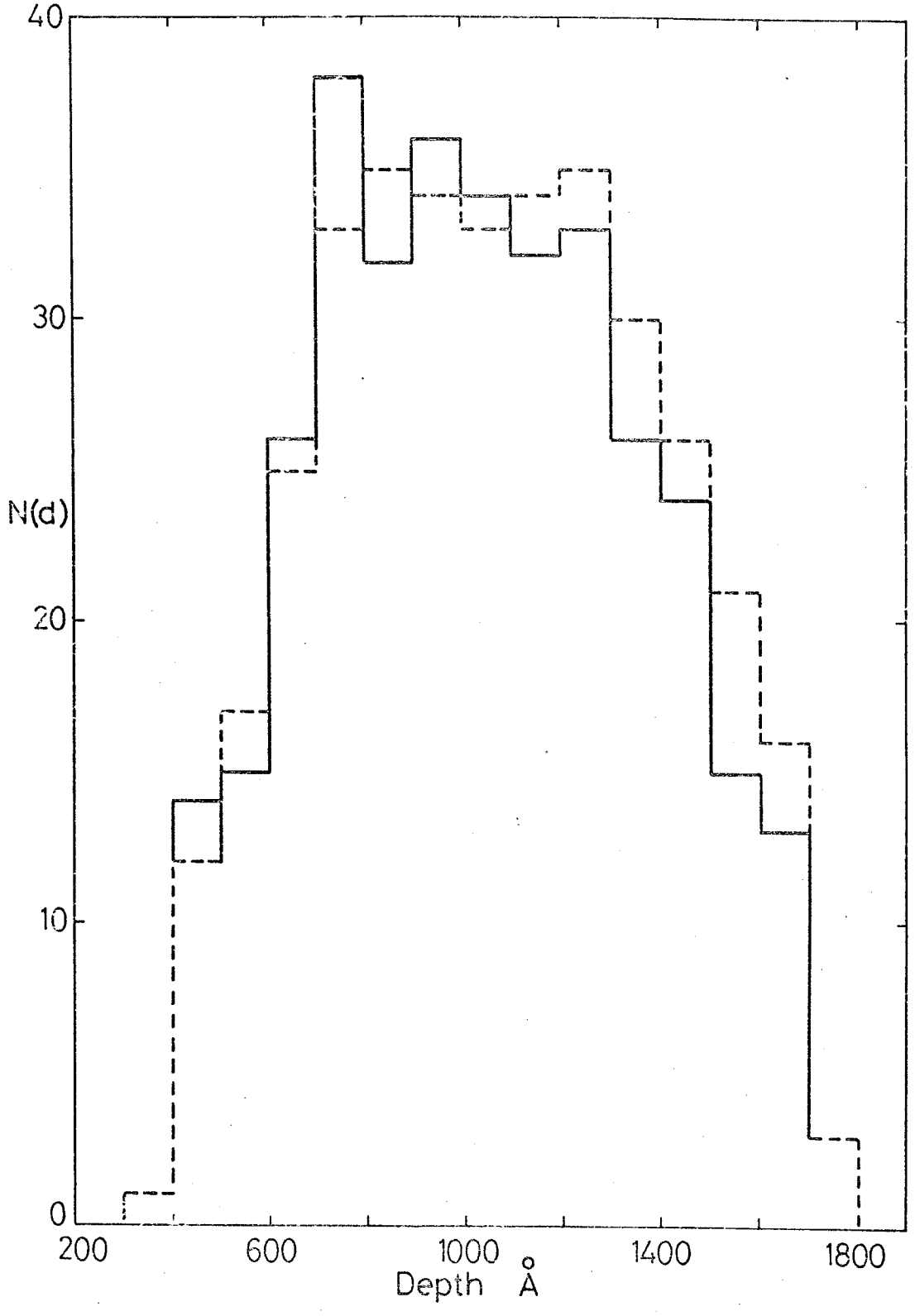
40
30
20
10
0
N(d)
200
600
1000
1400
1800
Depth Å

Fig. 7/42 Schematic view of the causes of a non-uniform distribution of loops in a thin foil specimen.

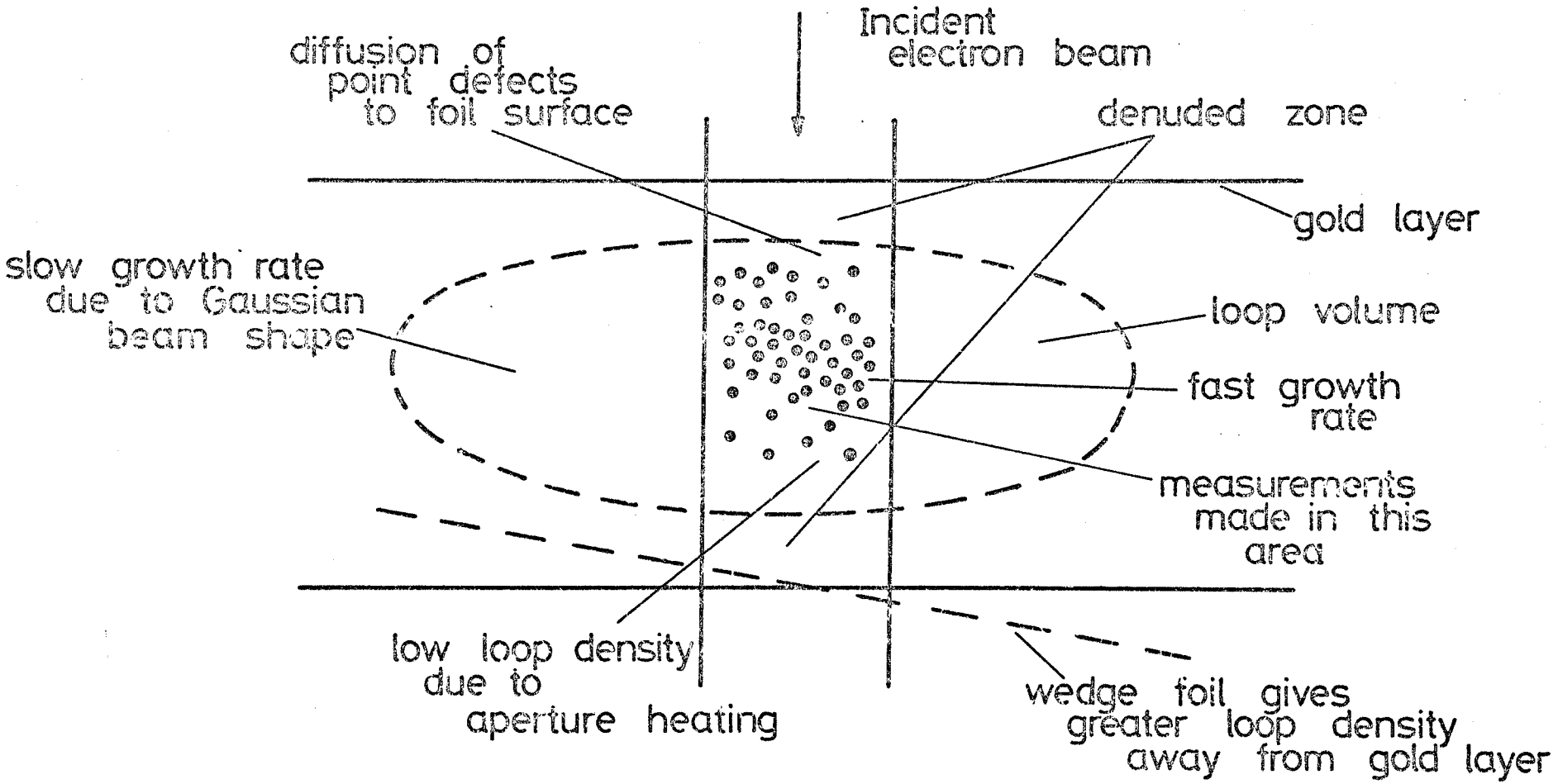
Incident
electron beam
diffusion of
point defects
to foil surface
denuded zone
gold layer
slow growth rate
due to Gaussian
beam shape
loop volume
fast growth
rate
measurements
made in this
area
low loop density
due to
aperture heating
wedge foil gives
greater loop density
away from gold layer

Fig. 7/43 Graph shows the effect that the surface diffusion parameter P_c has on the loop size distribution.

(a) Loops in an area of 8 x 8 cm. on Mag. x 36,000 were counted to give a density of $L_{centre} = 2 \times 10^{14}$ cm.$^{-3}$. There was little difference in the size distribution between $P_c = 236$ and $P_c = 85$, except for the denuded zones.

(b) This graph illustrates that for low values of P_c, the profile starts to resemble that expected for bulk foils ie. flat loop and steep sides.

340 loops were measured, in a small area to give a density at the foil centre of $L_c = 7.77 \times 10^{15}$ cm.$^{-3}$.

However in order to make a direct comparison with the 473°K profile, 2640 loops should have been measured in the area 8 cm. x 8 cm. at 36,000 mag. This implies that a multiplying factor of 7.7 must be applied to make a direct comparison.

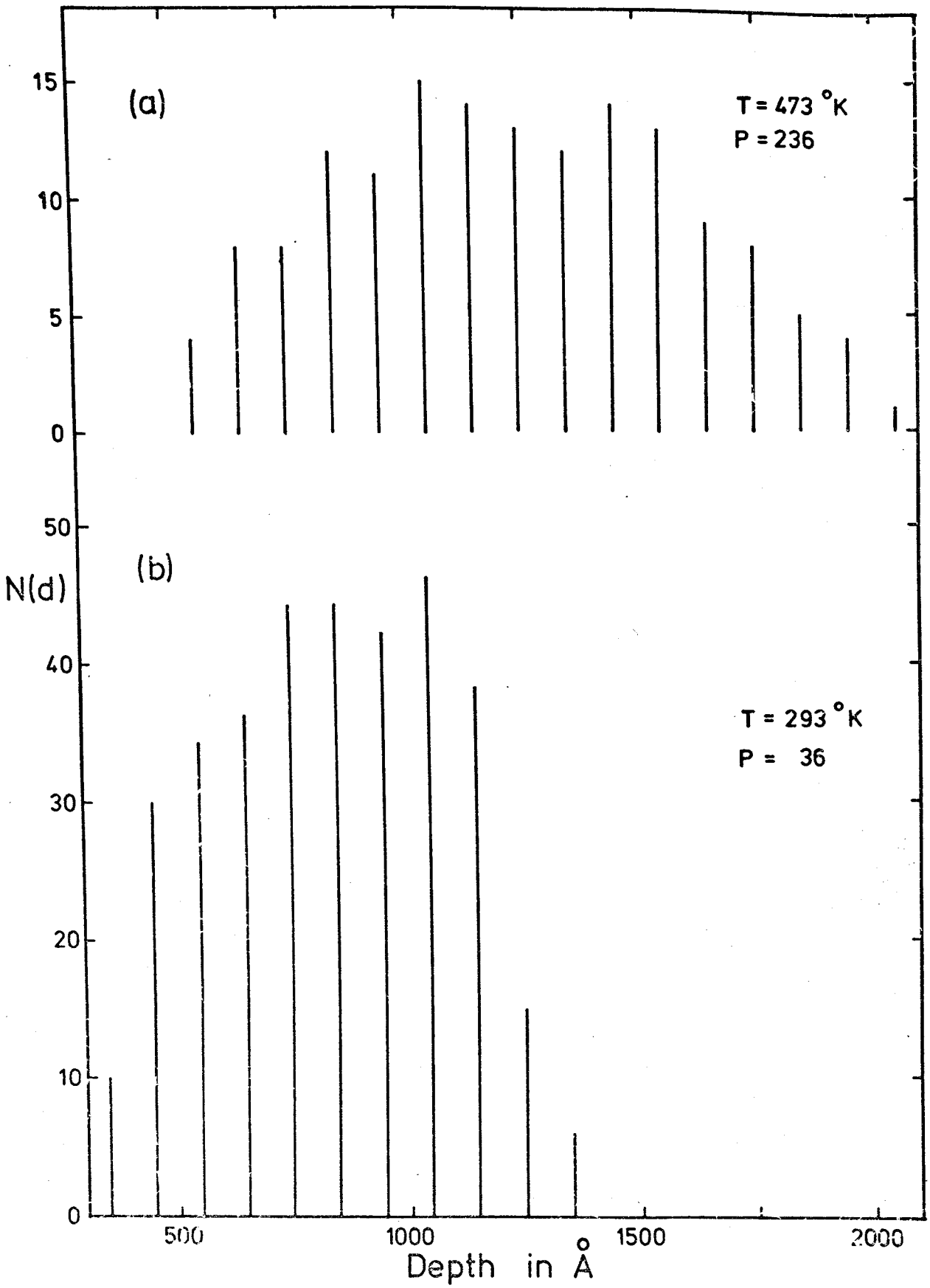
(a)
T = 473 °K
P = 236
(b)
T = 293 °K
P = 36
N(d)
Depth in Å
0
5
10
15
20
30
40
50
500
1000
1500
2000

Fig. 8/1 Cu 16% Al irradiated at $T_i = 240^{\circ}C$ after being annealed for 5 minutes at various temperatures T_a.

(A) $T_a = 280^{\circ}C$
(B) $T_a = 380^{\circ}C$
(C) $T_a = 440^{\circ}C$
(D) $T_a = 520^{\circ}C$

Note the increase in loop density at high values of T_a and the transition from perfect to imperfect loops as T_a increased.

Micrograph (D) also reveals the presence of a large number of very small Frank loops, which grow very slowly.

Foil polished at $-70^{\circ}C$, 4.4 volts.

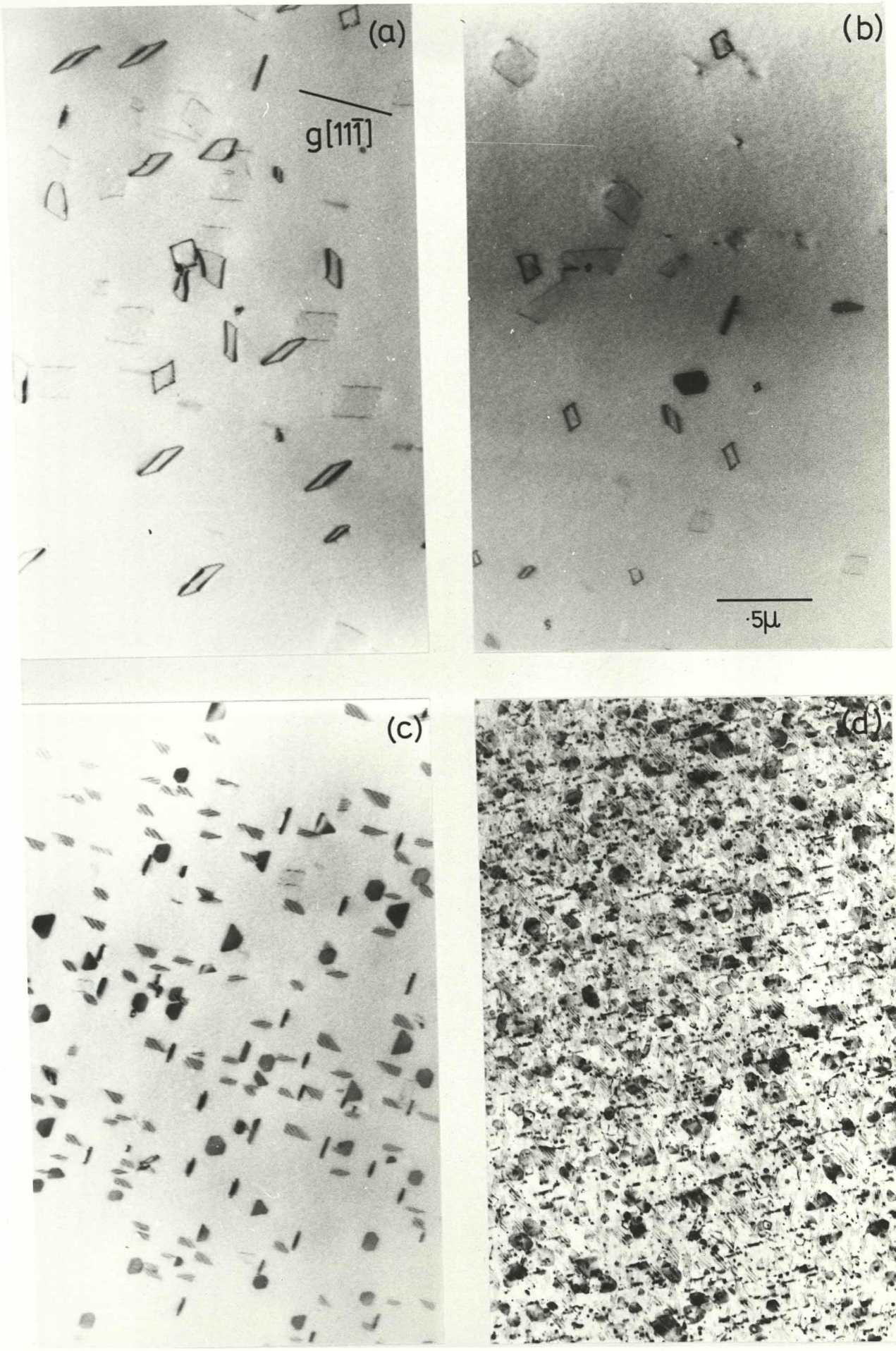
(a)
g[11$\bar{1}$]
(b)
·5μ
(c)
(d)

Fig. 8/2 Cu 16% Al irradiated at T_i = 265°C.

The graph shows the densities of Frank and perfect loops in a thin foil, as a function of annealing temperature T_a.

Hydrogen gas had already diffused out of the specimen before the high temperature anneals, causing the low initial but constant density up to the anneal temperature T_a = 390°C.

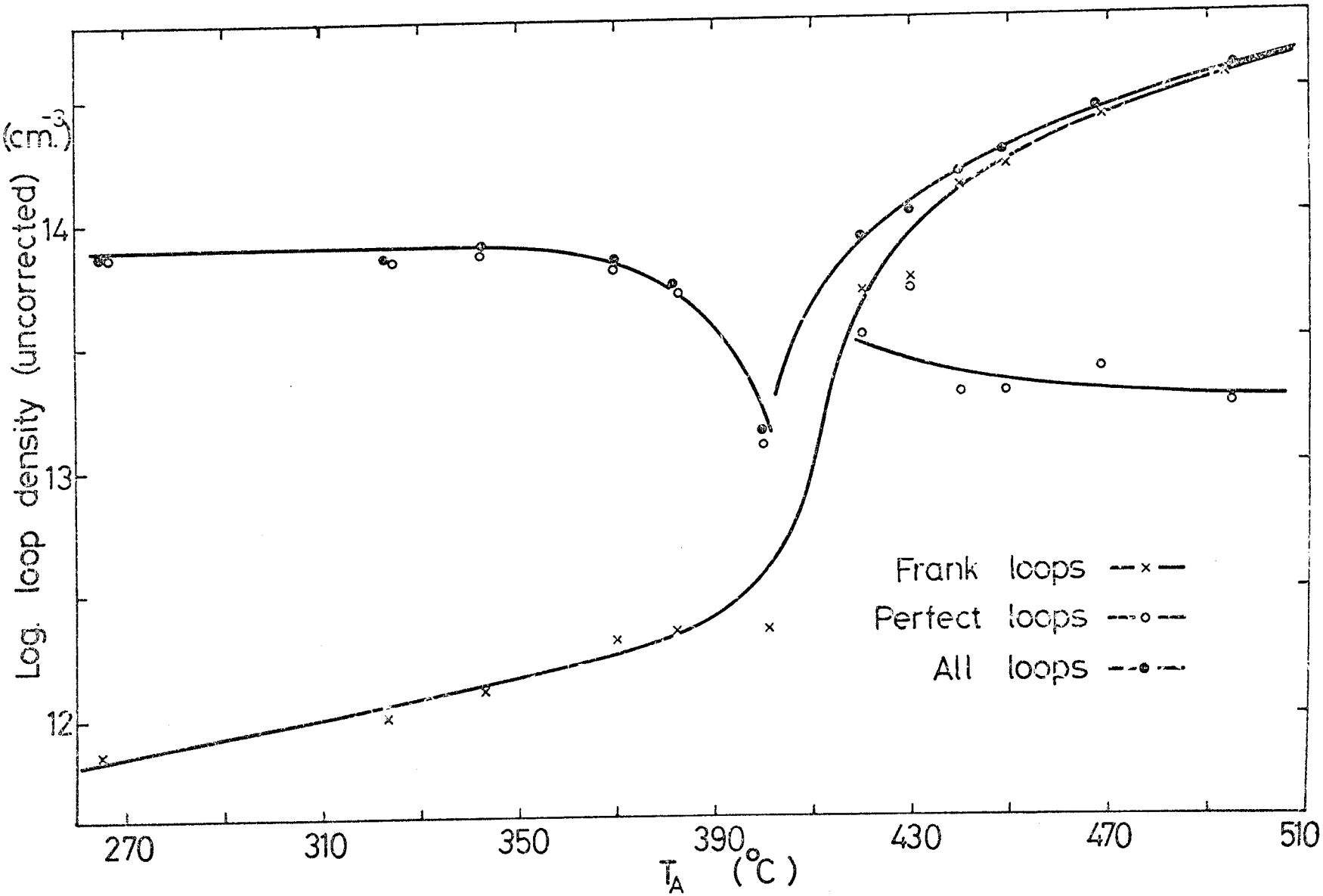
Log. loop density (uncorrected) (cm.$^{-3}$)
14
13
12
270
310
350
390
430
470
510
T_A (°C)
Frank loops
Perfect loops
All loops

Fig. 8/3 Cu 16% Al irradiated at T_i = 240°C.

Graph shows the saturation in Frank loop density as the anneal temperature is increased.

× uncorrected loop density

● corrected loop density, taking into account diffusion to the foil surfaces.

The dashed line represents the loop density of a specimen irradiated at 240°C after a 20 hour anneal at 750°C in a U.H.V. furnace.

The specimen was annealed after the electropolish treatment.

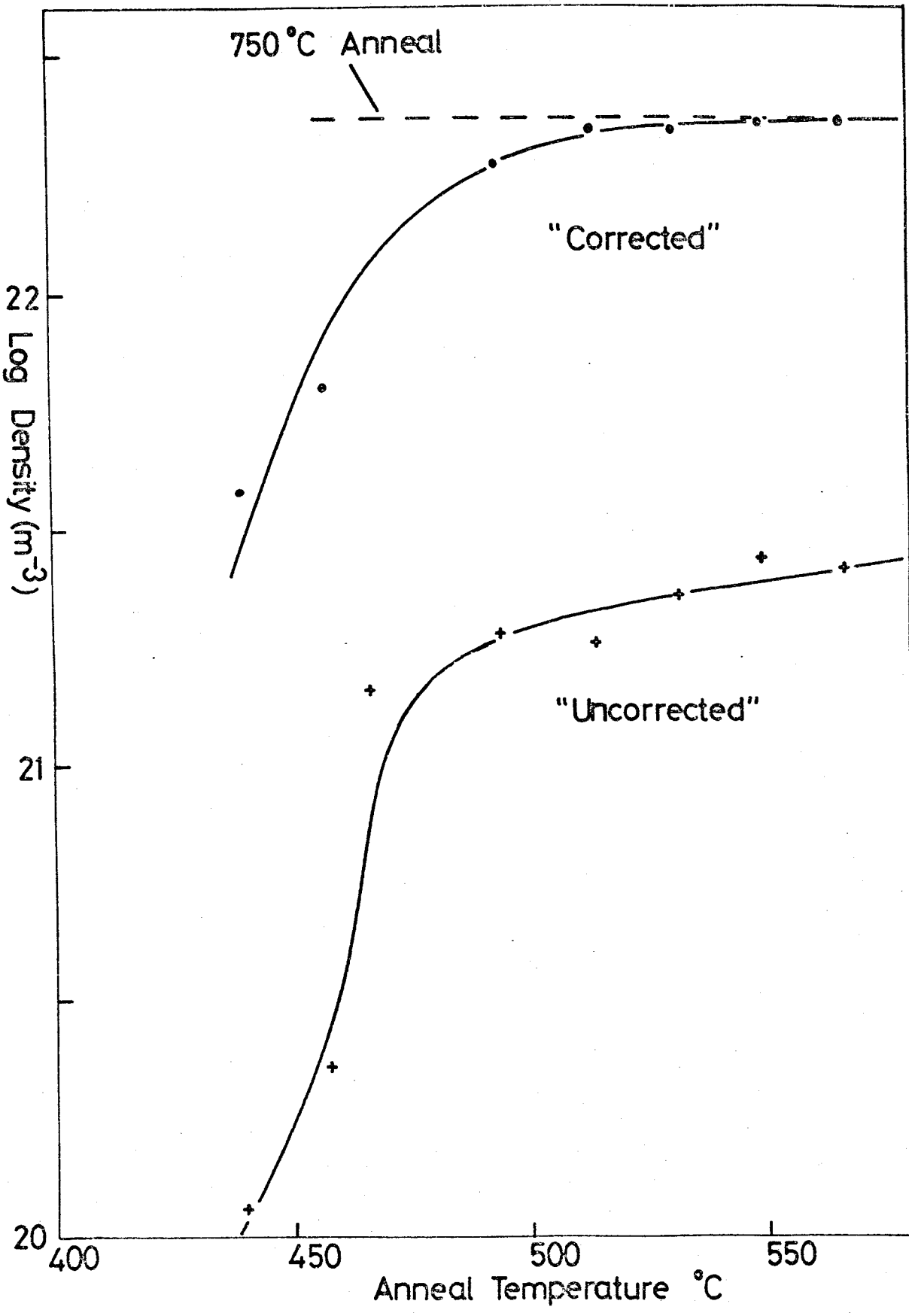
750 °C Anneal
"Corrected"
"Uncorrected"
Log Density (m-3)
22
21
20
400
450
500
550
Anneal Temperature °C

Fig. 8/4 Corrected loop density plotted against reciprocal temperature.

× Thin foil annealed for 300 seconds at 380°C in H.V.E.M.

• Thin foil annealed in U.H.V. furnace for 20 hours at 750°C in a vacuum of 1.2×10^{-9} torr.

Cu 16% Al generation rate $g = 3.79 \times 10^{19}$ cm.$^{-3}$ sec.$^{-1}$.

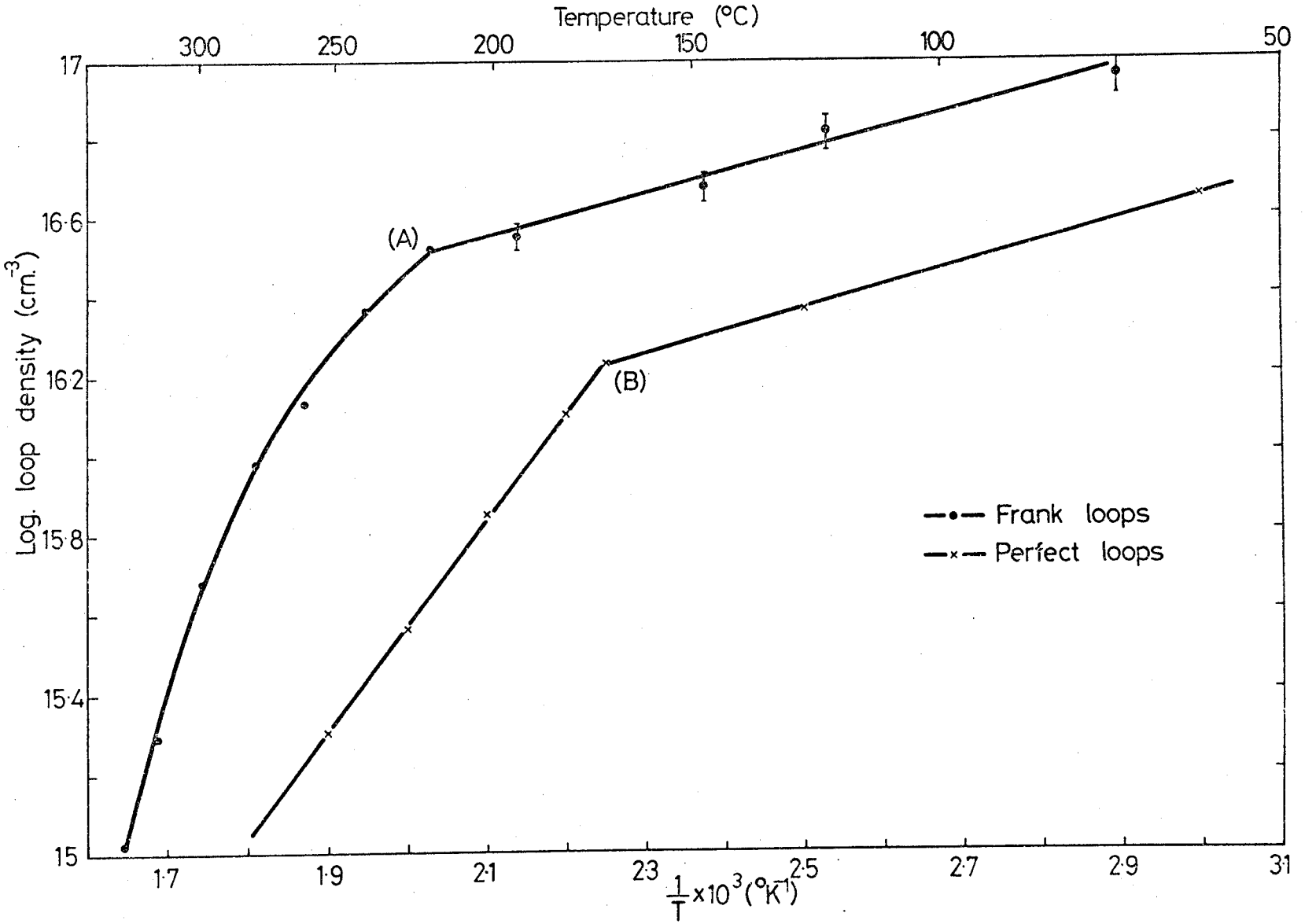
Temperature (°C)
300
250
200
150
100
50
17
16·6
16·2
15·8
15·4
15
Log. loop density (cm.$^{-3}$)
(A)
(B)
Frank loops
Perfect loops
1·7
1·9
2·1
2·3
2·5
2·7
2·9
3·1
$\frac{1}{T} \times 10^3$ (°K^{-1})

Fig. 8/5 shows the loop density uncorrected as a function of anneal temperature for a foil of Cu 2% Al irradiated at $T_i = 240^{\circ}C$.

Loop growth rates were also measured at A, B, C, D, E.

(A) gradient of logr/logt plot 1
$dr/dt = 2.03$ Å/sec.
$P_c = 515$

(B) gradient = .87
$dr/dt = 1.88$ Å/sec.
$P_c = 74$

(C) gradient = .89
$dr/dt = 1.42$ Å/sec.
$P_c = 561$

(D) gradient = .75
$dr/dt = 1.03$ Å/sec.
$P_c = 60$

(E) gradient = .78
$dr/dt = .55$ Å/sec.
$P_c = 43$

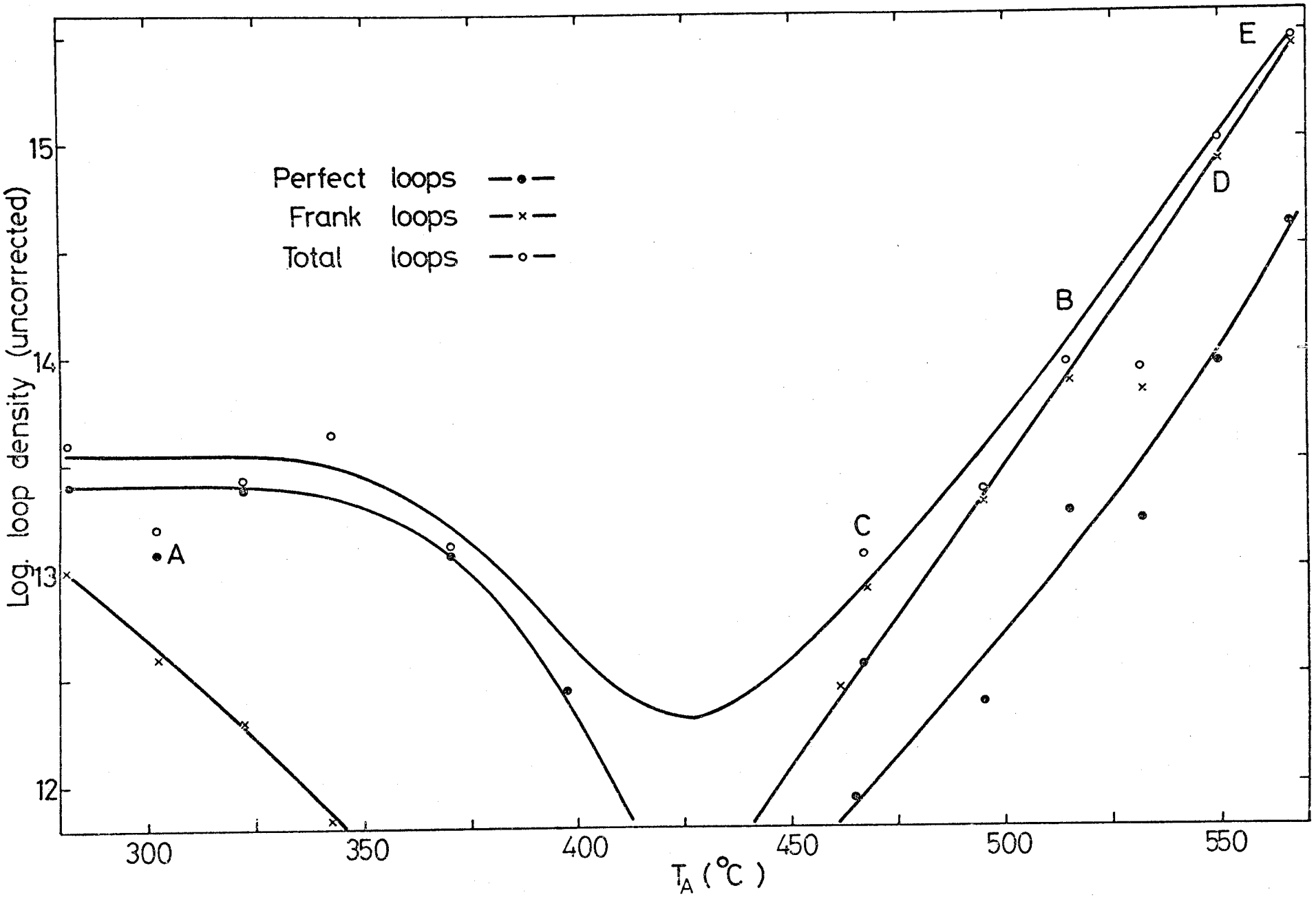
Perfect loops
Frank loops
Total loops
Log. loop density (uncorrected)
15
14
13
12
300
350
400
450
500
550
T_A (°C)
A
B
C
D
E

Fig. 8/6 Mean densities of Frank and perfect loops as a function of anneal temperature for a Cu 5% Al specimen.

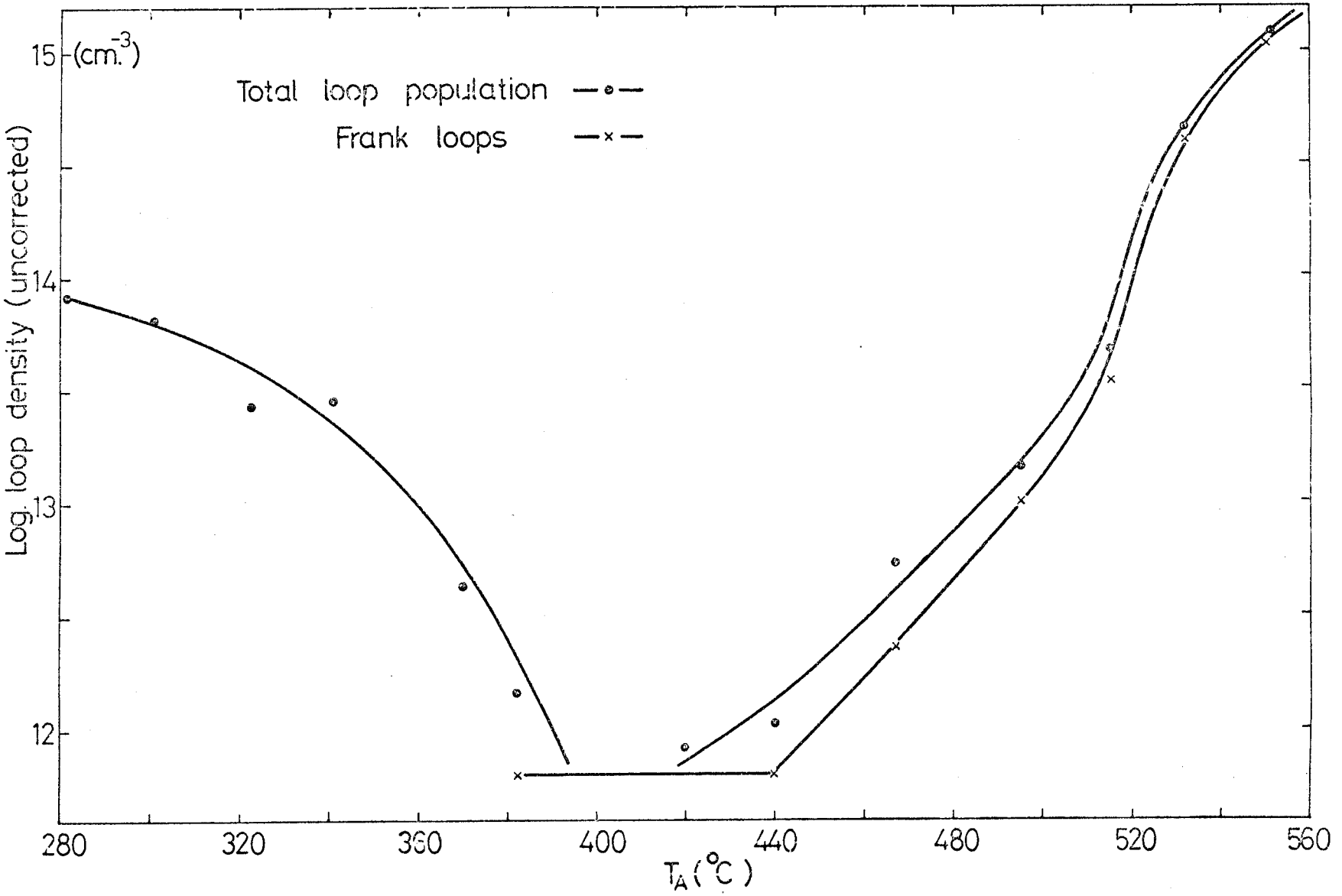
15
(cm.$^{-3}$)
Total loop population
Frank loops
Log. loop density (uncorrected)
14
13
12
280
320
360
400
440
480
520
560
T_A (°C)

Fig. 8/7 Comparison of total mean densities in Cu/Al foils after annealing at the temperatures indicated with irradiation at T_i = 240°C.

Dose rate = 1.5×10^{19} el./cm.^{2}/sec.

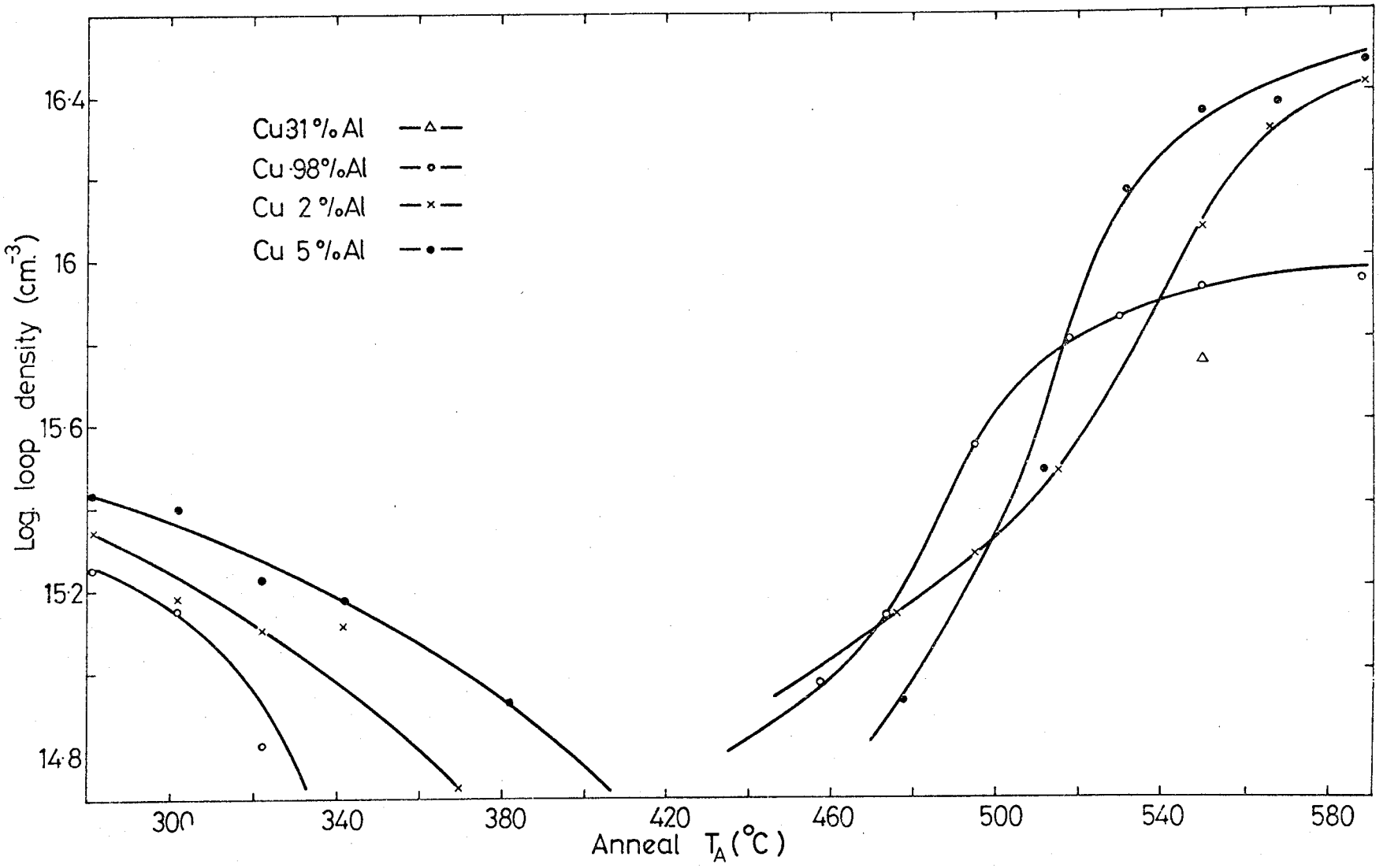
Cu31%Al
Cu·98%Al
Cu 2%Al
Cu 5%Al
Log. loop density (cm.$^{-3}$)
16·4
16
15·6
15·2
14·8
300
340
380
420
460
500
540
580
Anneal T_A (°C)

Fig. 8/8 Corrected loop density in a Cu 16% Al specimen as a function of annealing time at $T_a = 500^{\circ}C$. Irradiation temperature $T_i = 255^{\circ}C$.

Frank loops start to appear after about 1 minute of anneal then saturation of the loop density rapidly occurs.

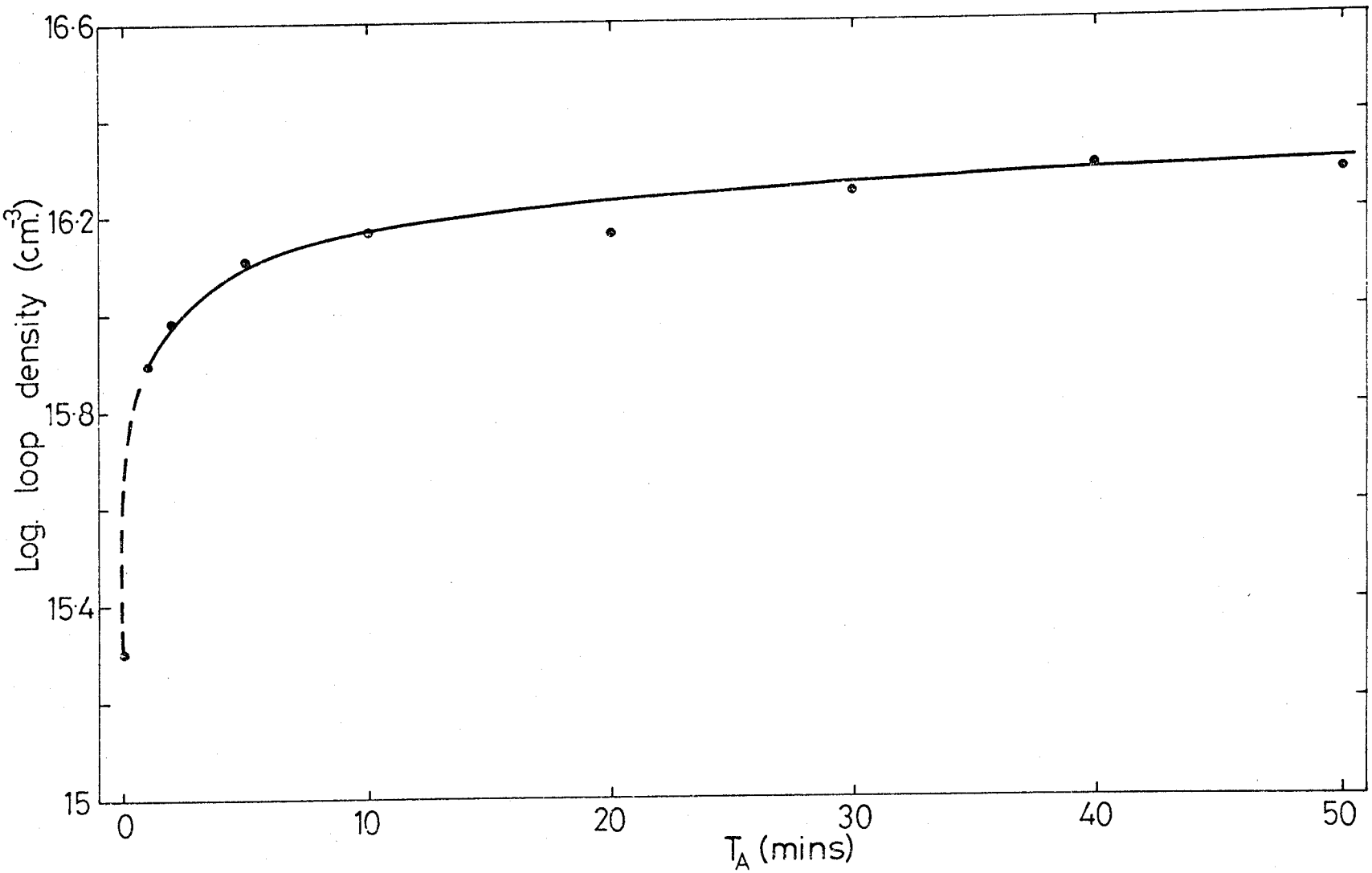
16·6
16·2
15·8
15·4
15
Log. loop density (cm.$^{-3}$)
0
10
20
30
40
50
T_A (mins)

Fig. 8/9 Cu 16% Al foil irradiated at $\simeq 10^{19}$ el./cm.^{2}/sec. at T_i = 255°C. after an annealing treatment in the microscope at a temperature of 500°C for increasing times. After one minute of anneal, a few Frank loops have nucleated and grown simultaneously with rhombus loops. After 10 minutes anneal, the large majority of loops are of Frank type. As the anneal time increases, the number of small loops in relation to the large loops increases.

(A) 1 minute anneal then irradiation at T_i = 255°C
(B) 10 minute anneal then irradiation at T_i = 255°C.
(C) 30 minute anneal then irradiation at T_i = 255°C.
(D) 50 minute anneal then irradiation at T_i = 255°C.

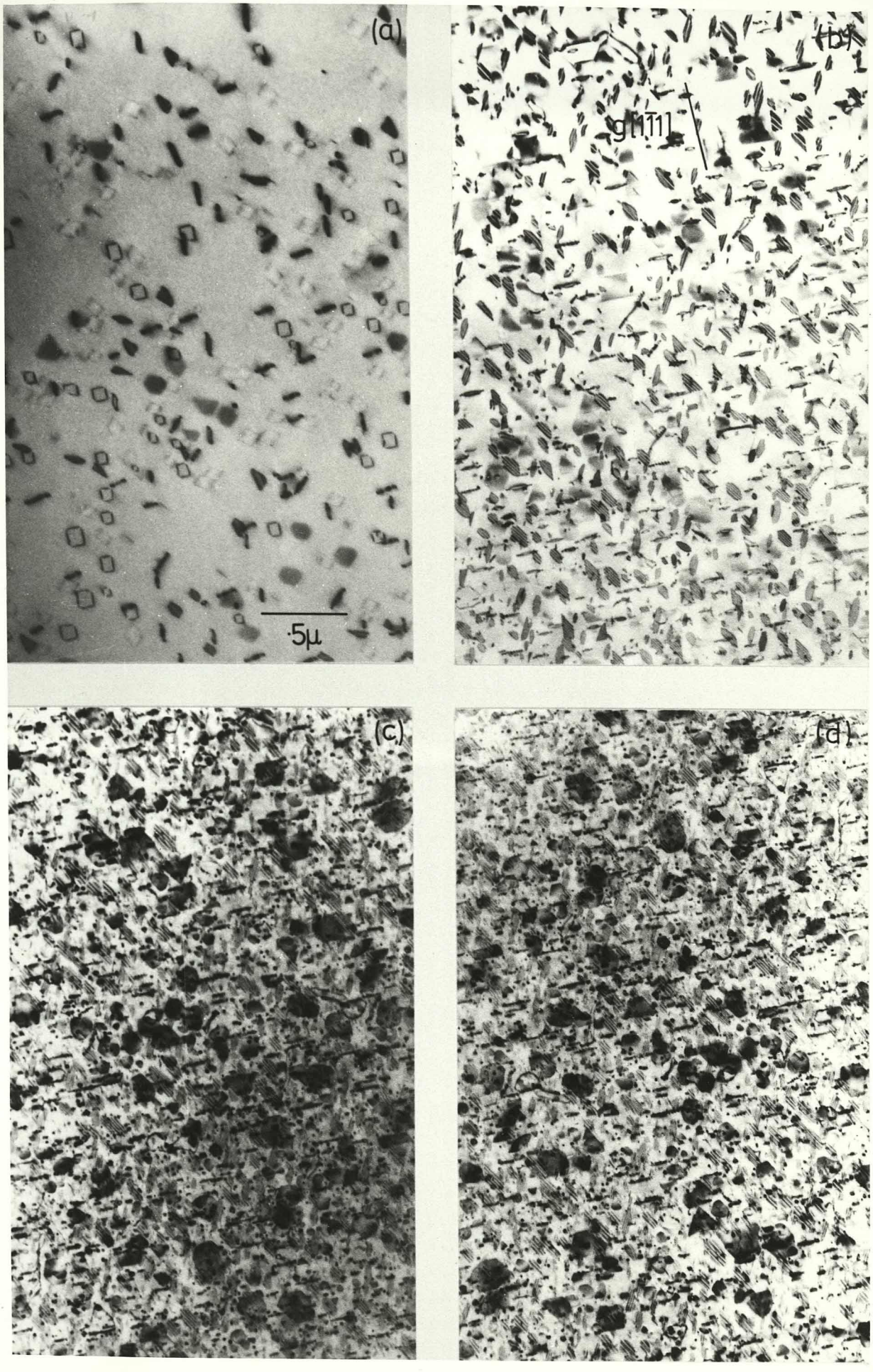
(a)
·5μ
(b)
g[111]
(c)
(d)

Fig. 8/10 Schematic diagram summarizing the possible explanations for the annealing effect in electropolished thin foils.

(α) specimens of Cu/Al alloys polished at temperatures $> -40^{o}C$ produce a high density of rhombus loops when irradiated as a result of the presence of hydrogen gas.

(β) specimens polished at $-75^{o}C$ produce a low density of rhombus loops, equivalent to a high temperature electropolished foil having been annealed in the H.V.E.M. for 5 minutes at $380^{o}C$ then irradiated.

(γ) This point represents the region where Frank loop density > rhombus loop density.

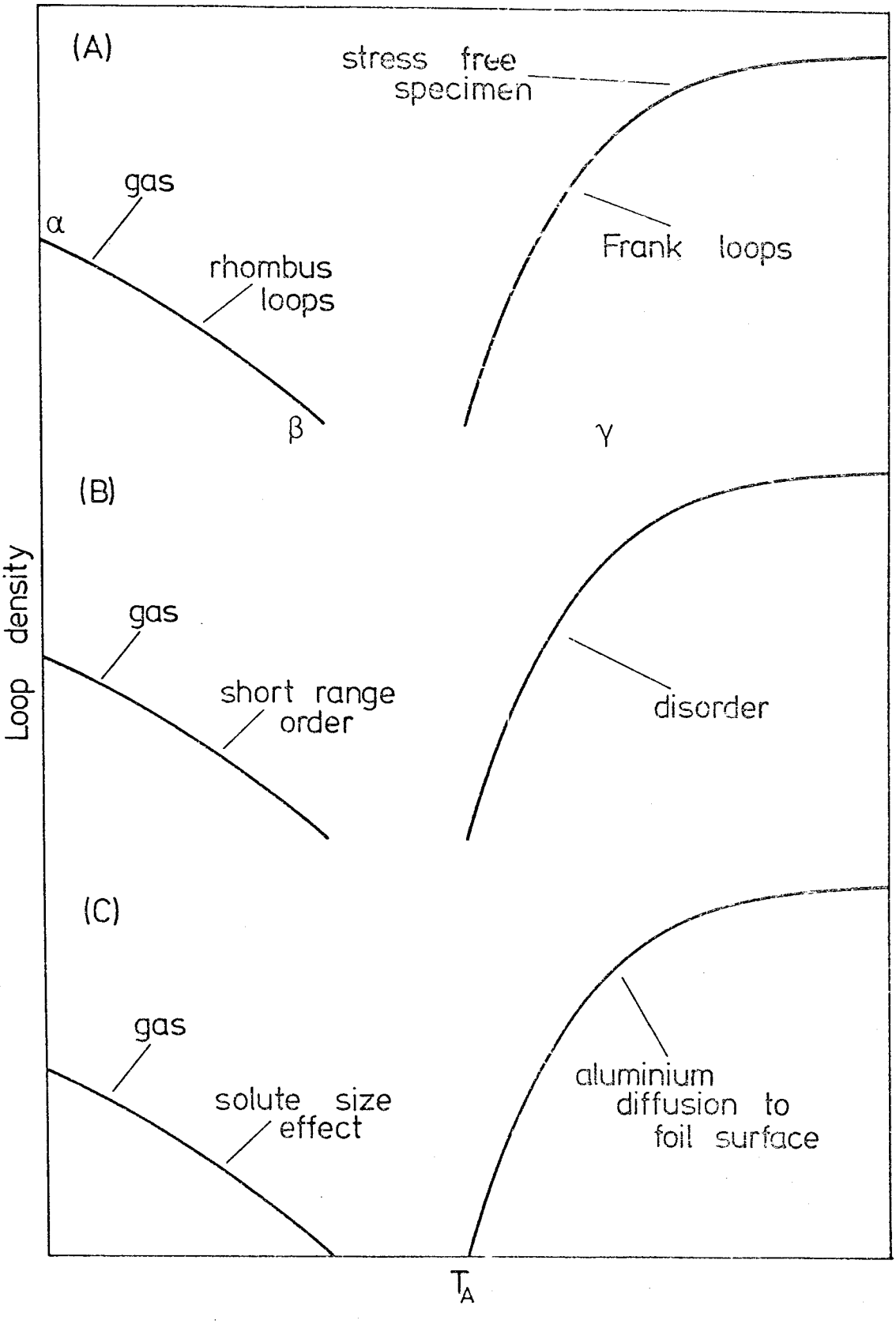
(A)
stress free specimen
gas
α
rhombus loops
Frank loops
β
γ
(B)
gas
short range order
disorder
(C)
gas
solute size effect
aluminium diffusion to foil surface
Loop density
T_A

Fig. 8/11 Graph shows the ratio of faulted to total loop population as a function of dilute alloy concentration, in foils polished at low temperatures and cut from slow grown crystals.

There is also a slight variation of R with each alloy as a function of irradiation temperature, the lower irradiation temperature giving the highest number of Frank loops.

$R \rightarrow .01$ at Cu 5% Al.

Foil thickness $\simeq$ 2500 Å

Measurements made in the temperature range 150°C to 240°C.

Preliminary experiments have indicated that the number of Frank loops increases in foils of thickness >3000 Å.

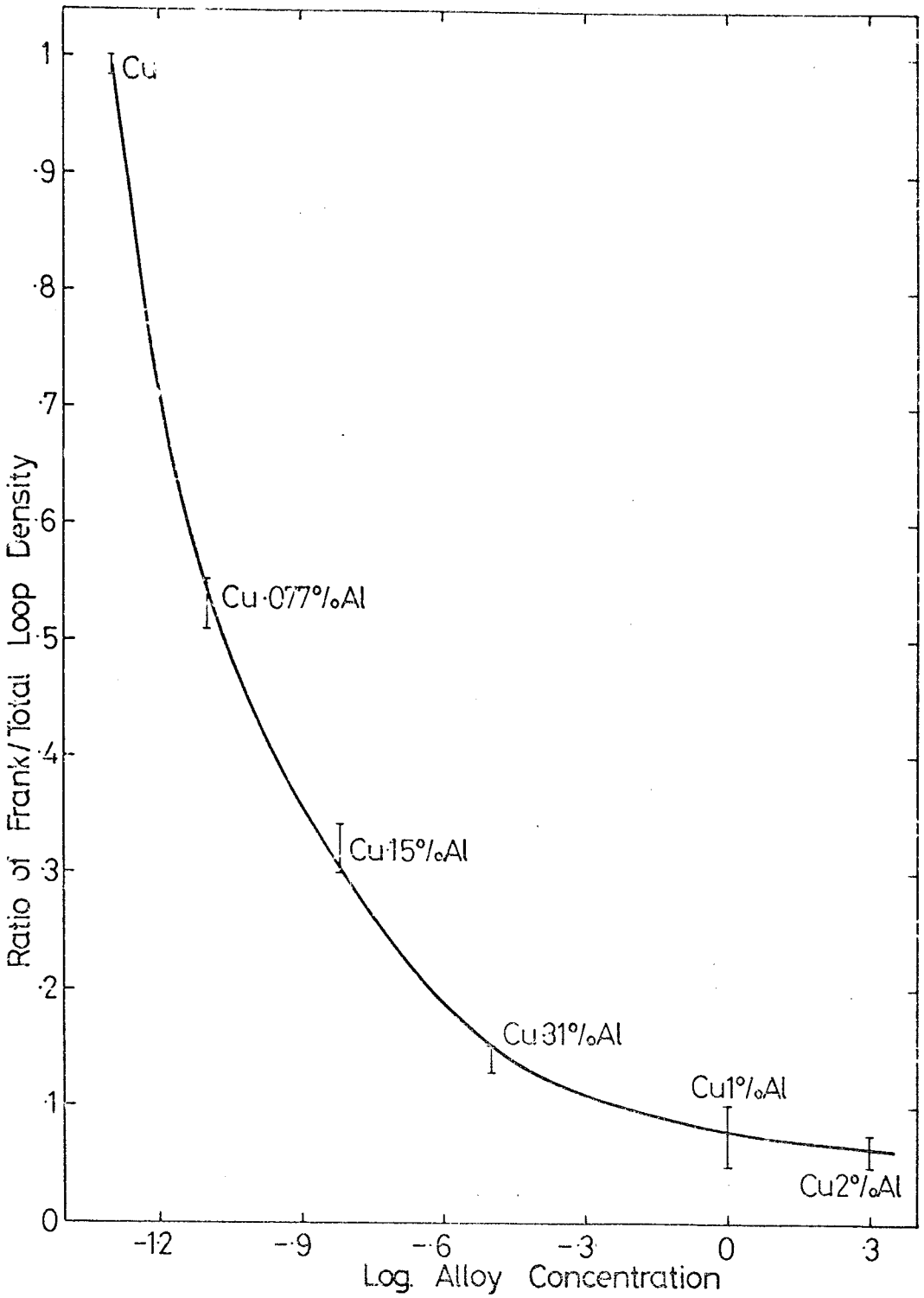
Cu
Cu·077%Al
Cu·15%Al
Cu·31%Al
Cu1%Al
Cu2%Al
Ratio of Frank/Total Loop Density
Log. Alloy Concentration
1
·9
·8
·7
·6
·5
·4
·3
·2
·1
0
-12
-9
-6
-3
0
3

Fig. 8/12 Atomic arrangement in two neighbouring (111) planes for an ordered structure of Cu and Al atoms built up from the two configurations above, (Borie and Sparks). The full circles and triangles denote Cu and Al atoms above the slip plane and the open circles and triangles those atoms below the slip plane.

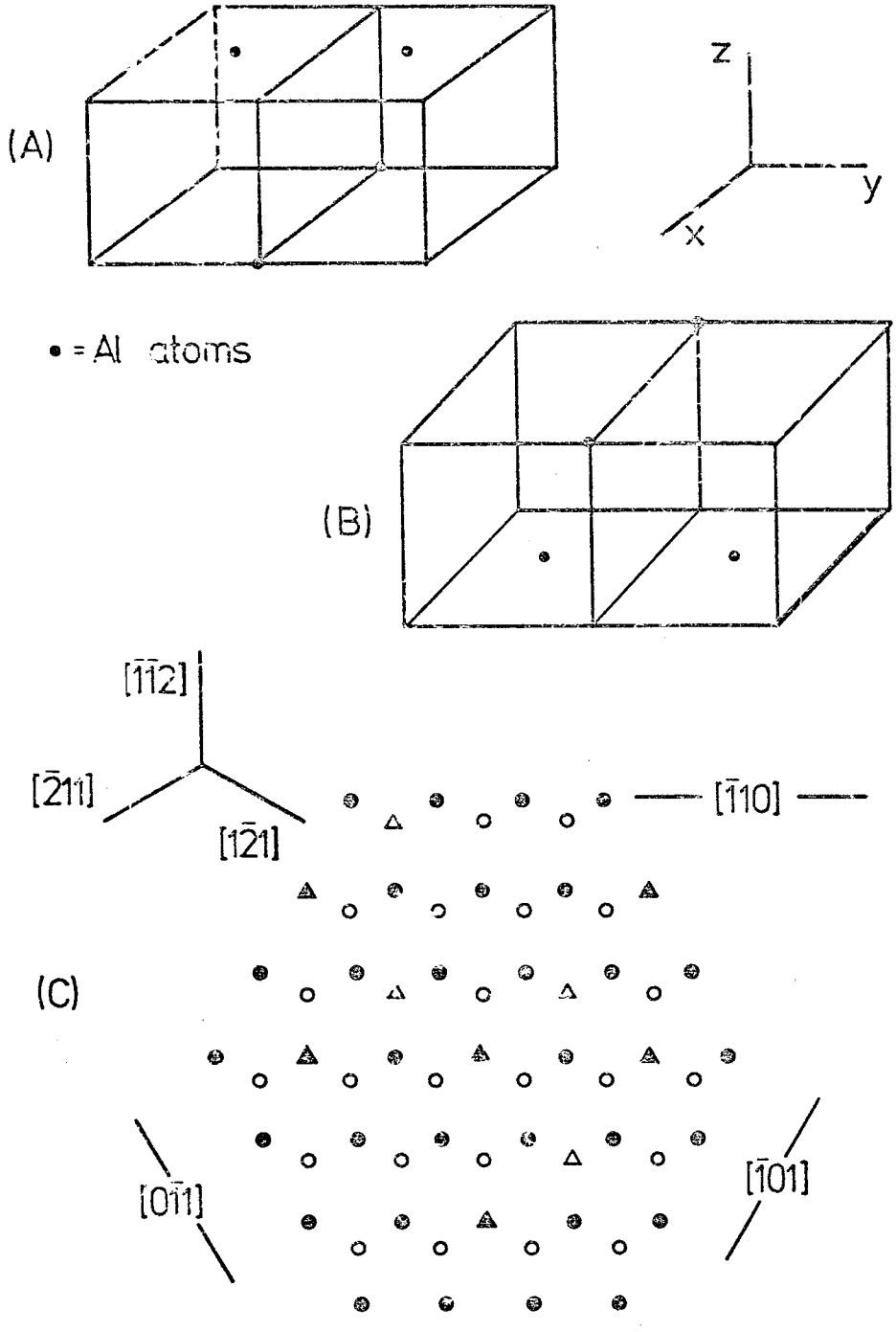
(A)
z
y
x
• = Al atoms
(B)
[1̄1̄2]
[2̄11]
[1̄2̄1]
[1̄10]
(C)
[01̄1]
[1̄01]

Fig. 8/13 Weak beam micrograph (g = <111> g/5g satisfied) of a domain like structure in a Cu 16% Al foil (unirradiated) cut from a slow grown crystal.


600Å

Fig. 8/14 Size distribution of faulted and unfaulted loops in a Cu 16% Al foil after irradiation at room temperature.

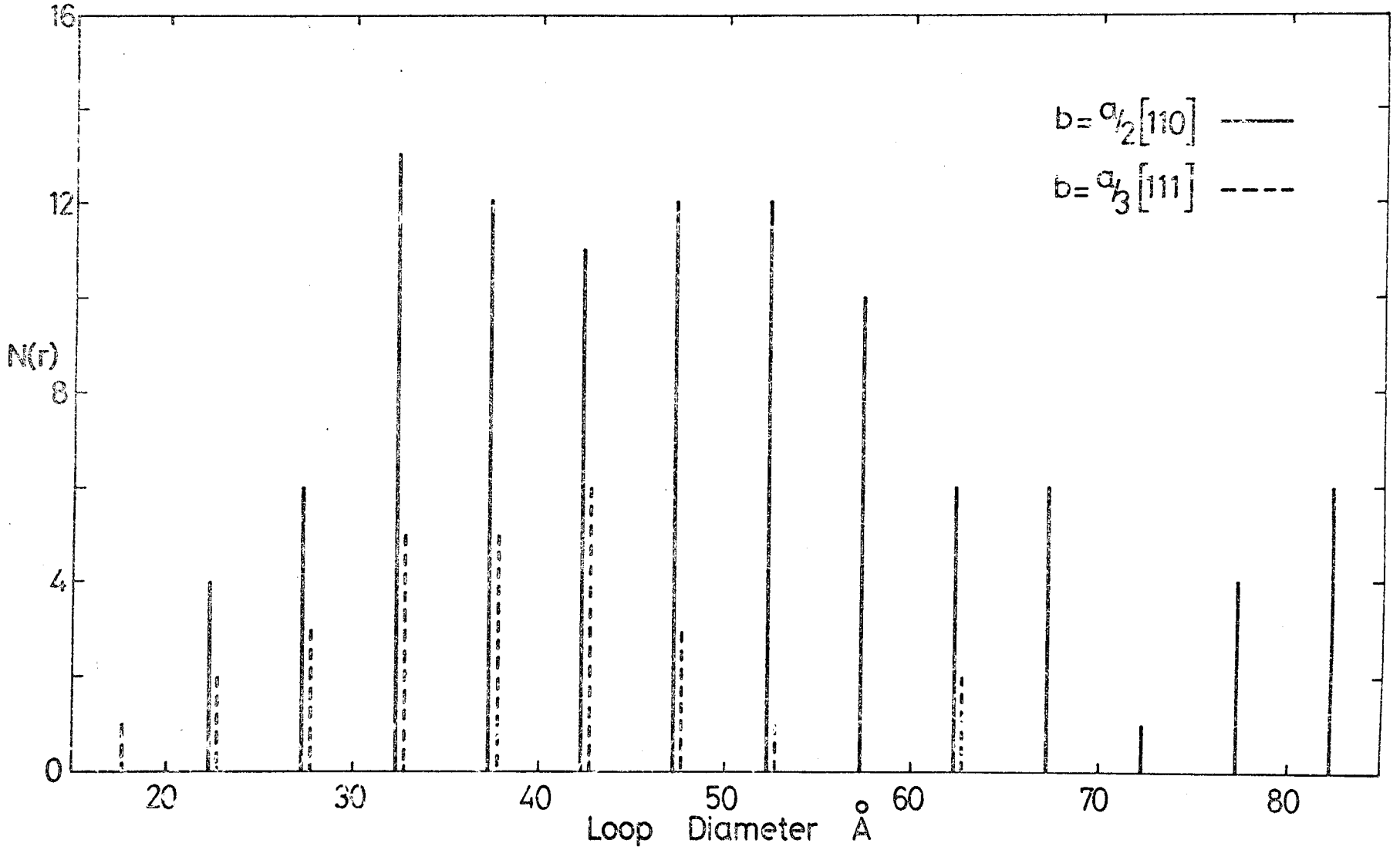
16
12
8
4
0
N(r)
20
30
40
50
60
70
80
Loop Diameter Å
b= a/2[110]
b= a/3[111]

Fig. 9/1 Void formation in copper aluminium alloys irradiated at $T_i = 250^{o}C$.
Fluence = 4.5×10^{-3} dpa/sec.
Dose = 45 dpa.

(a) Copper
(b) Cu 31% Al
(c) Cu 2% Al
(d) Cu 10% Al

These specimens were irradiated without previous in-situ anneal.

The first observations of void growths were:-

Cu $\simeq$ 5 dpa
Cu 31% Al $\simeq$ 5.4 dpa
Cu 2% Al $\simeq$ 15 dpa
Cu 5% Al no voids at 50 dpa
Cu 16% Al no voids at 67 dpa

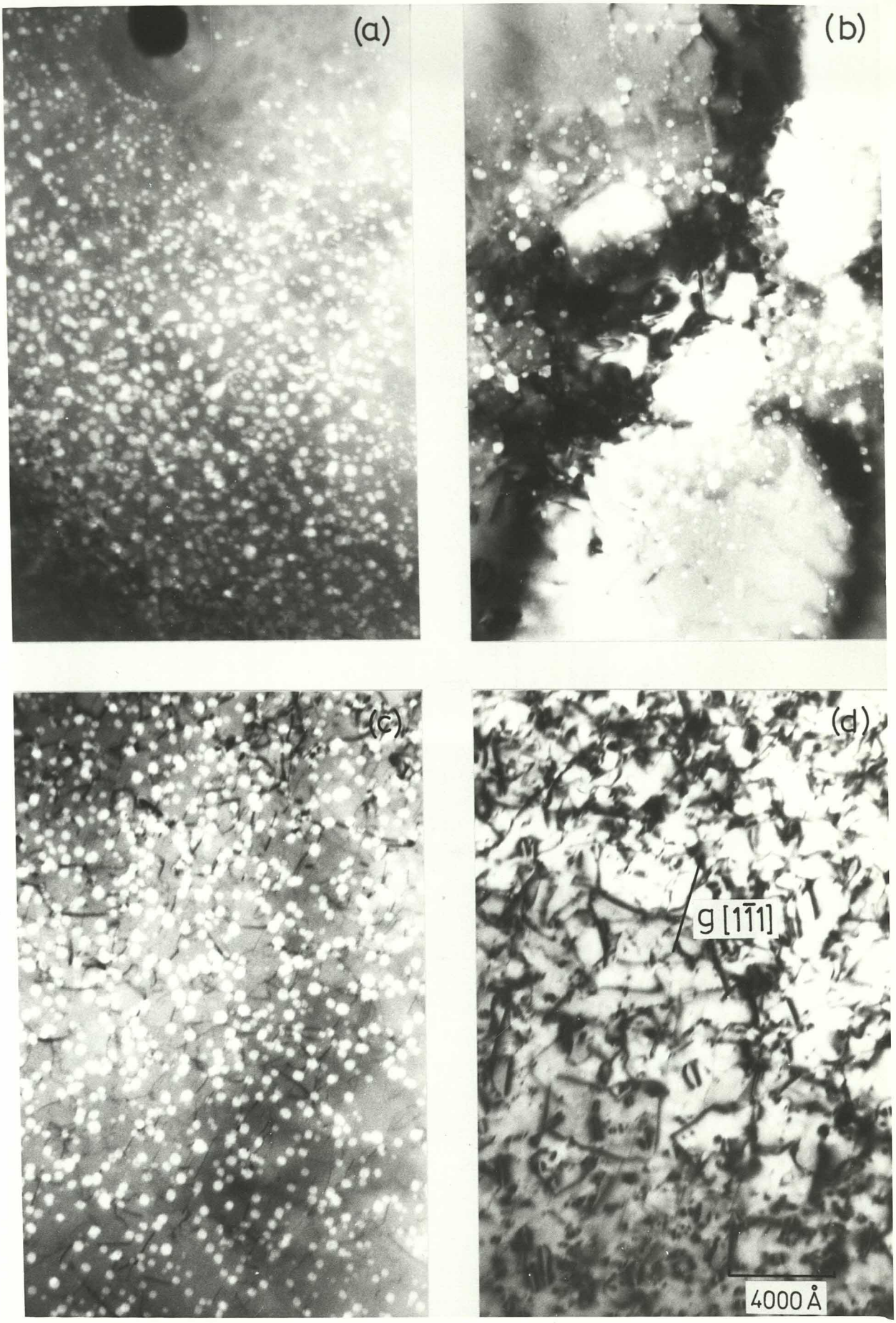
(a)
(b)
(c)
(d)
g [1$\bar{1}$1]
4000 Å

Fig. 9/2 Void growth in Cu 31% Al showing the development of voids along certain dislocations, after irradiation at T_i = 250°C.

(A) 10.3 dpa.

(B) 14.8 dpa.

(C) 21 dpa.

(D) 33 dpa.

Dose rate 4.7×10^{-3} dpa.sec.$^{-1}$.

No in-situ anneal treatment given to the specimen.

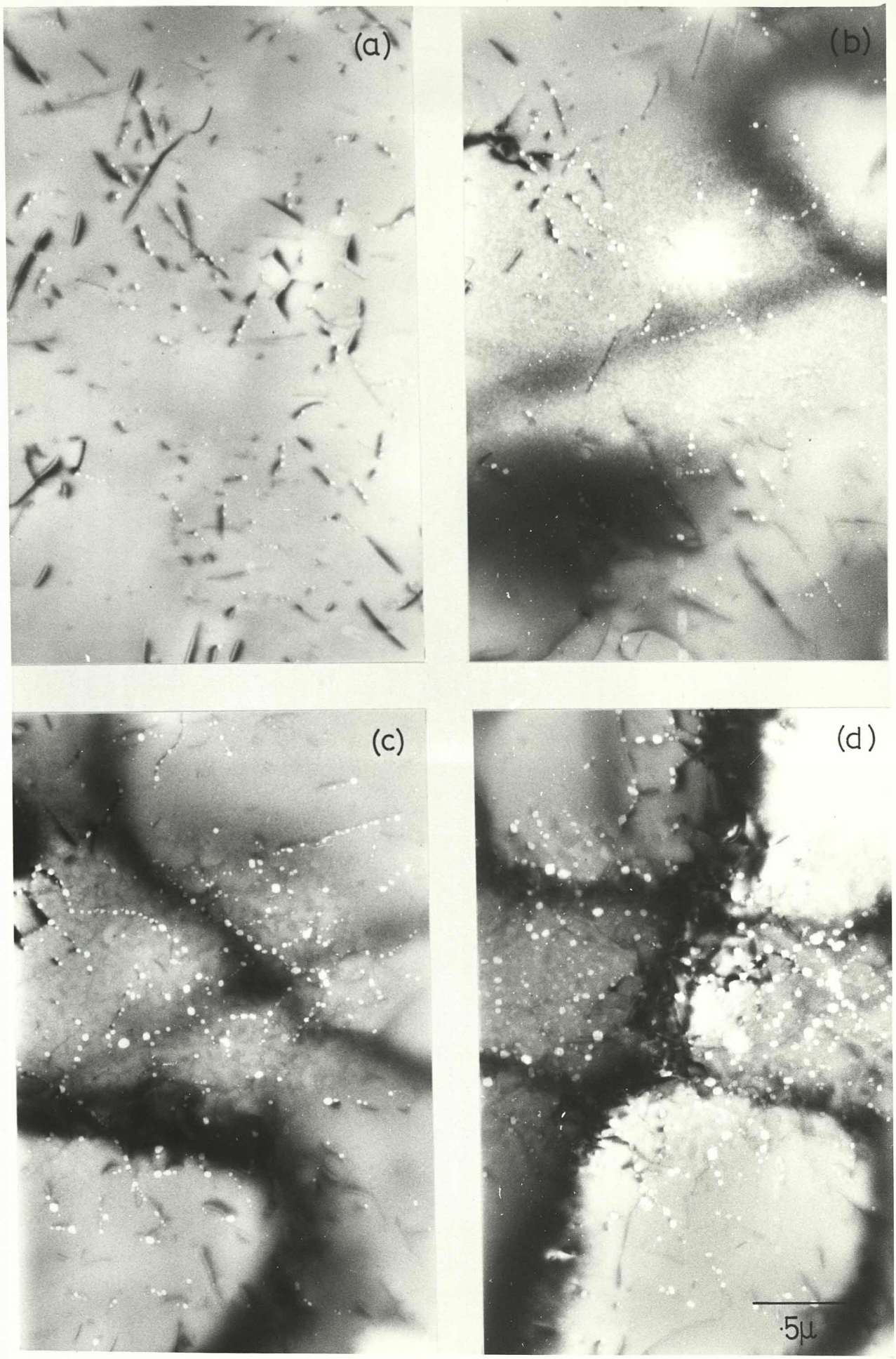
(a)
(b)
(c)
(d)
·5μ

Fig. 9/3 Cu 5% Al specimen irradiated to a dose of 19 dpa. at a temperature of 250°C.

(A) No in-situ anneal given. Rhombus loops grew initially, but then developed into a rapidly climbing dislocation tangle. Many small loops are also visible. No voids were grown.

(B) Specimens annealed in the H.V.E.M. for 10 minutes at 530°C prior to irradiation. Irradiation caused a high density of Frank loops to nucleate and develop into a slow climbing dislocation network. Voids first appeared after 5 dpa.

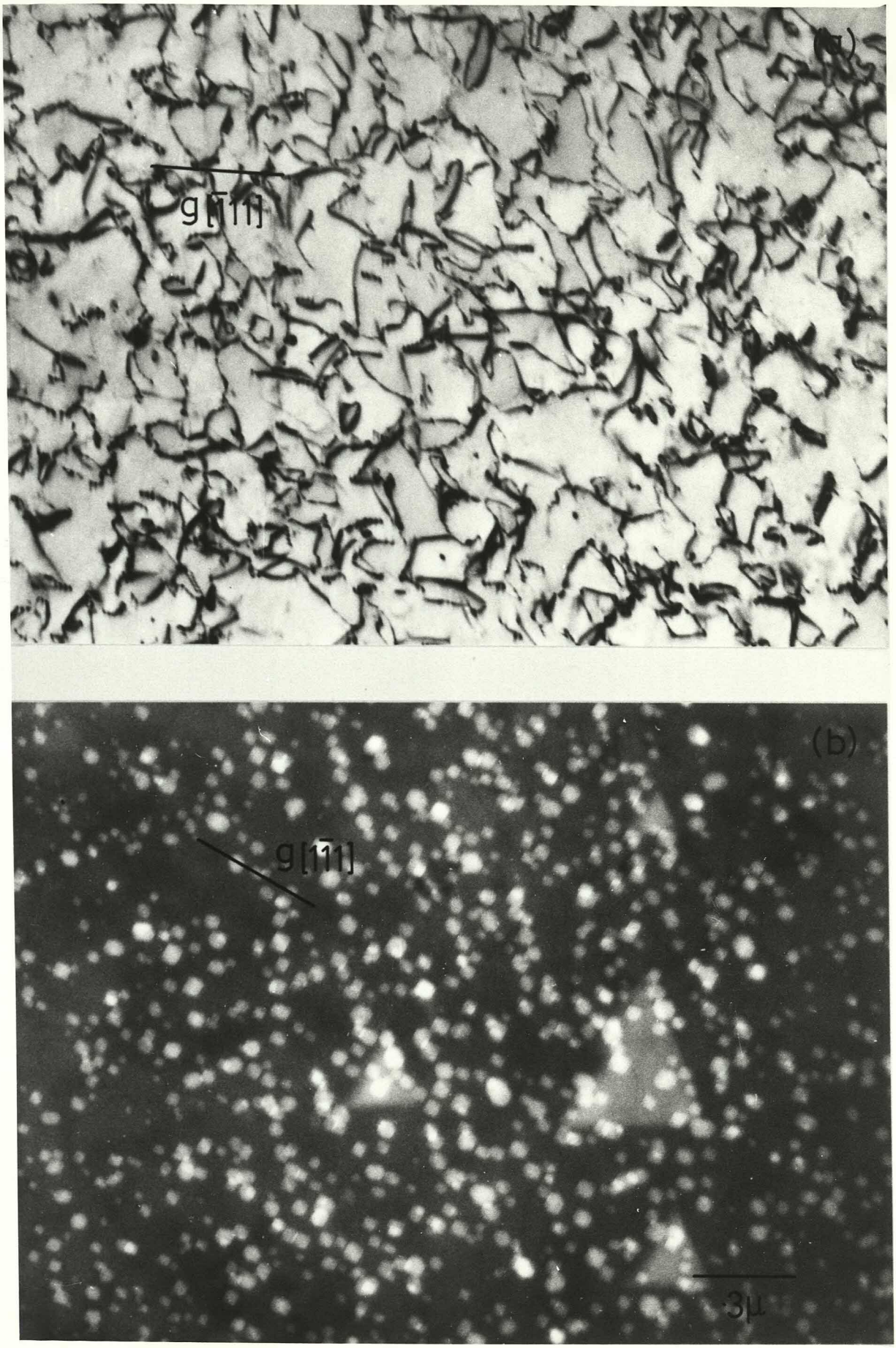
(a)
g[$\bar{1}$11]
(b)
g[$\bar{1}$11]
3μ

Fig. 10/1 Typical Frank loops in electron irradiated copper at T_i = 210°C. Growth rates of the numbered loops have been measured.

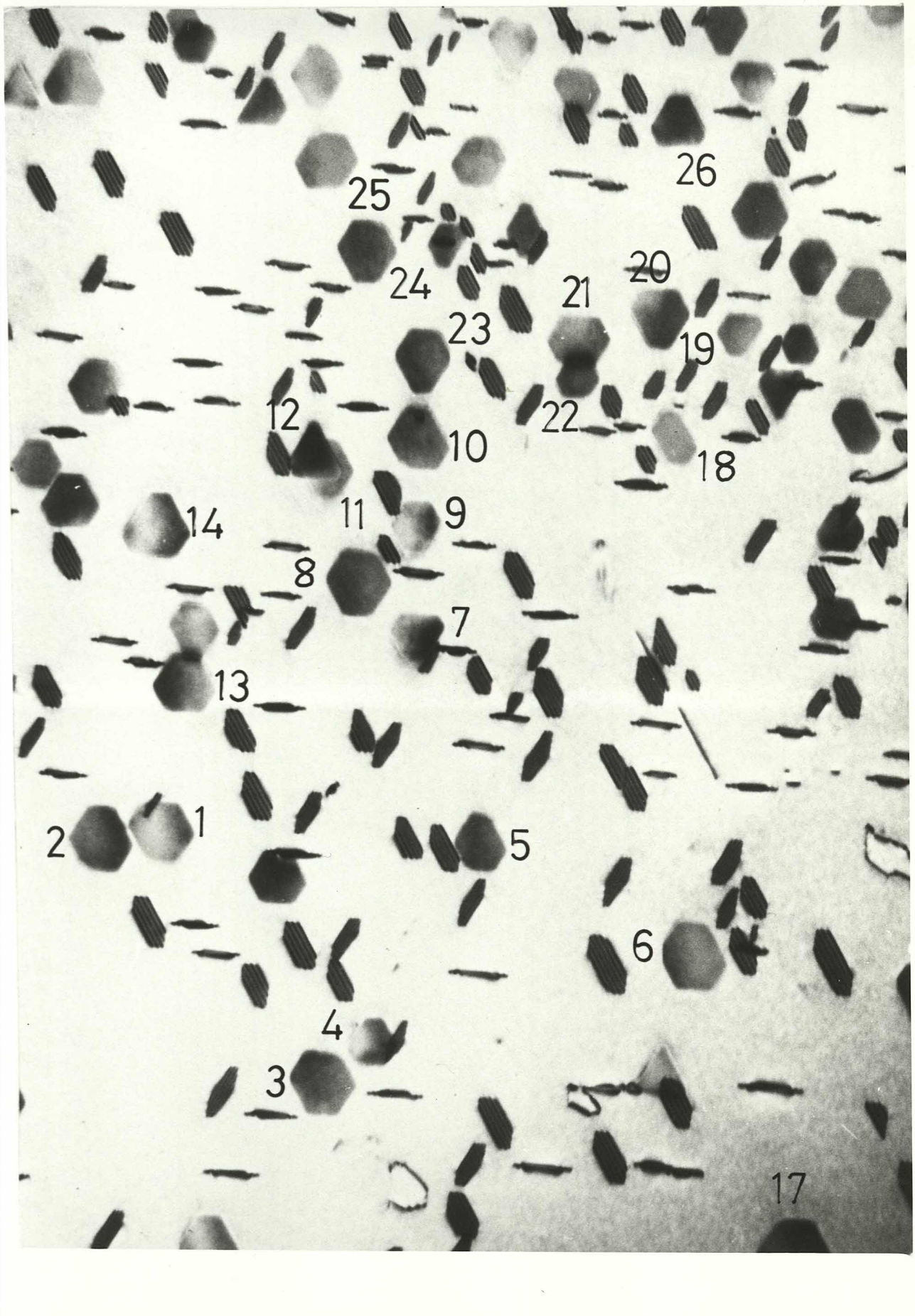
25
26
24
20
21
23
19
12
22
10
18
14
11
9
8
7
13
2
1
5
6
4
3
17

Fig. 10/2 Electron irradiated copper at T_i = 210°C.

Graph illustrates the differences in loop growth rates for Frank loops on various {111} planes. (The average growth rates of many loops were used).

Loops A .93 Å/sec.

Loops B and C .68 Å/sec.

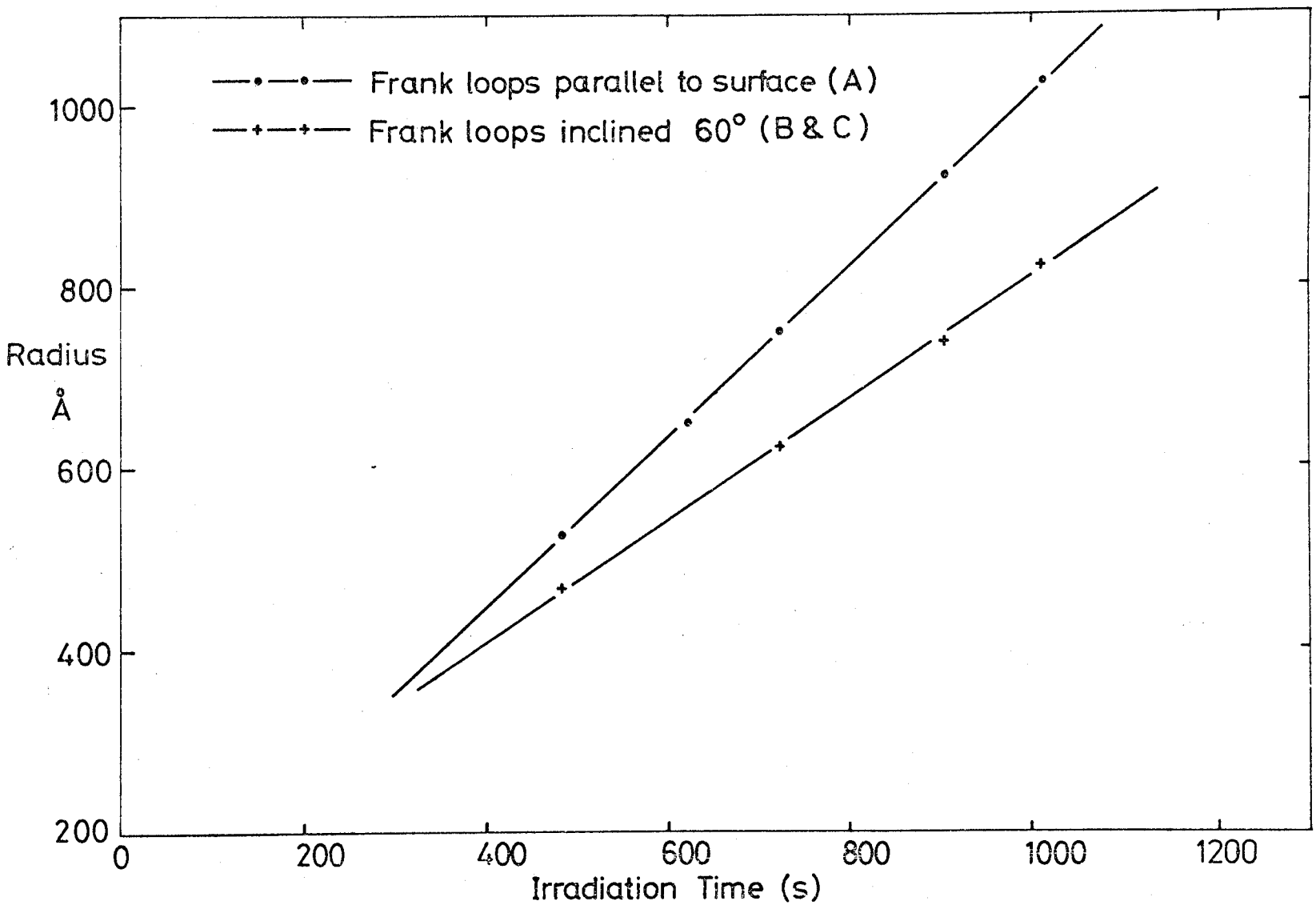
Frank loops parallel to surface (A)
Frank loops inclined 60° (B & C)
1000
800
600
400
200
Radius
Å
0
200
400
600
800
1000
1200
Irradiation Time (s)

Fig. 10/3 Growth rates as a function of depth for Frank loops in zone refined copper irradiated at 210°C, see fig. 10/1.

Curves 1 and 2 area measurements of loops 21 and 22.
Curve 4 average of 1 and 2.
Curve 3 and 5 long diameter measurement of loops 21 and 22.
Curve 6 area measurement of loop 11.
Curve 7 area measurement of loop 12.

Loops 21 and 22 overlap after 10 minutes of irradiation and the vertical separation measured by stereomicroscopy was $\triangleq$ 450 Å. Loop 21 was nearer the electron entrance surface.

Loops 11 and 12 overlap, but the growth rates from area measurements was linear. The measured separation was $\triangleq$ 1070 Å.

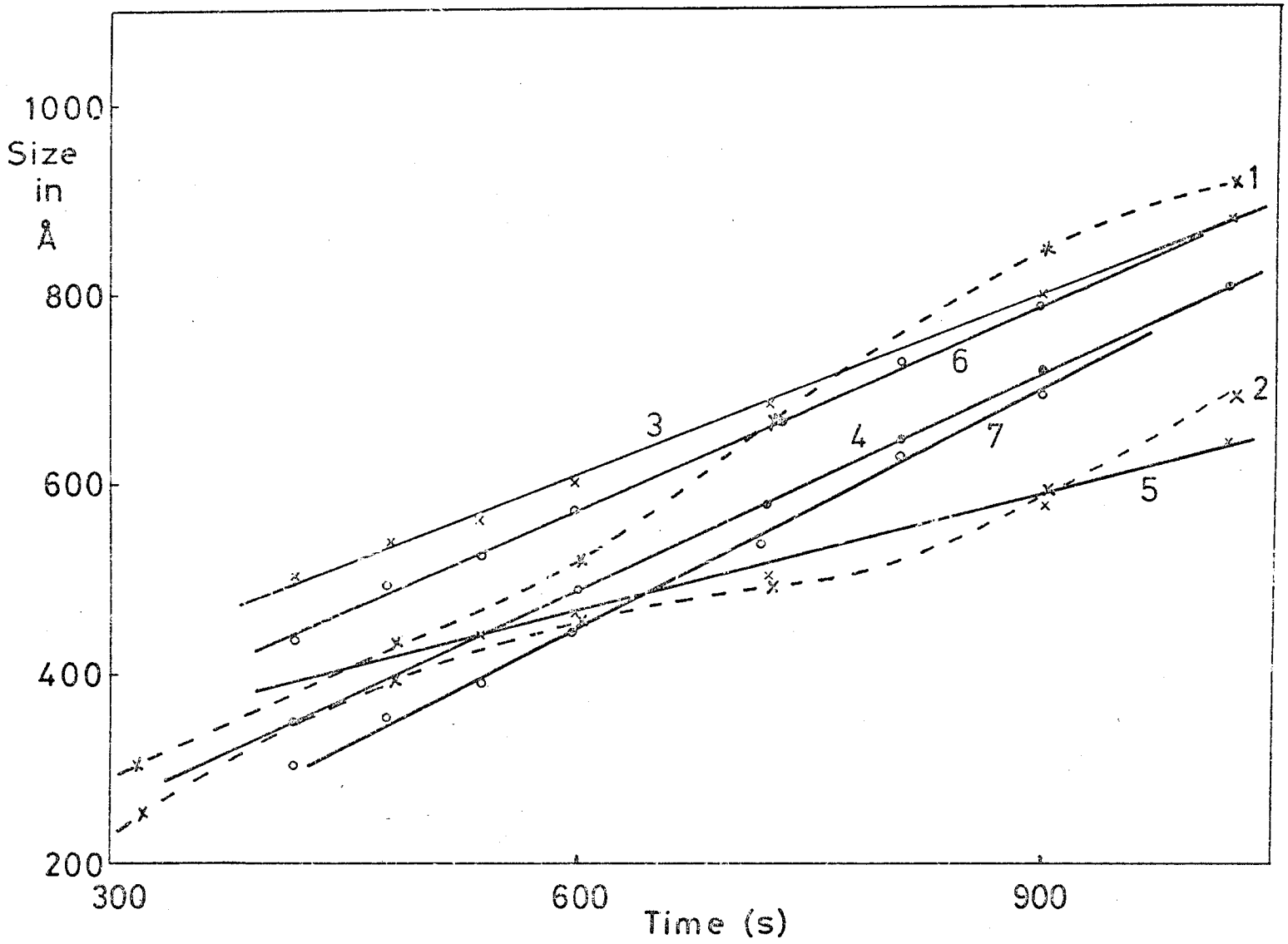
1000
Size
in
Å
800
600
400
200
300
600
900
Time (s)
x1
x2
3
4
5
6
7

Fig. 10/4 Growth rate of Frank loops in a copper foil of thickness 3500 Å during irradiation at T_i = 205°C.

Though the loops are of very irregular shape, the growth rate is regular. As the loop density increased in an irradiated foil, the degree of irregularity is also increased.

g <111> z <211>

(A) 20 minutes
(B) 26 minutes
(C) 37½ minutes
(D) 58½ minutes.

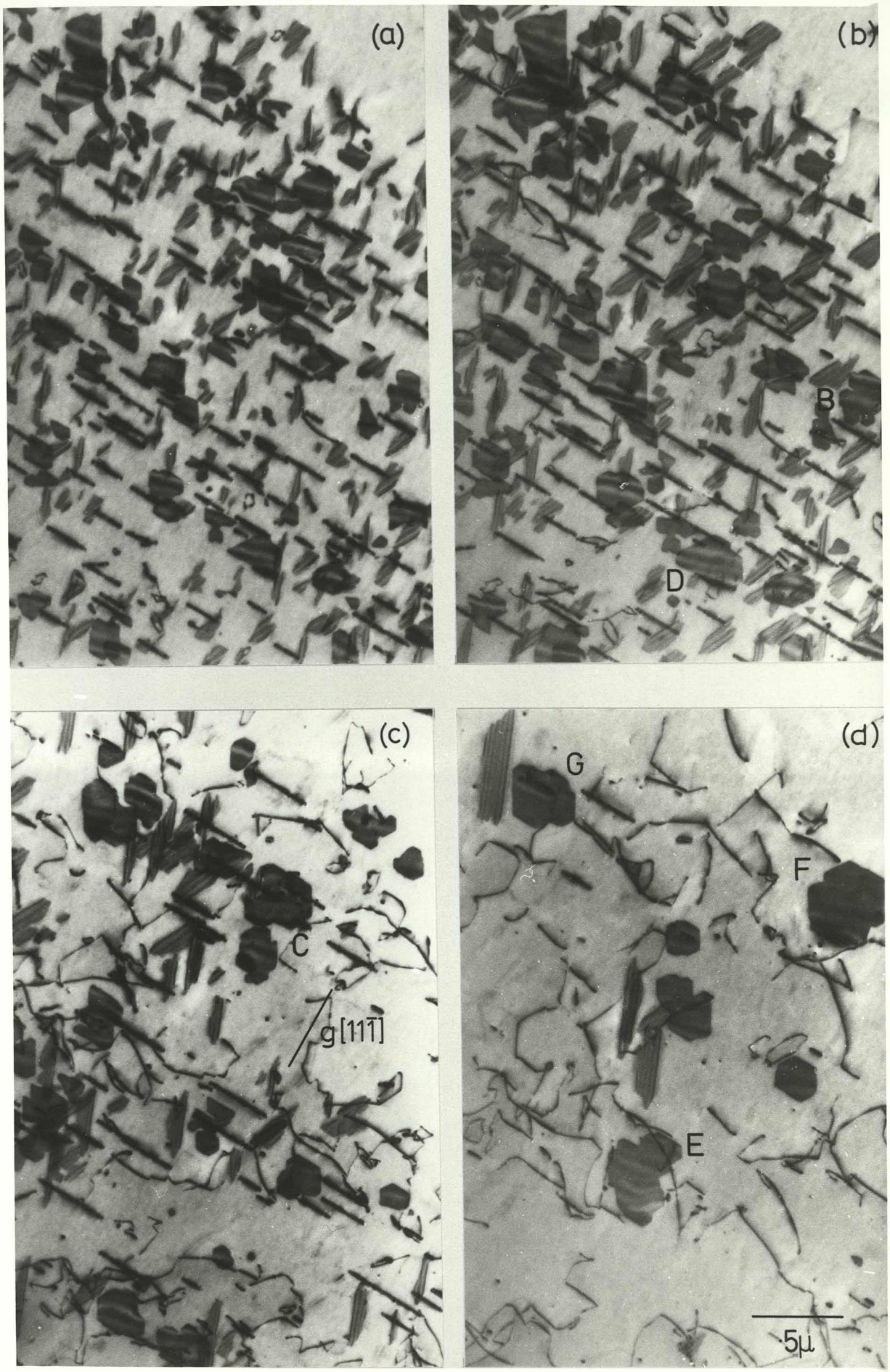
(a)
(b)
B
D
(c)
C
g[11$\bar{1}$]
(d)
G
F
E
5μ

Fig. 10/5 Frank loop growth in a thick foil of copper irradiated at 205°C.

(A) isolated large loop

(B) very deformed loop

(C) medium size loop

(D) medium size loop

(E) extremely deformed loop

(F)
(G) medium loop

After about 36-42 minutes most of the loops initially present have slipped to the surface, and hence loops (F) and (G) are isolated after this time. Loops (F) and (G) have nucleated long after the start of the irradiation.

Measurements made of loops in fig. 10/4.

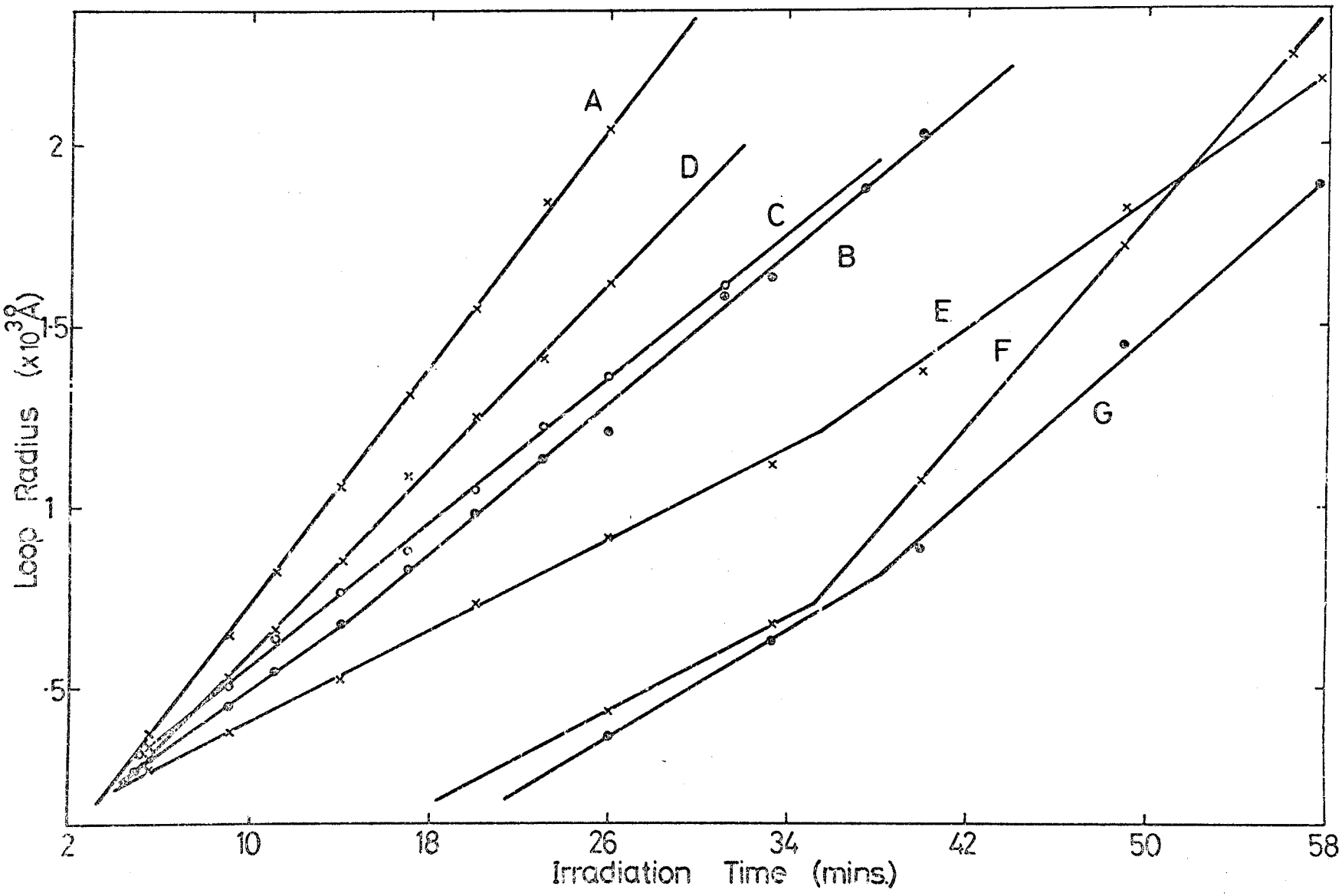
A
D
C
B
E
F
G
Loop Radius (x10^3 Å)
2
1.5
1
.5
2
10
18
26
34
42
50
58
Irradiation Time (mins.)

Fig. 10/6 Rhombus loop growth rates in a foil of Cu 16% Al irradiated at 170°C, fig. 7/31.

The anomalous growth of loops B, E, G appears to be due to loop interaction, causing the shape of one side of the loop to change. In these cases, when the interacting loop vanishes, the growth rate reverts back to the original gradient. The reduction in growth rate of C occurs when the loop grows within the sphere of the denuded zone.

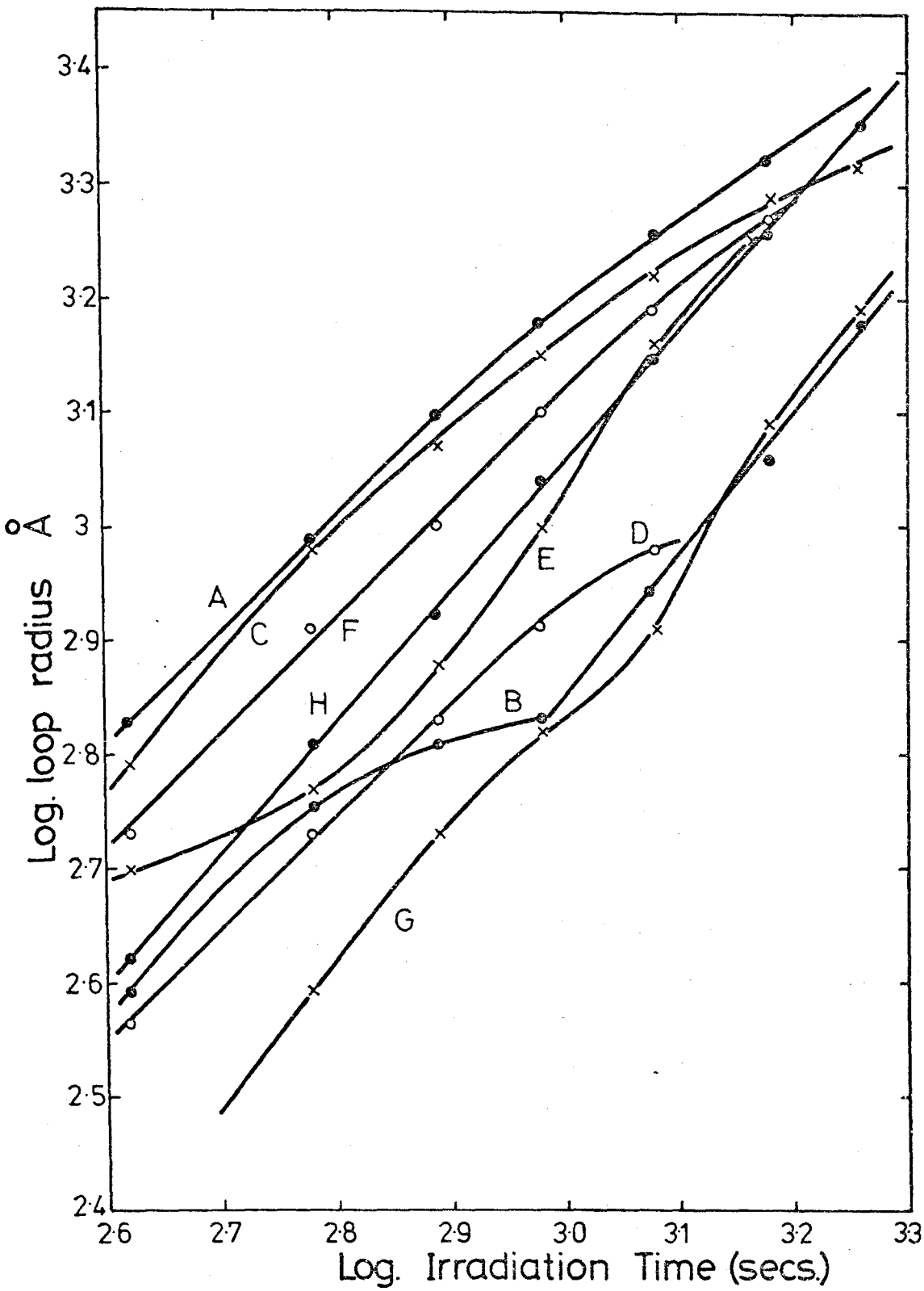
3·4
3·3
3·2
3·1
3
2·9
2·8
2·7
2·6
2·5
2·4
Log. loop radius Å
2·6
2·7
2·8
2·9
3·0
3·1
3·2
3·3
Log. Irradiation Time (secs.)
A
C
F
H
E
D
B
G

Fig. 10/7 Irregular rhombus loop growth in a foil of Cu 16% Al irradiated at $T_i = 235^{o}C$.

Loops A, B and C: growth ceases, when the loop grows within the denuded zones adjacent to the foil surface.

This can be seen in fig. (b) where the loops develop ledges at the corners. Loop growth still continues in a direction parallel to the surface.

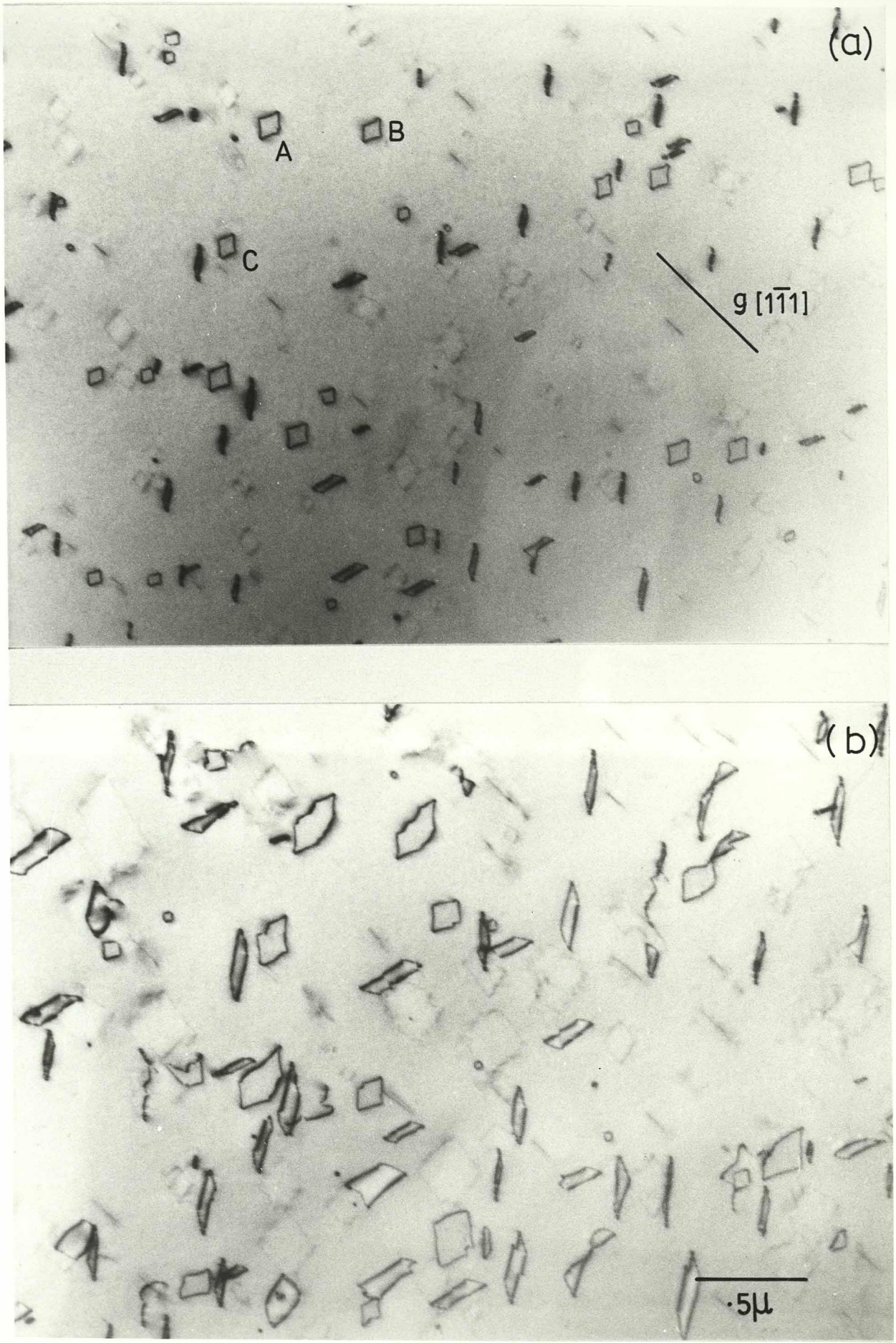
(a)
A
B
C
g [1$\bar{1}$1]
(b)
·5μ

Fig. 10/8 Frank loop growth in foils of Cu 2% Al after annealing for 5 minutes at increasing temperatures.

Irradiation temperature $T_i = 240^{\circ}C$.

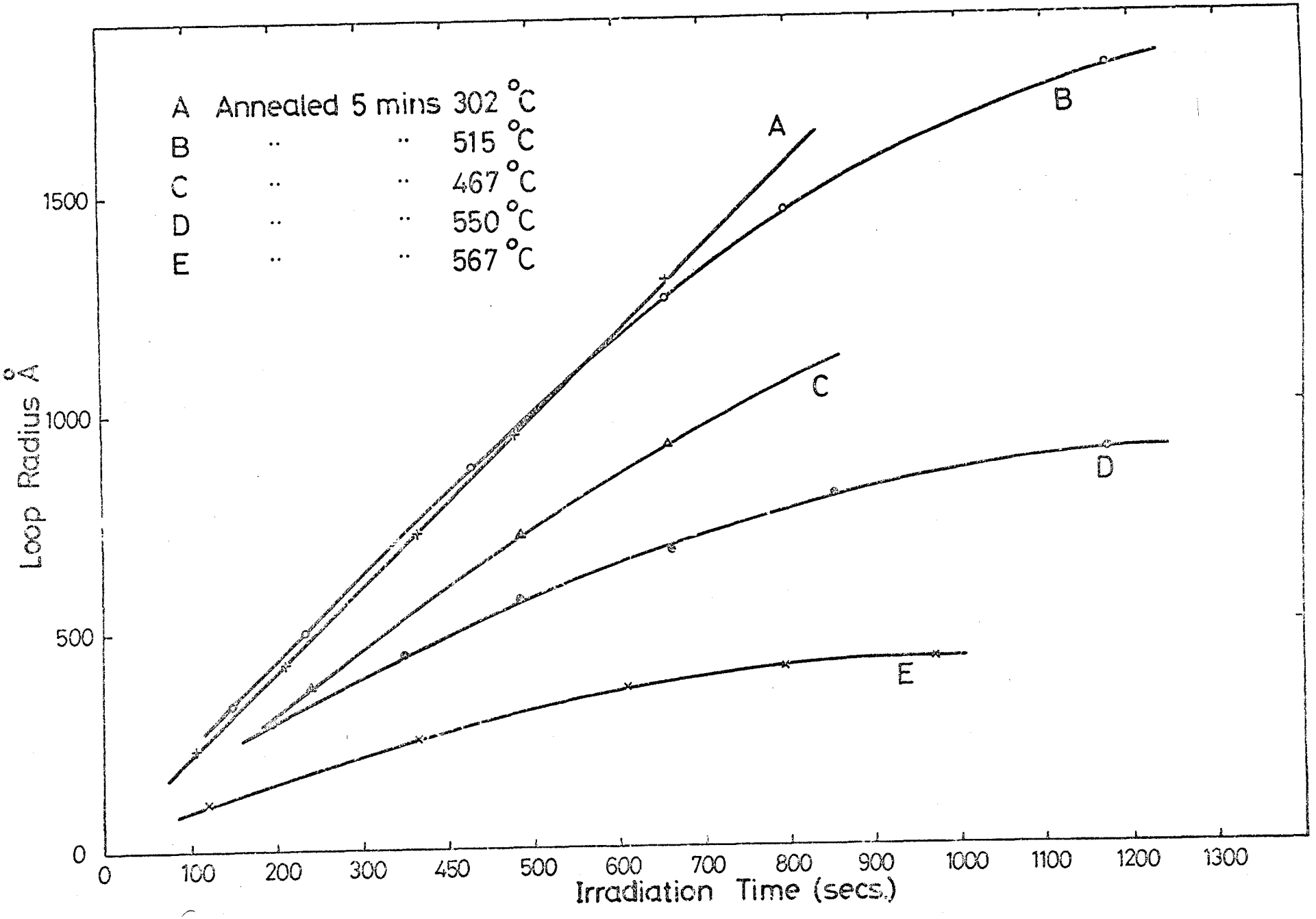
A Annealed 5 mins 302 °C
B .. .. 515 °C
C .. .. 467 °C
D .. .. 550 °C
E .. .. 567 °C
Loop Radius Å
1500
1000
500
0
0
100
200
300
450
500
600
700
800
900
1000
1100
1200
1300
Irradiation Time (secs.)
A
B
C
D
E

Fig. 10/9 Plot of n (from $r \propto t^n$) as a function of annealing temperature for a foil of Cu 2% Al.

(A) This gradient of the r/t curve occurs early in the irradiation, when the loops have a regular shape.

(B) In the later stages of irradiation a second gradient develops (when the loops are irregular) which is always less than the first gradient.

In the temperature range 350-450°C, it was not possible to grow enough loops in order to obtain an accurate result.

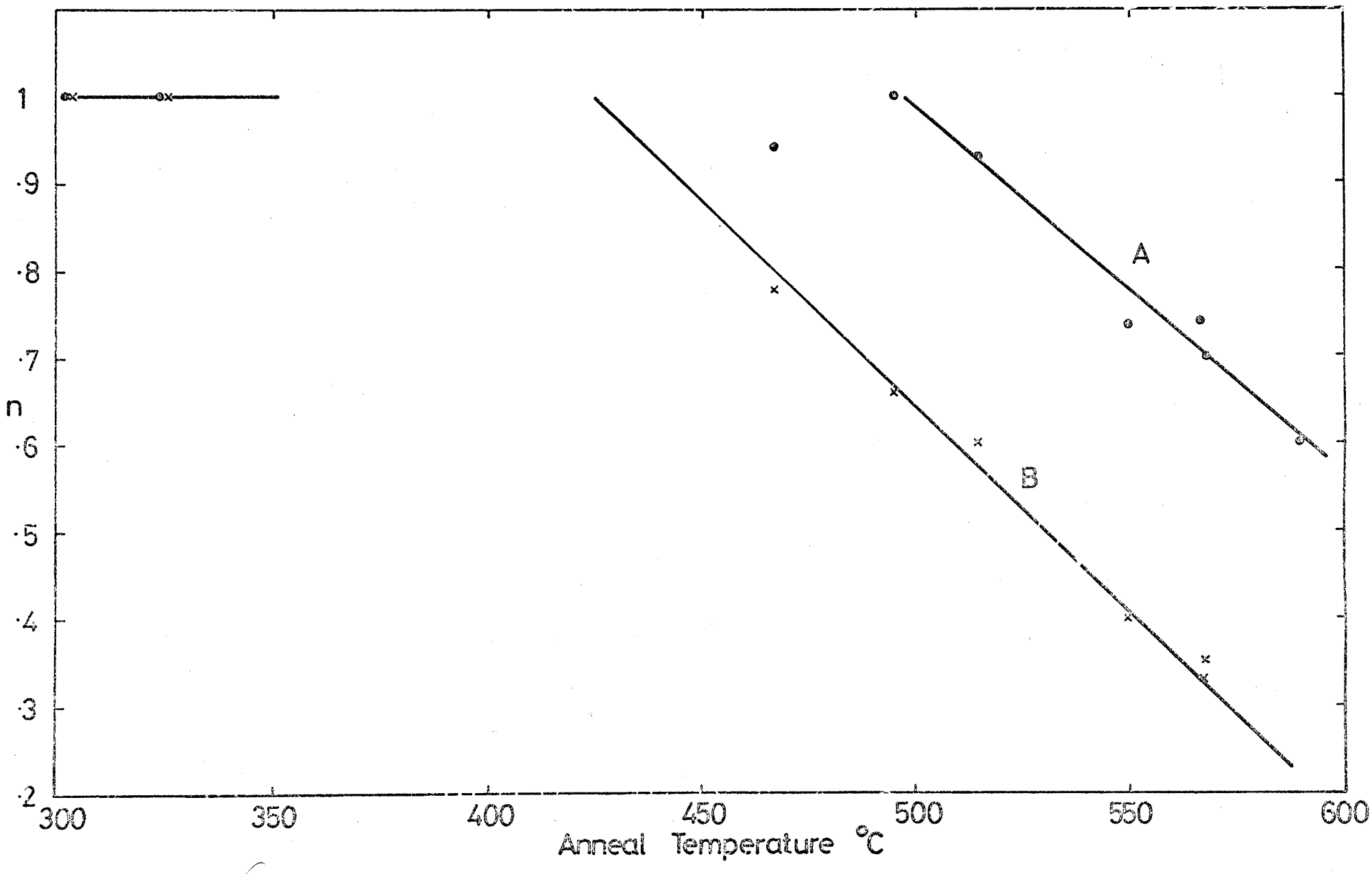
1
·9
·8
·7
·6
·5
·4
·3
·2
n
300
350
400
450
500
550
600
Anneal Temperature °C
A
B

Fig. 10/10 Frank loop growth in a Cu 16% Al foil after 5 minutes anneal at 590°C in the H.V.E.M.

In the $r \propto t^n$ equation, n has been plotted as a function of irradiation temperature. Each point represents the average of the growth rate of many loops.

n varies from .6 - 1.0, over the irradiation temperature range 240°C - 320°C. Above 320°C, loop growth could only be investigated by irradiation of loops nucleated at lower temperatures.

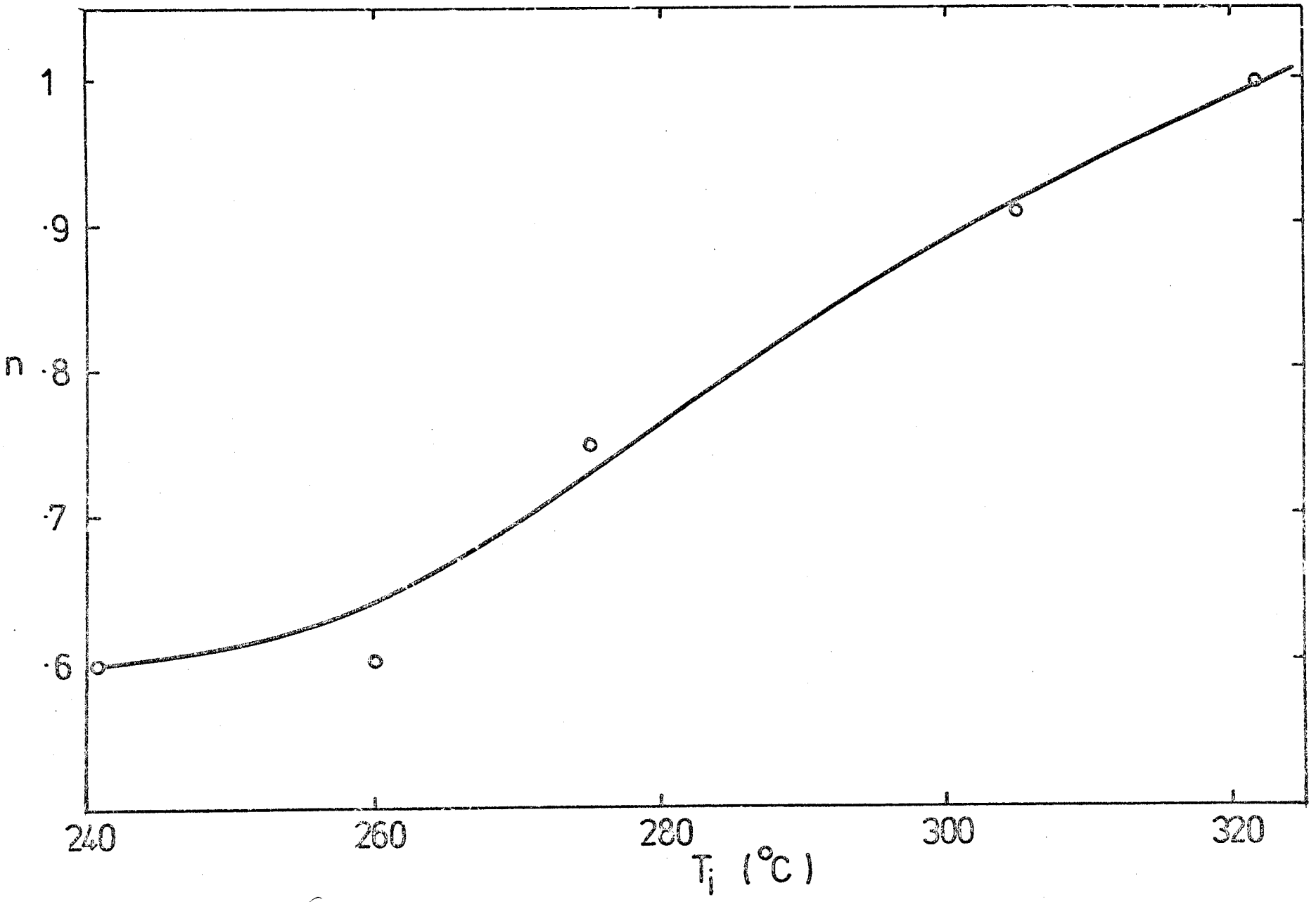
1
·9
·8
·7
·6
n
240
260
280
300
320
T_i (°C)

Fig. 10/11 Frank loop shrinkage in a foil of Cu 16% Al during an irradiation sequence at $T_i = 357^{\circ}C$.

Prior to the final irradiation, the foil had been annealed in the H.V.E.M. at $T_a = 495^{\circ}C$ and small loops nucleated by subsequent irradiation at $200^{\circ}C$ for a few minutes.

Under irradiation at $357^{\circ}C$ a few loops grew, but most remain the same size. Some however, shrink under irradiation, indicative that more vacancies are reaching the loop corners than interstitials.

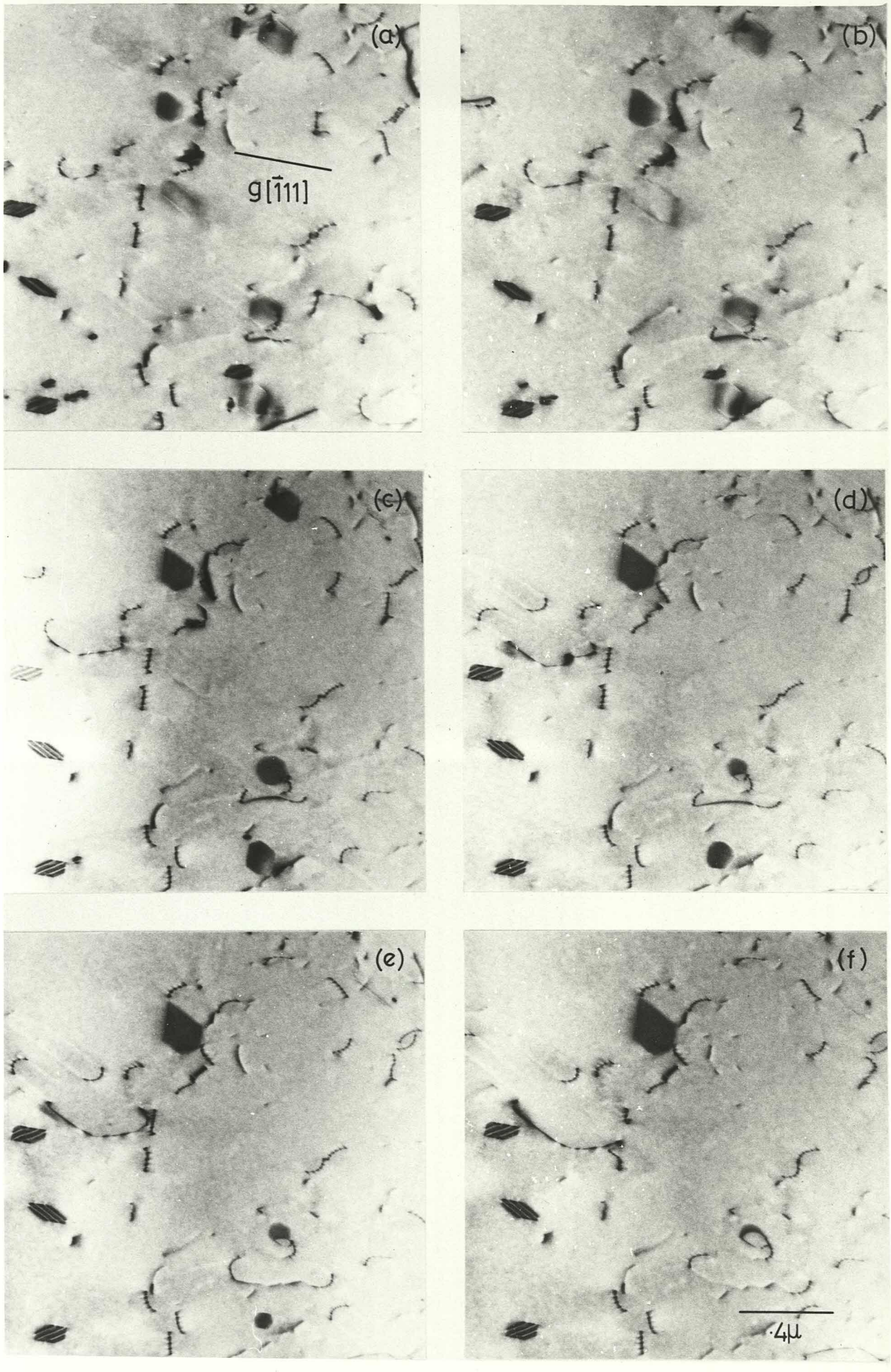
(a)
g[$\bar{1}$11]
(b)
(c)
(d)
(e)
(f)
·4μ

Fig. 10/12 Graph shows the loop growth rate as a function of temperature for Frank loops in copper and Cu 16% Al.

The apparent activation energy of the growth speed of loops in copper = .31 eV, while that for Cu 16% Al = .57 eV.

The Cu 16% Al specimen was annealed for 5 minutes at 495°C before irradiation, in order to nucleate Frank loops.

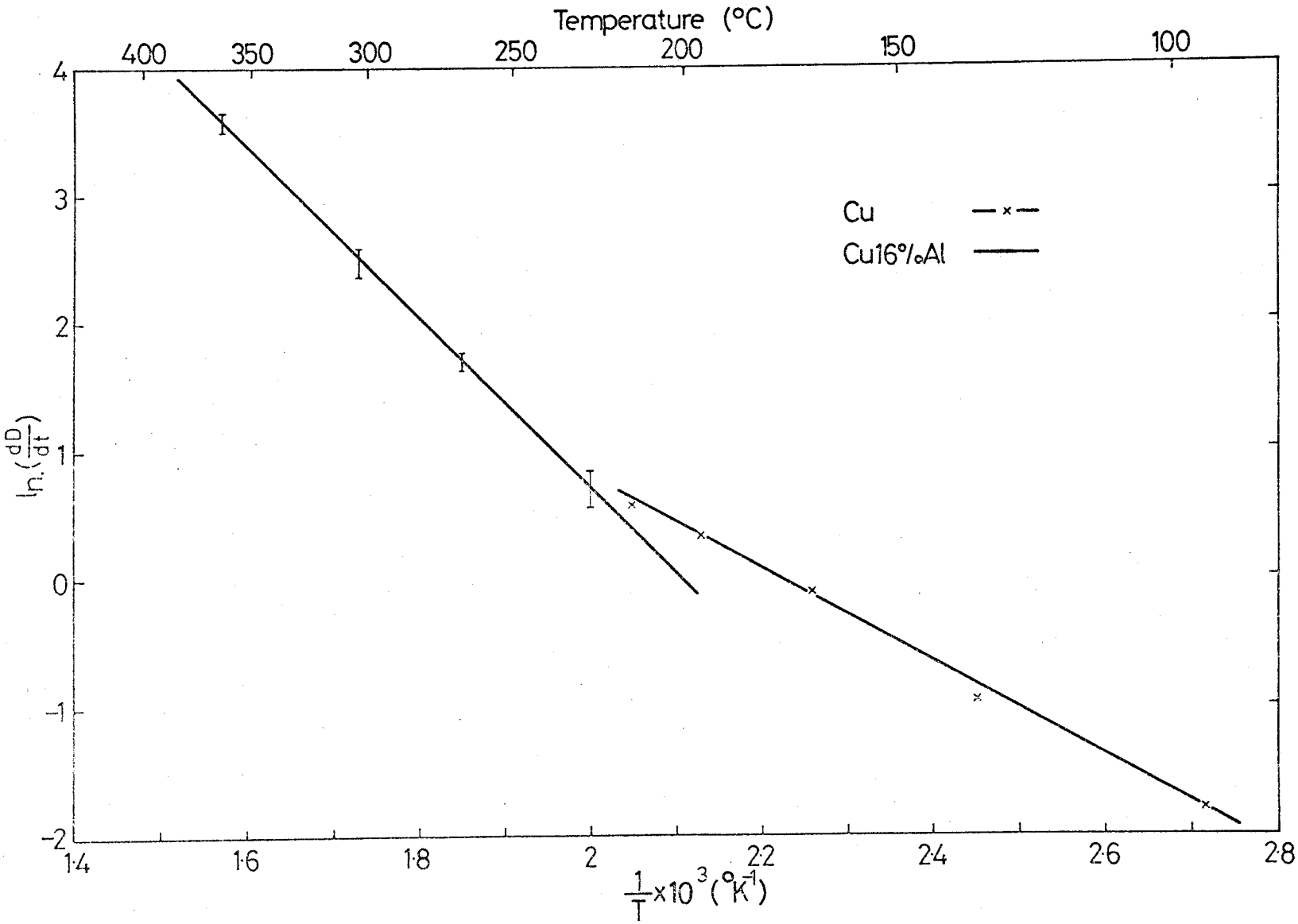
Temperature (°C)
400
350
300
250
200
150
100
4
3
2
1
0
−1
−2
ln.(dD/dt)
Cu
Cu16%Al
1·4
1·6
1·8
2
2·2
2·4
2·6
2·8
1/T x 10³ (°K⁻¹)

Fig. 10/13 Rhombus loop growth rates plotted as a function of temperature, for Cu .31 Al, Cu 5% Al and Cu 16% Al specimens.

Activation energy Cu .31% Al = .37 eV.
Activation energy Cu 5% Al = .48 eV.
Activation energy Cu 16% Al = .74 eV.

(A) high temperature growth rate activation energy is probably dependent on vacancy mobility.

(B) low temperature activation energy when vacancies were immobile and only the interstitials mobile.

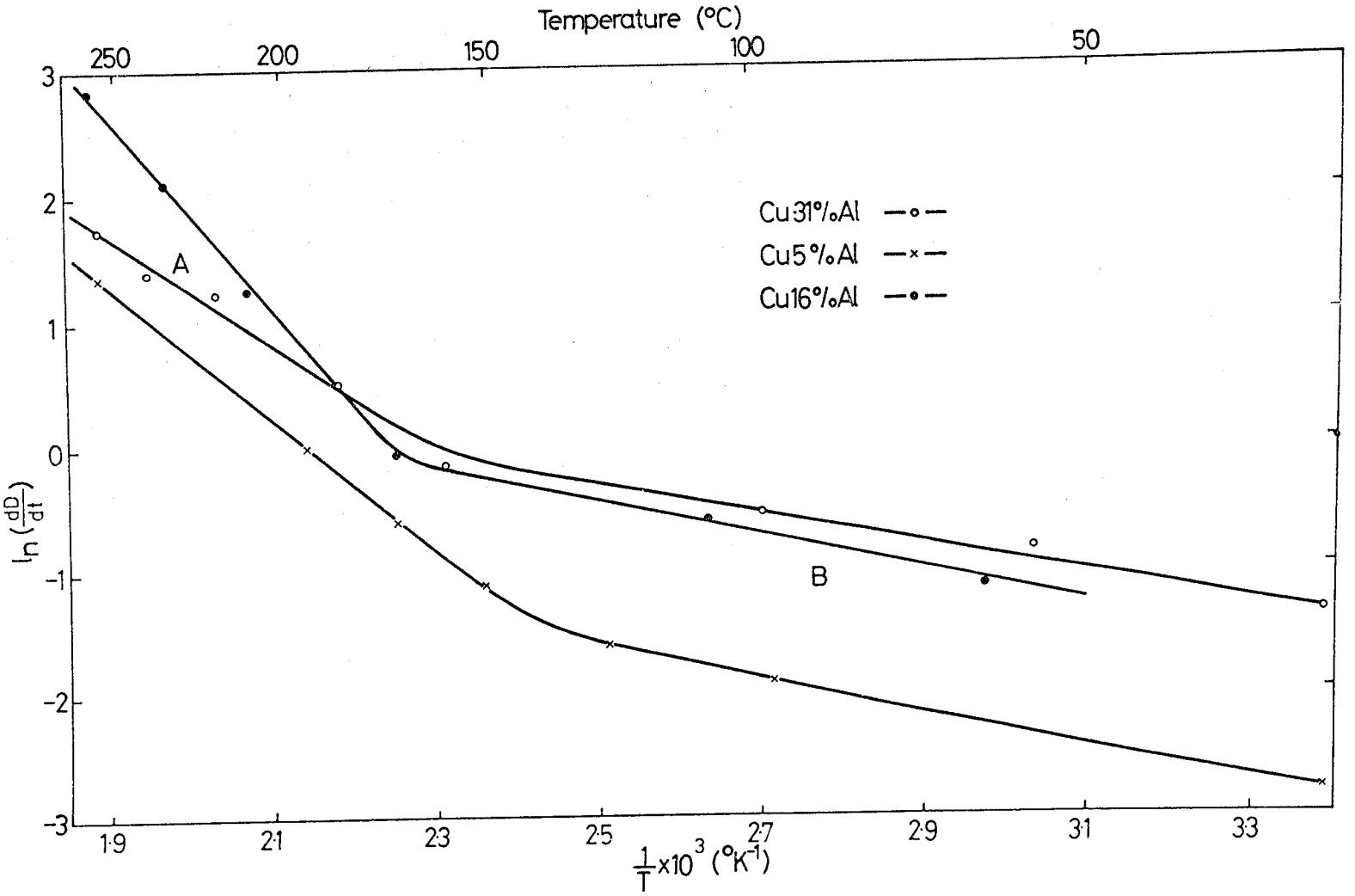
Temperature (°C)
250
200
150
100
50
3
2
1
0
-1
-2
-3
Cu 31% Al
Cu 5% Al
Cu 16% Al
A
B
$\ln\left(\frac{dD}{dt}\right)$
1·9
2·1
2·3
2·5
2·7
2·9
3·1
3·3
$\frac{1}{T} \times 10^3$ (°K^{-1})

Fig. 10/14 Graph shows the ratio of the growth rates of (111) Frank loops to vertically inclined rhombus loops in a foil of Cu .31% Al, as a function of temperature.

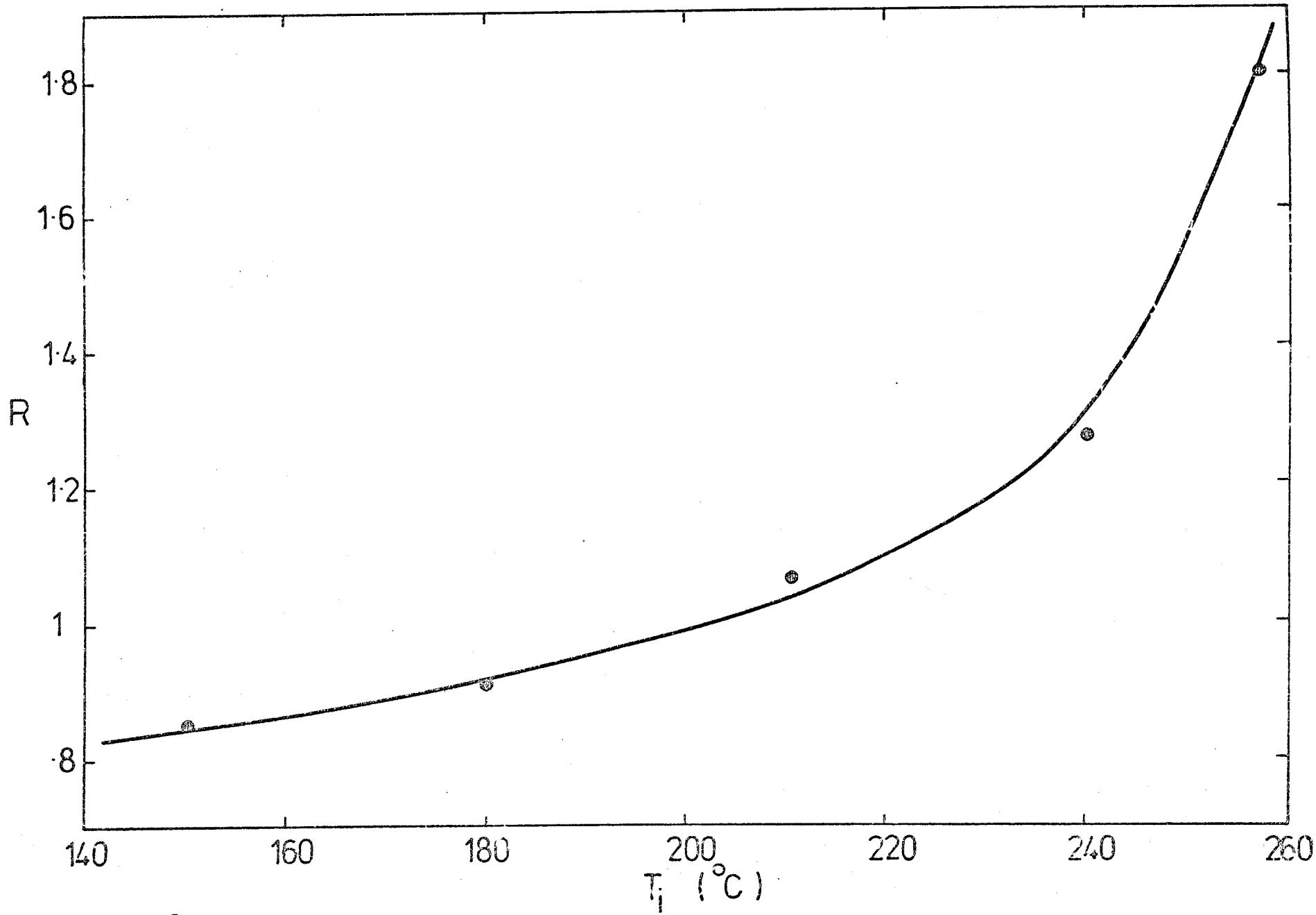
1·8
1·6
1·4
R
1·2
1
·8
140
160
180
200
220
240
260
T_i (°C)

Fig. 10/15 Micrograph illustrates the growth of a triangular Frank loop into a polygonal shaped loop in a foil of Cu 16% Al irradiated at $T_i = 260^{o}C$.

Specimen cut from a fast grown crystal.
Foil thickness $\simeq 2500$ Å.

Fig. 10/16 Graph showing the growth rate of the isolated Triangular Frank loop, in a foil of Cu 16% Al irradiated at $260^{o}C$ (fig. 10/15).

Dose rate = 1.5×10^{19} el./cm.^{2}/sec.

The loop area was measured and despite the irregularity of the shape, all the points lie on a straight line of gradient .61.

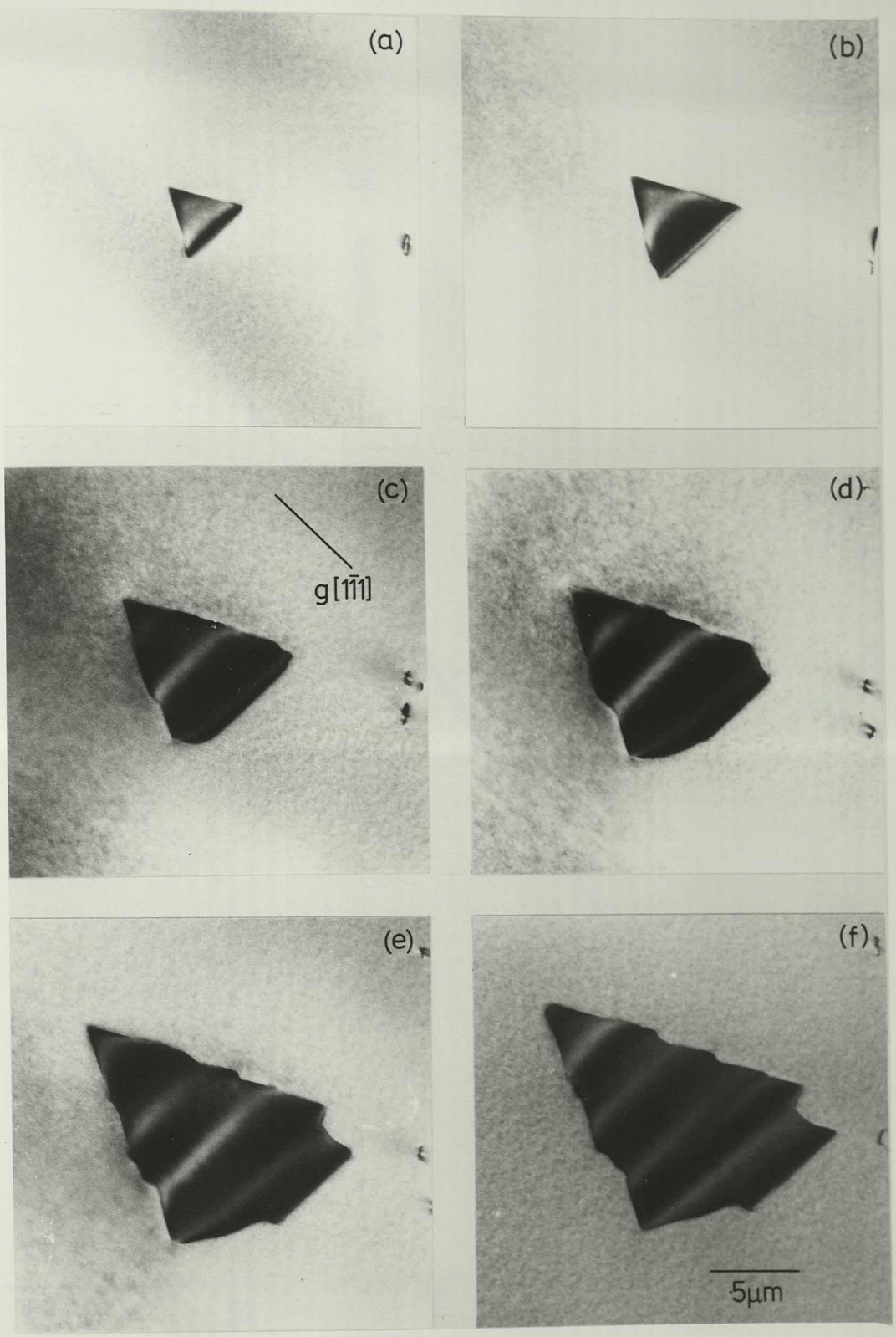

Fig.10/15

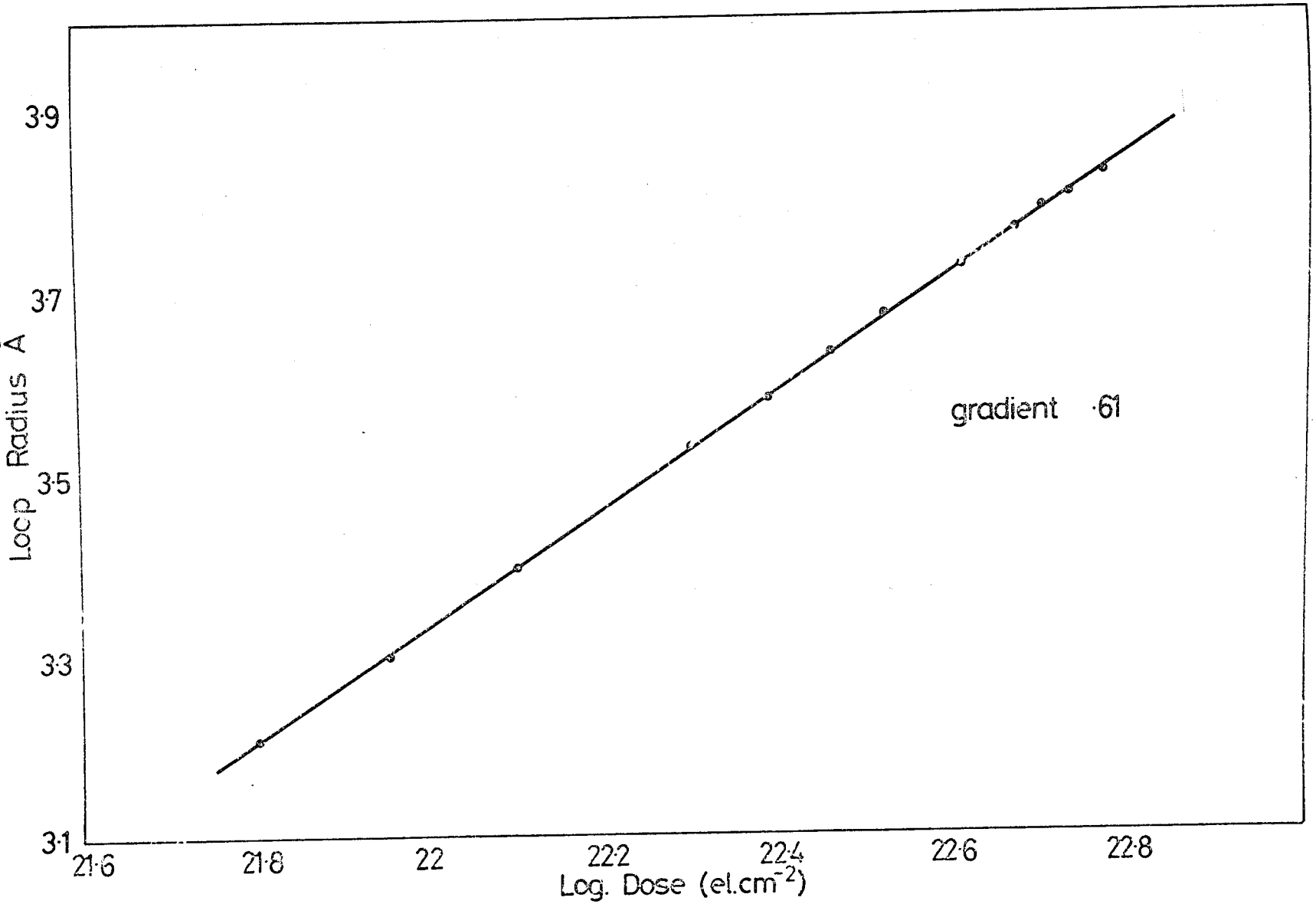
3·9
3·7
3·5
3·3
3·1
Loop Radius Å
gradient ·61
21·6
21·8
22
22·2
22·4
22·6
22·8
Log. Dose (el.cm^{-2})

Fig.10/16

Fig. 10/17 Growth of large irregular Frank loops on the (111) plane parallel to the foil surface in a foil of Cu 16% Al during irradiation at 280°C in the H.V.E.M. (The growth rates have been plotted in fig. 10/18).

Note (1) The growth of the Frank triangle loop (α) into a polygonal loop.

(2) The growth of a hexagonal loop (γ) towards a circular shape.

Fig. 10/18 Growth rates of Frank loops as a function of dose for specimens of Cu 16% Al cut from a fast grown crystal and irradiated at 280°C. See fig. 10/17.

Gradients Loop α .93, .63
Loop β 1.16, .84
Loop γ 1.06, .78
Loop δ 1, 2, 1
Loops $\alpha + \beta$ 1.09, .71

(A) Loops regular, with sides aligned <110> directions.

(B) Loops irregular with sides aligned along <112> and <532>.

The change in gradient from 1 to $\simeq .7$ occurs at a dose of $\simeq 10^{22}$ el./cm.^{2} for all loops independent of size.

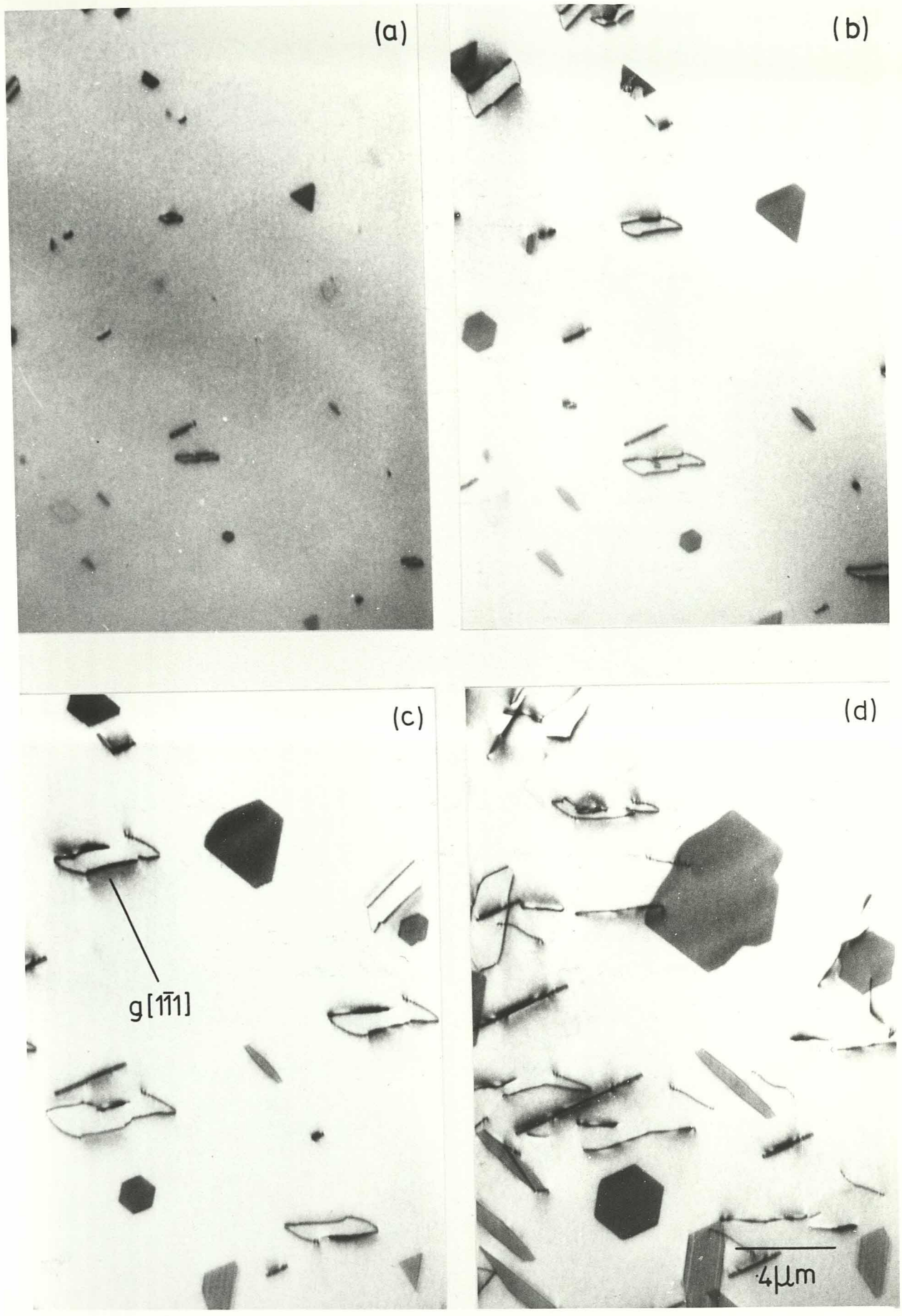

Fig.10/17

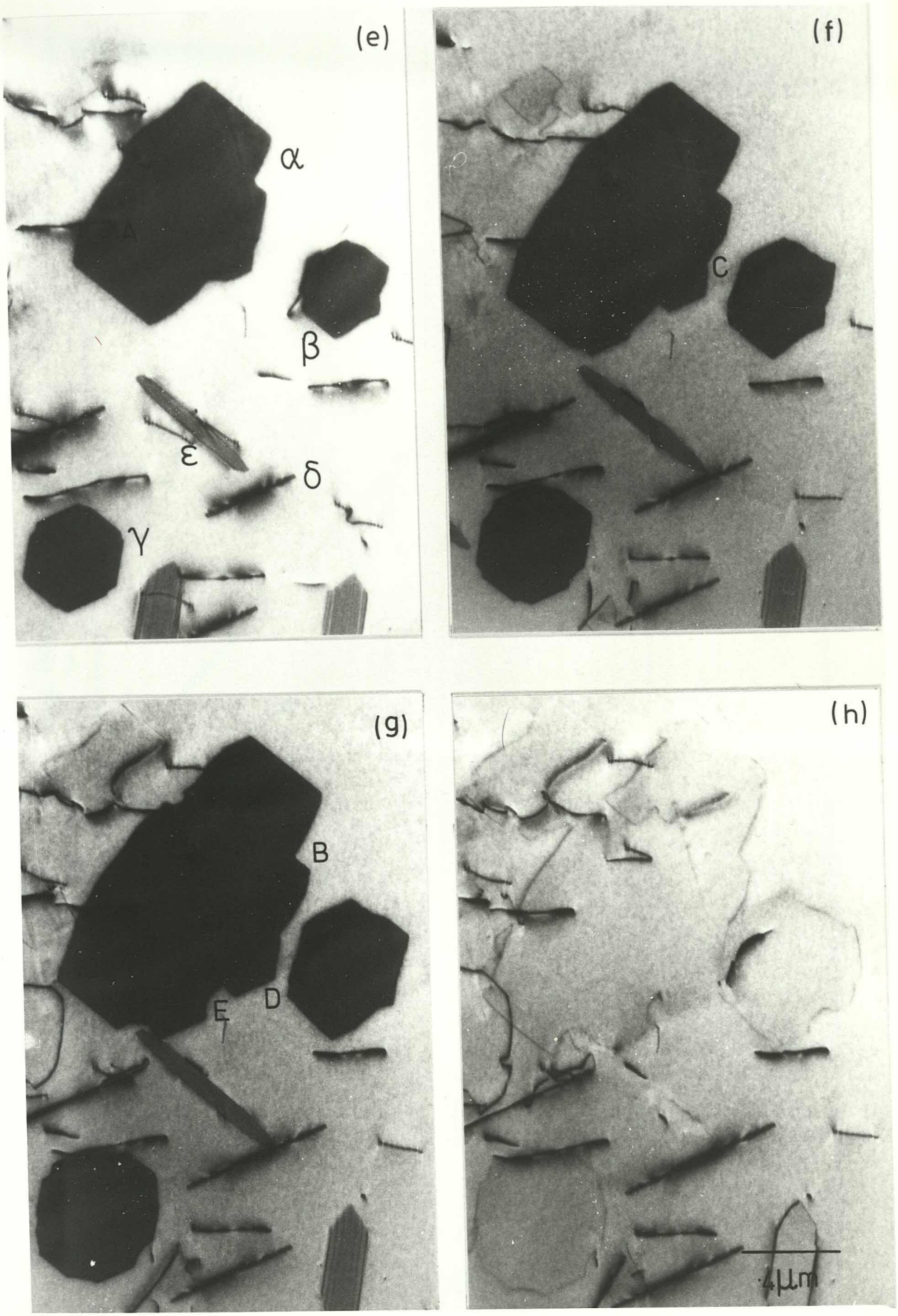

Fig.10/17

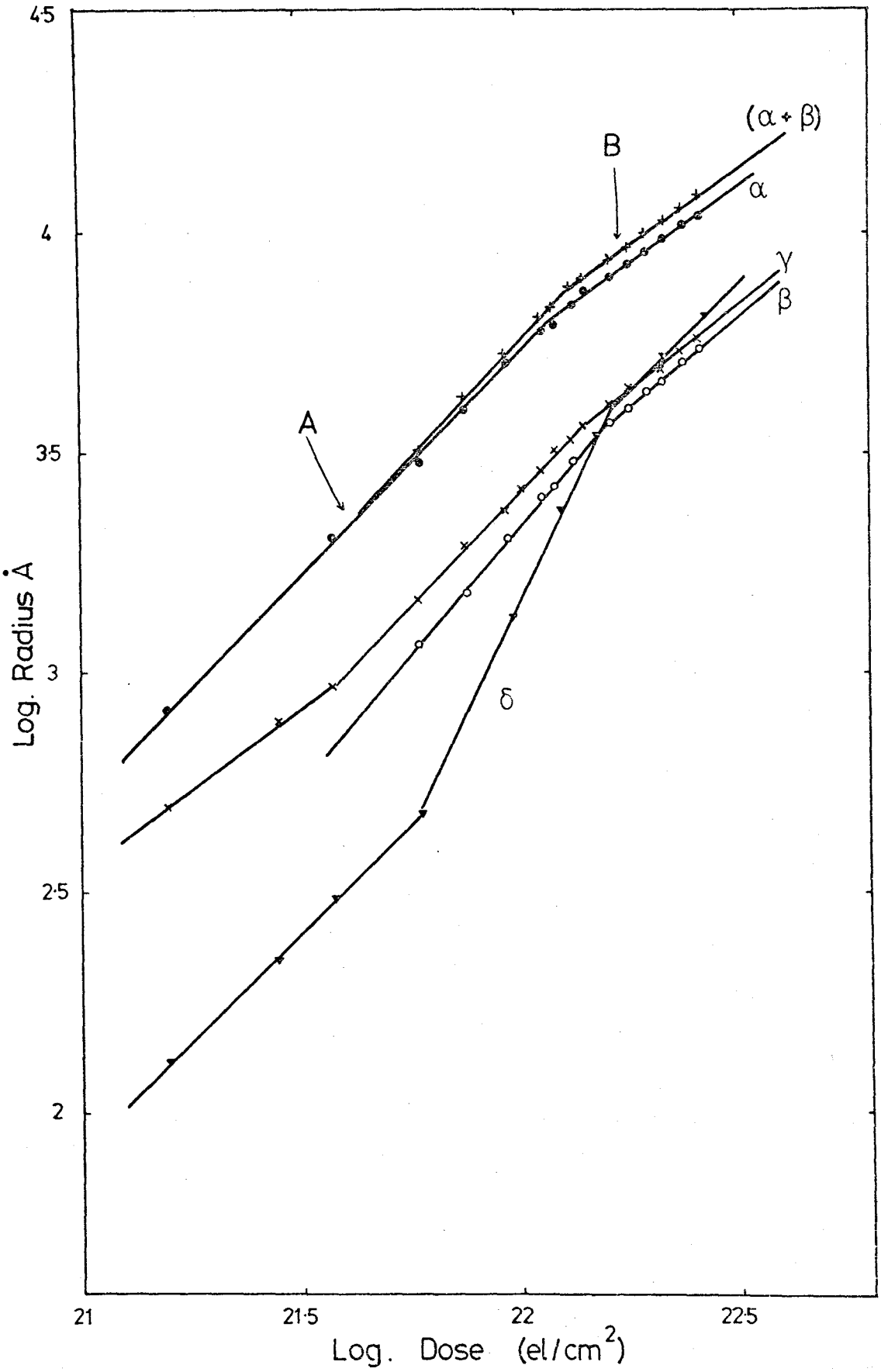

Fig.10/18

Fig. 10/19 Frank loop growth in a specimen cut from a fast grown crystal of Cu 5% Al and irradiated at $T_i = 308^{o}C$.

(a) 10 minutes irradiation
(b) 12 minutes irradiation
(c) 16 minutes irradiation
(d) 20 minutes irradiation
(e) 26 minutes irradiation
(f) 31 minutes irradiation.

g = <111>
z = <532>

Fig. 10/20 Growth of Frank loop fig. 10/19 in a foil of Cu 5% Al cut from gast grown crystal. The area of the loop was measured and the equivalent radius plotted as a function of time. Despite the irregularity of the loop shape, all the points lay accurately on a smooth curve.

Temperature of irradiation $T_i = 308^{o}C$.

$r \propto t^{n}$ where n = .87 to 2.6.

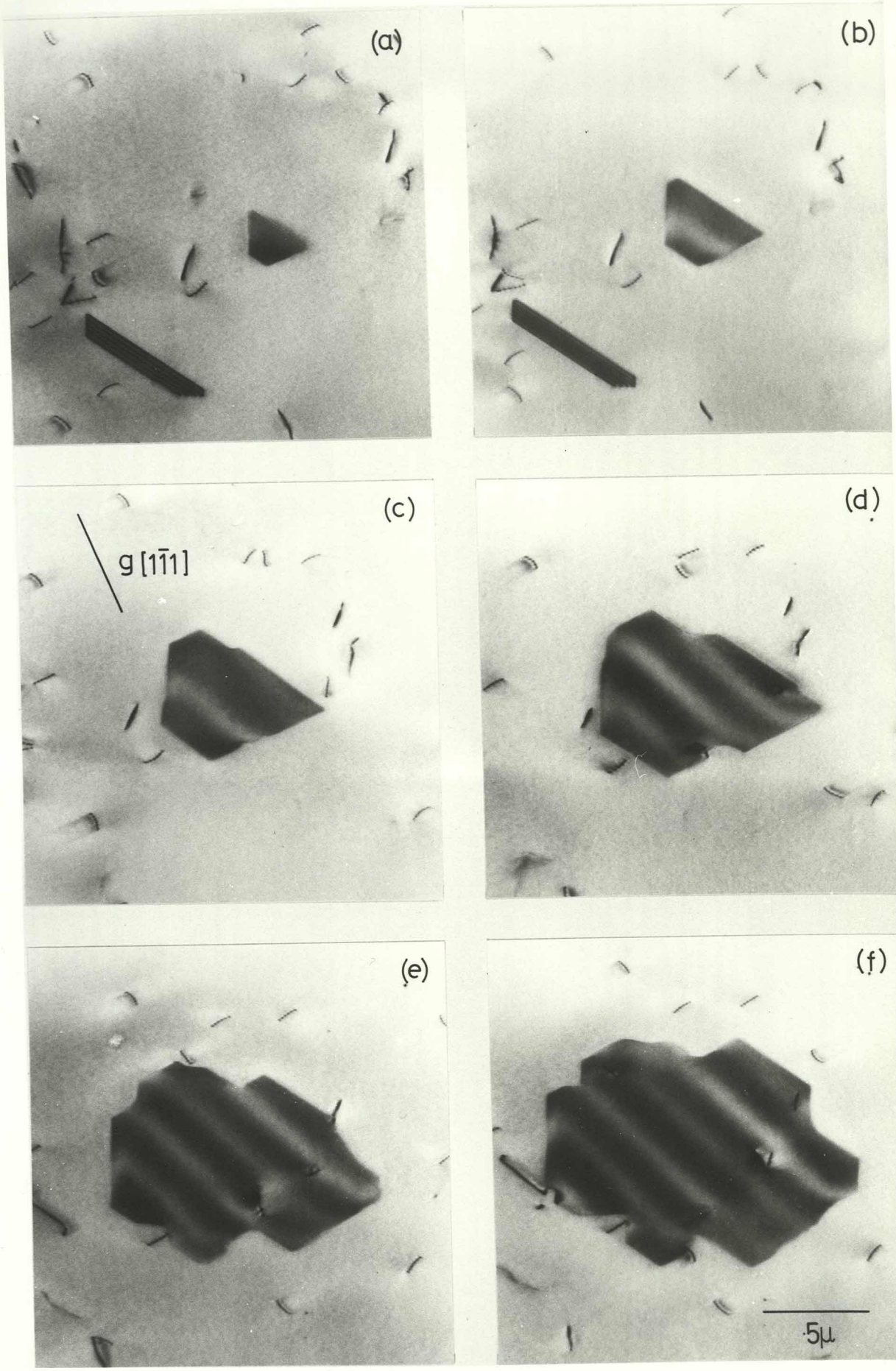
(a)
(b)
(c)
g [1$\bar{1}$1]
(d)
(e)
(f)
5μ

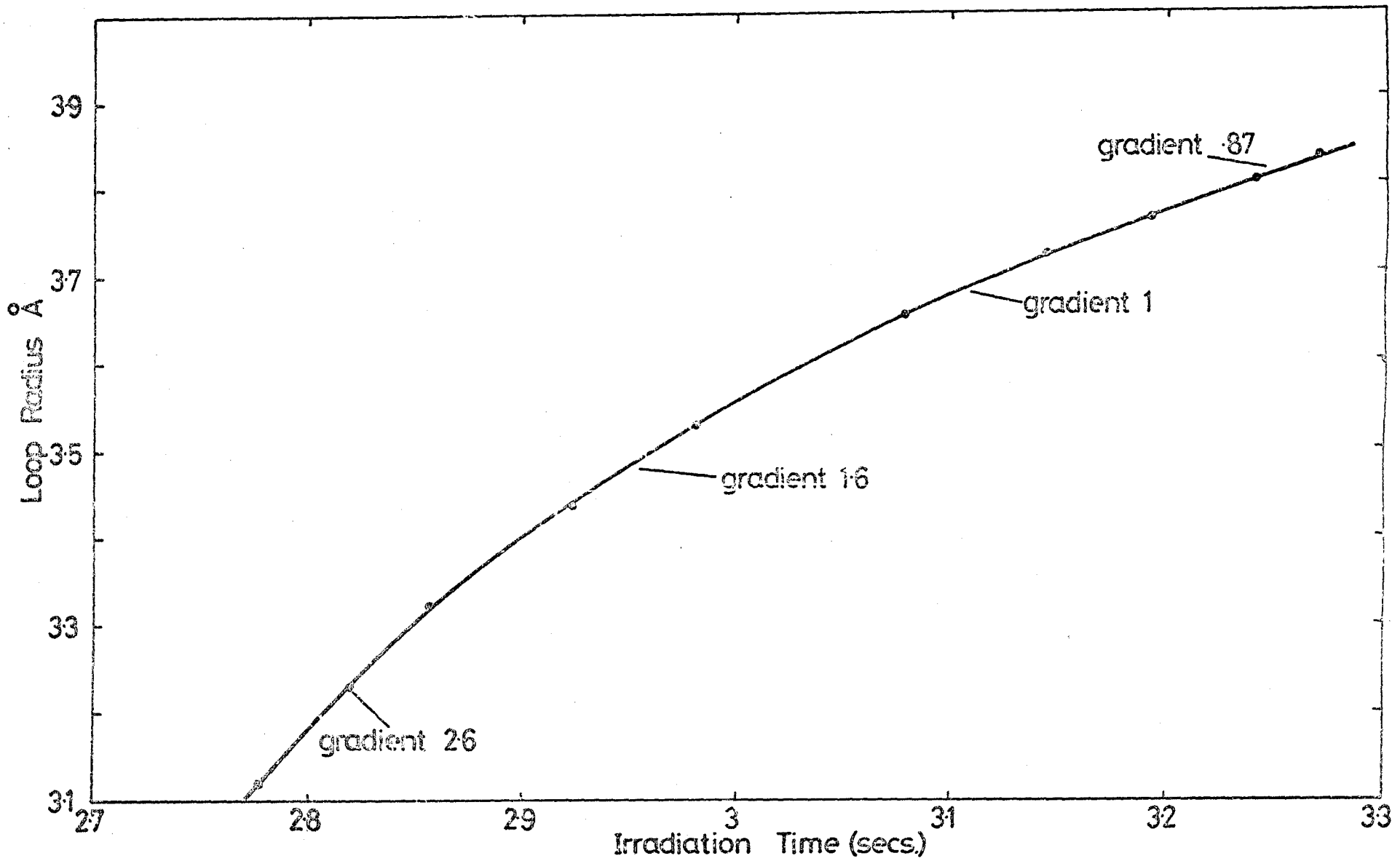
Loop Radius Å
3·9
3·7
3·5
3·3
3·1
2·7
2·8
2·9
3
3·1
3·2
3·3
Irradiation Time (secs.)
gradient ·87
gradient 1
gradient 1·6
gradient 2·6

Fig. 10/21 (A) Schematic diagram of an extended superjog on dissociated dislocation of Burgers vector $\overline{A\overline{B}}$. The dislocation segments not in the original glide plane are dissociated on the other {111} plane containing the Burgers vector; all faults are intrinsic. The acute jog has a stair-rod dipole with opposite Burgers vectors $\gamma\delta$ and $\delta\gamma$ of the type $\frac{a}{6}$ <110> and the obtuse jog has a stair-rod dipole with opposite Burgers vectors $^{AB}/_{\delta\gamma}$ and $^{\delta\gamma}/_{AB}$ of the type $\frac{a}{3}$ <100>. The line tension of these stair-rod dislocations probably pulls the Shockley partial dislocations together somewhat at the jogs, producing a partial constriction.

(B) The simplest model of the mechanism of jog formation on an extended dislocation requires the formation of a constriction in the dislocation by pinching together the Shockley partials to form a perfect dislocation which may climb by the formation of a jog pair.

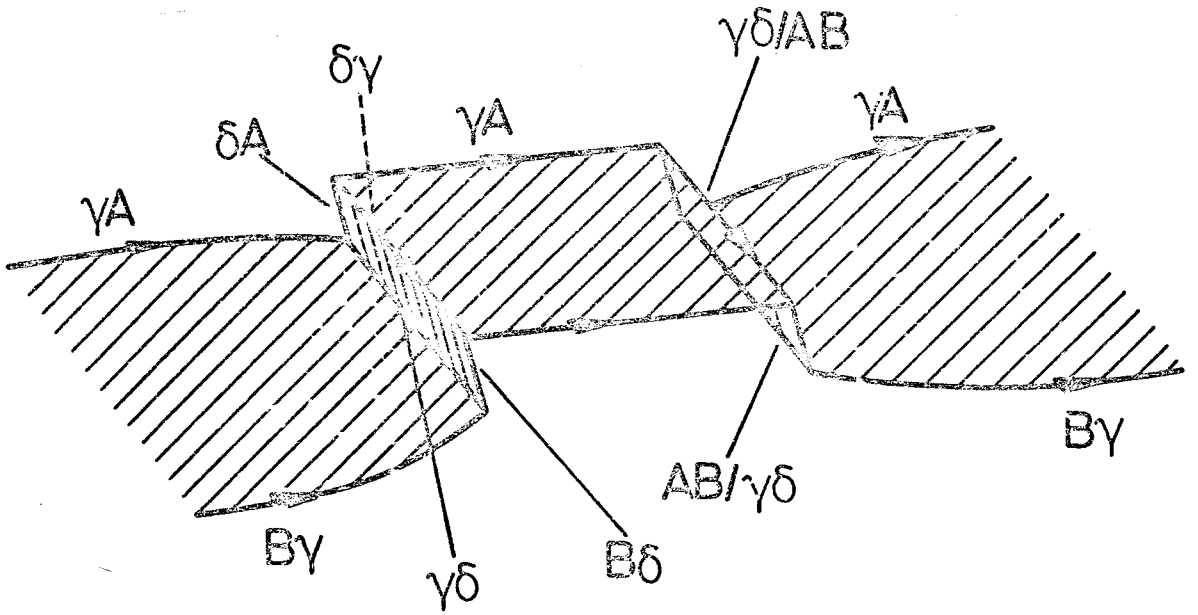

(A)

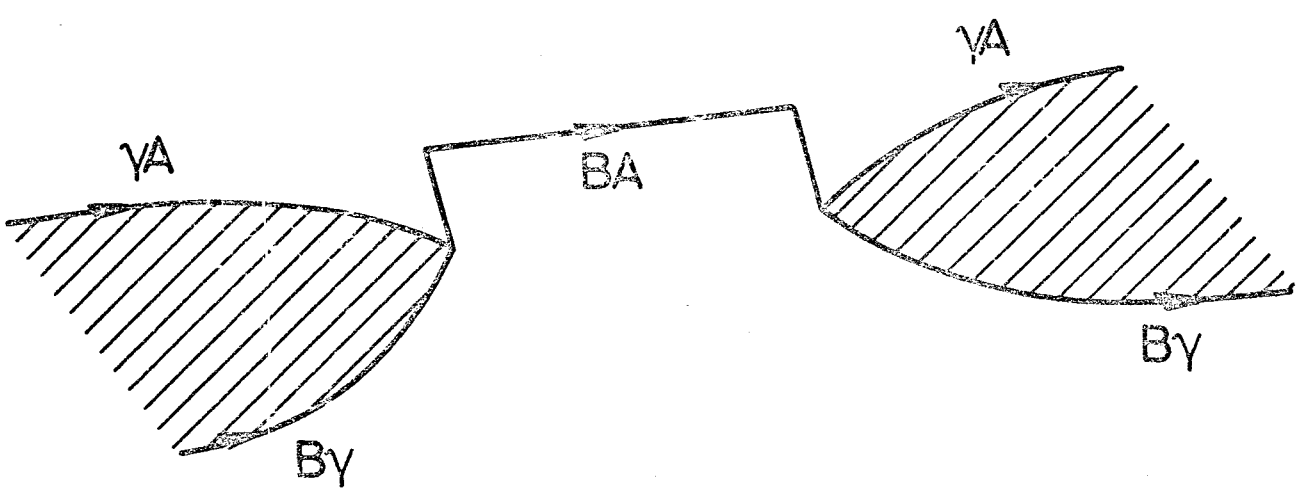

(B)

Fig. 10/22 (A) A triangular step on a stacking fault ribbon as suggested by Escaig.

(B) The stair-rod dipoles move one row to the left with the absorption or emission of each point defect.

(C) The configuration grows with a continuous decrease in the free energy of the crystal, until it reaches the other side of the extended dislocation and forms a double jogline.

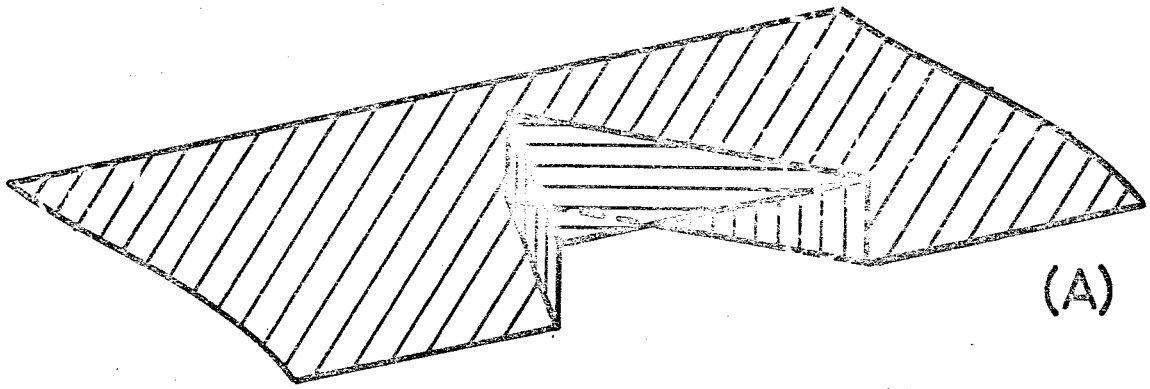

(A)

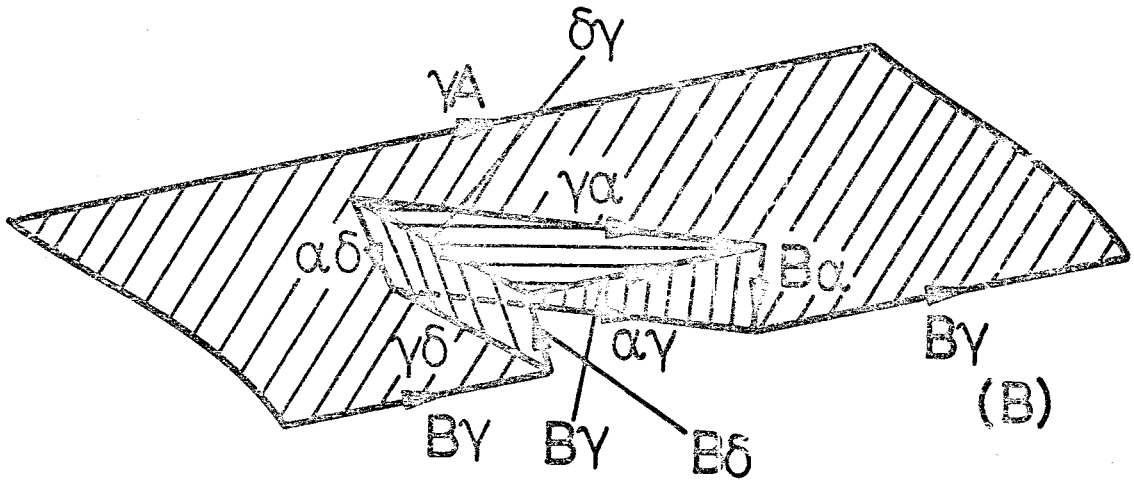

(B)

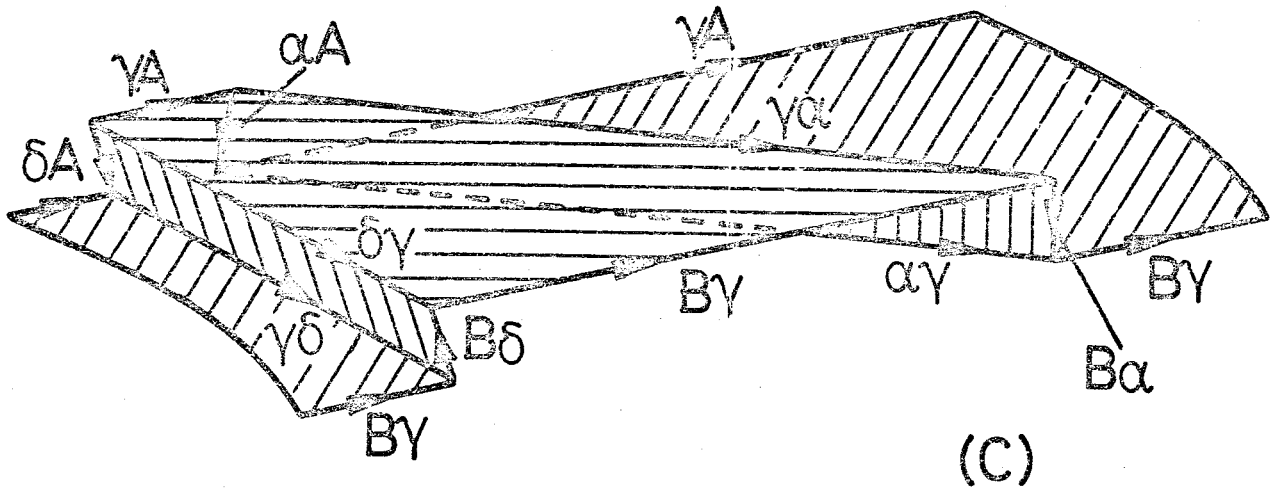

(C)

Fig. 10/23 Thomson and Balluffi model.

A row of point defects along one of the Shockley partials of an extended dislocation may be thought of as a small prismatic dislocation loop, which may dissociate to form an extended jog pair.

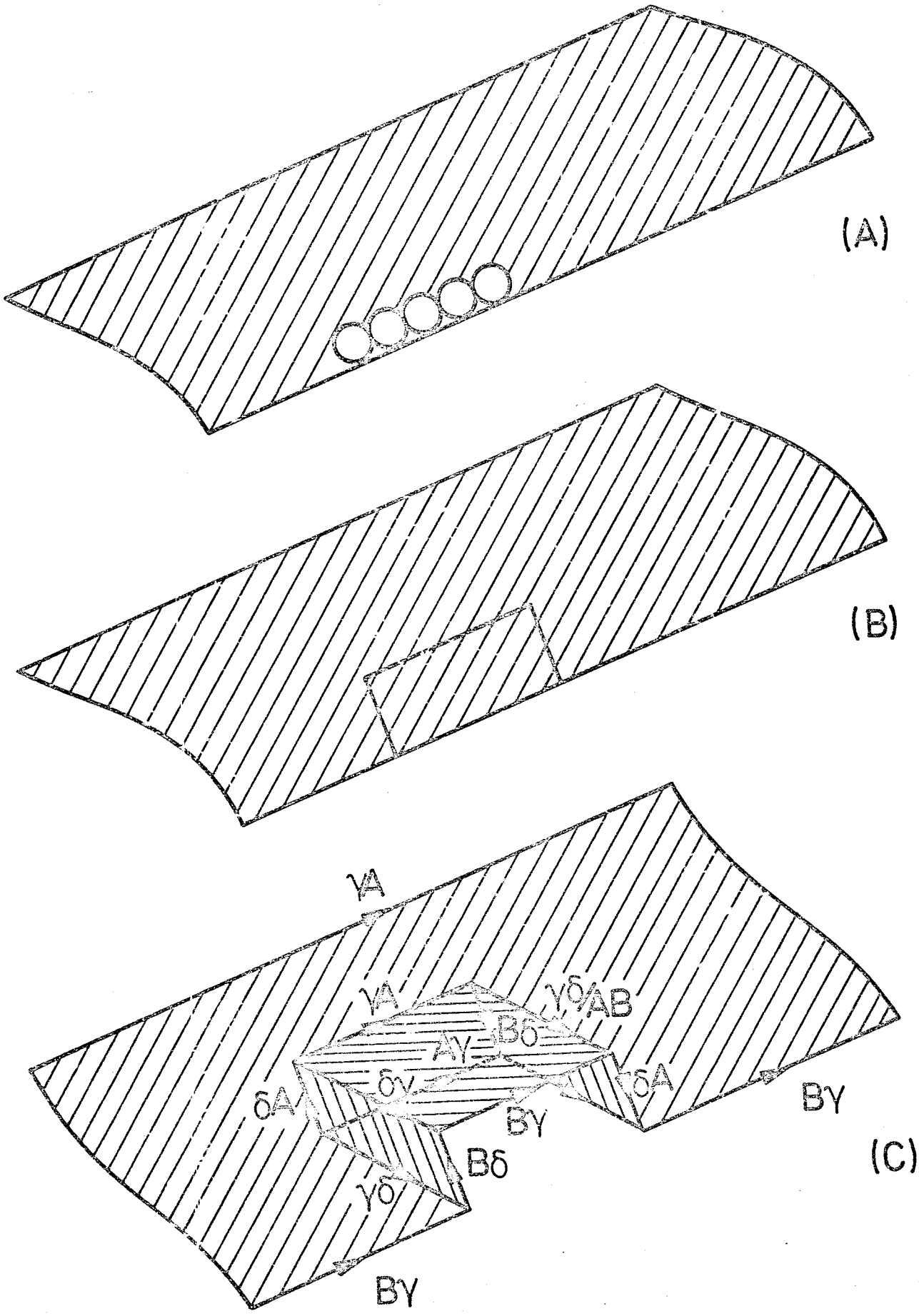
(A)
(B)
γA
γA
γδ
AB
Aγ
Bδ
δγ
δA
δA
Bγ
Bγ
Bδ
γδ
Bγ
(C)

Fig. 10/24 (A) A pure edge dislocation loop whose sides are dissociated and therefore lying exactly in the two {111} planes which contain the Burgers vector. The $(1\bar{1}0)$ plane of the loop intersects the (111) and $(\bar{1}\bar{1}1)$ planes along the $[\bar{1}\bar{1}2]$ and [112] directions respectively and so the loop sides lie along these directions.

(B) The formation of a jog at the corner of a loop requires the formation of only one stair-rod dipole, rather than two dipoles which are required to nucleate a pair of jogs on the loop side.

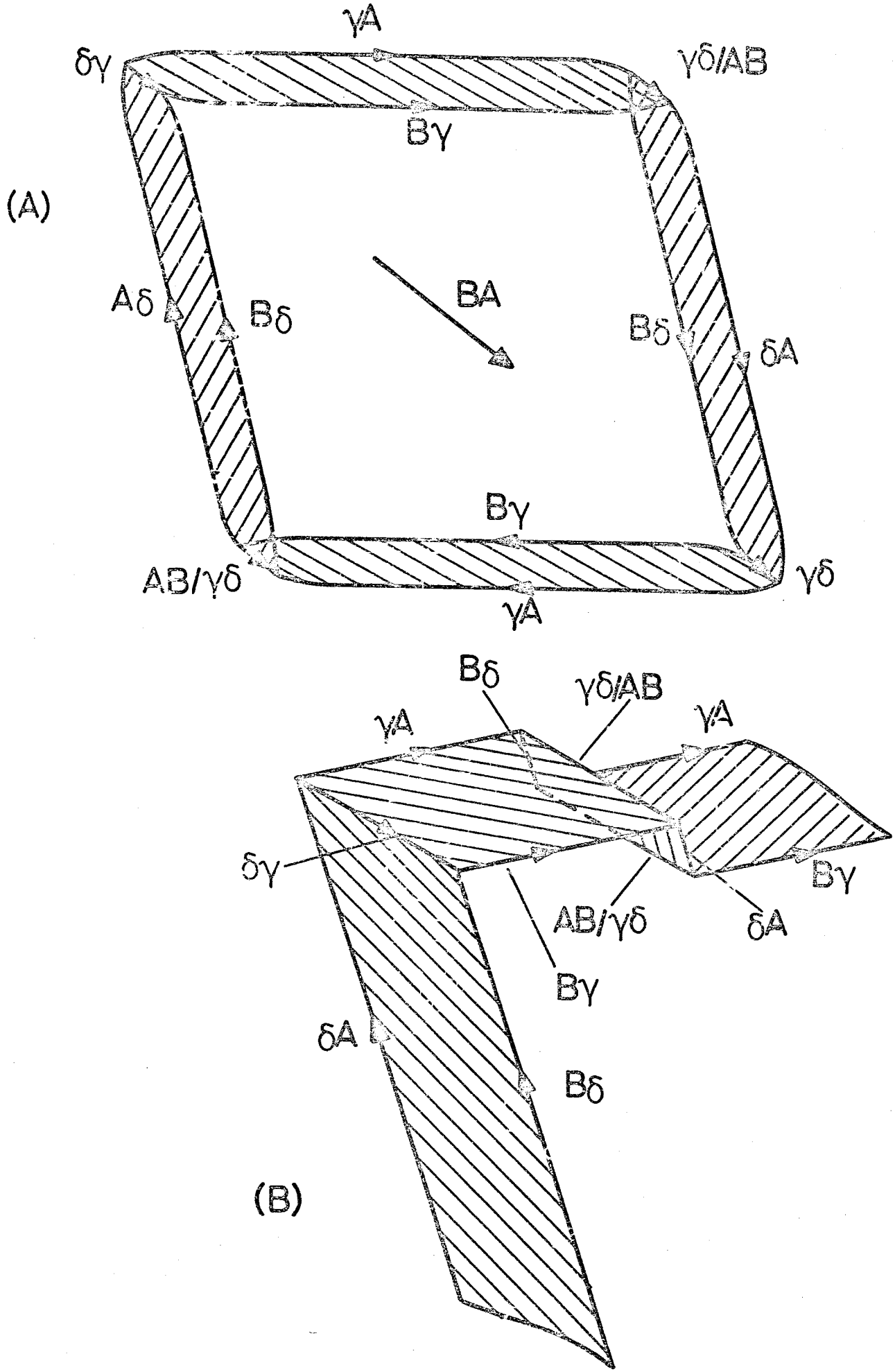
γA
δγ
γδ/AB
Bγ
(A)
Aδ
Bδ
BA
Bδ
δA
Bγ
AB/γδ
γδ
γA
Bδ
γδ/AB
γA
γA
δγ
Bγ
AB/γδ
δA
Bγ
δA
Bδ
(B)

Fig. 10/25 This micrograph, imaged in g $[1\bar{1}\bar{3}]$ at z = [110], illustrates that while the Frank loop can dissociate into its component Shockley partial and stair-rod dislocations along the $[1\bar{1}0]$ direction, no such dissociation takes place in any other growth direction, i.e. $[2\bar{3}1]$ or $[1\bar{2}1]$.

(A) Loop corner is rounded as a result of vacancy attraction. No dissociation takes place.

(B) Constriction of Shockley partials and difference in level of stair-rods.

(C), (D), (E) further constrictions.

(F) Additional side along $[2\bar{3}1]$ showing no dissociation.

(G) Corner along the $[1\bar{2}1]$ direction showing no dissociation.

The line directions $\bar{u}$ at the constrictions are the same as the line direction of the side to which they are moving.

Jogs B and D appear to be moving in opposite directions along the same edge.

This triangle appears to be in the process of forming new sides since when jog B arrives at A it will not find it easy to change its orientation of $[\bar{1}01]$ to that of $[0\bar{1}1]$, the line direction of the side to which it is moving. At A, a new side parallel to $[\bar{1}01]$ is being developed.

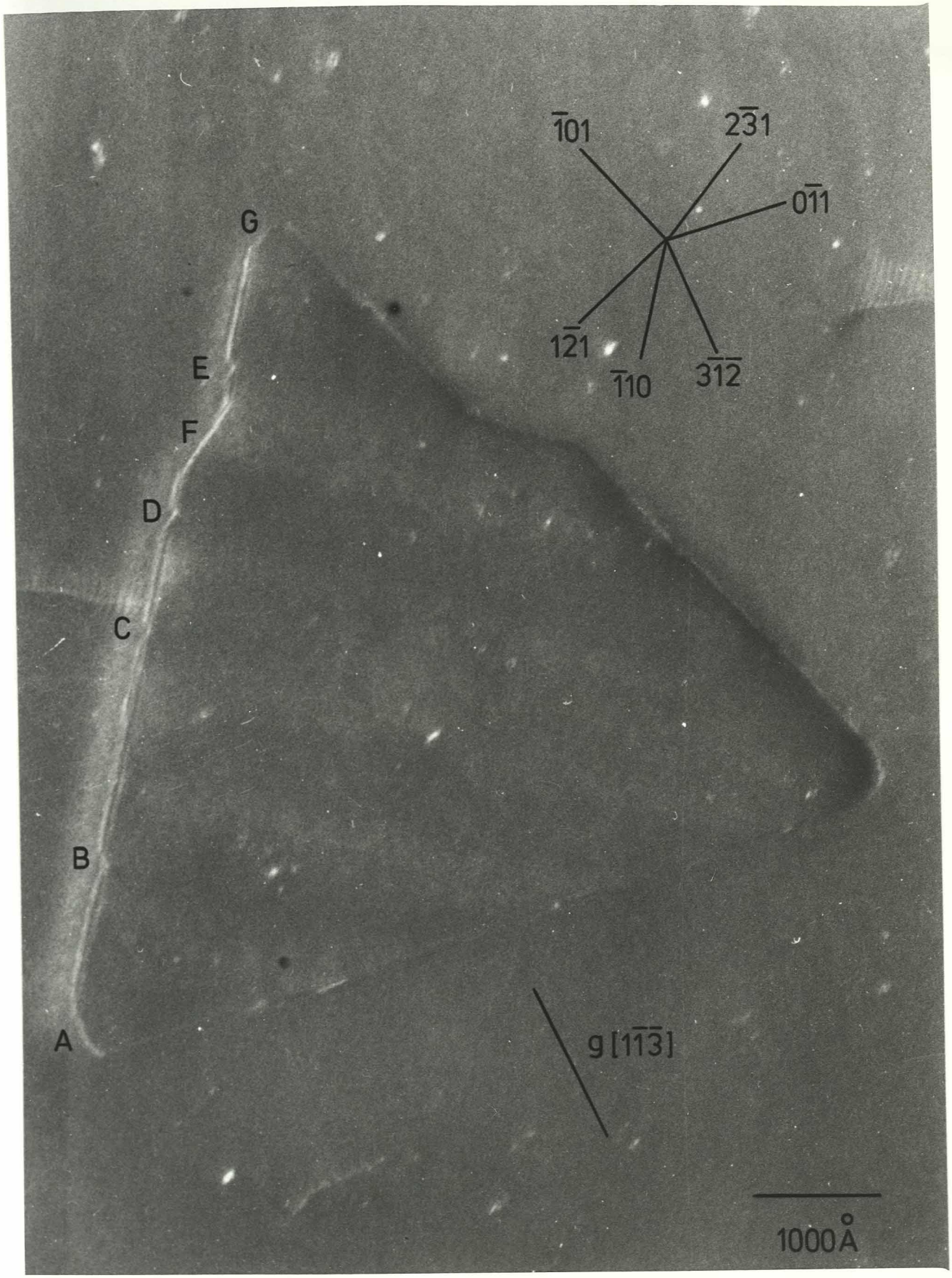
$\bar{1}01$
$2\bar{3}1$
$0\bar{1}1$
$1\bar{2}1$
$\bar{1}10$
$3\bar{1}\bar{2}$
G
E
F
D
C
B
A
g [$1\bar{1}\bar{3}$]
1000 Å

Fig. 10/26 (A) Schematic diagram of the dislocation configuration along the dissociated edge of the Frank loop in fig. 10/27(a). The dissociation width is so large that constriction has not occurred.

The Frank partial dissociation is

$$\frac{a}{3}[111] \rightarrow \frac{a}{6}[110] + \frac{a}{6}[112]$$

obtuse angled dissociation.

(The observer is located within the loop, on the (111) plane).

(B) Frank loop with a 300° corner, showing the extra stair-rod with no constriction.

(C) Heavily jogged non dissociated <123> segment on a Frank loop.

(D) Small jog along the <110> direction with dissociation and constriction.

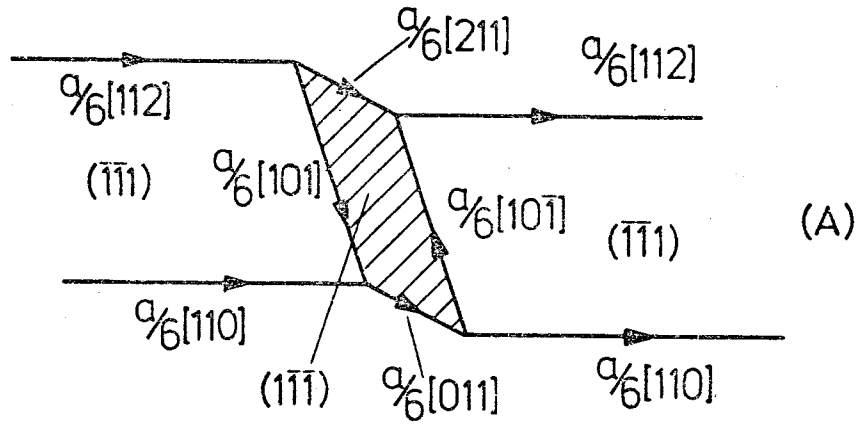
a/6[211]
a/6[112]
a/6[112]
(1̄1̄1)
a/6[101]
a/6[10 1̄]
(1 1̄1)
(A)
a/6[110]
(11 1̄)
a/6[011]
a/6[110]

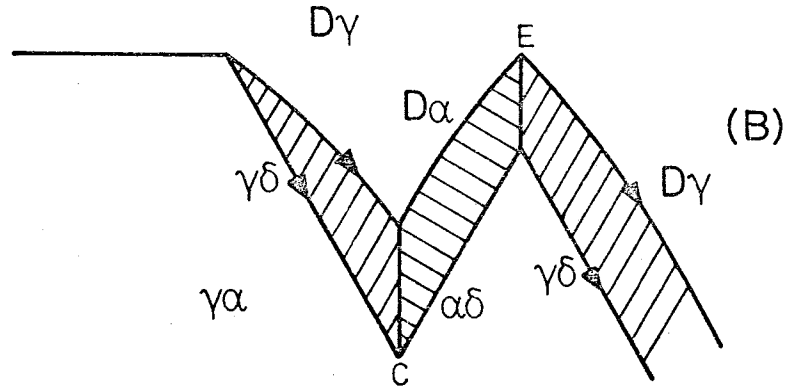
Dγ
E
Dα
(B)
γδ
Dγ
γα
αδ
γδ
C

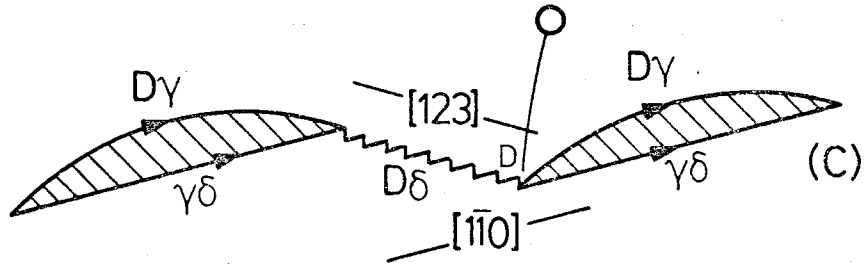
Dγ
[123]
Dγ
D
Dδ
γδ
γδ
(C)
[1 1̄0]

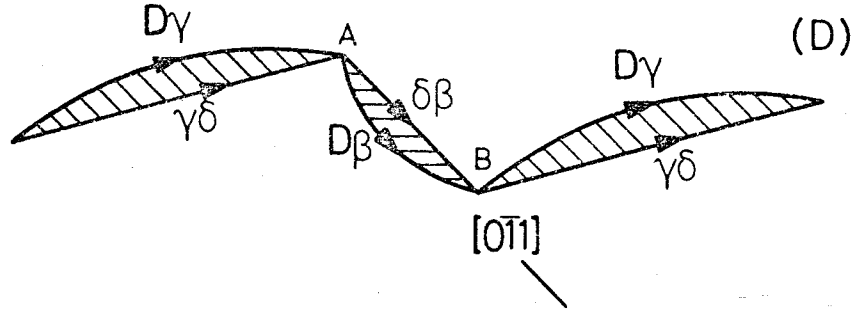
Dγ
A
(D)
δβ
Dγ
γδ
Dβ
B
γδ
[0 1̄1]

Fig. 10/27 Micrographs illustrating the dissociation of Frank loops in Cu 16% Al foils.

(a) $\bar{g}$ [$\bar{1}$11] $\bar{z}$ [211].

Growth of a Frank loop without constriction of the Shockley partial on the plane of dissociation. This loop exhibits an abnormally large dissociation separation and is the only evidence obtained to suggest that Frank loops can grow in this manner.

(b) $\bar{g}$ [$\bar{1}$1$\bar{3}$] $\bar{z}$ [110].

Illustration of the growth of a Frank loop by the movement of constrictions in the Shockley partial. The interesting point about this micrograph, is the increase in separation of constrictions from the lower left to upper right of the loop.

(c)(d) g [$\bar{2}$20] $\bar{z}$ [111].

Growth of a very small Frank loop without any constrictions and growth of a larger Frank loop with 3 constrictions.

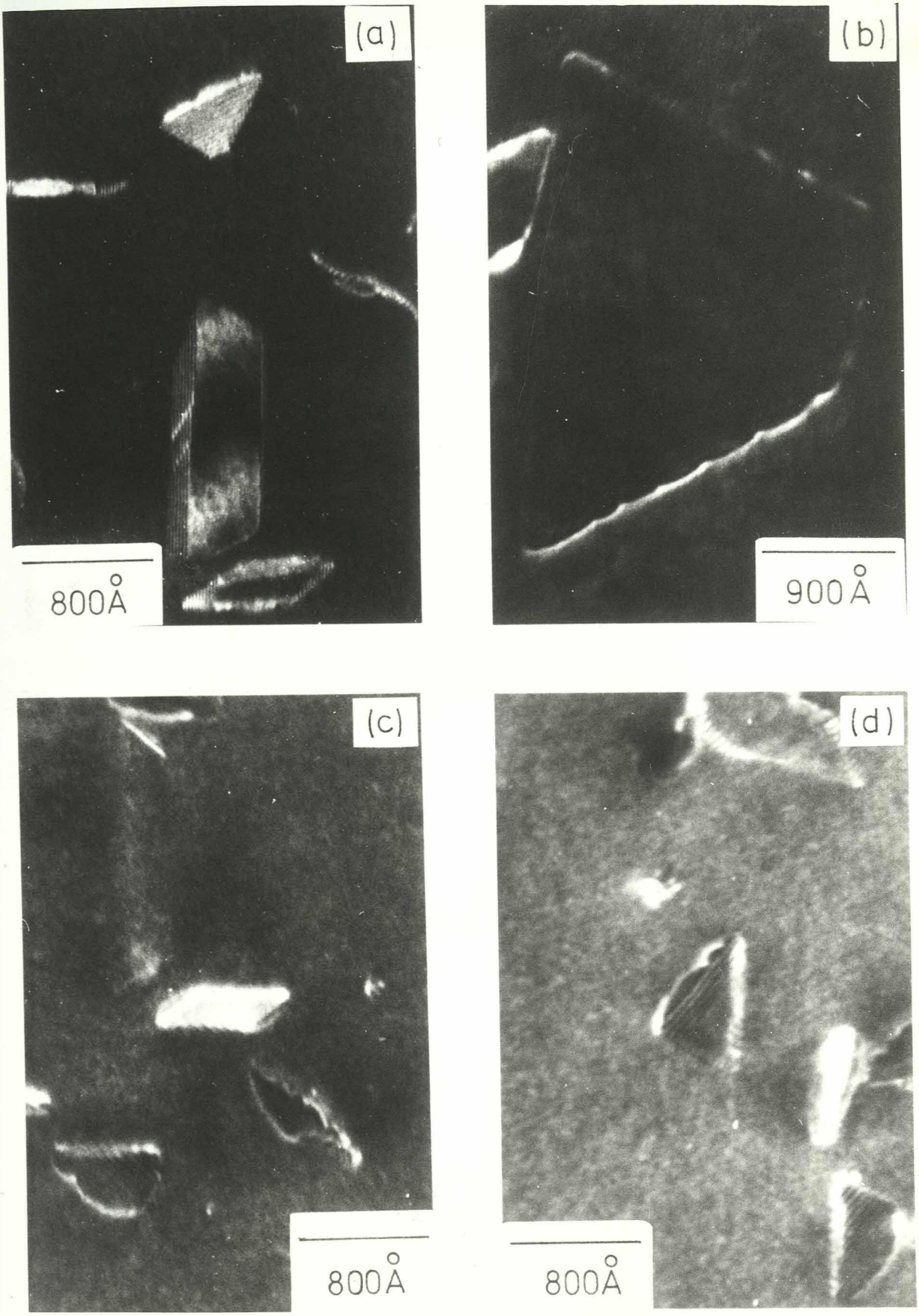
(a)
800Å
(b)
900Å
(c)
800Å
(d)
800Å

Fig. 10/28 Growth of a triangular Frank loop into an irregular loop in copper during electron irradiation at $T_i = 280^{\circ}C$. $\bar{g} = [1\bar{1}\bar{1}]$ $\bar{z}$ [211].

(a) 1 minute irradiation

(b) 3 minutes irradiation

(c) 8 minutes irradiation

(d) 12 minutes irradiation

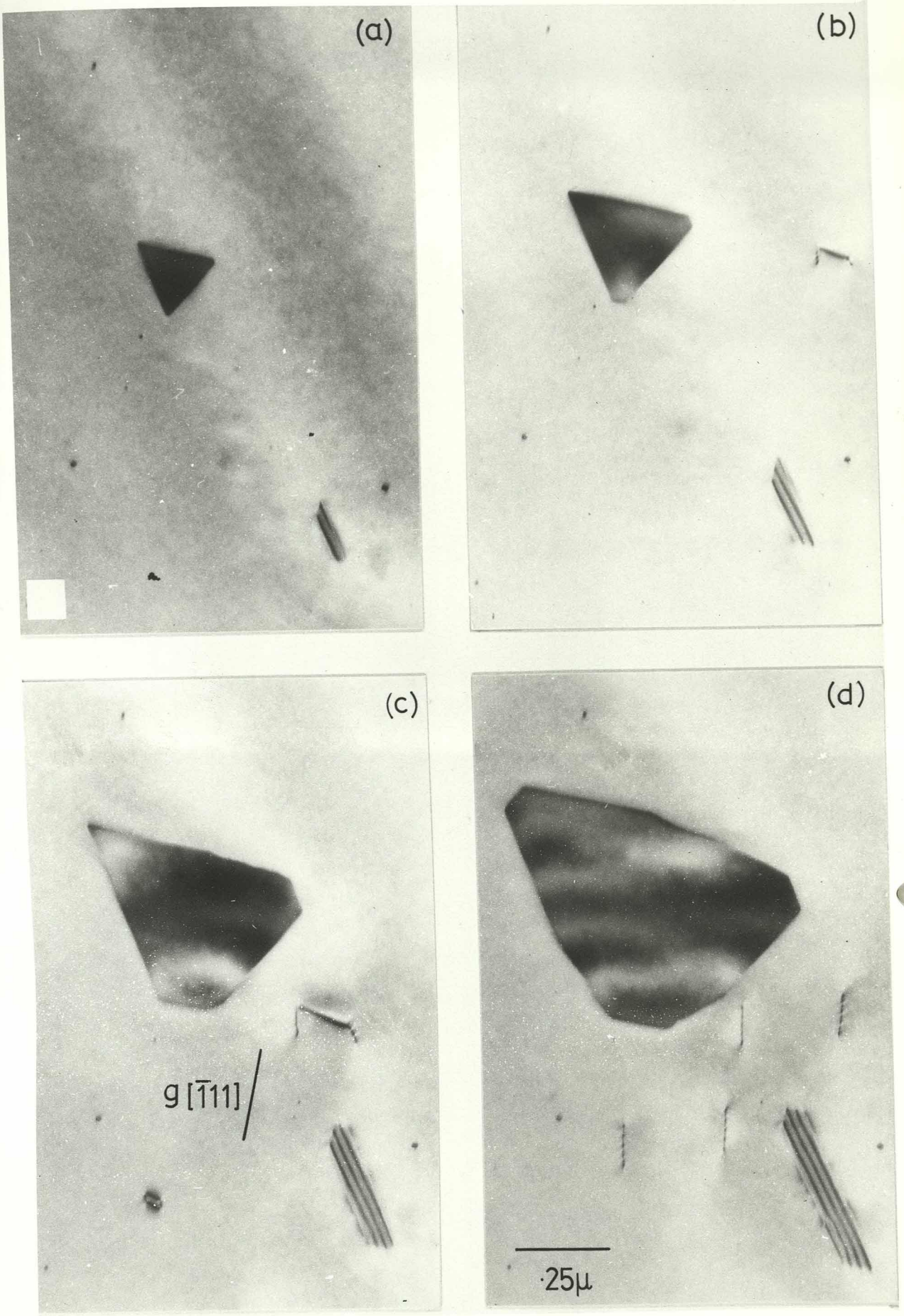
(a)
(b)
(c)
g [$\bar{1}$11]
(d)
·25μ

Fig. 10/29 Mechanism of growth of a triangular Frank loop into a polygonal shaped loop. All the loop corners are constricted.

Fig. D illustrates the resultant dislocation configuration after a dislocation interacted with the stacking fault of a Frank loop. Loop β in fig. 10/30.

Fig. 10/30 Growth of irregular Frank loops in Cu 16% Al after irradiation at $T_i \triangleq 250^{\circ}C$.

Loop α is almost rectangular in shape, with sides parallel to <112> directions. This loop is also interacting strongly with an inclined {111} Frank loop.

Loop β interacts strongly with a dislocation, which appears to be absorbing interstitials, leaving vacancies to agglomerate on the stacking fault. When the dislocation touched the Frank loop, it sheared into a perfect loop of $b = \frac{a}{2}$ <110>, but maintained its original shape.

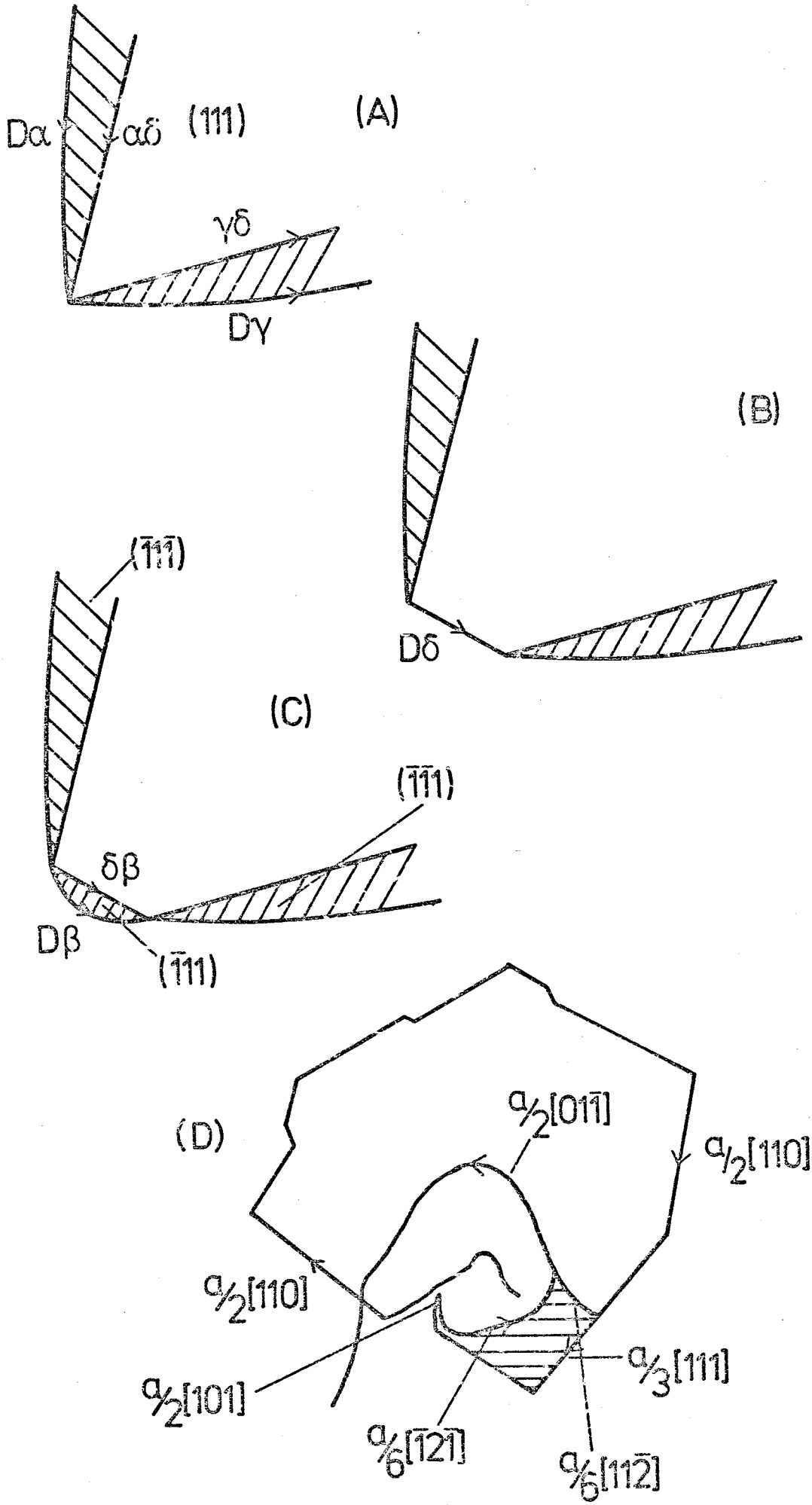
Dα
αδ
(111)
(A)
γδ
Dγ
(B)
Dδ
(C)
(111)
δβ
Dβ
(111)
(D)
a/2[011]
a/2[110]
a/2[110]
a/2[101]
a/3[111]
a/6[121]
a/6[112]

Fig.10/29

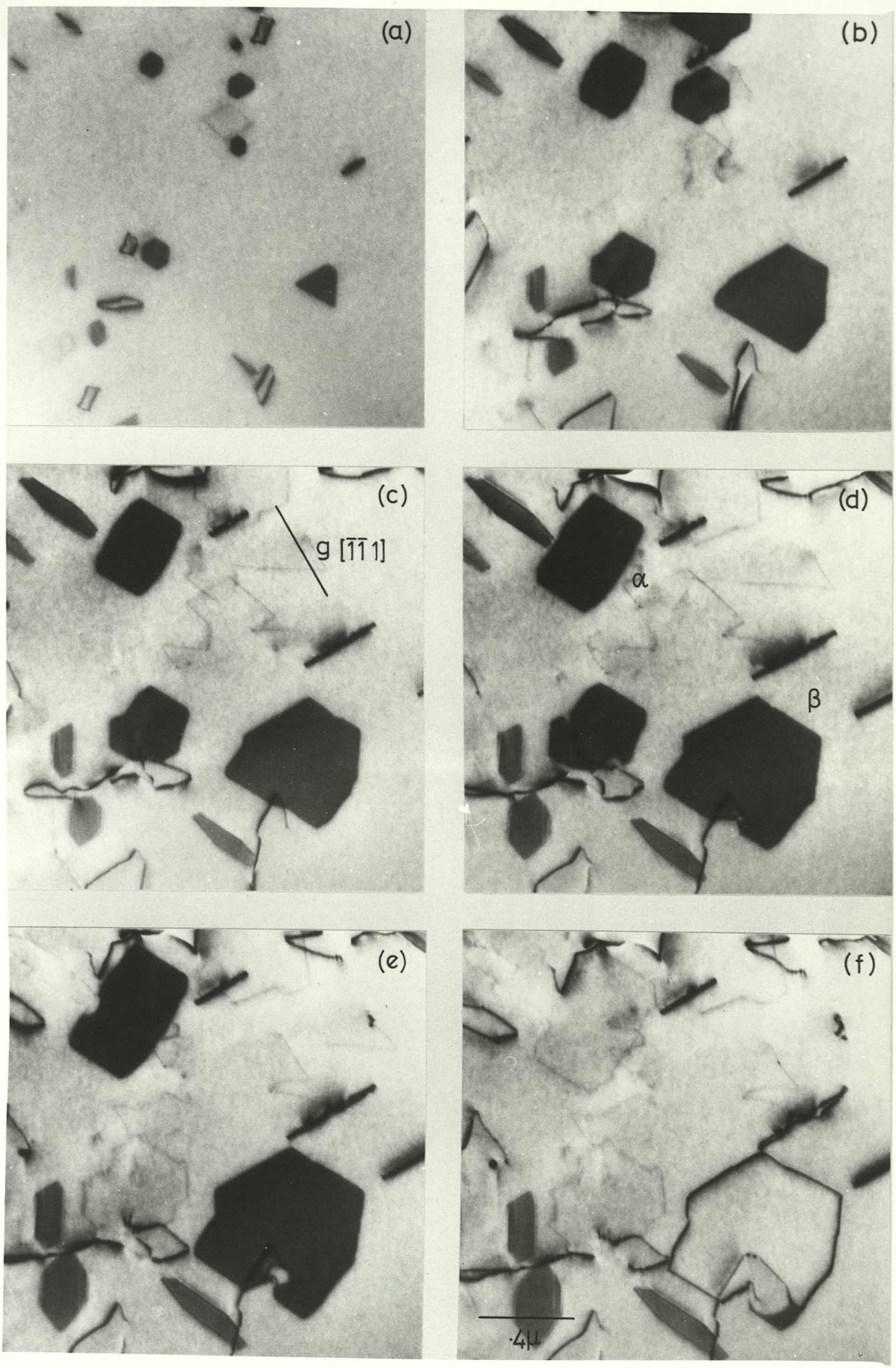

Fig.10/30

Fig. 11/1 Fig. (A) illustrates the distribution of rhombus perfect loops on $\{110\}$ planes as a function of irradiation temperature.

$g = [\bar{1}1\bar{1}]$ $z = [121]$.

(A) $\bar{b} = \frac{a}{2}[1\bar{1}0]$

(B) $\bar{b} = \frac{a}{2}[101]$ foil thickness $\triangleq$ 2400 Å

(C) $\bar{b} = \frac{a}{2}[0\bar{1}1]$

Fig. (B) shows the proportion of loops on each plane as a function of foil thickness $T_i = 210^{o}C$ $g = [\bar{1}\bar{1}1]$ $z = [112]$

(D) $\bar{b} = \frac{a}{2}[0\bar{1}1]$

(E) $b = \frac{a}{2}[10\bar{1}]$

(F) $\bar{b} = \frac{a}{2}[110]$

Cu 16% Al specimen cut from slow grown crystal.

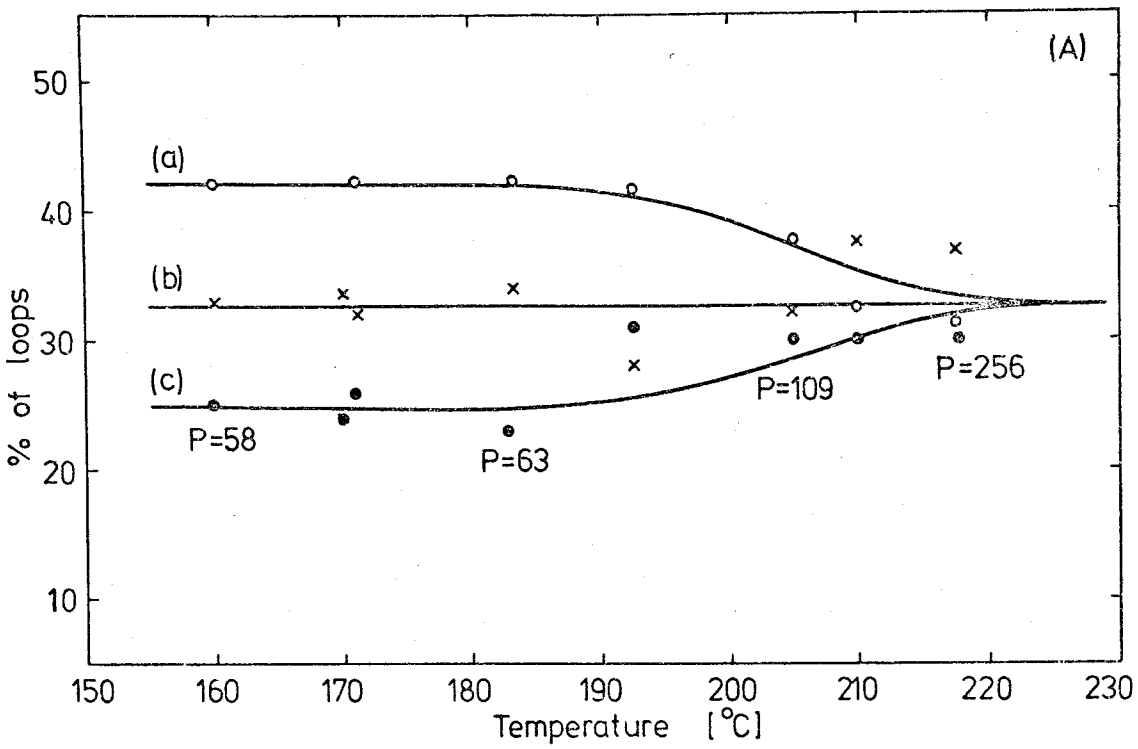
(A)
50
40
30
20
10
% of loops
(a)
(b)
(c)
P=58
P=63
P=109
P=256
150
160
170
180
190
200
210
220
230
Temperature [°C]

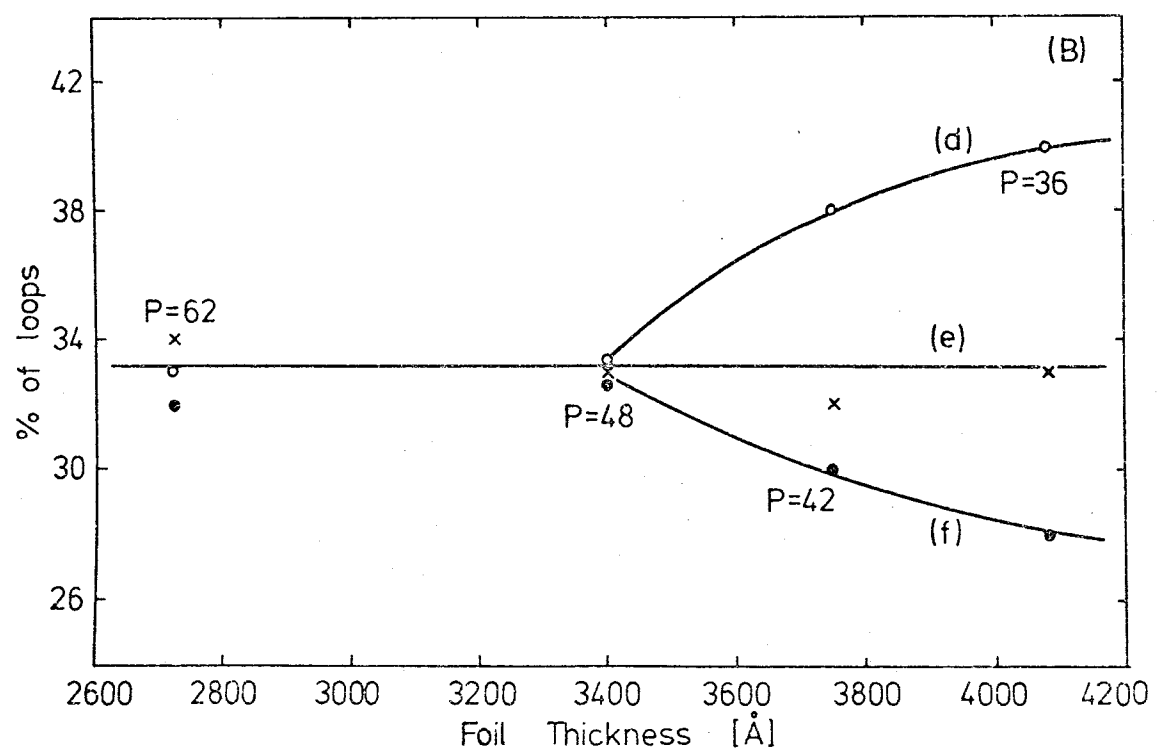
(B)
42
38
34
30
26
% of loops
(d)
P=36
P=62
(e)
P=48
P=42
(f)
2600
2800
3000
3200
3400
3600
3800
4000
4200
Foil Thickness [Å]